

PROCEEDINGS OF SPIE

EUROPTO
SERIES

Optics in Atmospheric Propagation and Adaptive Systems II

Anton Kohnle
Adam D. Devir
Chairs/Editors

23–24 September 1997
London, UK

DISTRIBUTION STATEMENT A

Approved for public release;
Distribution Unlimited

Sponsored by

CNR—The National Research Council of Italy

NASA—National Aeronautics and Space Administration (USA)

EOS—The European Optical Society

SPIE—The International Society for Optical Engineering

The Commission of the European Communities, Directorate General
for Science, Research, and Development

19980617 081



Volume 3219

REPORT DOCUMENTATION PAGE			Form Approved OMB No. 0704-0188	
Public reporting burden for this collection of information is estimated to average 1 hour per response, including the time for reviewing instructions, searching existing data sources, gathering and maintaining the data needed, and completing and reviewing the collection of information. Send comments regarding this burden estimate or any other aspect of this collection of information, including suggestions for reducing this burden to Washington Headquarters Services, Directorate for Information Operations and Reports, 1215 Jefferson Davis Highway, Suite 1204, Arlington, VA 22202-4302, and to the Office of Management and Budget, Paperwork Reduction Project (0704-0188), Washington, DC 20503.				
1. AGENCY USE ONLY (Leave blank)		2. REPORT DATE 21 May 1998		3. REPORT TYPE AND DATES COVERED Conference Proceedings
4. TITLE AND SUBTITLE Optics in Atmospheric Propagation and Adaptive Systems II			5. FUNDING NUMBERS F7LEOBF6170897W0251	
6. AUTHOR(S) Anton Kohnle and Adam D. Devir (Conference Chairs/Editors)				
7. PERFORMING ORGANIZATION NAME(S) AND ADDRESS(ES) Research Institute for Optics Schloss Kressbach Tubingen D 72072 Germany			8. PERFORMING ORGANIZATION REPORT NUMBER N/A	
9. SPONSORING/MONITORING AGENCY NAME(S) AND ADDRESS(ES) EOARD PSC 802 BOX 14 FPO 09499-0200			10. SPONSORING/MONITORING AGENCY REPORT NUMBER CSP 97-1066	
11. SUPPLEMENTARY NOTES				
12a. DISTRIBUTION/AVAILABILITY STATEMENT Approved for public release; distribution is unlimited.			12b. DISTRIBUTION CODE A	
13. ABSTRACT (Maximum 200 words) The Final Proceedings for Optics in Atmospheric Propagation and Adaptive Systems II, 23 September 1997 - 26 September 1997 Propagation and imaging through optical turbulence; propagation and imaging through inhomogeneous and dense media; multiple scattering effects on LIDAR and imager performance; imaging of ground based and airborne objects from space and vice versa; propagation models and correction methods for atmospheric effects in remote sensing; techniques for mitigation of atmospheric effects.				
14. SUBJECT TERMS Remote Sensing, Atmospheric Propagation			15. NUMBER OF PAGES 160	
			16. PRICE CODE N/A	
17. SECURITY CLASSIFICATION OF REPORT UNCLASSIFIED	18. SECURITY CLASSIFICATION OF THIS PAGE UNCLASSIFIED	19. SECURITY CLASSIFICATION OF ABSTRACT UNCLASSIFIED	20. LIMITATION OF ABSTRACT UL	

PROCEEDINGS OF SPIE
EUROPTO
SERIES

***Optics in Atmospheric
Propagation and Adaptive
Systems II***

**Anton Kohnle
Adam D. Devir**
Chairs/Editors

**23–24 September 1997
London, UK**

Sponsored by

CNR—The National Research Council of Italy
NASA—National Aeronautics and Space Administration (USA)
EOS—The European Optical Society
SPIE—The International Society for Optical Engineering
The Commission of the European Communities, Directorate General
for Science, Research, and Development

Published by

SPIE—The International Society for Optical Engineering



Volume 3219

SPIE is an international technical society dedicated to advancing engineering and scientific applications of optical, photonic, imaging, electronic, and optoelectronic technologies.

DTIC QUALITY INSPECTED 1



The papers appearing in this book comprise the proceedings of the meeting mentioned on the cover and title page. They reflect the authors' opinions and are published as presented and without change, in the interests of timely dissemination. Their inclusion in this publication does not necessarily constitute endorsement by the editors or by SPIE.

Please use the following format to cite material from this book:

Author(s), "Title of paper," in *Optics in Atmospheric Propagation and Adaptive Systems II*, Anton Kohnle, Adam D. Devir, Editors, Proceedings of SPIE Vol. 3219, page numbers (1998).

ISSN 0277-786X

ISBN 0-8194-2651-2

Published by

SPIE—The International Society for Optical Engineering

P.O. Box 10, Bellingham, Washington 98227-0010 USA

Telephone 360/676-3290 (Pacific Time) • Fax 360/647-1445

Copyright ©1998, The Society of Photo-Optical Instrumentation Engineers.

Copying of material in this book for internal or personal use, or for the internal or personal use of specific clients, beyond the fair use provisions granted by the U.S. Copyright Law is authorized by SPIE subject to payment of copying fees. The Transactional Reporting Service base fee for this volume is \$10.00 per article (or portion thereof), which should be paid directly to the Copyright Clearance Center (CCC), 222 Rosewood Drive, Danvers, MA 01923. Payment may also be made electronically through CCC Online at <http://www.directory.net/copyright/>. Other copying for republication, resale, advertising or promotion, or any form of systematic or multiple reproduction of any material in this book is prohibited except with permission in writing from the publisher. The CCC fee code is 0277-786X/98/\$10.00.

Printed in the United States of America.

Contents

v *Conference Committee*

SESSION 1 CHARACTERIZATION OF THE PROPAGATION ENVIRONMENT

- 2 **Comparison of atmospheric transmittance measurements in the 3- to 5- μ m and 8- to 12- μ m spectral regions with MODTRAN: considerations for long near-horizontal path geometries [3219-01]**
A. J. Ratkowski, G. P. Anderson, J. H. Chetwynd, R. M. Nadile, Air Force Research Lab. (USA); A. D. Devir, Technion—Israel Institute of Technology; T. D. Conley, Boston College (USA)
- 11 **Performance characterization and ground testing of an airborne CO₂ differential absorption lidar system [3219-02]**
D. C. Senft, Boeing Defense and Space Group (USA); M. J. Fox, Air Force Research Lab. (USA); R. R. Bousek, Boeing Defense and Space Group (USA); J. A. Dowling, Applied Technology Associates (USA); D. A. Richter, Kaman Sciences Corp. (USA); B. T. Kelly, Applied Technology Associates (USA)
- 20 **Multifunctional laser system for measuring regular and random optical refraction in the atmosphere [3219-03]**
Yu. D. Kopytin, V. V. Nosov, E. V. Nosov, Institute of Atmospheric Optics (Russia)
- 29 **Use of nondispersion correlation spectroscopy for remote sensing of CO in combustion gases [3219-05]**
V. P. Kabashnikov, N. V. Kuzmina, N. S. Metelskaya, Institute of Physics (Belarus)
- 34 **Optical characteristics of aerosol in the coastal area [3219-07]**
T. Skakalova, I. Grigorov, O. Parvanov, I. N. Kolev, Institute of Electronics (Bulgaria)

SESSION 2 PROPAGATION AND IMAGING THROUGH INHOMOGENOUS MEDIA

- 44 **Aerosol light scatter vs turbulence effects in image blur [3219-08]**
N. S. Kopeika, D. Sadot, I. Dror, Ben-Gurion Univ. of the Negev (Israel)
- 52 **Characteristics of shipborne targets in warm coastal environments in mid- and longwave IR [3219-09]**
K. Stein, FGAN Forschungsinstitut für Optik (FRG)
- 65 **Satellite feature reconstruction using reflective tomography: field results [3219-10]**
C. L. Matson, Air Force Research Lab. (USA); D. Holland, Lockheed Martin Engineering and Science/NASA Stennis Space Ctr. (USA); D. F. Pierrottet, Air Force Research Lab. (USA); D. Ruffatto, Textron Systems Division (USA); S. R. Czyzak, D. E. Mosley, Air Force Research Lab. (USA)
- 73 **Low-cost seeing monitor to measure the isokinetic patch on the edge of the moon [3219-12]**
A. Ghedina, Univ. of Padua (Italy); R. Ragazzoni, A. Baruffolo, Astronomical Observatory of Padua (Italy); J. Farinato, Univ. of Padua (Italy)

SESSION 3 PROPAGATION AND IMAGING THROUGH OPTICAL TURBULENCE

- 84 **Carrier-to-noise ratio for an equal-gain coherent laser radar receiver array system: theory and experiment [3219-14]**
L. C. Andrews, D. E. Kelly, R. L. Phillips, A. R. Weeks, J. E. Harvey, J. Xu, C. L. Gagge, A. Notash, G. Luvera, R. G. Sellar, Univ. of Central Florida and CREOL/Univ. of Central Florida (USA)
- 93 **Some aspects of the beam-pointing instability problems in laser beacon generation [3219-16]**
V. A. Parfenov, S.I. Vavilov State Optical Institute (Russia)
- 98 **Effective outer scale of turbulence for imaging through the atmosphere [3219-17]**
V. P. Lukin, B. V. Fortes, E. V. Nosov, Institute of Atmospheric Optics (Russia)
- 107 **Method for fast computation of infrared radiation from heated turbulent jets viewed through thick atmospheric layers [3219-18]**
A. I. Bril, V. P. Kabashnikov, Yu. V. Khodyko, N. V. Kuzmina, Institute of Physics (Belarus)
- 116 **Probability distribution of laser-beam wandering on near-land atmospheric range [3219-19]**
V. L. Okoulov, G. Yu. Snezhkov, A. P. Shestakov, V. I. Venglyuk, Research Institute for Complex Testing of Optoelectronic Devices (Russia)

SESSION 4 MITIGATION OF ATMOSPHERIC EFFECTS AND SYSTEMS PERFORMANCE

- 124 **Linear phase conjugation for atmospheric aberration compensation [3219-21]**
R. J. Grasso, E. A. Stappaerts, Northrop Grumman Corp. (USA)
- 133 **Negative optical feedback correction for the extended range of distortions [3219-24]**
V. Yu. Venediktov, S.I. Vavilov State Optical Institute (Russia)
- 138 **Adaptive optics using a liquid crystal phase modulator in conjunction with a Shack-Hartmann wavefront sensor and zonal control algorithm [3219-25]**
D. C. Dayton, S. C. Sandven, Applied Technology Associates (USA); J. D. Gonglewski, Air Force Research Lab. (USA); S. L. Browne, Optical Sciences Co. (USA); S. C. Rogers, Willow Systems, Ltd. (USA); S. W. McDermott, Logicon R&D Associates (USA)
- 147 **Polychrome correction for telescope lens distortions using a liquid crystal optically addressed spatial light modulator [3219-26]**
V. A. Berenberg, A. A. Leshchev, M. V. Vasil'ev, V. Yu. Venediktov, S.I. Vavilov State Optical Institute (Russia)
- 152 **System electronic design for a telescope-mounted deformable mirror system [3219-27]**
S. C. Rogers, S. W. McDermott, Logicon R&D Associates (USA); S. C. Sandven, Applied Technology Associates, Inc. (USA)
- 160 *Author Index*

Conference Committee

Conference Chairs

Anton Kohnle, FGAN Forschungsinstitut für Optik (FRG)
Adam D. Devir, Technion—Israel Institute of Technology

Cochairs

Luc R. Bissonnette, Defence Research Establishment Valcartier (Canada)
Piero Bruscaaglioni, University of Florence (Italy)
Christopher Dainty, Imperial College of Science, Technology and Medicine (UK)
John D. Goglewski, Air Force Research Laboratory (USA)
Marc Séchaud, ONERA (France)
Jennifer C. Ricklin, Army Research Laboratory (USA)

Session Chairs

- 1 Characterization of the Propagation Environment
Adam D. Devir, Technion—Israel Institute of Technology
- 2 Propagation and Imaging through Inhomogenous Media
Anton Kohnle, FGAN Forschungsinstitut für Optik (FRG)
- 3 Propagation and Imaging through Optical Turbulence
Jennifer C. Ricklin, Army Research Laboratory (USA)
Christopher Dainty, Imperial College of Science, Technology and Medicine (UK)
- 4 Mitigation of Atmospheric Effects and Systems Performance
John D. Goglewski, Air Force Research Laboratory (USA)

SESSION 1

Characterization of the Propagation Environment

A comparison of atmospheric transmittance measurements in the 3-5 μ m and 8-12 μ m spectral regions with MODTRAN: considerations for long near-horizontal path geometries

A. J. Ratkowski*, G. P. Anderson*, J. H. Chetwynd*, R. M. Nadile*, A. D. Devir** and
T. D. Conley***

(*) USAF Phillips Laboratory, Optical Effects Division (PL/GPO), 29 Randolph Road, Hanscom AFB,
MA 01731-3010, USA

(**) Technion Research and Development Foundation, Electro-Optics Research and Development
Division (EORD), Technion City, Haifa 32000, Israel

(***) Boston College, Institute for Scientific Research, Newton, MA,
02159-1164, USA

ABSTRACT

Radiance measurements conducted during tropospheric operations to detect objects on the Earth's surface from a manned aircraft or from an unmanned airborne vehicle (UAV) will involve long, near-horizontal viewing geometries. The computer code MODTRAN is widely used for the prediction of the propagation of infrared radiation through the lower atmosphere. Consequently, we have undertaken to test the predictions of MODTRAN for the 3-5 and 8-12 micron spectral regions under mid-Eastern desert conditions.

1. MODTRAN

The new MODTRAN4 band model, with its correlated-k Beer's Law algorithm, can efficiently and correctly (usually within 3-5%) calculate the scattering and absorption properties of realistic molecular, aerosol and cloudy environments in the lower and middle atmosphere. The current approach for molecular scattering accommodates line overlap and partial correlations between both molecular species and the solar irradiance, while maintaining automated band model spectral resolution at 2 or 15 cm^{-1} . This new level of evolution and validation will permit improved syntheses and analyses of solar (direct or scattered) and thermal energy as observed from a variety of platforms. This capability is a product of the standard MODTRAN calculations of transmittance, radiance and irradiance, including thermal, solar, and lunar sources.

For instance, comprehensive validation is provided through two basic avenues. The first involves direct comparisons with line-by-line (LBL) calculations, as exemplified by FASE (the line-by-line algorithm jointly developed from FASCOD¹ by DoD and DOE) which provides the molecular standard for layer-effective optical depths, single-scattering albedos, and transmittances. This enables the MODTRAN4 algorithm to be refined for more adaptable spectral resolution plus efficient determination of those layer quantities necessary for multiple-scattering applications, (e.g., DISORT²). The second validation step centers on comparisons with a variety of measurements. Among the latter are ground-based measurements of atmospheric transmission using the sun as a source in the SWIR (3-5 μ m) and LWIR (8-12 μ m); examples for such validation are presented here.

With the development of MODTRAN4^{3,4}, a flexible tool for radiative energy budget calculations is now available. While this version of MODTRAN is grounded in the prior series of USAF radiative-transfer low-resolution band-model (BM) algorithms⁵⁻⁷ and moderate-resolution band-model (BM) algorithms⁸⁻¹⁰, it is distinct in its ability to employ Beer's law to describe local-layer, species-specific transmittance for input to the radiance calculations. While this capability is not always necessary, it allows appropriate handling of multiple scattering (MS) using existing non-BM algorithms^{2,11}. MODTRAN4, while maintaining the basic 2 cm^{-1} spectral resolution, can now complement the MS routines by introducing a correlated-k (CK) capability which is compatible with Beer's law formulations. MODTRAN4 also provides greatly improved predictive capabilities under cloudy and/or heavy aerosol loading conditions in both the visible and IR. It allows the explicit definition of water and ice cloud vertical profiles and spectral data, either by scaling and combining default model clouds or by redefining entirely new model clouds with micro-layering options. More information on MODTRAN4 and its beta release (expected in December 1997) was already presented¹². Note that significant changes have been made in MODTRAN4 to the models of the H_2O continuum, the N_2 pressure-induced continuum, the radiance algorithms, and the band models. Calculations in the IR, when compared to both measurement¹³ and to LBL calculations, usually fall within 5% for all spectral ranges, even at relatively high spectral resolution (less than 5 cm^{-1} , for example).

2. MEASUREMENTS

As noted above, comparisons with measurements are a required validation step. The long, near-horizontal-path atmospheric transmittance measurements were performed from Mount Miron at an altitude of 1200m using the rising sun as a source¹⁴. They were based on accurate radiometric measurements of the sun. Auxiliary to such radiometric measurements, good measurements of the atmospheric profiles: pressure, temperature, water vapor density (in gr/m^3) along the path are highly desired. The theoretical calculations in this paper employ radiosonde data obtained from the Israeli Meteorological Service to specify the pressure, temperature and relative humidity (or water vapor density) of the different atmospheric layers. In the absence of a complete *in situ* sonde measurements (since the sonde profiles were not intersected by the spectroradiometer's line of sight) the sonde profile had to be modified: this modification is based on the results of a sensitivity analysis of the climatology of the desert atmosphere - analysis conducted to assess the importance of variations in temperature, pressure and water density along long optical paths¹⁴. This sensitivity study had shown that the temperature profiles of 4 different months for altitudes up to 11km can be approximated by a single profile that is shifted by a constant temperature difference as shown in Figure 1. In the same way, the study had shown that the profiles of the water vapor density (in gr/m^3) of 4 different months for altitudes up to 11km can be approximated by a single profile that is shifted by a constant multiplicative factor as shown in Figure 2. A similar but almost negligible multiplicative factor is also used for shifting the respective pressure profiles. Following these models, the sonde temperature and water vapor density data were corrected by clamping their profiles to the ground temperature and to the water vapor density conditions that were measured on the ground at an altitude of 1200m. This kind of scaling was found to be within a few percent of the actual measured values. The visibility was measured with a VF-500 visibility sensor (HSS, Inc.). The values of the visibility were found to vary between 35km and 45km during the field test, and were consistent with the observed values (as evaluated by a trained observer) for that day. A rural aerosol model was used since the wind speed was too low to use a desert model and since the values of the visibility confirmed this model.

The actual measurement technique employs the sun as a 5900K blackbody source for transmittance measurements conducted in a near-horizontal, long-slant-path geometry. The measurements were conducted with a dual-channel spectroradiometer with an aperture of 20 cm and a field of view (FOV) of 2 mrad. A circular-variable-filter (CVF) with spectral resolution of 4% of the transmitted wavelength covering the spectral regions from 2.8 to $5.6\mu\text{m}$ and from 6.9 to $13.8\mu\text{m}$ was employed to measure the transmitted solar spectral radiance. A dichroic mirror separated these two spectral regions to two separate InSb and MCT detectors. The center of the FOV was aligned with a precise theodolite and the spectral measurements were performed at predetermined zenith angles, when the FOV was filled by the disc of the sun. After each measurement of the sun, the FOV was aimed outside the sun disc to check for scattered radiation. The scattered IR radiation was negligible in comparison to the direct sun radiation. The same can be said about the effect of the radiation from the internal blackbody of the radiometer and the calculated path radiance. The measured transmittance values were obtained from a comparison between the radiometric signal of the sun and that of a 1273K blackbody source. Additional details on the experiment and the measurements can be found in the literature¹⁴.

3. CALCULATED RESULTS

The measurements reported earlier¹⁴ were for 11 different solar elevations (90°- the zenith angle): 0°, 1°, 2°, 4°, 6°, 8°, 10°, 14°, 18°, 25° and 30°. In this paper the results for only four solar elevations will be reported: 1°, 2°, 8°, and 30°. Initial calculations were based on the predictions of the old (and now obsolete) LOWTRAN7 code. The predicted transmittance values were convolved to match the slit-response-function (SRF) of the CVF used for wavelength dispersion of the measured spectral data. It should be noted that MODTRAN4 has a new capability to register the calculations in wavelength with wavelength-driven scanning and/or filter functions. The old predicted transmittance values (after the above mentioned convolution) indicated that especially for very low observing angles (1° and 2°), the spectral match between the measured data and a LOWTRAN7 calculation, were not good. This discrepancy is more pronounced when the shape factor in the 3-5 μ m spectral region is considered. However, there is now an excellent agreement in this spectral region when the data is compared with MODTRAN4, as shown in Figures 3 and 4. Similar agreement was obtained for moderate and high solar elevation angles (8° and 30°), as shown in Figures 5 and 6.

The differences between the experimental data and the predictions of MODTRAN4 in the 8-12 μ m spectral region at very low observing angles (1° and 2°) remain in the shape of the predicted spectra. The differences are more pronounced with respect to the relative magnitudes of the two transmittance peaks, at 8.5 μ m and at 10.5 μ m. These feature differences still appear in the MODTRAN4 calculations and require further investigation, as seen from Figures 7 and 8. However, the growth rate of the measured transmittance at high solar elevation angles (8° and 30°) is in excellent agreement with the measurements, as shown in Figures 9 and 10. It should be noted that the 8-12 μ m spectral region is very sensitive to changes in the water density - changes that can occur in the lower layers of the atmosphere at very long distance from the radiometer, especially for near-horizon optical paths as shown in Figure 5.

CONCLUSIONS

This paper compares experimental measurements in geometries of interest to the UAV or aircraft platform communities with calculations using the latest version of MODTRAN. Previous results indicate a strong dependence of the spectral features of signatures transmitted through the lower atmosphere on the aerosol and on the water vapor content. We plan to conduct sensitivity studies to address their relative importance.

REFERENCES

1. S.A. Clough, F. X. Kneizys, G. T. Anderson, E. P. Shettle, J. H. Chetwynd, L. W. Abreu, and L. A. Hall, "FASCOD3 spectral simulation" *Proceedings of the International Radiation Symposium 1988*, Lenoble and Geleyn, Deepak Publishing.
2. K.S. Stamnes, S. C. Tsay, W. J. Wiscombe, and K. Jayaweera, "Numerically stable algorithm for Discrete-Ordinate-Method Radiative Transfer in multiple scattering and emitting layered media", *Appl. Optics*, 27, pp. 2502-2509, 1988.
3. L.S. Bernstein, A. Berk, D. C. Robertson, P. K. Acharya, G. P. Anderson, and J. H. Chetwynd, "Addition of a correlated-k capability to MODTRAN," *Proceeding of the 1996 IRIS Targets, Backgrounds, and Discrimination Meeting*, 1996.
4. L.S. Bernstein, A. Berk, P.K. Acharya, D.C. Robertson, G.P. Anderson, J.H. Chetwynd and L.M. Kimball, "Very narrow band model calculations of atmospheric fluxes and cooling rates using the MODTRAN code", *J. Atm. Sci.*, 53, pp. 2887-2904, 1996.
5. F.X. Kneizys, E.P. Shettle, W.O. Gallery, J.H. Chetwynd, L.W. Abreu, J.E.A. Selby, R.W. Fenn and R.A. McClatchey, "Atmospheric Transmittance/Radiance: Computer Code LOWTRAN 5", *AFGL-TR-80-0067*, AD A058643, 1980.
6. F.X. Kneizys, E.P. Shettle, W.O. Gallery, J.H. Chetwynd, L.W. Abreu, J.E.A. Selby, S.A. Clough and R.W. Fenn, "Atmospheric Transmittance/Radiance: Computer Code LOWTRAN 6", *AFGL-TR-83-0187*, AD A137796, 1983.
7. F.X. Kneizys, E.P. Shettle, J.H. Chetwynd, L.W. Abreu, G.P. Anderson, W.O. Gallery, J.E.A. Selby and S.A. Clough, "Users Guide to LOWTRAN 7", *AFGL-TR-88-0177*, 1988.
8. A. Berk, L. S. Bernstein, and D. C. Robertson, "MODTRAN: A Moderate Resolution Model for LOWTRAN7", *GL-TR-89-0122*, Air Force Geophys. Lab., Bedford, MA, 1989.
9. F.X. Kneizys, M.L. Hoke, L.W. Abreu, E.P. Shettle, "MODTRAN2: Suitability for remote sensing", *Proc. SPIE*, 1954, *Remote Sensing*, 1993.
10. A. Berk, "Upgrades to the MODTRAN layer cloud/rain models," *Report. SSI-SR-56*, Spectral Sciences, Inc., 99 S. Bedford St., Burlington, MA, 1995.

11. R.G. Isaacs, W. C. Wang, R. D. Worsham, and S. Goldenberg, "Multiple scattering LOWTRAN and FASCOD models," *Appl. Optics*, 26, pp. 1272-1281, 1987.
12. G.P. Anderson, J.H. Chetwynd, A. Berk, L.S. Bernstein and P.K. Acharya, "An algorithm for hyperspectral remote sensing: solar and thermal regimes", Optical Society of America, *Proceedings of Optical Remote Sensing of the Atmosphere*, Sante-Fe, February 10-14, 1997.
13. J. Wang, G.P. Anderson, H.E. Revercomb and R.O. Knuteson, "Validation of FASCOD3 and MODTRAN3: Comparison of model calculations with ground-based and airborne interferometer observations under clear-sky conditions", *Appl. Optics*, 35, pp. 6028-6039, 1996.
14. A.D. Devir, N. Brandman, B. Barzilai and A. Ben-Shalom, "Ground-to-space atmospheric transmittance measurements in the 3-5 μ m and 8-12 μ m spectral regions: Comparisons with LOWTRAN7", *SPIE*, 1971, *Proceedings of the 8th Meeting on Optical Engineering in Israel*, pp. 35-49, 1992.

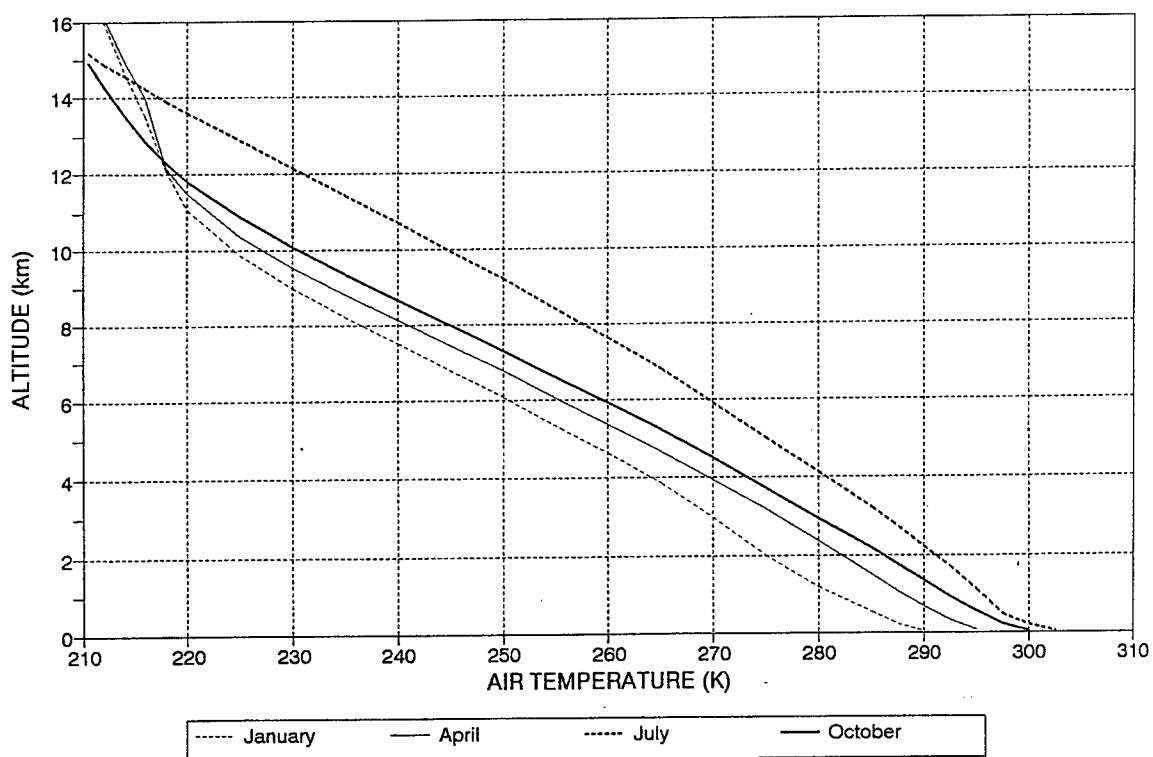


Figure 1: The altitude dependence of day-time temperature profile for four different months.

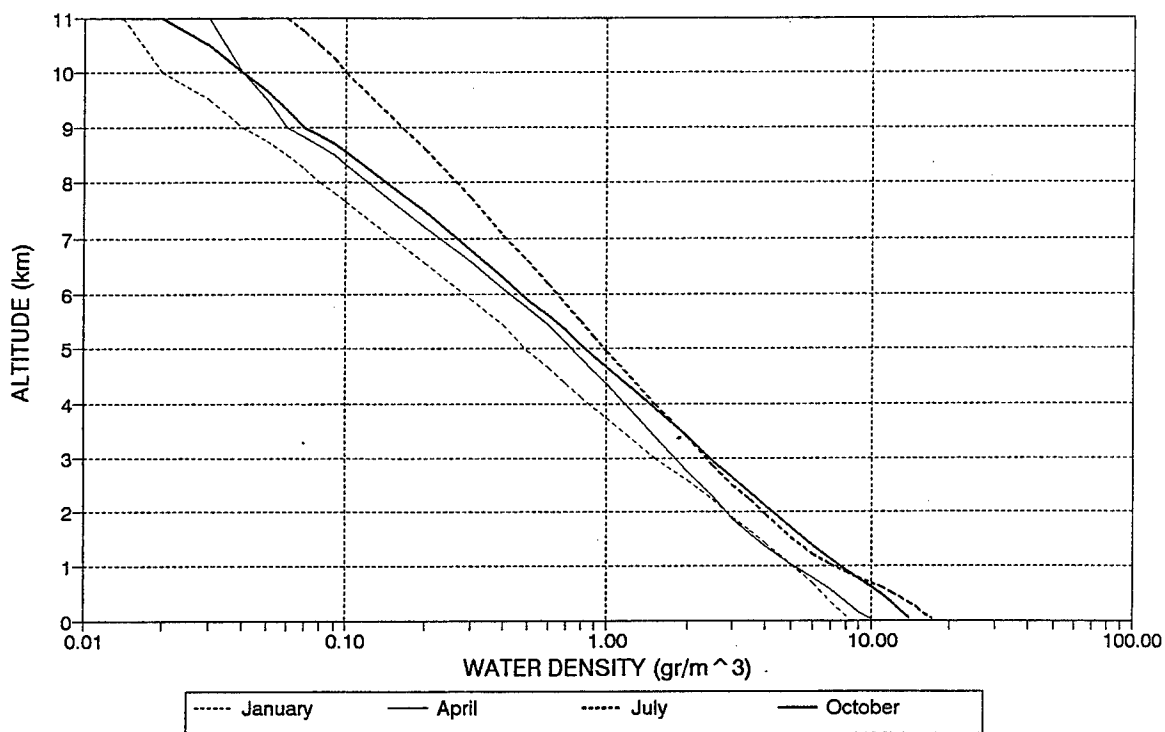


Figure 2: The altitude dependence of day-time water vapor density (gr/m^3) profile for four different months.

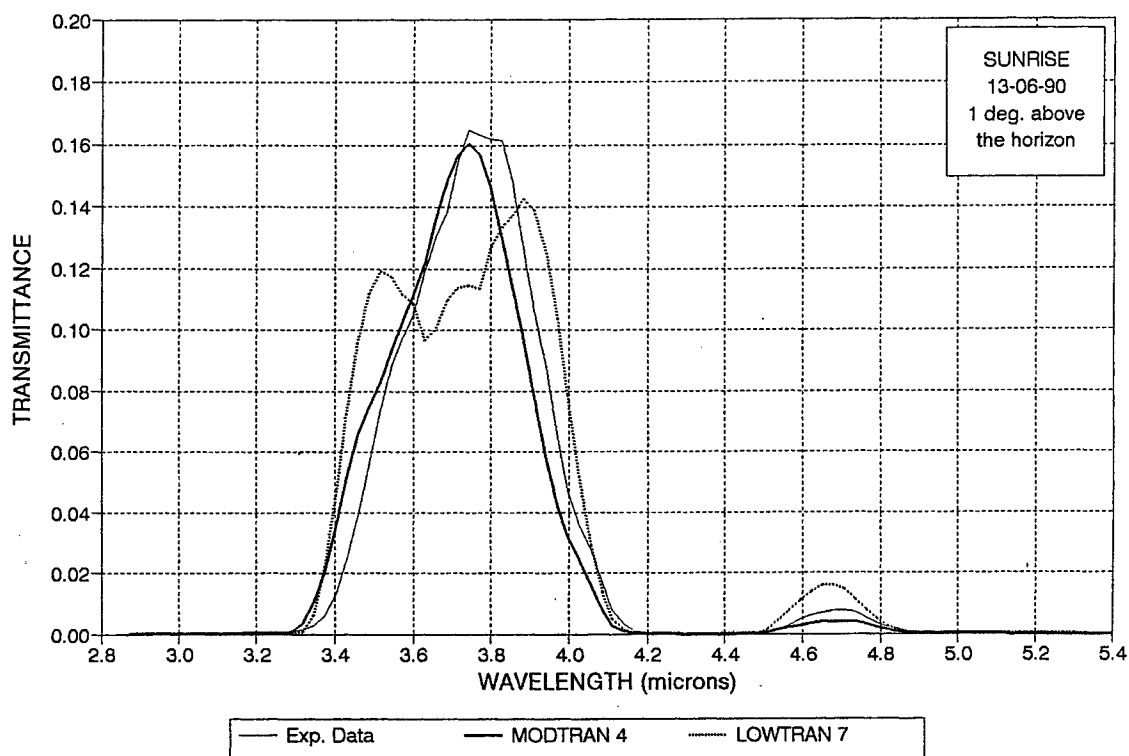


Figure 3: Predicted and measured atmospheric transmittance in the 3-5 μ m spectral region for 1° ground-to-space slant path.

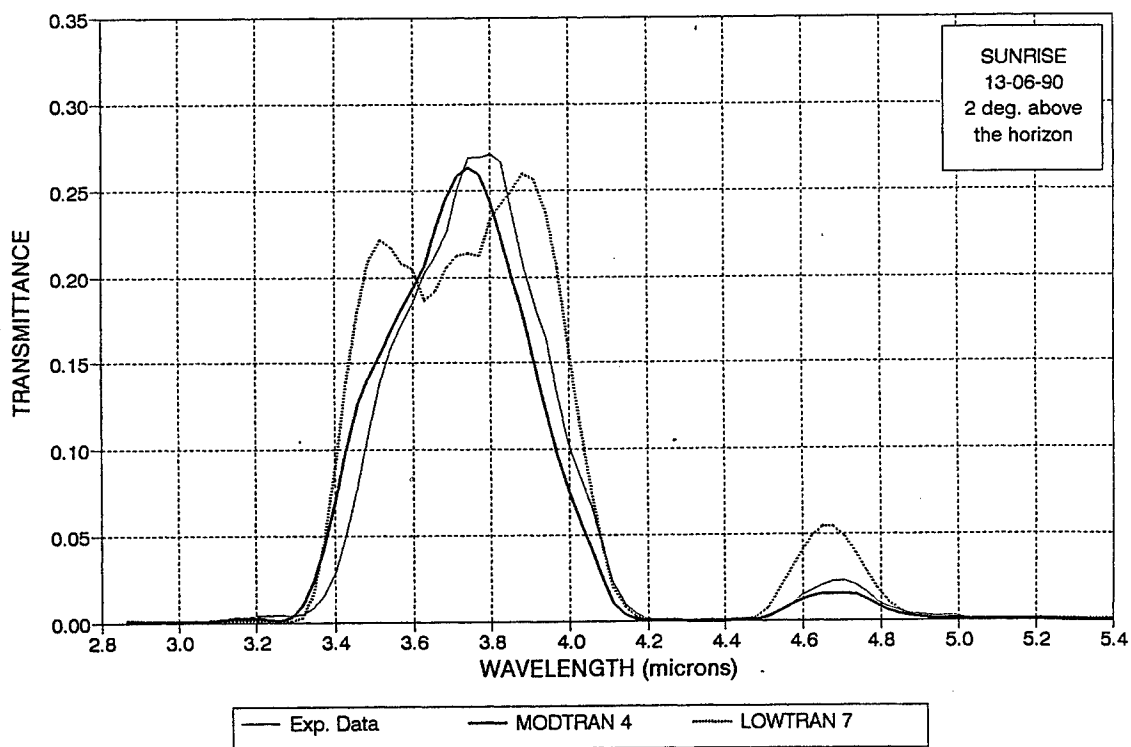


Figure 4: Predicted and measured atmospheric transmittance in the 3-5 μ m spectral region for 2° ground-to-space slant path.

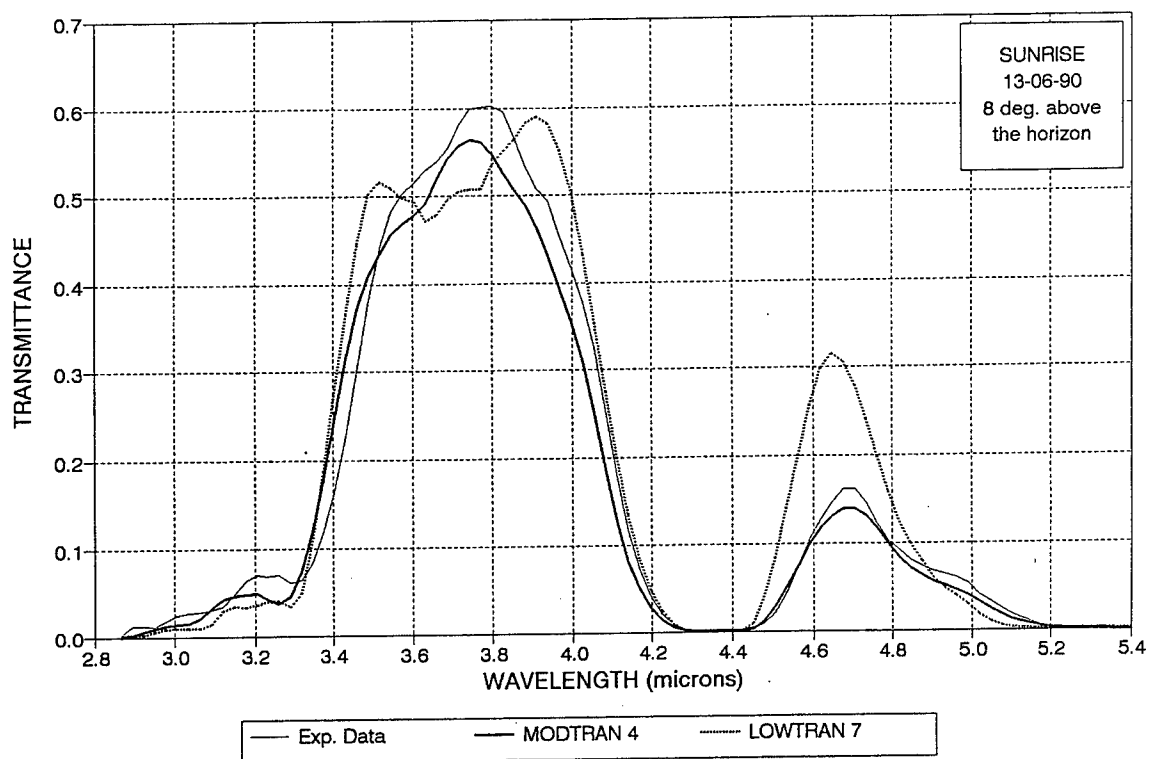


Figure 5: Predicted and measured atmospheric transmittance in the 3-5 μ m spectral region for 8° ground-to-space slant path.

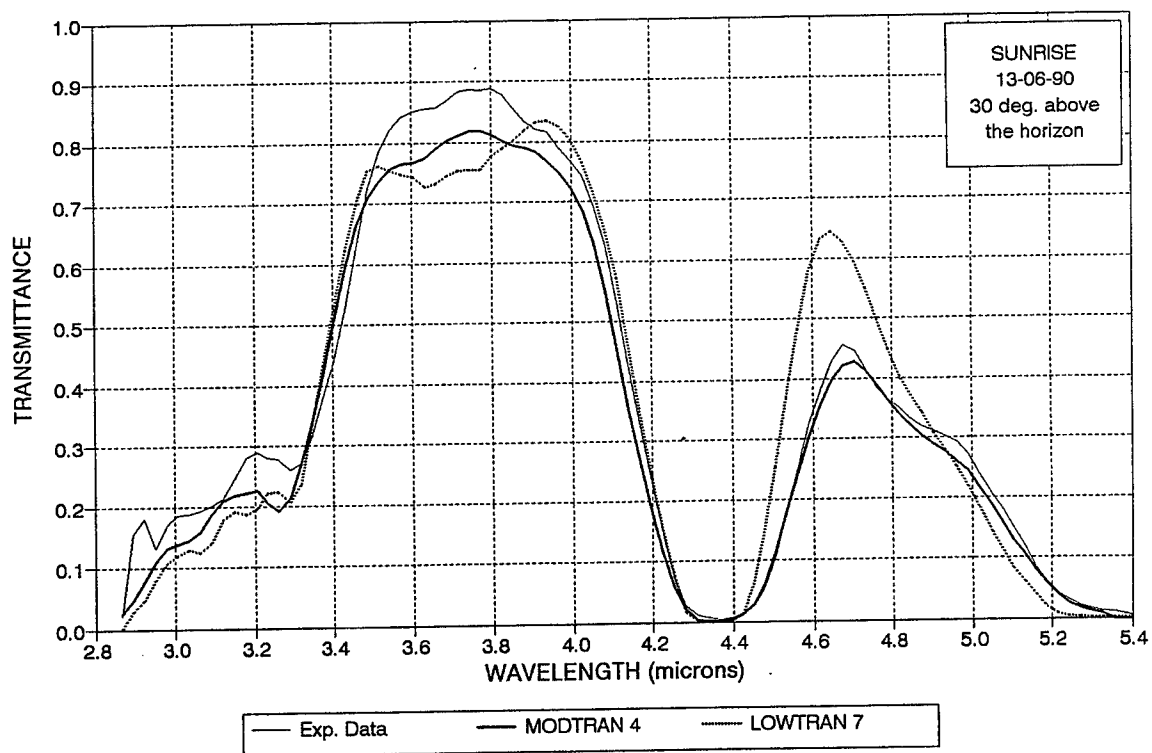


Figure 6: Predicted and measured atmospheric transmittance in the 3-5 μ m spectral region for 30° ground-to-space slant path.

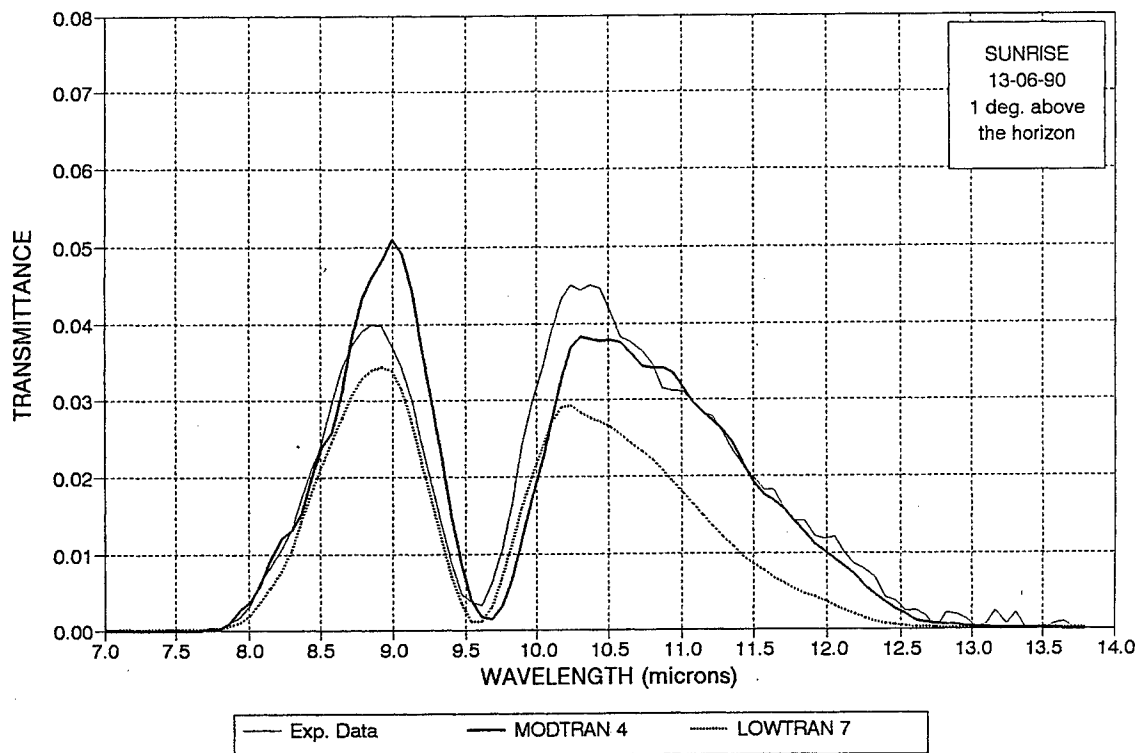


Figure 7: Predicted and measured atmospheric transmittance in the 8-12 μ m spectral region for 1° ground-to-space slant path.

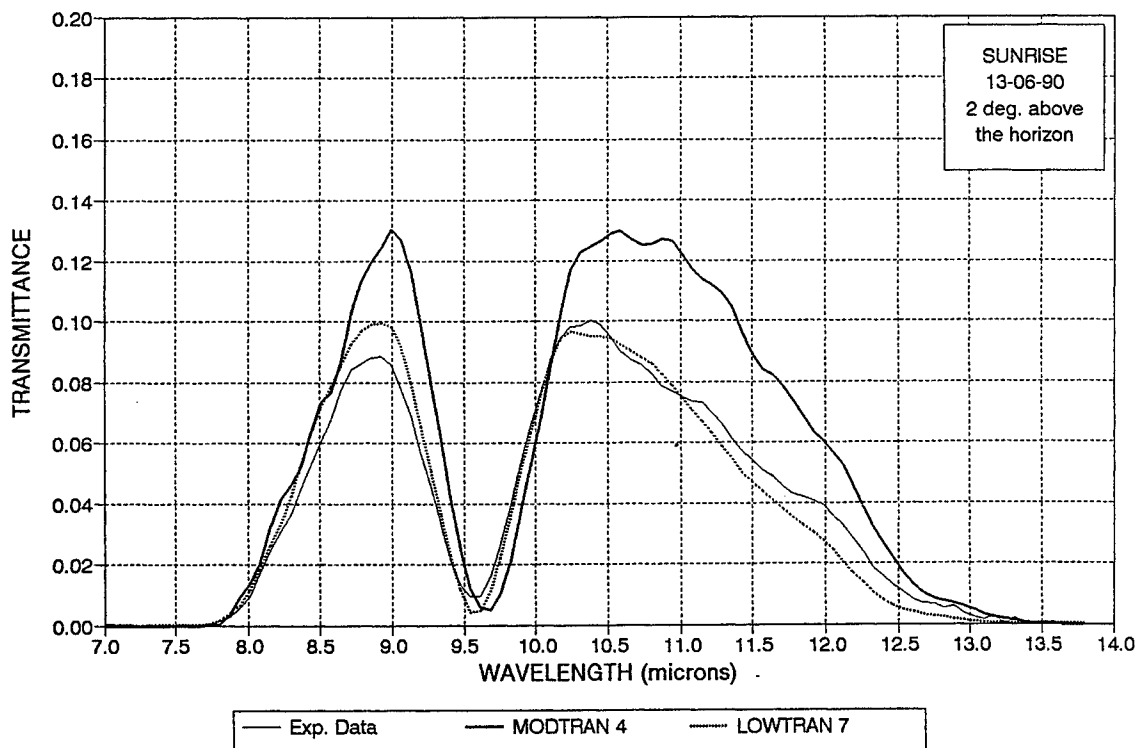


Figure 8: Predicted and measured atmospheric transmittance in the 8-12 μ m spectral region for 2° ground-to-space slant path.

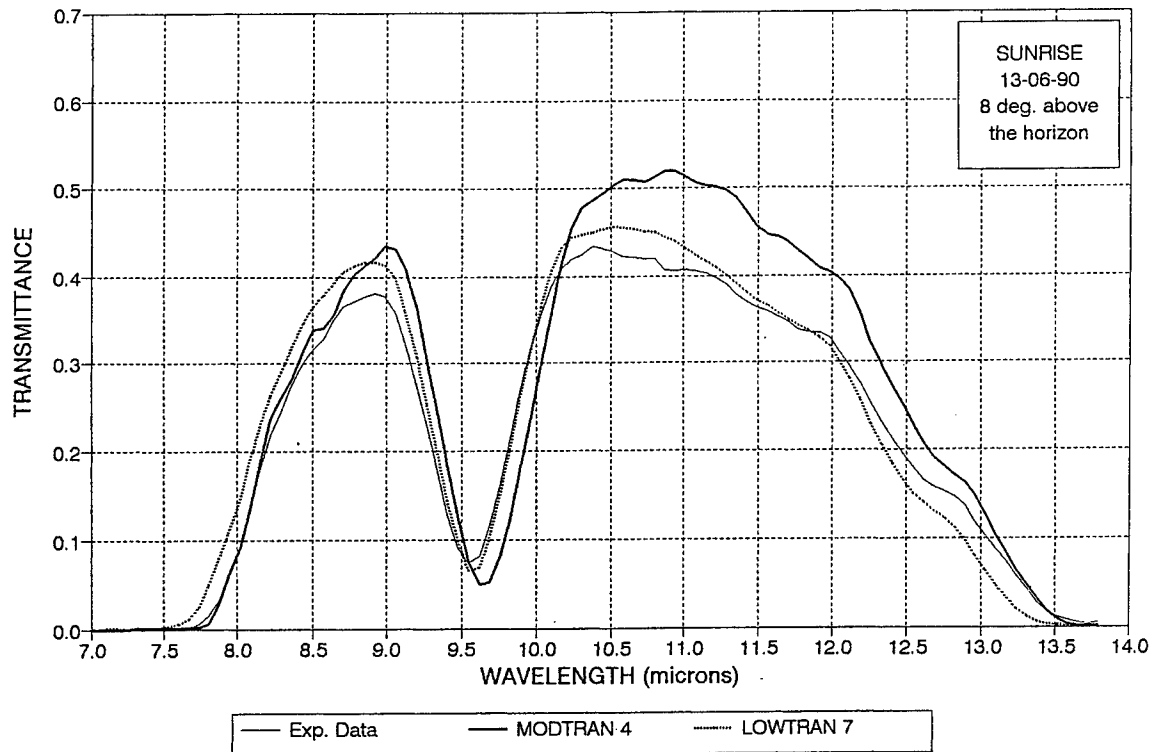


Figure 9: Predicted and measured atmospheric transmittance in the 8-12 μ m spectral region for 8° ground-to-space slant path.

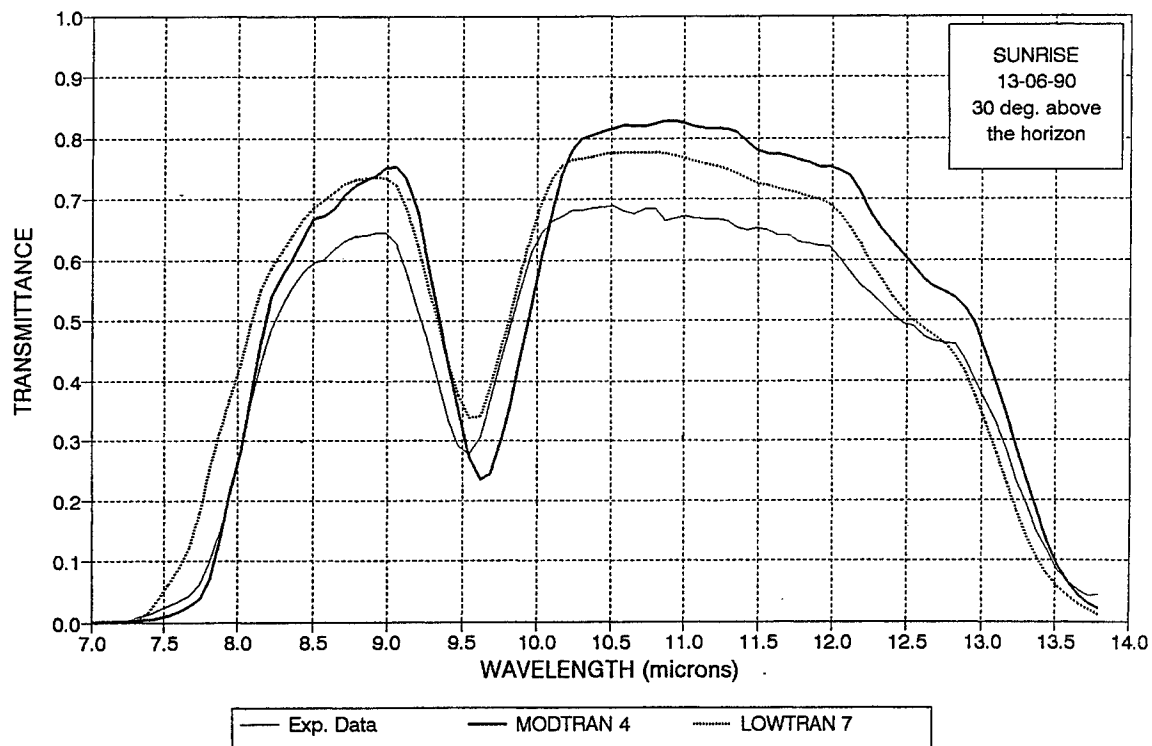


Figure 10: Predicted and measured atmospheric transmittance in the 8-12 μ m spectral region for 30° ground-to-space slant path

Performance Characterization and Ground Testing of an Airborne CO₂ Differential Absorption Lidar System

D. C. Senft¹, M. J. Fox², R. R. Bousek¹, J. A. Dowling³,
D. A. Richter⁴, and B. T. Kelly³

¹Boeing Defense and Space Group
Kirtland AFB, NM

²Phillips Laboratory, PL/LIMS
Kirtland AFB, NM

³Applied Technology Associates
Albuquerque, NM

⁴Kaman Sciences Corporation
Albuquerque, NM

ABSTRACT

The Phillips Laboratory Remote Optical Sensors (ROS) program is developing the Laser Airborne Remote Sensing (LARS) system for chemical detection using the differential absorption lidar (DIAL) technique. The system is based upon a high-power CO₂ laser which can use either the standard ¹²C¹⁶O₂ or the ¹³C¹⁶O₂ carbon dioxide isotopes as the lasing medium, and has output energies in excess of 4 J on the stronger laser transitions. The laser, transmitter optics, receiver telescope and optics, and monitoring equipment are mounted on a flight-qualified optical breadboard designed to mount in the Argus C-135E optical testbed aircraft operated by Phillips Laboratory. The LARS system is being prepared for initial flight experiments at Kirtland AFB, NM, in August 1997, and for chemical detection flight experiments at the Idaho National Engineering Laboratory (INEL) in September 1997. This paper will briefly describe the system characterization, and present some results from the pre-flight ground testing.

Keywords: lidar, airborne lidar, CO₂ DIAL, laser remote sensing

1. SYSTEM CHARACTERIZATION

The optical layout of the LARS system on the flight bench is shown in Figure 1. The system is based upon a high-power CO₂ laser developed by Textron Systems Corporation, and uses a 16" diameter optical telescope. The laser is frequency-agile (able to transmit a different wavelength for each pulse), with a maximum pulse repetition frequency (PRF) of 30 Hz. The laser beam is transmitted and received through a 43 cm x 43 cm ZnSe window mounted on the side of the aircraft. The full-angle divergence of the transmitted beam is ~ 300 μrad, and the receiver full-angle field-of-view is 350 μrad. Pointing and tracking capabilities are provided by the existing Argus gimbal system, and can operate in either an inertial (GPS) mode, or in a very high accuracy contrast tracking mode. Further information on the system development, characteristics, and future direction has been reported previously¹.

The outgoing and return laser pulses are sampled and stored on a per-pulse basis using a 60 MSa/s 12-bit digitizer. The data acquisition system, which is based on a DEC Alpha VME chassis, also computes the basic pulse parameters (such as peak and integrated signal, and time-of-flight) from the digitized data for use in in-flight real-time analysis. The sampling, storage and data reduction is done in real-time for each pulse.

Figure 2 shows the laser output energy on selected $^{12}\text{C}^{16}\text{O}_2$ (C12) and $^{13}\text{C}^{16}\text{O}_2$ (C13) laser lines. The laser windows have been optimized for performance in the C13 9R and 9P region, since these laser lines have significantly lower pulse energies than the 10R and 10P lines. There are approximately 50 lines available for C13 operation (40 lines were measured and displayed in Figure 2), and approximately 60 usable lines for C12. A typical laser pulse is shown in Figure 3. The pulse consists of the gain-switch spike which has a FWHM of ~ 200 ns and contains $\sim 15\%$ of the laser energy, and the pulse tail which extends to ~ 10 μs after the start of the pulse and contains $\sim 85\%$ of the pulse energy.

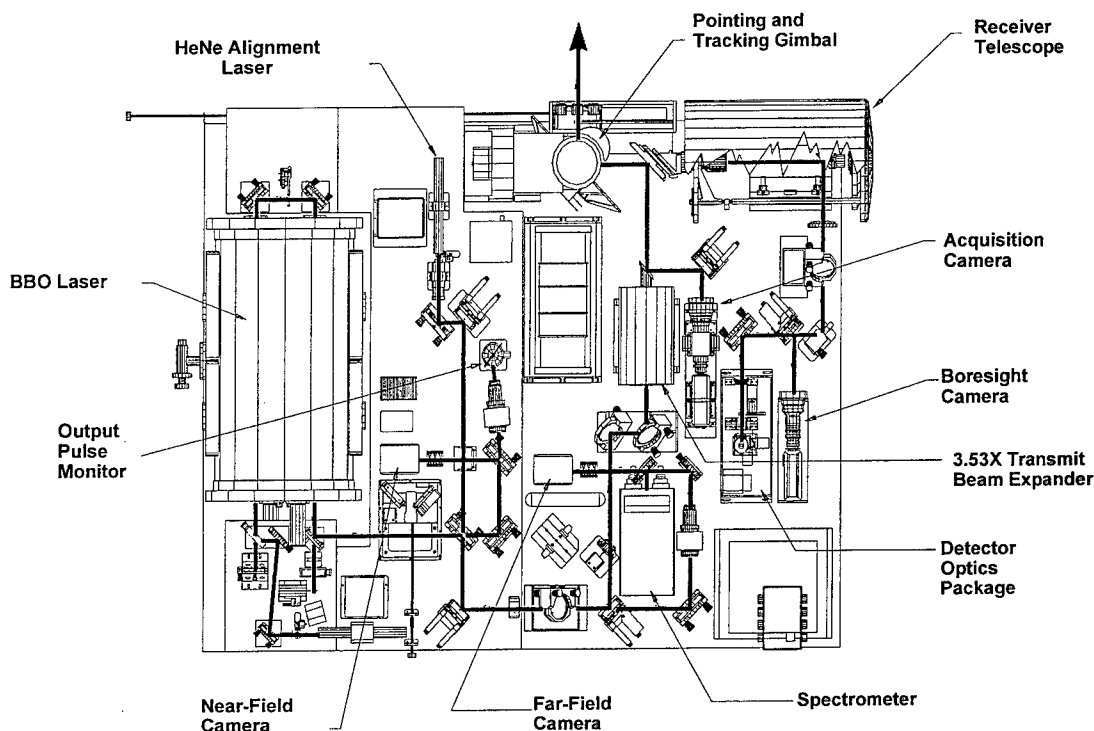


Figure 1. LARS flight bench diagram.

2. EXPERIMENTAL LAYOUT

Ground testing of the LARS system was performed at the ROS test range at Kirtland AFB, beginning in March 1997. The ROS test range (Figure 4) includes downrange target sites (denoted as 2KS, 4KS, 5KS, 6KS, and 7KS) at 2.2, 4.4, 5.8, 6.7, and 7.5 km. A number of transmitter sites are available in the vicinity of the Argus hanger, including a laboratory located inside the hanger, mobile trailers located on the tarmac near the hanger (Pad 4), the Airborne Optical Calibration Facility, and the Argus aircraft itself. The ground test results presented in this paper were accomplished from March to July 1997, with the transmitter system housed in the laboratory located in the Argus hanger. Integration of the system onto the Argus aircraft was begun in July, with additional ground tests scheduled for July and August using the same downrange sites. Ground tests from the aircraft are performed with the aircraft inside the hanger using an elevated roll-up door in the wall of the hanger that faces the target sites, or with the aircraft positioned outside the hanger on Pad 4.

The downrange target sites at 4, 5, 6, and 7 km consist of large earthen berms with concrete pads on top. The 2 km site is located on the side of an arroyo facing the transmitter sites. For the LARS ground tests, 8' x 8' targets made of prepared polystyrene insulation sheets (commonly referred to as 'blueboard') were located at the 2 km and 7 km target sites. Blueboard is commonly used as a target material because it is highly reflective at CO_2 laser wavelengths, and is reasonably Lambertian when the outer skin is removed. Samples of the targets used were measured in the laboratory for

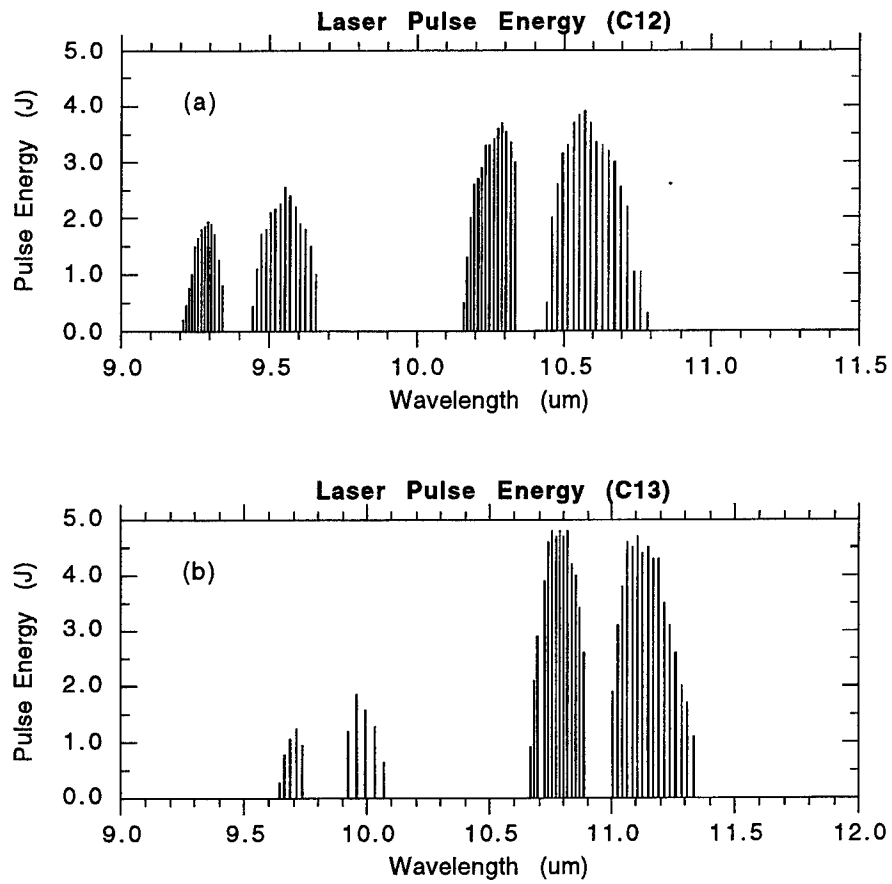


Figure 2. C12 (a) and C13 (b) laser pulse energies.

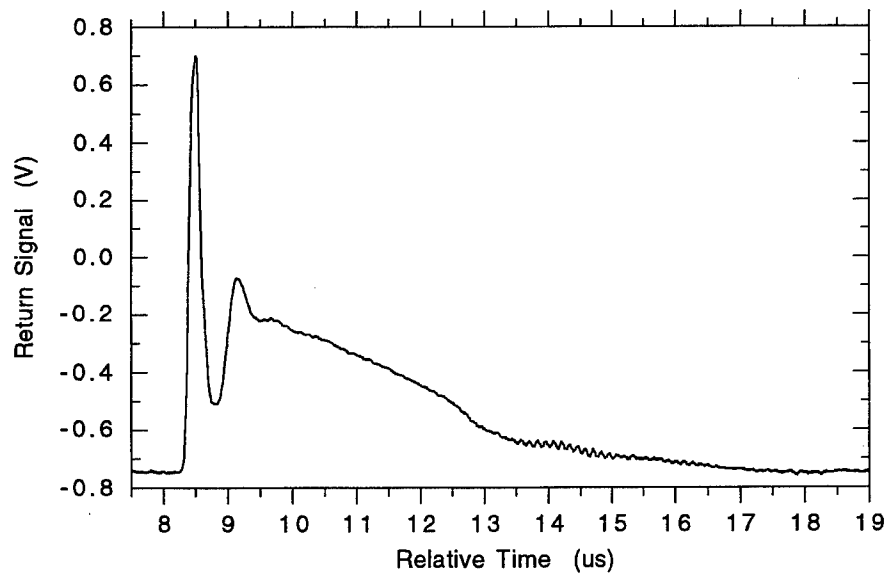


Figure 3. Typical laser pulse temporal waveform.

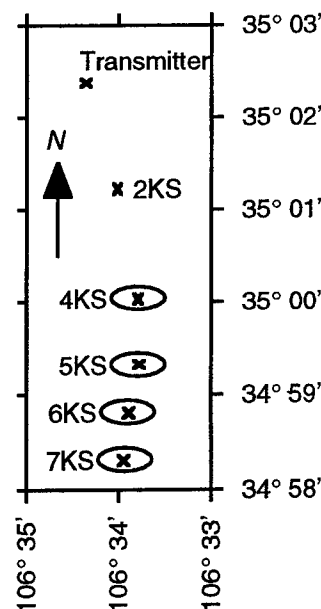


Figure 4. ROS lidar test range.

absolute reflectivity as a function of angle at the C13 10P20 wavelength (11.149 μm), providing a calibrated target for the downrange tests. The 2 km site has a large cinderblock wall, where a 4' x 4' flame-sprayed aluminum target sheet was attached. The flame-sprayed aluminum sheet was prepared in a fashion similar to that described in Kavaya et al.², and provides a very high reflectivity with little wavelength variability.

3. RADIOMETRY

A major emphasis of the LARS ground testing was validation of the system performance simulations. Having accurate system performance estimates is critical for an airborne system, since the high cost of flight time necessitates having reliable information on the system capabilities for use in pre-flight test planning. The baseline test used to compare actual performance with predictions uses the 8' x 8' blueboard target located at the 2 km site. The relatively short range to the target site reduces the impact of atmospheric absorption, allowing a better estimate of the system performance. This test also allows the LARS system performance to be compared with the results from the Non-Proliferation Airborne Laser Experiment (N-ABLE) system. The N-ABLE system is a shorter range airborne CO₂ DIAL system that was developed jointly by the U.S. Air Force Phillips Laboratory, the U.S. Army Edgewood Research, Development, and Engineering Center (ERDEC), and Los Alamos National Laboratory. The N-ABLE system was also ground tested at the ROS lidar test range at Kirtland AFB prior to flight experiments at INEL in October-November 1996, allowing the performance of the two systems to be compared.

Table 1 lists the measured return energy \hat{E}_r incident on the detector, the expected energy \tilde{E}_r , and the ratio \hat{E}_r / \tilde{E}_r . The predictions for both systems agree within a factor of 1.3 - 2.3, which is reasonable considering the uncertainties in the measurement resulting from atmospheric transmission, detector spectral responsivity (for both transmit and receive detectors), system optical transmission, and other factors. This level of agreement provides some confidence that the system performance simulations can be relied upon for planning airborne experiments.

Considerable effort was expended to obtain and characterize a high-bandwidth low-noise detector. The detector currently in use is a 0.5 mm diameter liquid nitrogen cooled HgCdTe manufactured by Société Anonyme de Télécommunications (SAT). A customized preamplifier was constructed to match the detector, and the detector / preamplifier combination was exhaustively tested and characterized. The major noise sources were determined to be photon noise from the background scene temperature, bias current noise, Johnson noise from the detector and preamplifier resistances, 1/f noise, and preamplifier input current noise. The noise-equivalent-power (NEP) for each of these sources is listed in Table 2. The total NEP is given by the root-sum-of-squares (rss) of the individual sources. The measured NEP values from tests done using the topographic returns from the 7KS, 6KS, and 5KS berms are also given in the table, and are in good agreement with the predicted total NEP.

Table 1. Comparison of Measured and Predicted System Performance

System	LARS	LARS	N-ABLE
Test Date	23 May 1997	9 May 1997	3 March 1997
Measured Return Energy \hat{E}_r	2.25 nJ	5.96 nJ	0.082 nJ
Predicted Return Energy \tilde{E}_r	1.79 nJ	2.63 nJ	0.188 nJ
Ratio \hat{E}_r / \tilde{E}_r	1.3	2.3	0.44 (= 1 / 2.3)

Table 2. Detector / Receiver Electronics Noise Sources

Source	Predicted NEP	Measured NEP
Background Light	1.13 nW	
Bias Current	2.88 nW	
Johnson Noise	1.14 nW	
1/f Noise	1.42 nW	
Preamp Input Current	0.47 nW	
TOTAL	3.62 nW	3.50 nW (7KS)
		5.00 nW (6KS)
		5.17 nW (5KS)

4. DIAL EXPERIMENTS

Differential absorption measurements of chemical species were conducted using a 4' x 4' x 4' gas cell placed in the transmit / receive beam path slightly downrange of the final steering mirror. The cell consists of an aluminum frame and aluminum plates on the top, bottom, and two sides. The beam is transmitted through thin polyethylene sheets on the other two sides of the cell. Fans are mounted on all of the aluminum plates to insure that the chemical of interest is well-mixed in the cell. The two gases tested were sulfur hexafluoride (SF₆) and ammonia (NH₃). SF₆ is commonly used as a test gas for CO₂ DIAL systems because of its high absorption cross-section, overlap with the strong C12 10P laser lines, and ease of handling. NH₃ is a more difficult gas to measure with a C12 laser, since it has very sharp spectral features which do not overlap strong C12 laser lines. The SF₆ was inserted into the cell by evacuating a 50 cc sample bottle, then filling it with SF₆ to a pressure 6 psi over ambient atmospheric pressure. The sample bottle was then connected to a bulkhead gas connector on the cell, and the excess SF₆ pressure was released into the cell. The NH₃ was inserted into the cell as liquid NH₄OH, consisting of 30% NH₃ and 70% H₂O when evaporated. A Petry dish was placed on a ceramic heater inside the cell, and the liquid NH₄OH was poured into the Petry dish through a funnel on the top of the cell. Three cc of NH₄OH was placed into the dish, and a steady-state absorption level was reached within a minute, indicating that all of the inserted liquid was in the vapor state.

The DIAL tests reported here were conducted using C12 laser lines, with the 8' x 8' blueboard at 2 km as the target. A data set was run with no gas cell in the propagation path, and then a data set was taken with the cell in the path, but no

gas. This allows the effects of the polyethylene cell windows to be determined. The next data sets were taken during the SF_6 insertion, and then with the SF_6 well mixed in the cell. These tests were followed by a data set during the insertion of the NH_3 , and then by a test with the NH_3 well mixed. The measurements made with the empty cell provide the baseline for determining the SF_6 absorption, and the measurements with the well-mixed (steady-state) SF_6 are used as the baseline to determine the NH_3 absorption. Figure 5 shows the change in absorption over time for selected laser lines (both absorbing and non-absorbing) as the SF_6 and NH_3 were inserted into the cell. The SF_6 has numerous absorbing lines in the 10P branch, while the NH_3 has only two significantly absorbing lines. The absorbing lines for SF_6 shown in Figure 5(a) are 10P16 and 10P20, and the non-absorbing (or low absorption) lines are 09P14, 10R18, and 10P10. Figure 5(b) shows the NH_3 -absorbing 10R08, and the non-absorbing 09R14, 10R12, and 10P16 lines.

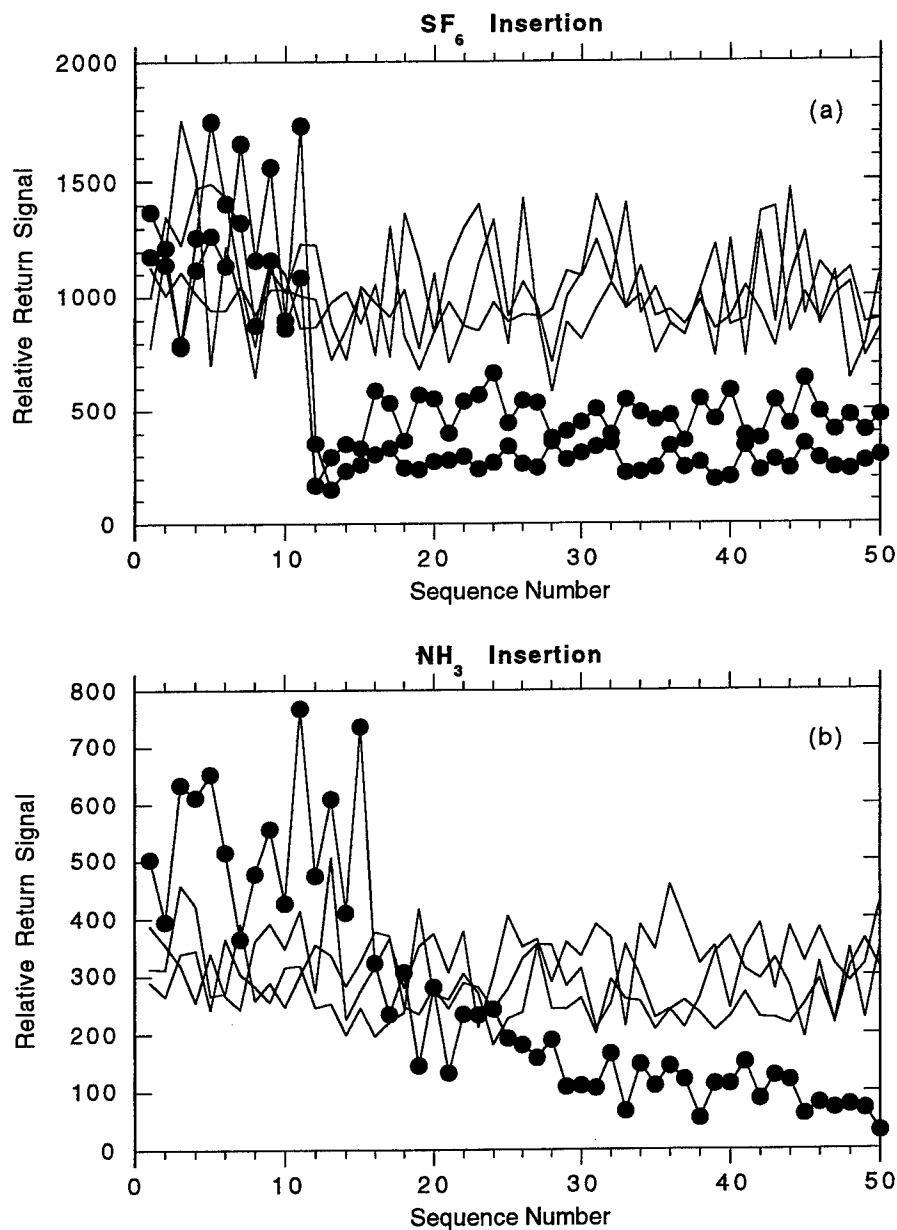


Figure 5. Variation in return signal for absorbing (dots) and non-absorbing laser lines for (a) SF_6 and (b) NH_3 .

Figure 6 shows the measured absorption caused by the SF_6 and NH_3 for each transmitted wavelength once steady-state conditions have been reached. The SF_6 absorption can be seen on the C12 10P lines, while the NH_3 absorption occurs mainly on the 09R16 and 10R08 lines. NH_3 absorption also occurs on the 09R30 line, but this line was not plotted in Figure 6 since the very low laser pulse energy resulted in a high standard deviation for the return signal. The 10R20 line has also not been plotted, since it was almost completely absorbed by atmospheric water vapor. The predicted absorptionspectra are also shown on the Figure (hatched bars). The predicted SF_6 absorption was calculated using a CL product of 16 ppm·m, corresponding to the amount of SF_6 believed to have been introduced into the gas cell. The predicted NH_3 absorption corresponds to a CL product of 710 ppm·m, which is the best estimate of the amount of NH_3 inserted into the cell.

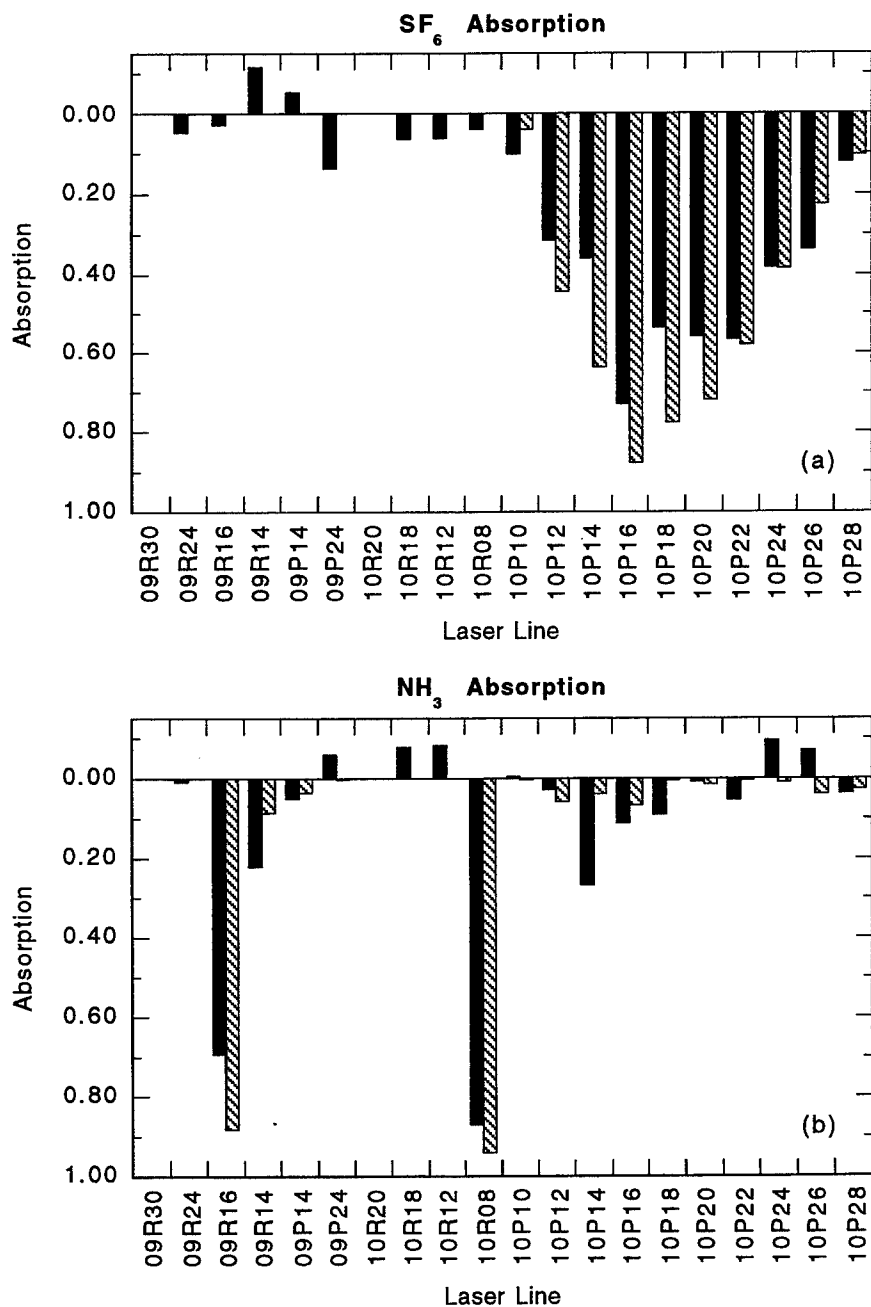


Figure 6. SF_6 (a) and NH_3 (b) measured (black) and predicted (hatched) absorption.

An interesting method of detecting and identifying airborne chemicals is to compute the autocorrelation of the return signal. Transients in the concentration-pathlength (CL) product tend to cause slow variations in the return signal with respect to the temporal spacing between laser pulses at the same wavelength, resulting in correlation between the pulses. These transients may be caused by the insertion and initial mixing of a gas, such as in these ground tests, or by eddies and turbulence in the atmosphere, such as with the release of chemicals from a smokestack. This has been referred to as the 'plume billowing effect', and has been studied using both the autocorrelation of a single wavelength, and the cross-correlation of different wavelengths³. Figure 7(a) shows the autocorrelation of the return signal during the insertion of SF₆ into the cell, while Figure 7(b) shows the autocorrelation during the NH₃ insertion. A single lag corresponds to the temporal spacing between adjacent pulses at the same wavelength. For these experiments, a 20-line sequence was run with a 10 Hz laser PRF, resulting in 2 sec between same-wavelength pulses. As can be seen in the Figures, the SF₆ mixes rapidly, resulting in negligible correlation after ~ 20 sec. Since the NH₃ must be evaporated from liquid, it reaches a steady-state condition much more slowly, resulting in correlation of the received signal even beyond the 50 sec shown in Figure 7(b). The high correlations from NH₃ absorption are seen on the 10R08 and 09R16 lines. There is also a slight correlation observed from an unknown cause apparent on the 10P12 line. In many instances, using autocorrelation and/or cross-correlation information may be an efficient method for detection and identification of airborne chemicals.

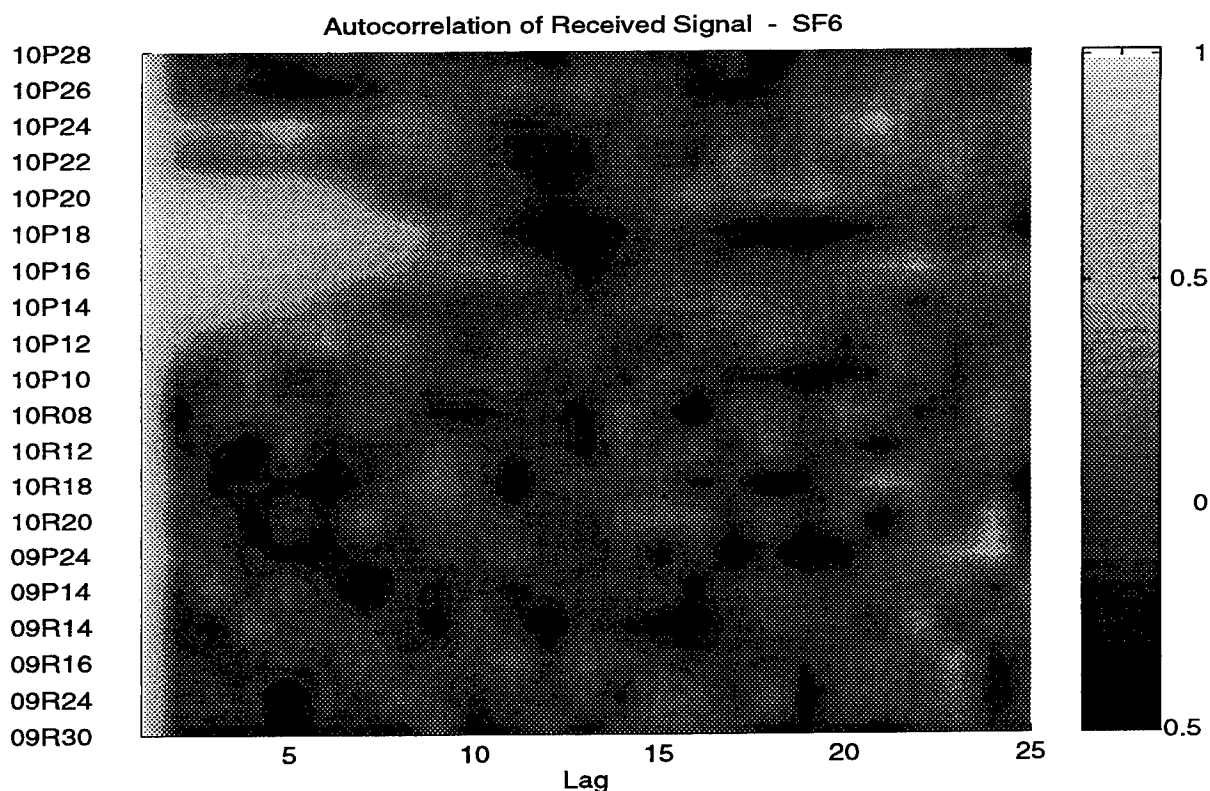


Figure 7a. Autocorrelation of return signal during SF₆ gas insertion.

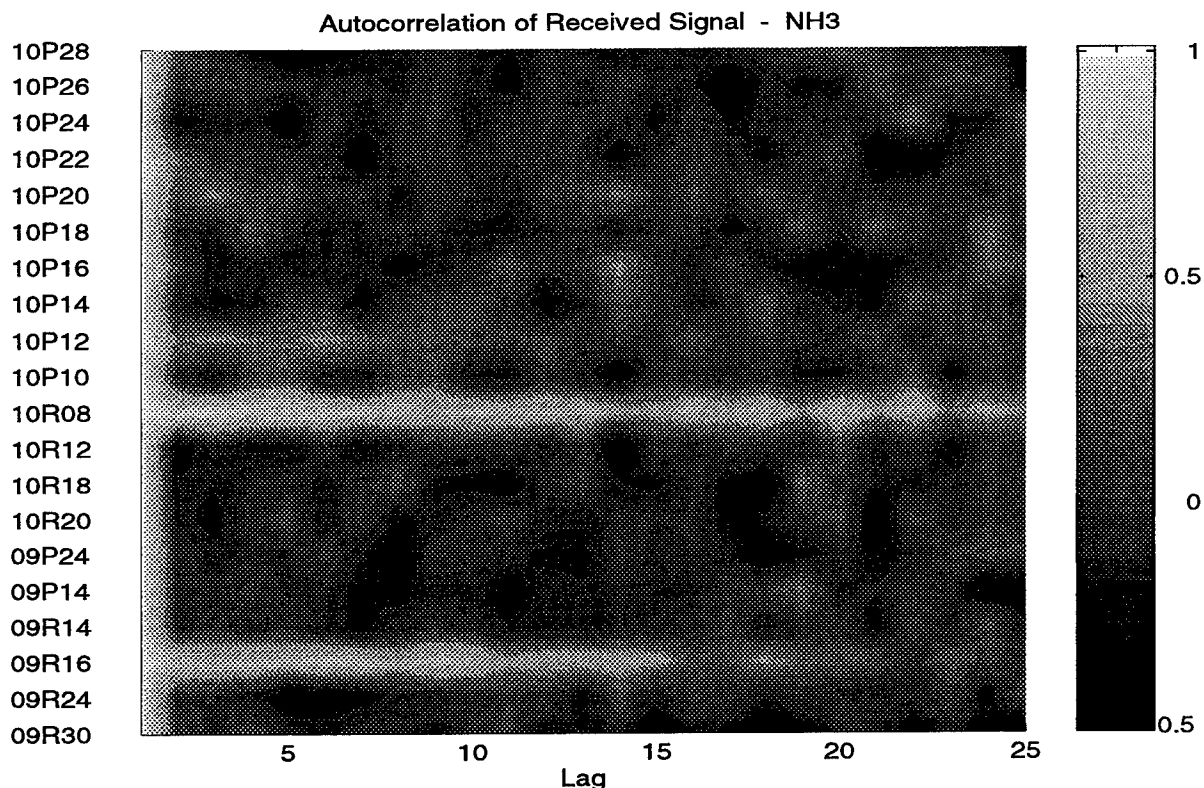


Figure 7b. Autocorrelation of return signal during NH₃ gas insertion.

ACKNOWLEDGEMENTS

The authors would like to acknowledge the contributions of the numerous individuals who have been involved in the design and development of the LARS system, and without whom the work presented in this paper would not have been possible. These include Bill Carrion (Textron Systems Corporation), N. Scott Higdon (Kaman Sciences Corporation), Robert Babnick (Applied Technology Associates), Ken Rowland (Boeing Defense and Space Group), the Metrolaser Argus support personnel, and the members of the Phillips Laboratory Argus flight test branch.

REFERENCES

1. M.J. Fox, N.S. Higdon, D.R. Dean, C.M. Hamilton, D.C. Senft, J.A. Dowling, D. Pierrottet, S. Ghoshroy, and S.B. Alejandro, 'CO₂ differential absorption lidar (DIAL) research at the Air Force Phillips Laboratory,' *18th International Laser Radar Conference*, Berlin, Germany, 1996.
2. M.J. Kavaya, R.T. Menzies, D.A. Haner, U.P. Oppenheim, and P.H. Flamant, 'Target reflectance measurements for calibration of lidar atmospheric backscatter data', *Appl. Opt.*, 22, 2619-2628, 1983.
3. E.P. MacKerrow, B.D. McVey, M.J. Schmitt, J.J. Tiee, 'Determination of lidar absorption signatures using the cross-correlation of multi-wavelength lidar signals', *Appl. Opt.*, accepted for publication, manuscript # AO-013127, 1997.

Multifunctional Laser System for Measuring Regular and Random Optical Refraction in the Atmosphere

Yu.D. Kopytin, V.V. Nosov, and E.V. Nosov*

(Institute of Atmospheric Optics, Siberian Branch of the Russian Academy of Sciences,
1 Akademicheskii Prospekt, Tomsk 634055, Russia)

ABSTRACT

In the context of modern radio physics approach, it is demonstrated theoretically and experimentally that diffraction properties of the received optical radiation may significantly affect the refraction angle measured with a phase sensitive receiving-recording system. Based on this approach harnessing coherent laser phenomena in plane and spherical waves, we suggest and develop to engineering procedures methods for determining the refraction angles from one-wave optical measurements. These methods are also applicable under conditions of highly inhomogeneous optical paths in the turbulent atmosphere.

The LIRA multifunctional precision laser system for measuring regular and random optical refraction has been developed. In contrast with the known multiwave methods for remote refraction measurements, this system harnesses one-wave laser radiation. Its operation is based on instantaneous determination of the refraction angle from measurements of the image energy centre of gravity of a remote laser source. Measurements are carried out with sampling frequencies up to 1000 Hz. The horizontal field-of-view angle is 100 sec of arc and the vertical field-of-view angle is up to 2 deg of arc. Average angular refraction is measured in the range 0.2-200 sec of arc. The measurement error is 0.2 sec of arc. Relative variance of angular refraction is measured in the range 0.1-1.0 sec of arc. Atmospheric path length varies between 0.5 and 30 km. The wavelength of the laser source is 0.63 μm . Laser sources generating other wavelengths can also be used in the system.

Key words: atmosphere, regular and random optical refraction, laser refractometer.

1. INTRODUCTION

Wide use of optical systems for laser detection and ranging, communications, and so on calls for consideration of refractive bending of wave propagation paths in the atmosphere. In practice, laser systems are often used for measuring the angular position of a target. It is clear that in case of angular measurements, in addition to the error due to turbulent broadening of the angular wave spectrum, the error due to the regular refraction is introduced. It is conventional to specify bending of a beam trajectory with the following angles:

- angle of the total geodetic refraction σ , defined as an angle between the tangents to the beam trajectory at points of transmission and reception;
- refraction angles at points of transmission (r_{12}) and reception (r_{21}), defined as the angles between the straight line connecting these points and the corresponding tangents to the curvilinear beam trajectory, where $\sigma = r_{12} + r_{21}$. In practice, the angle σ is determined from simultaneous measurements of zenith refraction angles θ_{12} and θ_{21} by the formula $\sigma = \pi - (\theta_{12} + \theta_{21})$.

The theory of optical refraction is developed in ample detail in the geometrical optics approximation.¹⁻³ In the context of this theory, the angles of refraction are functions of the air refractive index profile. In its turn, the refractive index is a function of the meteorological parameters. It is mainly determined by the profiles of the air density and temperature and varies with the air humidity. For this reason, profiles of these parameters should be measured to predict the angles of regular refraction (only temperature is commonly measured).

However, this conventional theory completely ignores diffraction phenomena and therefore imposes limitations on the propa-

Further authors information: -

* Yu.D.K., V.V.N., E.V.N.: Email: root@conv.tsk.ru

gation path length. In addition, the geometrical optics approximation does not describe strong wave field fluctuations in a turbulent medium². In this connection, a novel approach has been developed in recent years. It is based on exact radio physics methods of studying the propagation of the optical radiation in a turbulent medium with regular refraction index gradient. Here, the regular refraction is a part of the general phenomenon, namely, refractive banding of optical beam trajectories in the atmosphere, considered as a complex turbulent refraction medium. Based on this radio physics approach, a number of new results on the optical refraction in the atmosphere was obtained by Vinogradov et al.⁴ and Banakh et al.⁵ In particular, it was established (first theoretically^{4,5} then experimentally^{5,6}) that the diffraction properties of the received beam may significantly affect the refraction angle being measured with a phase-sensitive receiving-recording system. Stationarity effect of the ratio of the refraction angles at two opposite ends of the propagation path was established.⁴ Based on results of the theory of wave propagation in a turbulent medium, Nosov⁷ suggested remote optical methods for simultaneous measurements of angles of regular refraction and characteristics of the atmospheric turbulence.

In the present paper, based on an analysis of theoretical methods for determining random and regular optical refraction harnessing the radio physics approach to the solution of the problem of optical wave propagation in the Earth's atmosphere, we suggest and develop to engineering procedures and algorithms methods for determining absolute values of the optical refraction angles in vertical and azimuth planes that can be used under conditions of optically inhomogeneous near-ground paths as well. Their essential and principal difference is the use of one-wave laser radiation, in contrast with the known multiwave methods for remote measurements.

In conclusion, the developed multifunctional laser system for measuring optical refraction¹⁰ is briefly described including its composition and specifications.

2. PROCEDURE FOR MEASURING ANGLES OF REFRACTION OF THE OPTICAL RADIATION

The block diagram of the system for measuring the refraction of the optical radiation – refractometer – is shown in Fig. 1. A laser with an autonomic power supply unit is used as a source. It generates the laser radiation at the wavelength λ . The radius of a transmitting aperture is a , the curvature radius of the wave front on the transmitting aperture is F , and the coherence radius is ρ_c . The parameters F and ρ_c are related with the angles of total divergence of the laser beam φ_0 and φ , where φ_0 is the total angle of initial geometrical beam divergence and φ specifies the beam divergence caused by diffraction on the aperture and partial beam coherence (that is, diffraction on the coherence radius).

Fig. 1. Scheme of measuring the refraction angle with a receiver. The measurement path is between a source and the receiver. A laser is used as a source.

A single-mode laser generates completely coherent radiation, that is, its coherence radius ρ_c is equal to infinity. For this laser, the angle of beam divergence is related with the output wave-front curvature radius F by the formula

$$-\frac{1}{F} = \frac{1}{a} \tan\left(\frac{\varphi_0}{2}\right). \quad (1)$$

A multimode laser generates partially coherent radiation with $\rho_c \gg a$ (for a heat source, $\rho_c = 0$). In this case, the coherence radius can be expressed in terms of the angle φ

$$\frac{1}{\rho_c} = k \left| \tan^2\left(\frac{\varphi}{2}\right) - \frac{1}{k^2 a^2} \right|^{1/2}. \quad (2)$$

For each particular laser, the angles φ and φ_0 can be measured based on Eqs. (1) and (2).

2.1. Calibration of Source Arrangement

The laser is mounted on a platform of a portable unit (with a tripod). The platform of the portable unit has a geodetic level to test the elevation angle between the platform and the Earth's axis. With the help of the level, the platform is placed strictly perpendicular to the Earth's axis. In this case, the laser beam axis can be adjusted in the vertical plane at a given angle to the Earth's axis (measured from the zenith) using a turntable mounted on the platform.

A high-precision compass mounted on the platform is used to measure the azimuth angle of the laser beam. The compass measures the angular displacement of the laser beam axis from the magnetic north-south direction (the angle from the magnetic north-south direction is measured clockwise). After measuring the azimuth and zenith angles, the calibration of the source arrangement is terminated.

2.2. Receiver

The receiver of the optical radiation is placed in the atmosphere at distance z from the source. A telescope comprising a system of lenses, further referred to as an input lens, is used as a receiver. Let us denote by Δ the thickness of the input lens (the maximum distance between the external and internal surfaces of the system of lenses). A quadratic photodetector is placed in the recording plane of the telescope (located at distance l from the input lens). If l_1 is the distance from the internal surface of the input lens to the input window of the quadratic photodetector, then $l = l_1 + \Delta/2$. A transparency with the linear transmittance (of the radiation intensity) τ is placed immediately before the input window of the quadratic photodetector. The co-ordinates of the image centre of gravity of the laser source $\rho_i = (y_i, x_i)$, where y_i is the vertical co-ordinate and x_i is the horizontal co-ordinate of the image centre of gravity, are determined from the measured light flux transmitted through the transparency.

The quantity $a_i = \rho_i / l$, $a_i = (a_{ix}, a_{iy})$ is the angular displacement of the image from the receiver optical axis in the vertical ($a_{iy} = y_i / l$) and horizontal ($a_{ix} = x_i / l$) directions. Let us denote by a_i the input aperture radius of the receiver and by F_i the focal length of the receiving lens.

Let y be the vertical co-ordinate in the recording plane, directed upward from the Earth's surface (its origin is on the optical receiver axis). Then the transparency with the transmittance by the intensity

$$\tau = \tau(y) = c_1 + c_2 y, \quad c_1 = \text{const} > 0, \quad c_2 = \text{const} > 0,$$

will lead to the positive vertical co-ordinate of the image centre of gravity y_i ($y_i > 0$), if in the recording plane the image is displaced upward from the optical axis of the receiver. This transparency is more transparent at the top (with respect to the Earth's surface).

Analogously, for the horizontal co-ordinate x in the recording plane and the transparency with the transmittance

$$\tau = \tau(x) = c_3 + c_4 x, \quad c_3 = \text{const} > 0, \quad c_4 = \text{const} > 0,$$

the horizontal co-ordinate of the image centre of gravity x_i will be positive ($x_i > 0$), if the image is displaced in the positive direction of the OX axis. The positive direction of the OX axis is specified by the transparency with the transmittance $\tau(x)$, namely, more transparent part of the transparency is located in the positive direction of the OX axis.

2.3. Calibration of Receiver Arrangement

After mounting in the desired place, the receiver is calibrated. The calibration comprises measuring the angle between the receiver axis and the Earth's axis and the azimuth angle between the receiver axis and the magnetic north-south direction clockwise. The angles can be measured directly. To this end, the receiver is mounted on a special platform adjusted at the known angles (measured with the geodetic level and compass) to the Earth's axis and the magnetic north-south direction.

2.4. Procedures for Measuring Angles of Optical Refraction on Horizontal Near-Ground Paths

A. Homogeneous Path. Short-Term Observations

The procedure for measuring the angles of regular refraction

$$r_{12} = \frac{z}{2} \int_0^1 d\xi (1 - \xi) \left[\nabla_{\perp} v(\xi z, \rho') \right] \Big|_{\rho'=0},$$

$$r_{21} = \frac{z}{2} \int_0^1 d\xi \cdot \xi \left[\nabla_{\perp} v(\xi z, \rho') \right] \Big|_{\rho'=0},$$

where z is the optical path length, $\rho' = (y', x')$ is the vector of the transverse co-ordinates, $[\nabla_{\perp} v(\xi z, \rho')]_{\rho'=0}$ is the transverse gradient of permittivity, which is a function of the current path length ξz , is based on the formula⁸

$$\alpha_t = r_{21} - \frac{\rho}{z} + R(z) \left(r_{12} + \frac{\rho}{z} + \alpha \right),$$

$$R(z) = \frac{1 - \frac{z}{F} + \frac{a_t^2}{a^2} \left(1 + \frac{z}{l} - \frac{z}{F_t} \right)}{\left(1 - \frac{z}{F} \right)^2 + \frac{z^2}{k^2 a^4} \left(1 + \frac{a^2}{\rho_c^2} \right) + \frac{a_t^2}{a^2}}.$$

Here, α_t denotes the angle of refraction measured by the receiver; α is the angle between the source and receiver optical axes; F , $k = 2\pi/\lambda$, a , ρ_c , and ρ are the parameters of the laser source, namely, the curvature radius of the wave front on the transmitting aperture, the wave number, the radius of the transmitting aperture, the transverse radius vector which specifies the distance between the receiver optical axis and the laser source centre; a_t , l , and F_t are the parameters of the receiver: the input aperture radius, the distance from the input lens centre to the recording plane, and the focal length, respectively.

The refraction angle measured by the receiver α_t , the angle α determined through the calibration of the source and the receiver, and three unknown vector variables ρ , r_{12} , and r_{21} are related by equality (3).

In the outdoor atmosphere, not only regular (low-frequency) gradients of the refractive index, but also the atmospheric turbulence (varying with higher frequencies) causes variations of the refraction angle α_t . After averaging of the measured angles over the period T , the frequencies of variation of the average angle α_t will be less than $2\pi/T$. To average completely the turbulent fluctuations, $T = 100$ s is commonly used.

The angle α is determined by the calibration of the source and receiver arrangements. Its vertical α_y and horizontal α_x components are calculated by the formulas

$$\alpha_y = m(\pi - \alpha_{21} + z/R_0),$$

$$\alpha_x = n(\pi + \beta_{21} + \beta_{12}),$$

where α_{21} and β_{21} are the zenith and azimuth angles of the receiver, α_{12} and β_{12} are the zenith and azimuth angles of the source, z/R_0 specifies the angle between the source and the receiver as observed from the Earth's centre, $R_0 = 6340$ km is the Earth's radius, and the parameters m and n take the values $+1$ or -1 , versus directions of the OY and OX axes affixed to the receiver: $m = +1(-1)$ when the vertical axis is oriented upward (downward) with respect to the Earth's surface and $n = +1(-1)$ when the horizontal axis is oriented from right to left (from left to right), when the recording plane is observed from the receiving lens. The angles α_x and β_{21} are determined to integral number of complete revolutions, that is, if $\alpha_x > 2\pi$, $\alpha_x - 2\pi$ is taken as α_x .

For homogeneous horizontal paths with identical warming of the underlying surface by the solar radiation (above an even surface, for example, above the sea surface, where the path length may reach several tens of kilometres), the transverse gradient of the permittivity $[\nabla_{\perp} v(\xi z, \rho')]_{\rho'=0} = m(\xi z)$ can be considered constant, that is, $m(\xi z) = \text{const}$. In this case,

$$r_{12} = r_{21} = m_c z / 4,$$

and Eq. (3) assumes the form

$$\alpha_t - R(z)\alpha = (R(z) + 1) \frac{m_c z}{4} + (R(z) - 1) \frac{\rho}{z}. \quad (3a)$$

The equality (3a) relates the angle α_t measured in the atmosphere, the angle α determined from the calibration of the source and the receiver, and two unknowns m_c and ρ . Based on Eq. (3a), a system of two vector equations should be constructed to find two unknowns m_c and ρ , for two different values of the parameter $R(z)$. Specifying (for example, through corresponding

changes of the source parameters F , λ , a , and ρ_c) two significantly different values R_1 and R_2 of the parameter $R(z)$ and measuring the angle α_t (α_{t1} for R_1 and α_{t2} for R_2), from Eq. (3a) we obtain the following system of equations:

$$\begin{aligned}\alpha_{t1} - R_1\alpha &= (R_1 + 1)\frac{m_c z}{4} + (R_1 - 1)\frac{\rho}{z}, \\ \alpha_{t2} - R_2\alpha &= (R_2 + 1)\frac{m_c z}{4} + (R_2 - 1)\frac{\rho}{z}.\end{aligned}$$

The solution of this system is

$$\begin{aligned}m_c &= \frac{2}{z} \left(\alpha_{t1} \frac{R_2 - 1}{R_2 - R_1} + \alpha_{t2} \frac{1 - R_1}{R_2 - R_1} - \alpha \right), \\ \rho &= \frac{z}{2} \left(\alpha_{t1} \frac{R_2 + 1}{R_2 - R_1} + \alpha_{t2} \frac{1 + R_1}{R_2 - R_1} - \alpha \right).\end{aligned}\quad (4)$$

The first equality defines the permittivity gradient m_c on the homogeneous path and the refraction angles $r_{12} = r_{21} = m_c z / 4$ from the angles α_{t1} and α_{t2} measured by the receiver. Thus, formulas (4) yield the refraction angles r_{12} and r_{21} on the homogeneous path in case of short-term observations.

It can be demonstrated that the error in measuring the refraction angles decreases significantly if the employ the values of the parameter $R(z)$ that differ significantly, for example, $R_1 = 1$ and $R_2 = 0$. These values can be obtained by various means, for example, a) when the parameters of the source are changed, whereas the parameters of the receiver remain unchanged, b) when the parameters of the receiver are changed, whereas the parameters of the source remain unchanged, and c) when the parameters of the receiver and source are changed.

For a collimated ($1/F = 0$) coherent ($1/\rho_c = 0$) laser beam in the near diffraction zone ($z \ll ka^2$) we derive from Eq. (3)

$$R(z) = \left(1 + \frac{a_t^2}{a^2} \left(1 + \frac{z}{l} - \frac{z}{F_t} \right) \right) / \left(1 + \frac{a_t^2}{a^2} \right).$$

When the receiver size is larger than the source size ($a_t \gg a$), $R(z) = 1$ at $l = F_t$ and $R(z) = 0$ at $l + z/l - z/F_t = 0$. Therefore, locating the image recording plane of the receiver successively in the focal plane ($l = F_t$) and in the plane of the sharp image ($l + z/l - z/F_t = 0$), we obtain two significantly different values of the parameter $R(z)$, namely, $R_1 = 0$ and $R_2 = 1$.

When the recording plane is at the receiver focus ($l = F_t$), we derive from Eq. (3) for the coherent ($1/\rho_c = 0$) laser which generates a collimated beam ($1/F = 0$) the following formula:

$$R(z) = \left(1 + \frac{a_t^2}{a^2} \right) / \left(1 + \frac{z^2}{k^2 a^4} + \frac{a_t^2}{a^2} \right).$$

From this it follows that $R(z) = 1$ is realised in the far diffraction zone ($z \gg ka^2$) on the source aperture and in the near diffraction zone ($z \ll ka^2$) on the receiver aperture. For the far diffraction zone, $R(z) = 0$ is realised on the receiver and source apertures.

When the parameters of the receiver are fixed, the recording plane is at the focus ($l = F_t$), and the receiver is in the near diffraction zone on the aperture of the coherent source ($z \ll ka^2$ and $1/\rho_c = 0$), we derive from Eq. (3) on account of Eq. (1)

$$R(z) = \left(1 + \frac{z}{a} \tan\left(\frac{\varphi_0}{2}\right) + \frac{a_t^2}{a^2} \right) / \left(\left(1 + \frac{z}{a} \tan\left(\frac{\varphi_0}{2}\right) \right)^2 + \frac{a_t^2}{a^2} \right).$$

Here, φ_0 is the total angle of the initial geometrical divergence of the coherent laser beam. Taking φ_0 first close to zero (the collimated beam) and then exceeding the angle $2a/z$, at which the source is seen from the point of location of the receiver, we also obtain two significantly different values of the parameter $R(z)$: $R_1 = 0$ and $R_2 = 1$.

B. Homogeneous Path. Long-Term Observations

When the source image is observed only in two recording planes, namely, in the focal plane and in the sharp image plane, the parameter $R(z) = 0$ corresponds to the situation when the effective diffraction radius of the laser beam at the end of the path

$$a_e(z) = a \left(\left(1 - \frac{z}{F} \right)^2 + \frac{z^2}{k^2 a^4} \left(1 + \frac{a^2}{\rho_c^2} \right) \right)^{1/2}$$

significantly exceeds the receiver radius a_t . Then $R(z) = 1$ can be easily obtained if this radius is less than or comparable with the receiver radius ($a_e(z) \leq a_t$).

For long-term sessions of measuring the refraction angles (for example, during 24 hours) the beam with the effective radius $a_e(z)$, comparable with the receiver radius a_t , falls beyond the receiver aperture. This effect can be eliminated by two ways, namely, by continuous adjustment of the source (adjusting the angles α_{21} and β_{21}) or using the beam with the effective radius $a_e(z)$, significantly exceeding the receiver radius a_t . The first way is inefficient, because an operator should be permanently presented near the source. The second way can be realised without the operator near the source. In this case, the parameter $R(z)$ becomes small due to the condition $a_e(z) \gg a_t$, and from Eq. (3a) it follows that

$$r_{21} = \alpha_t + \rho / z \quad (4a)$$

For the known value of the distance ρ calculated with the use of the second equality of Eq. (4) from the short-term measurements with two values of the parameter $R(z)$ ($R_1 = 0$ and $R_2 = 1$), the last formula can be used to measure the refraction angle r_{21} during long time without adjustment of the source (without the operator at the source site).

On homogeneous paths at the initial moment of time t_0 , $r_{12}(t_0) = r_{21}(t_0)$. Based on the stationarity of the ratio $|r_{12}| / |r_{21}|$ (see Ref. 4), we obtain that $r_{12}(t) = r_{21}(t)$ for any t . Thus, formula (4a) yields the values of the refraction angles r_{12} and r_{21} on the homogeneous path in case of long-term measurements.

C. Inhomogeneous Path. Short-Term observations

For an extended inhomogeneous path of length z , we divide the entire path into N homogeneous sections of lengths z_i . The degree of warming of the underlying surface is considered constant for each section of the path, but different for different sections.

For the first section of the path of length z_1 , we determine the value m_{c1} by the method described above. Then we displace the source at the distance $z = z_1 + z_2$. In so doing, we should take into account that the angle α_t entering Eq. (3) is already connected with the values of m_{c1} and m_{c2} . For two different values of the parameter $R(z)$ ($R_1 = 0$ and $R_2 = 1$), we obtain the system of two (vector) equations for two unknowns m_{c2} and ρ_2 . For the measured angles α_t (α_{t1} and α_{t2}) and known value of m_{c1} (for the first section of the path of length z_1), we obtain m_{c2} and ρ_2 .

The above-described procedure allows one to determine the parameters m_{cN} and ρ_N for the last N th section of the path (adjacent to the receiver) in the N th measurement from the known values m_{ci} and ρ_i for the preceding sections ($i = 1, \dots, N-1$). After successive determination of the values m_{ci} and ρ_i for all N sections, we determine the refraction angles in case of short-term observations on the inhomogeneous path of length z comprising N homogeneous sections of lengths z_i , $i = 1, \dots, N$, $z = z_1 + \dots + z_N$.

D. Inhomogeneous Path. Long-Term Observations

The long-term observations on an inhomogeneous path are carried out analogously to the long-term observations on the homogeneous path (see Sec. B).

3. SPECIFICATIONS OF THE ADAPTIVE LASER SYSTEM FOR EXPRESS MEASUREMENTS OF REGULAR AND RANDOM OPTICAL REFRACTION

Below we describe the adaptive laser system for express measurements of regular and random optical refraction, its composition, arrangement, and specifications. This system is an integral part of the LIRA multipurpose laser refractometer.

Application

This system is intended for high-precision determination of corrections for regular and random optical refraction in goniometric and light ranging measurements on near-ground atmospheric paths as well as for detection of turbulent flows in the ground layer of the atmosphere accompanying, for example, depressurisation of oil and gas pipelines or district heating systems, from the intensity of the random optical refraction.

Composition

The system comprises an optical train of an aberrationless telescope, a photometric recording unit, a precision turntable, a processing unit built around a computing complex with a microcomputer, a portable unit of a single-mode laser transmitter with a 2T2 theodolite. Its operation is based on the Fourier analysis of refractive distortions of reference plane and spherical waves generated by the laser source.

Specifications

1. Range of measuring the mean refraction angles, sec of arc	0.2 – 200
2. Measurement error, sec of arc	0.2
3. Range of measuring the relative variance of the refraction angles	0.1 – 1.0
4. Time of averaging, s	100
5. Atmospheric path length, km	0.5 – 30
6. Wavelength of the laser source, μm	0.63
7. Data presentation	on the screen of a monitor and digital printing
8. Overall dimensions, mm	1000×300×200
9. Mass, kg	45
10. Power supply, kW	up to 0.5
11. Measurable angle of vertical refraction, deg	up to 2
12. Sampling frequency of instantaneous values of the refraction angles	up to 1000 Hz
13. Effective focal distance of the receiving optical system objective-ocular, m	from 10 to 30
14. Range of operation in the daytime for the indicated output laser powers at 0.63 μm	500 m at 2 mW 5000 m at 50 mW

Complete equipment

1. Objective, $D = 100 \text{ mm}$, $f = 1000 \text{ mm}$	} Optical system } with $f_{\text{eff}} = 10 - 30 \text{ m}$ }
2. Ocular, $f = 20 - 56 \text{ mm}$	
3. Prism of servo mechanism	
4. Stepping motor of servo mechanism	
5. Prism	
6. Light filter (KS – 11 or interference)	
7. Field stop, 100 sec of arc	
8. Adjustment lamp to adjust the supply voltage of PMTs I and II	
9. Light splitter	
10. Optical image analyser	
11. Light scatterer	
12. Photomultiplier FEU-79	
13. Controller of the system	
14. Interactive computing complex (ICC)	

The system determines the instantaneous refraction angles from the measured positions of the image energy centre of gravity of a distant source. The data can be sampled with frequencies up to 1000 Hz. The field-of-view angle is 100 sec of arc. To increase the vertical field-of-view angle up to 2 sec of arc, a computer-controlled servo mechanism with a stepping motor is used, which corrects every 100 s the position of the source image on the optical axis of the receiving system. The correction angle M_y is equal to the angular displacement of the image centre of gravity averaged over a time period of 100 s. The current refraction angle is given by the formula

$$A_n = M_{y1} + M_{y2} + \dots + M_{ym},$$

where n is the serial number of the 100-s realisation.

The position of the energy centre of gravity Y_c is calculated from the formula

$$Y_c = \frac{P_y}{P_0} = \frac{\int_S t(x, y) J(x, y) dx dy}{\int_S J(x, y) dx dy},$$

where P_0 is the light flux proportional to the total flux received by the optical receiving system; P_y is the light flux proportional to the flux transmitted through the optical image analyser with the transmittance $t(x, y)$, which represents a neutral plane filter with the transmittance increasing linearly from 0.05 to 0.80 as the y co-ordinate increases, that is, the transmittance is described by the formula $t(x, y) = ky$, where k is the slope of the straight line; $J(x, y)$ specifies the spatial distribution of the light intensity across the input pupil of the receiving photomultiplier of area S .

REFERENCES

1. M.A. Kolosov and A.V. Shebel'nikov, *Refraction of Electromagnetic Waves in the Atmospheres of the Earth, Venus, and Mars* (Sov. Radio, Moscow, 1978).
2. S.M. Rytov, Yu.A. Kravtsov, and V.I. Tatarskii, *Introduction into Statistical Radio Physics. Part 2* (Nauka, Moscow, 1978).
3. A.V. Alekseev, M.V. Kabanov, and N.F. Kushtin, *Optical Refraction in the Earth's Atmosphere* (Nauka, Novosibirsk, 1982).
4. V.V. Vinogradov, A.G. Kosterin, A.S. Medovikov, and A.I. Saichev, *Izv. Vyssh. Uchebn. Zaved. SSSR. Radiotekhn.* **28**, No. 10, 1227-1232 (1985).
5. V.A. Banakh, A.E. Melamud, V.L. Mironov, V.V. Nosov, and B.N. Chen, *Opt. Spektr.* **62**, No. 5, 1136-1140 (1987).
6. V.A. Banakh, A.R. Larichev, V.M. Sazanovich, R.Sh. Zvyk, and B.N. Chen, *Atmos. Optics* **3**, No. 3, 273-278 (1990).
7. V.V. Nosov, *Opt. Atmos.* **1**, No. 1, 122-125 (1988).
8. Yu.D. Kopytin, V.V. Nosov, and E.V. Nosov, "LIRA multifunctional laser refractometer. I. A review of theoretical and experimental methods for investigating the refraction of the light radiation in the Earth's atmosphere," *VINITI*, No. 3158-V96, Moscow, 1996, 35 pp.
9. Yu.D. Kopytin, V.V. Nosov, and E.V. Nosov, "LIRA multifunctional laser refractometer. II. Procedure for measuring angles of regular refraction of optical radiation," *VINITI*, No. 3159-V96, Moscow, 1996, 36 pp.
10. Yu.D. Kopytin, V.V. Nosov, and E.V. Nosov, "LIRA multifunctional laser refractometer. III. Adaptive laser system for express measurements of regular and random optical refraction," *VINITI*, No. 3234-V96, Moscow, 1996, 12 pp.

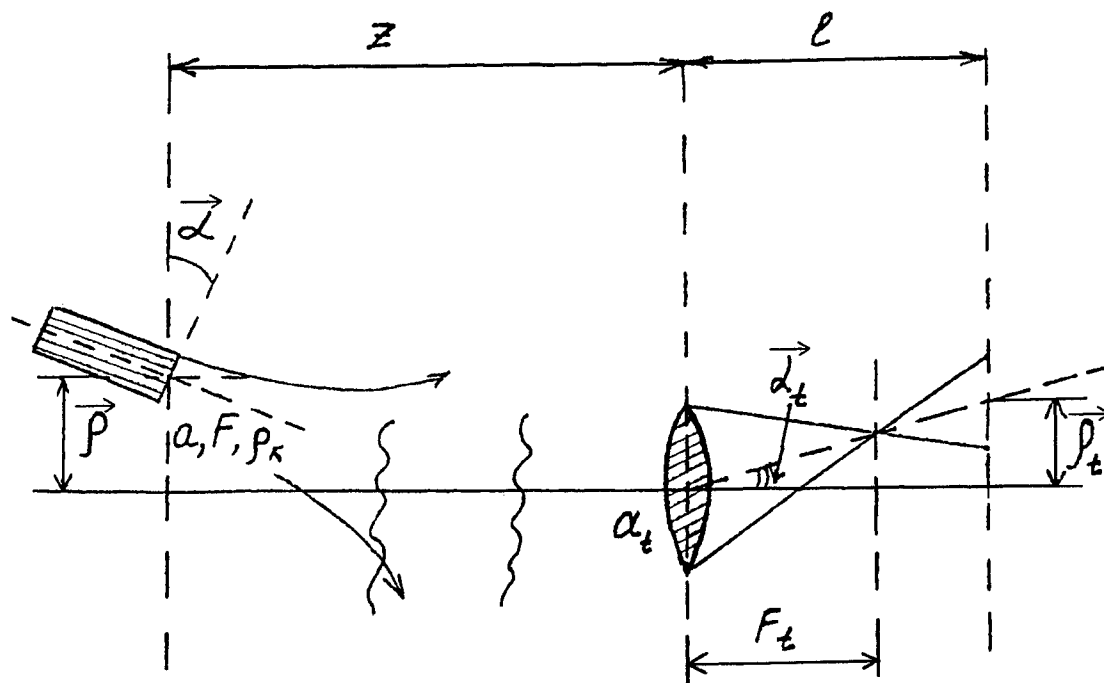


Fig. 1. Measuring the refraction angle in the receiver. Source – a laser.

Use of nondispersion correlation spectroscopy for remote sensing of CO in combustion gases

Vitaly P. Kabashnikov, Natalya V. Kuzmina, Natalya S. Metelskaya
Institute of Physics, Belarus Academy of Sciences
68, Scaryna ave., Minsk, 220072, Belarus

ABSTRACT

A possibility to use the own infrared radiation of a gas mixture to detect CO in combustion products by means of nondispersion correlation method has been investigated. Water vapour and carbon dioxide in atmosphere has a little effect on the signal. But atmosphere CO restricts registration distances to about 100 m. Presence of H_2O and CO_2 in a jet causes two-valued property of the calibration curve and may bring indeterminacy in detection of CO in jet. Nevertheless, registration of CO absorption mass over 0.1 atm cm in combustion products using own radiation of combustion products is possible.

Keywords: nondispersion correlation spectroscopy, remote sensing, carbon monoxide, combustion gases, heated exhaust jets, infrared radiation.

1. INTRODUCTION

Interest in remote sensing of molecular gases has increased greatly during the last 20 years because of wide applications in controlling of the atmosphere pollutants.

Optical methods for gas analysis may be divided to methods of absorption spectroscopy, methods of correlation spectroscopy and laser methods. Methods and devices of absorption spectroscopy are the most simple in technical realisation and are used as a rule in local measurements. But they are unsuitable if the gas mixture contains impurities with the spectral bands overlapping with the spectral band of the gas under investigation. Methods of correlation spectroscopy allows one to reach high selectivity with respect to the gas under consideration and to carry out not only local, but also remote measurements.

Analytical methods of correlation spectroscopy may be divided to dispersion and nondispersion methods. The main group of dispersion correlation analysers includes analysers using special optical masks that transmit radiation only in spectral lines of the gas mixture. Such methods are described in works of Bottema, Plummer, Strong^{1,2} and other authors³⁻⁵. This paper deals with nondispersion correlation method. Most of the previous works referred to nondispersion correlation spectroscopy⁶⁻¹⁰ deal with outer (artificial or natural) sources of radiation. These methods may be referred to as active methods. We concentrate in this paper on the passive method in which own infrared radiation of the heated gas mixture is registered. Such problem arises at the remote sensing of combustion products such as exhaust jets outgoing from plant smoke-stacks.

2. ANALYSIS

Consider the operation of the analyser based on nondispersion correlation method. A basic diagram of the analyser is given in Fig. 1. An outer radiation passed through the gas mixture 1 (active method) or the own radiation of the heated gas mixture (passive method) next passes through the filter 2 selecting the absorption band of the gas under control, the chopper 3, and through the correlation cuvette 4 with the fixed quantity of the same gas as the gas being measured and a neutral attenuator 5 alternatively. Radiative fluxes through a correlation cuvette H_c and through a neutral attenuator H_n are registered by the detector 6. Frequency-averaged transmittance of the cuvette must be equal to the transmittance of

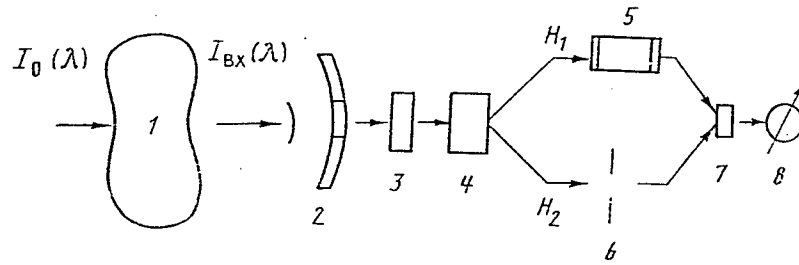


Fig. 1. A basic diagram of the nondispersion correlation analyser.

the attenuator. The difference of signals H_c and H_n normalized with the respect to their sum depends on absorption mass of the gas being investigated in the gas mixture.

Simulating the jet by a flat uniform layer, we have that the total intensity of the radiation passed through a correlation cuvette is

$$H_c = B \langle (1 - \tau_{jet}) \tau_{atm} \tau_{cuv} \rangle \quad (1)$$

where $B = B_{jet} - B_{atm}$ is excess of the Planck function at the gas mixture temperature over the background radiation of atmosphere; τ_{jet} is the transmittance of the gas mixture; τ_{atm} is the transmittance of atmosphere; τ_{cuv} is the transmittance of the correlation cuvette. Angular brackets mean frequency averaging over the transmittance band of the filter.

The total intensity of the radiation passed through a neutral attenuator is

$$H_n = B \langle (1 - \tau_{jet}) \tau_{atm} \rangle \langle \tau_{cuv} \rangle, \quad (2)$$

when the calibration condition is fulfilled

$$\tau_n = \langle \tau_{cuv} \rangle, \quad (3)$$

where τ_n is transmittance of neutral attenuator.

An electronic system forms a signal

$$H = \frac{H_n - H_c}{H_n + H_c}, \quad (4)$$

which contains an information about the absorption mass of the gas in jet being measured.

3. RESULTS

In this section we consider the infrared thermal radiation of CO in the band 4,6 mm for remote control of the carbon monoxide content in heated combustion products of hydrocarbon fuel. Line-by-line calculations based on database [11] were used. All the results presented in Figures were calculated with the jet temperature 373K, atmosphere and cuvette temperature 273K and pressure 1 atm.

Consider a signal H as a function of absorption mass of gas under investigation. Calibration characteristics for CO analyser with different absorption masses of CO in correlation cuvette and with no foreign gas in jet are shown in Fig.2. Value of the signal H increases when absorption mass of correlation cuvette increases. It is seen that the influence of the atmosphere containing only H_2O and CO_2 on behaviour H is negligible. But as it follows from numerical calculation, presence of CO in atmosphere affects signal beginning with the viewing distances about 100 m. The jet temperature has a little effect on the signal if the temperature is below 450K.

Carbon dioxide and water vapour are the main products of burning. They have the absorption bands overlapping with the 4,6 mm band of CO. This circumstance involves difficulties in detection of CO radiation. The method of nondispersion correlation spectroscopy allowed to select CO radiation from H_2O and CO_2 radiation. Figures 3, 4 show signals at typical absorption masses of H_2O and CO_2 in plant smoke- stacks. It can be seen that in contrary to the active method the calibrations curves become two-valued that causes indeterminacy in detection of CO in jet. This situation requires some additional information to find the content of CO in a jet. But reliable registration of CO absorption masses over 0.1 atm cm is possible with no additional information.

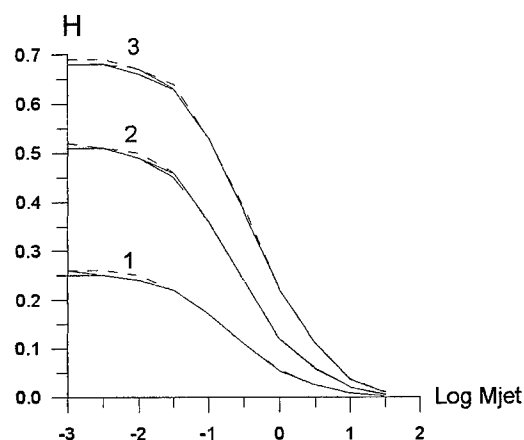


Fig. 2. Signal vs absorption mass of CO in a jet at different absorption masses of CO in correlation cuvette and at different viewing distances D . CO_2 and H_2O are absent in a jet. Curves 1 - absorption mass in cuvette $M_c = 0.03$ atm.cm; Curves 2 - $M_c = 0.1$ atm.cm; Curves 3 - $M_c = 0.3$ atm.cm. Solid lines - viewing distances $D = 0$; dashed lines - $D = 100$ m; dotted lines - $D = 1$ km.

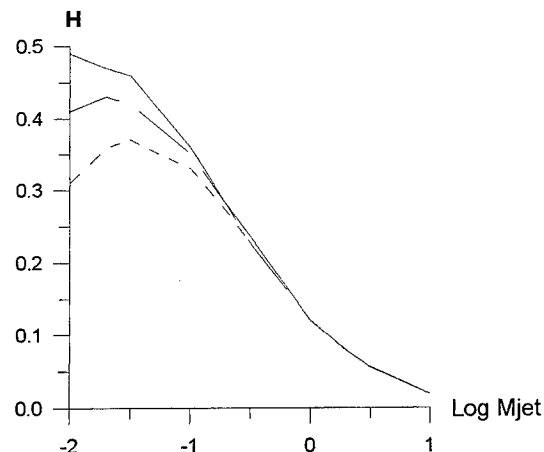


Fig. 3. Signal vs absorption mass of CO in a jet. Absorption mass of CO in correlation cuvette is 0.1 atm.cm. Viewing distance $D=0$. CO_2 is absent in a jet. Solid line - no H_2O in a jet; dashed - 3 atm.cm of H_2O in a jet; dotted - 10 atm.cm of H_2O in a jet.

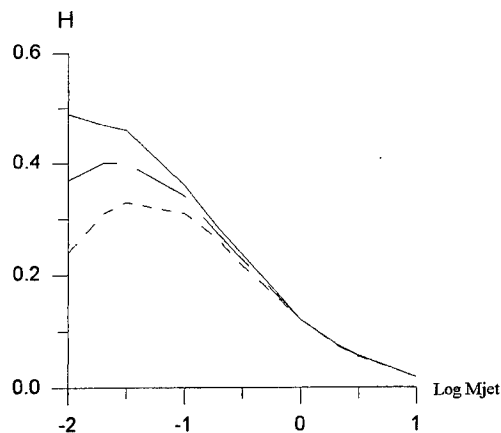


Fig. 4. Signal vs absorption mass of CO in a jet. Absorption mass of CO in correlation cuvette is 0.1 atm.cm. Viewing distance $D=0$. H_2O is absent in a jet. Solid line - no CO_2 in a jet; dashed - 3 atm.cm of CO_2 in a jet; dotted - 10 atm.cm of CO_2 in a jet.

4. CONCLUSION

A possibility to use the own infrared radiation of a gas mixture to detect CO in combustion products by means of nondispersion correlation method has been investigated. Water vapour and carbon dioxide in atmosphere has a little effect on the signal. But atmosphere CO restricts registration distances to about 100 m. Presence of H_2O and CO_2 in a jet causes two-valued property of the calibration curve and brings indeterminacy in detection of CO in jet. Nevertheless registration of CO absorption mass over 0.1 atm cm in combustion products using own radiation of combustion products is possible.

ACKNOWLEDGEMENTS

This work was partially supported by the International Science Foundation and the Government of the Republic of Belarus under the grant # F95100.

REFERENCES

1. M. Bottema, W. Plummer and J. Strong, "Water vapor in the atmosphere of Venus", *Astrophys. J.* **139**, #3, pp. 1021-1022, 1964.
2. M. Bottema, W. Plummer, J. Strong and R. Zander, "Composition of clouds of Venus", *Astrophys. J.* **140**, #4, pp. 1640-1641, 1964.
3. R. B. Kay, "Absorption spectra apparatus using optical correlation for the detection of trace amounts of SO₂", *Appl. Opt.* **6**, #4, pp. 776-778, 1967.
4. D. T. Williams and B. L. Kolitz, "Molecular correlation spectrometer", *Appl. Opt.* **7**, #4, pp. 607-616, 1968.
5. G. A. Decker, "Hadamard-transform exhaust analysis spectrometer", *Appl. Opt.* **10**, #1, pp. 24-27, 1971.
6. P. L. Hanst, "Optical measurement of atmospheric pollutants: accomplishments and problems", *Optic. and Quant. electr.* **8**, #2, pp. 87-93, 1976.
7. T. V. Ward and H. H. Zwick, "Gas cell correlation spectrometer", *Appl. Opt.* **14**, #12, pp. 2896-2904, 1975.
8. J. M. Pussel, J. H. Park and S. R. Drayson, "Global monitoring of stratospheric halogen compounds from a satellite using gas-filter spectroscopy in the solar occultation mode", *Appl. Opt.* **16**, #3, pp. 607-612, 1977.
9. W. F. Herget, A. J. Jahnke e. a., "Infrared gas-filter correlation instrument for in situ measurement of gaseous pollutant concentrations", *Appl. Opt.* **15**, #5, pp. 1222-1228, 1976.
10. L. L. Acton M. Griggs e. a., "Remote measurement of carbon monoxide by a gas-filter correlation instrument", *AIAA Journal* **11**, #7, pp. 899-900, 1973.
11. J. S. Garing and R. A. McClatchey, "Atmospheric absorption line parameters compilation", *Appl. Opt.* **12**, #5, pp. 2545-2554, 1973.

Investigations of the optical characteristics of aerosol in the coastal area

T. Skakalova, I. Grigorov, O. Parvanov, I. Kolev
Institute of Electronics, Bulgarian Academy of Sciences

72 Tsarigradsko shosse blvd., Sofia 1784, Bulgaria
Phone: +359 (2) 750096; FAX: +359 (2) 9753201; e-mail: blteam@phys.acad.bg

ABSTRACT

The paper continues our previous investigations, based on the backscattering coefficient distribution, of the optical properties of aerosol in a coastal zone. The material presents some results of an elastic-backscattering lidar experiment carried out in the Bulgarian Black Sea coastal area in September 1992. The lidar experimental results are presented as 2-D images of the cross-sections of the variation of the extinction as a function of the height and the distance along the sounded path at different elevations. The value of the volume extinction coefficient is calculated according to Klett's inversion method, based on single elastic scattering of the laser emission. Along with the lidar measurements a conventionally measured meteorological parameters are presented. The experimental data considered in the paper demonstrates the lidar sensitivity to undrelying surface influence over the optical characteristics of the aerosol.

Keywords: Lidar, coastal zone, breeze flows, aerosol extinction.

1. INTRODUCTION

The data discussed in the present paper was taken during an experiment varried out in September 9-14, 1992, in the region of the village Shkorpilovtzi (in a station, belonging to the Institute of Oceanography, Bulgarian Academy of Sciences). The ground-based elastic backscattering lidar [1], used during the experiment, was installed at 12 m above the sea level and about 120 m away from the shoreline. A meteorological surface layer station and pilot balloons [1] were use for obtaining the basic meteorological parameters: temperature and humidity diurnal behavior and wind profiles. The lidar data considered in the paper were obtained by scanning vertically with different steps along various azimuths, in dependence on the scale and duration of the observed phenomena.

The synoptic conditions during the experiment were quiet, sunny weather with well developed breeze circulation.

2. THEORETICAL BACKGROUND

The value of the volume extinction coefficient $\alpha(r)$ is calculated according to Klett's inversion method [2, 3], based on single elastic scattering of the laser emission:

$$\alpha(r) = \frac{\exp\{[S(r) - S(r_m)]/k\}}{\frac{1}{\alpha(r_m)} + \frac{2}{k} \int_r^{r_m} \exp\{[S(r') - S(r_m)]/k\} dr'}$$

this equation $\alpha(r)$ is the value of the volume extinction coefficient in a spatial interval Δr , r is the distance away from the lidar, $S(r)=\ln[P(r)r^2]$ is the logarithm of the received power of the dispersed laser emission $P(r)$ multiplied by the square value of the distance, and m is an index, related to the predefined referent distance at the end of the sounding trace. As it was shown [2, 3] the equation written above possesses the tendency to approach the correct solution curve in spite of a poor estimate of the boundary volume. Without preliminary data about the contents and distribution by dimensions of the sounded aerosol particles, a power law between volume backscatter coefficient and is assumed:

$$\beta(r) = C_1 [\alpha(r)]^k$$

where C_1 is a constant value, and the value of k is chosen according to the assessment of the meteorological visibility distance in the ground layer during the particular lidar measuring. The assessment of $\alpha(r_m)$ at the end of the trace is performed by using the slope method, as proposed in [2], for clean and for turbid atmosphere.

The lidar experimental results are presented as 2-D images, constructed by compiling profiles taken successively at certain elevations along a fixed azimuth (Az) with respect to the North. The grey scale of the images displays the variations of the volume extinction coefficient as a function of the height (H) and the distance (R) from the lidar.

3. EXPERIMENTAL RESULTS

Experimental data taken during different stages of the local breeze circulation development are presented and analysed.

A. Case of Land-to-Sea Breeze

Fig. 1 presents a vertical cross-section, obtained in the early morning hours (06:57-07:05 LST, sunrise - 06:50 LST) over the sea surface, perpendicular to the shoreline (Az=90°). As it is seen from the figure the extinction coefficient of the air masses spread up to height of about H=50 m and from H=100 m to H=200 m has higher values than the one of the surrounding air. The observed distribution suggests an aerosol structure, which is in good agreement with the temperature and humidity profiles for that part of the day shown in Fig. 2 (the figure presents summarized results, obtained during some earlier serial meteorological observations, carried out in the same area/region of investigation [4]). Having in mind the temperature and humidity profiles, one may come to the conclusion that the observed higher values of the extinction coefficient are due to aerosol layers formed by wet aerosols generated over the sea surface and trapped by the temperature inversions.

Next figure (Fig. 3) presents a vertical scan (07:16-07:23 LST) over the sea, Az=135°. Up to approximately H=200 m over the sea surface and again over height of about H=600 m high values of the extinction coefficient are observed. The advection of cooler and dry air from the land over the warmer surface of the water leads to formation of a haze over the sea, as it was observed and recorded in the experimental diary.

Fig. 4 shows a vertical scan, taken two and a half hours after the sunrise (09:33-09:40 LST) on the same day, over the land Az=305°. The extinction coefficient of the air over the surface up to heights of about H=200 m seems to have higher magnitude than the one of the air at greater heights. Most probably this is a result of the considerable evaporation by the underlying grass surface. The intensive sun heating during that part of the day leads to an increase in the humidity of the aerosol layers in contact with the surface. Looking at the pilot balloon wind profile in Fig. 5 recorded at the same time (09:30 LST) one can see that up to heights of about H=600 m a zone of decay exists. In Fig. 4 up to about the same heights zone of lower contrast is observed. The higher extinction coefficient of the air mass above 600m is probably caused by the more humid air transported by the sea-to-land flow observed at these heights (Fig. 5).

B. Case of Sea-to-Land Breeze

Similar distribution of the volume extinction coefficient is observed in Fig. 6 (10:03-10:11 LST), presenting data obtained over the land $Az=360^\circ$, parallel to the shoreline. As it is seen from the image the coefficient's values in the layer up to height of about $H=300$ m stretching to $R=800$ m away from the lidar and at greater distances up to height of $H=200$ m are higher than the values in the air above; almost the same values are observed again at heights greater than $H=600$ m. About $R=600-700$ m northward of the lidar location the sandbank widens to about 200-250 m inside the land. The extinction coefficient values in the layer over the sand surface are smaller than the ones in the air over the lawn situated near the lidar, due most probably to the weak evaporation from sand at that time.

Fig. 7 presents data obtained in the late morning hours (11:11-11:19 LST) over the land surface along $Az=345^\circ$. The values of the extinction coefficient are almost the same within the whole scan. As it is seen from the wind profiles shown in Fig. 5 this is a calm period of the breeze circulation, that precedes the change of the wind direction. The air mass spread over the land surface contains basically dry aerosol generated over the ground. The formation at that time of the mixing layer leads to comparatively uniform distribution of the aerosol within the boundaries of the mixing layer.

Fig. 8 shows a lidar cross-section of the volume extinction coefficient, taken after midday (13:44-14:02 LST) over the land, along $Az=360^\circ$, parallel to the shoreline. The scanning is performed with a step of 1° up to 10° , focusing in this way on the microscale structure of turbulence in the lowest atmospheric layers. As one can see from the image the extinction coefficient values are almost the same at distances to $R=1000$ m away from the lidar and increase at greater ones. The intensive turbulence, taking place in the atmosphere and prevailing over the breeze circulation leads to mixing of the wet aerosol penetrating with the wind flow (Fig. 9) from the sea with the one situated over the land surface. As it is mentioned above at distances greater than $R=700$ m from the lidar the underlying surface is sand, which most probably causes higher temperature gradient between the strand and the water than in the case of grass strand and consequently more intensive sea-to-land flows.

4. DISCUSSION AND CONCLUSIONS

As it is seen from the experimental data presented one can distinguish between the lidar images of the volume extinction coefficient distribution observed over the land and sea surface, as well as between the images compiling data acquired during different phases of the breeze circulation. This proves the ability of using the atmospheric aerosol particles as tracer for investigation of the micro- and mesoscale phenomena taking place in coastal zones and the influence of the latter on the optical characteristics of the atmospheric aerosol.

During the autumn the temperature of the sea in the morning hours is higher than the temperature of the air above it. As it is observed in Fig. 3 in this case the land-to-sea flow of cooler air gives rise to haze over the warmer evaporating sea surface.

Figs. 4, 6 and 7 actually picture the different stages of the mixing layer formation over the land surface in contrast to Fig. 1 where stable stratification of atmosphere is observed. Fig. 4 presents the extinction coefficient distribution two and a half hours after the sunrise over comparatively monotonous underlying surface. In Fig. 6 vertical cross-section of the mixing layer parallel to the boundary between the land and water surface is shown. The scanning is performed over two underlying surfaces, viz. grass and sand, with considerably different properties. In the figure one can distinguish between the aerosol distributions formed under the influence of the different underlying surfaces: the height of the plume over the grass at distance from $R=200$ m to about $R=700$ m away from the lidar reaches about 200 m, while the plume over the sand area stretches up to about 400 m. With the progress of the mixing layer development, as it can be seen in Fig. 7 (about three and a half hours after the sunrise), the influence of the underlying surface grows weak and as a result of the intensive turbulent processes the aerosol within the mixing layer is uniformly distributed.

The last figure, Fig. 8 compiling data obtained about seven hours after the sunrise, again attests to difference between the optical characteristics of aerosol over the sand and grass surfaces. In this case the moisture transported by

the sea-to-land flow over the sand area is higher than the one over the grass region round the lidar. The high gradient of the temperature between the sand and water surface intensifies the flow.

Summarizing, it should be noticed that the underlying surface as well as the processes of formation and development of the Sea Planetary Boundary Layer exert influence on the optical characteristics, in this instance on the extinction coefficient by changing the microphysical characteristics of the coastal aerosol.

Comparing the results of our previous investigations of the atmosphere aerosol stratification in the coastal zone [1], based on lidar cross-sections of the back-scattering coefficient distribution, with the present observations we could draw the following conclusions:

A. Both optical parameters, namely the volume extinction and the back-scattering coefficients gives possibility of reliable study of the micro- and mesoscale phenomena in coastal zones.

B. The usage of the back-scattering coefficient is preferable in cases of considerable gradient in aerosol particle concentration or in meteorological parameters as for instance in humidity, while the volume extinction coefficient turns to be of practical value in case of homogeneous atmosphere, i.e. in case of intensive turbulence and high visibility in the atmosphere.

REFERENCES

1. I. Kolev, O. Parvanov, B. Kaprielov, E. Donev, "Lidar observations of aerosol stratification in the case of sea breeze circulation near the shore", *Comptus rendus de l'Academie bulgarie des Sciences*, **Tome 47**, No. 11, pp. 21-24, 1994
2. J.D. Klett, "A stable analytical inversion solution for processing lidar returns", *Appl. Opt.*, **Vol. 20**, No. 2, pp. 211-220, 1981
3. J.D. Klett, "Sensitivity of a lidar inversion algorithm to parameters relating atmospheric backscattering and extinction", *Appl. Opt.*, **Vol. 24**, No. 11, pp. 1638-1643, 1985
4. Z.K. Belberov, V.I. Zahariev, et. al. *Interaction of the atmosphere, hydrosphere and lithosphere in the nearshore zone - results of the international experiment Kamchiya '79*, Publishing House of Bulg. Acad. of Sciences, Sofia, 1983.

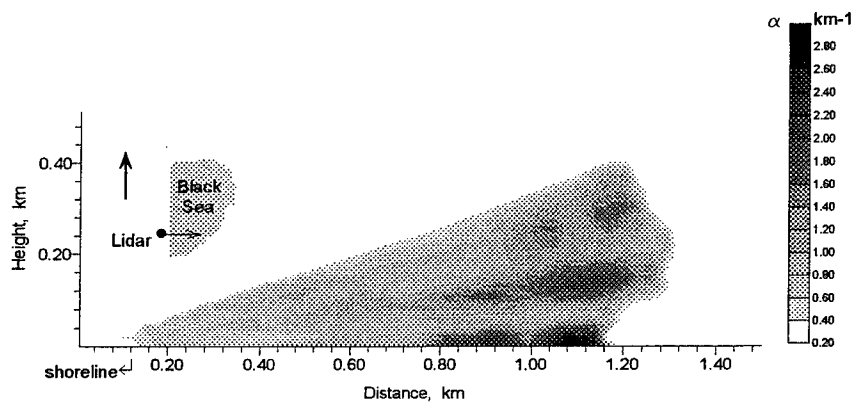


Fig.1. Lidar map; 14.09.92, Az=90, 06:57-07:05 LST

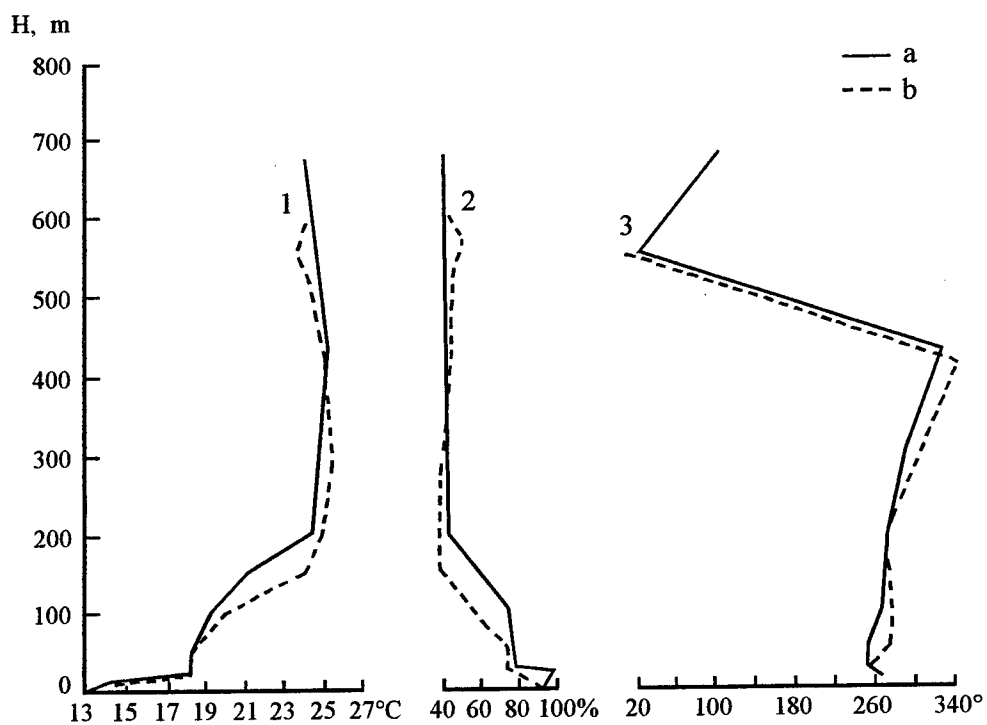


Fig.2. Vertical profiles of temperature (1), humidity (2) and wind direction (3); a-ascending and b-descending tethered balloon; Sept.24, 07:10-07:40 LST

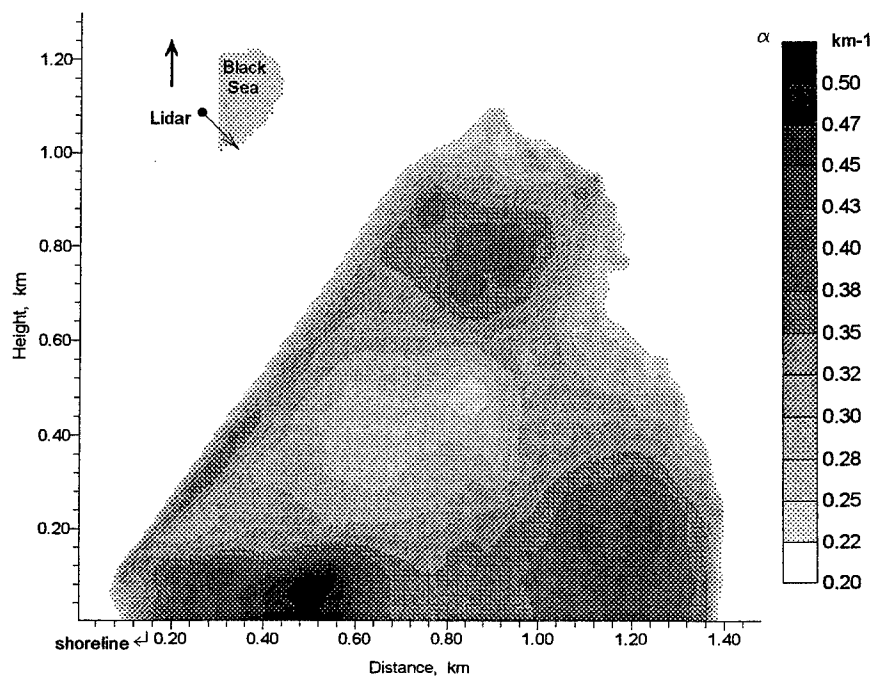


Fig.3. Lidar map; 14.09.92, Az=135, 07:16-07:23

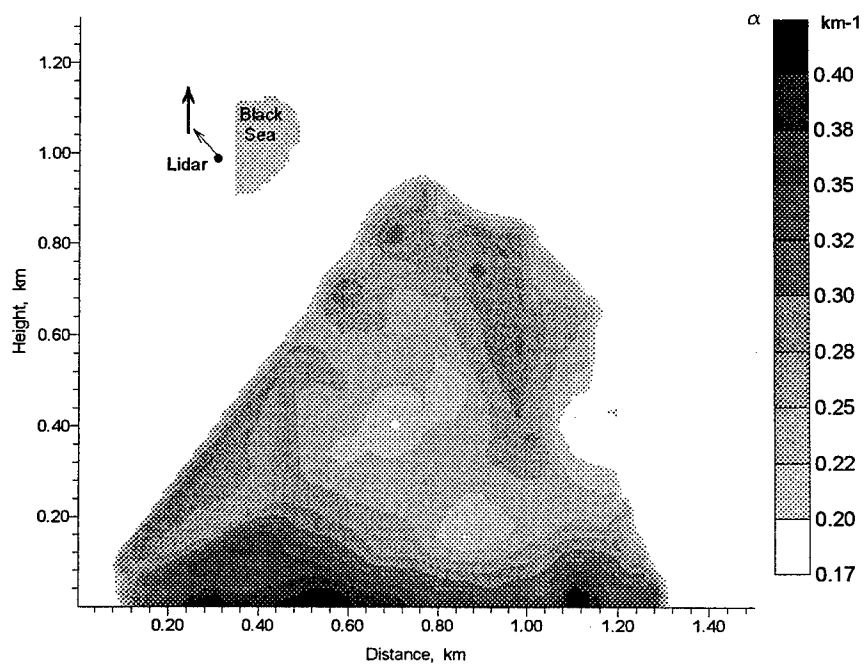


Fig.4. Lidar map; 14.09.92, Az=305, 09:33-09:40

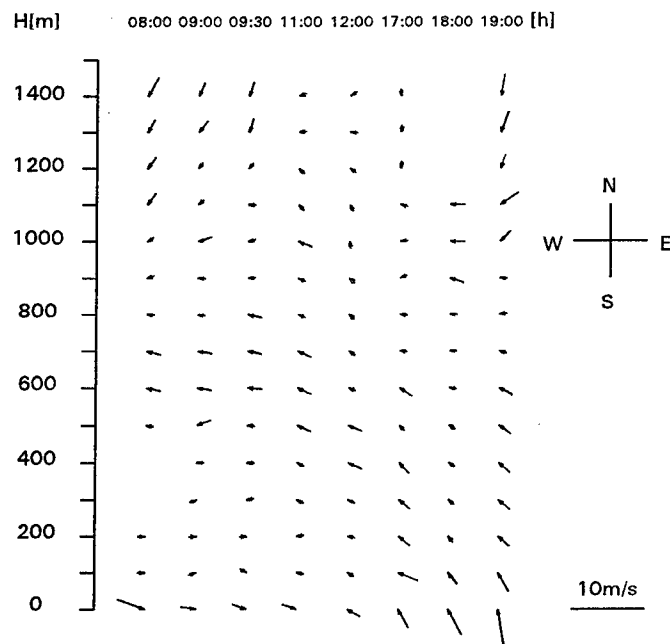


Fig. 5 Pilot Balloon Wind Profiles 14.09.1992

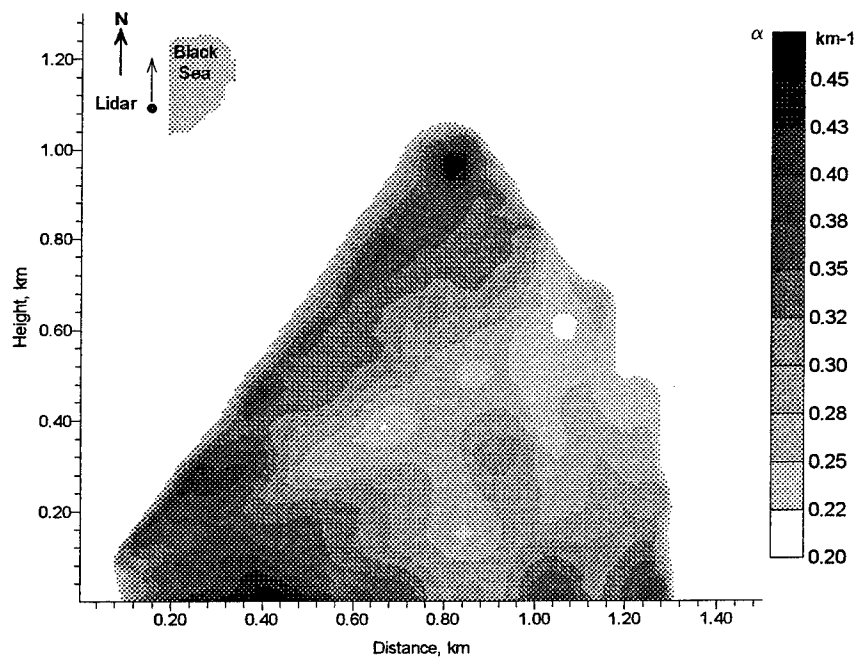


Fig.6 Lidar map; 14.09.92, Az=360, 10:03-10:11 LST

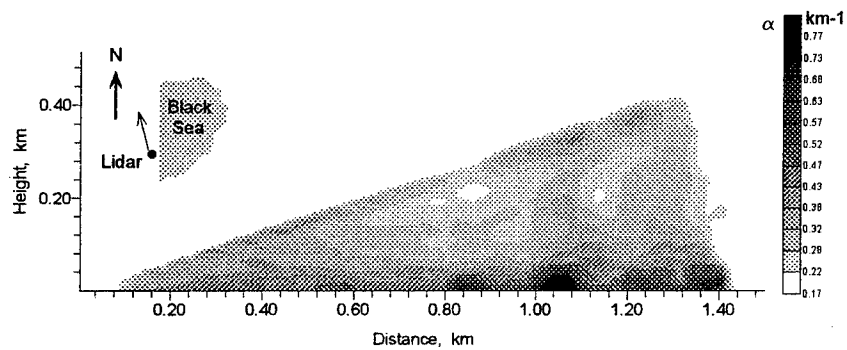


Fig.7. Lidar map; 14.09.92, Az=345, 11:11-11:19 LST

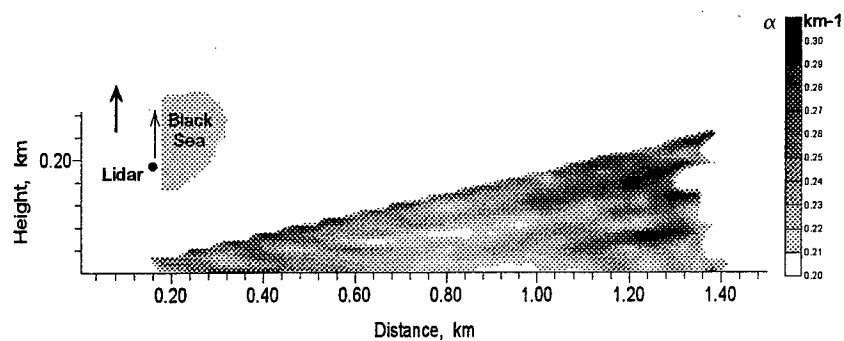


Fig.8. Lidar map; 10.09.92, Az=360, 13:44-14:02 LST

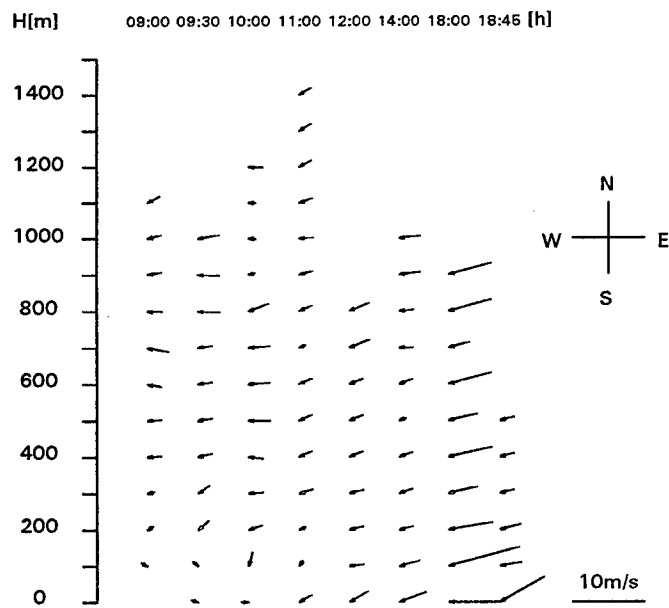


Fig. 9 Pilot Balloon Wind Profiles 08001009.pbp

SESSION 2

Propagation and Imaging through Inhomogenous Media

Aerosol light scatter vs turbulence effects in image blur

N. S. Kopeika, D. Sadot, and I. Dror

Department of Electrical and Computer Engineering, Ben-Gurion University of the Negev
Beer-Sheva, Israel

ABSTRACT

A recent paper by Belen'kii proposed an inner scale turbulence MTF theory model to explain one of the many types of aerosol MTF experimental results by Dror, Sadot, and Kopeika. A broad comparison is made here between Belen'kii's inner scale turbulence MTF and our practical instrumentation-based aerosol MTF models and experiments. Belen'kii's model is strongly contradicted by those experimental results themselves, as well as by the many other published results not considered by Belen'kii. The Dror, Sadot, Kopeika experiments all contain comparisons of practical instrumentation-based aerosol MTF modeling which was calculated from aerosol size distributions actually measured during the experiments. These aerosol MTF calculations validated rather accurately the practical aerosol MTF model measurements. A summary of 9 independent different types of measurements and analyses which show we measured aerosol MTF and not any form of turbulence MTF is included, as well as specific contradictions between Belen'kii's model and our actual measurements. These also indicate our measurements of turbulence MTF were indeed correct, and that a broad system engineering approach to atmospheric optics should be encouraged instead of the narrow pure turbulence, pure aerosol, or pure absorbing atmospheric models often used.

Keywords: atmospheric optics, turbulence, aerosols, light scatter, modulation transfer function, imaging, image restoration

In a recent paper,¹ M. Belen'kii suggested an inner scale turbulence MTF model to explain our atmospheric MTF measurements which indicated a significant aerosol MTF component.² He concluded "the results obtained here eliminate the discrepancies between the conclusions of S & K [Sadot and Kopeika]² and the data of the previous studies [refs. 5 - 9 in Belen'kii ¹]." He also concluded "the implication is that no revision of the classical aerosol MTF theory is required for interpreting the measured data analyzed by S & K". The main point of Belen'kii's paper¹ is his claim that our experimental measurements of overall atmospheric MTF,^{2,3} which we claim include a very significant instrumentation-dependent aerosol MTF,^{2,4} can be explained on the basis of inner scale turbulence effects instead of aerosol MTF. Much of his criticism is based on his claim we used plane wave MTF formulation instead of spherical wave. As pointed out and shown below, this claim is *factually incorrect*.

Belen'kii's presentation of our experimental results is based on turbulence MTF alone, with an implicitly clear assumption that essentially all atmospheric blur derives from turbulence alone including inner scale effects. He considers only one experiment of ours.² The purpose of this paper is to present a broad comparison of his inner scale turbulence and our practical aerosol MTF models with our experiments. The verification of a significant practical aerosol MTF has been performed in a fairly large number of independent experiments not considered by Belen'kii. In addition, his model is contradicted quite clearly by all of our experimental results. In his concluding sentence, Belen'kii admits "nevertheless, an additional experimental study that includes simultaneous measurements of the overall atmospheric MTF and optical measurements of both C_n^2 and l_0 [inner scale] is required for complete validation of the presented theoretical model". In other words, Belen'kii tried to interpret our experimental measurements on the basis of his theory alone without considering effects of aerosol MTF on our experiments.

Our approach is based on some philosophical assumptions which we believe are self-evident. Such postulations are needed because there exist several different atmospheric optics communities which are essentially completely isolated from one another with little or no interaction whatsoever. These communities are the turbulence community, the aerosol community, and the atmospheric absorption community. We postulate that in the real world

1. There is no such thing as a purely turbulent atmosphere.
2. There is no such thing as a purely particulate scattering atmosphere.
3. There is no such thing as a purely absorbing atmosphere.
4. All efforts to model or interpret experimental results in terms of a purely turbulent, or purely scattering, or purely absorbing atmosphere should therefore be strongly discouraged. Only under extreme circumstances when there is no alternative can it be justified to "make pretend".

The real world atmosphere involves turbulence, particulate scatter, and gaseous and particulate absorption all taking place simultaneously. In general, one can say

1. Gaseous and particulate absorption and large angle particulate scatter are manifested as attenuation of electromagnetic radiation.
2. Small angle particulate scatter and turbulence cause blur.
3. Time dynamic processes such as scintillations and image dancing arise primarily from turbulence.

Interactions between these processes do exist. For example, although aerosols do not directly affect scintillations or image dancing, aerosol loading affects humidity and temperature gradients⁵⁻⁹ and therefore affects the value of C_n^2 which determines the time dynamics of turbulence. This means aerosols do affect time-dynamic properties of turbulence, such as scintillations and image dancing, but do so indirectly. It is most probably no coincidence that vertical profiles of C_n^2 and aerosol loading through the atmosphere are similar, with both usually exhibiting increases at 15 - 25 km elevation.⁵ Also, although atmospheric absorption affects primarily atmospheric transmission, it also affects aerosol MTF for single-interaction events of photons with particulates because it is the clear image from received unscattered light which is attenuated by absorption much more than the blurred image emanating from received scattered light.¹⁰ Hence, when modeling atmospheric optics processes and interpreting experimental results, a broad system-engineering approach is rather necessary instead of the assumption that only one mechanism such as turbulence causes significant atmospheric blur¹.

That small angle forward scatter causes blur has been proved experimentally under controlled laboratory conditions by Kuga and Ishimaru¹¹ and by Donelli, et al.¹² Aerosol MTF modeling is also supported by Monte Carlo simulations by Valley¹³, Bruscalioni et al.¹⁴, as well as much of the data in the book by Zege, et al.¹⁵ The question that should be addressed is therefore not if aerosol scatter causes blur but rather the relative roles of aerosol and turbulence MTFs in imaging through the atmosphere. Belen'kii accepts the classical aerosol MTF models¹⁵⁻²⁰ but takes exception to our practical instrumentation-based aerosol MTF model^{2,4} which, in accordance with extensive measurements,^{3,9,21-27} extends aerosol MTF variation out to much higher spatial frequencies than a few cycles-rad⁻¹. The classical aerosol MTF models predict little aerosol blur of small detail except possibly under very poor transmission conditions. The reason is that it predicts aerosol MTF decrease from unity at zero spatial frequency to a value equal to atmospheric transmission at the "knee" spatial frequency a/λ cycles-rad⁻¹, where a is particulate radius and λ is wavelength.¹⁵⁻²⁰ The value of a/λ is typically on the order of a few cycles-rad⁻¹. For spatial frequencies greater than a/λ , classical aerosol MTF retains the constant value of atmospheric transmission. The assumption here is that the scatter diagram or phase function is maximum at zero degrees (unscattered light) and decreases towards zero at the diffraction angle limit of λ/a , which is on the order of radians. The *unscattered* light is an impulse function in angle space, whose Fourier transform is a constant in angular spatial frequency space of amplitude equal to atmospheric transmission. The *scattered* light image, which exhibits a broad range of scatter angles out to the diffraction limit λ/a , exhibits a narrow Fourier transform from zero out to the angular spatial frequency a/λ . The superpositions of both images and MTFs yield the overall images and MTFs respectively.

The practical instrumentation-based aerosol MTF considers the actual aerosol MTF recorded in the image, rather than that input to the optics. It is simply physically impossible for the aerosol MTF actually recorded in the image to be that which is input to the optics. For example, although the aerosol scattering diagram goes out to scatter angles on the order of λ/a radians, receiver field-of-view is typically much, much smaller, being on the order of milliradians. Hence, the angles of scattered light actually recorded in the image are limited to milliradians rather than radians, thus reducing

blur extent by orders of magnitude and increasing the knee angular spatial frequency of the aerosol MTF by orders of magnitude. In actual practice, since the unscattered light intensity is so much greater than that of the scattered light, instrumentation dynamic range limitations may truncate the scattering pattern actually recorded in the image at even smaller scatter angles than optics field-of-view, thus broadening aerosol MTF knee frequency even further.^{2,4} In such dynamic range truncation effects on the maximal values of light scatter actually recordable in the image, it is important to consider the effect of finite spatial frequency bandwidth of the instrumentation.^{2,4} This broadens the unscattered light portion of the spread function from an angular impulse function to hundreds of microradians typically.²⁻⁴ Such broadening then causes reduction of the amplitude of the unscattered light portion of the spread function by several orders of magnitude since energy must be conserved.^{2,4} The result of this is that the *amplitudes of the unscattered and scattered light portions of the spread function are brought much closer to each other by several orders of magnitude* than if the spatial frequency bandwidth were infinite.^{2,4} It is the light scatter at small angles on the order of tens, hundreds, and thousands of microradians which cause the aerosol blur actually recorded in images. These values of scatter angles are similar to the values of wavefront tilts caused by turbulence, which also are typically on the order of tens and hundreds of microradians.²⁸ As a result, the practical aerosol MTF extends out to high spatial frequencies similar to those affected by turbulence.^{2,4} The "knee" spatial frequency predicted by the classical aerosol MTF models does exist, but at a spatial frequency orders of magnitude larger, with the knee spatial frequency varying according to instrumentation and aerosol scattering phase function. This changes with aerosol size distribution which changes with weather. Belen'kii's conclusion that "no revision of the classical aerosol MTF theory is required for interpreting the measured data analyzed by S & K" is simply a physical impossibility since there is no way a 2 mrad field-of-view (in our experiments) can see imaged scattered light over several radians.^{2,21}

The practical aerosol MTF model has been confirmed experimentally through many different types of experiments.^{3,9,21-27} all of which have shown strong correlation between model prediction and actual experimental measurement. The lines-of-sight for the visible and near infrared imaging are either 5.5 or 6.5 km, and involve *optical depths on the order of 1 to 3*. Average elevation is on the order of 15 m for the 5.5 km path and 25 m for the 6.5 km path. For the 3 - 5 μm wavelength thermal imaging the line-of-sight was also 6.5 km with 25 m average elevation. For the 8 - 13 μm wavelength imaging the line-of-sight was 2 km, with about 15 m average elevation. In these experiments, actual coarse aerosol size distributions have been *measured*. These change strongly with weather. The size distributions of the small or fine particulates, which change very little with weather, have been taken from LOWTRAN/MODTRAN. The scattering diagrams of phase functions have been calculated from the size distributions. From them the specific intensities or aerosol point spread functions have been obtained. The Fourier transforms of the specific intensities are the aerosol MTFs. The entire calculation procedure is described step-by-step in reference 4. Indeed, examples of specific intensity or spread function calculations based on aerosol parameter measurements are shown in refs. 21 and 26. They are quite close to the actual spread function measurements, some examples of which are shown in ref. 9. Always there is strong correlation between the measured practical aerosol MTF and that predicted by the model and also between the measured and expected knee spatial frequencies. These corroborations of practical aerosol MTF involve independent measurements and techniques over a wide range of concepts.^{3,9,21-27} It is no coincidence that the titles of most of the above referenced papers contain the words "and verification" or "and validation" because of the accompanying comparisons between theoretical aerosol MTF calculation (based on actual aerosol parameter measurement) and aerosol MTF measured in experiment. A refutation of the practical aerosol MTF must relate to *all* of these independent techniques, which include

1. Measurements of aerosol MTF in the visible and near infrared over the same pixels simultaneous to and independent of measurements of C_n^2 , and comparisons to predicted practical aerosol MTF calculated from actually measured aerosol size distributions^{3,9,21,24,25,27}. Had we measured, instead, inner scale turbulence MTF there would be no correlation with the aerosol size distribution based aerosol MTF.
2. Measurements of overall atmospheric MTF, calculation of practical aerosol MTF, and comparison between them in the long wave infrared (8 - 12 μm wavelength) at spatial frequencies and wavelengths where *turbulence is insignificant*,^{22,23} *almost nonexistent*. Hence, the atmospheric MTF in these experiments was essentially *aerosol MTF only*.
3. Same as above, but over the 3 - 5 μm range.²⁶
4. Measurements of long exposure and short exposure aerosol MTFs which turned out to be essentially identical.²⁵ If our practical aerosol MTF were instead inner scale turbulence MTF then long and short

exposure measurements of it would definitely be very different, with the short exposure MTF much higher and broader. The fact that those short and long exposure MTFs were so identical is a *very strong indication* that what we measured was actually aerosol MTF. Short exposure time was 0.83 ms. Long exposures were 1000 short exposures.²⁵

5. Development of an atmospheric Wiener filter technique to restore atmospherically blurred images with *essentially total* correction,^{27,29} based upon the existence of both turbulence and practical aerosol MTFs, which enhances selectively the information content of those high spatial frequencies least affected by turbulence jitter.²⁷ Aerosol MTF jitter is neglected. If our practical aerosol MTF were indeed inner scale turbulence effects, such jitter could not be neglected while obtaining essentially total correction for atmospheric blur.^{27,29}
6. Measurements of Fried's resolution parameter r_0 by means of cardboard apertures of different sizes which show clearly that actual r_0 is significantly smaller than that deriving from C_n .^{2, 25}
7. Measurements of long exposure turbulence and aerosol MTFs using two different imaging systems, which show very similar turbulence MTFs and very different aerosol MTFs including very different knee spatial frequencies.⁹ This cannot be explained on the basis of inner scale turbulence MTF instead of practical aerosol MTF since the inner scale (l_0) is unaffected by instrumentation while practical aerosol MTF is very much dependent upon the limitation imposed by instrumentation on scatter angles actually recorded in the image.^{2-4, 21-26}
8. Prediction of aerosol MTF and the knee spatial frequency according to weather-predicted aerosol size distribution.⁹ Such aerosol MTF predictions show good correlation with measurement.⁹ Had the atmospheric MTF measurements been of inner scale turbulence MTF, there would be no correlation with aerosol size distribution prediction. Implementation of such aerosol weather models in our atmospheric Wiener filter²⁷ yields excellent image restorations according to weather in which atmospheric effects are essentially corrected for totally.
9. In all the above, as well as in recent restorations of satellite images³⁰ based upon weather-predicted atmospheric MTF (turbulence MTF and practical aerosol MTF), there existed good correlation between atmospheric transmission and the high spatial frequency aerosol MTF asymptote. Belen'kii's inner scale turbulence MTF model has nothing to do with atmospheric transmission and does not make any such prediction.

In addition to the above corroborations of practical aerosol MTF rather than inner scale turbulence MTF, there are a number of contradictions between Belen'kii's model¹ itself and our experiments. They are listed here in chronological order.

1. Belen'kii claims "it is easy to see that S & K's conclusions contradict the results of the experimental studies (his references 5 - 9)." We wish to point out aerosol MTF can affect only image blur and irradiance. Aerosols have very little direct effect on scintillations, image dancing, angle-of-arrival fluctuations, etc. Hence, some of his references 5 - 9 are totally irrelevant to aerosol MTF. Furthermore, practical aerosol MTF depends strongly upon the imaging system being used, so that in large field-of-view and/or large dynamic range systems it is of much decreased importance. Also, if the weather is such that there is a large number of large particles, as in Bissonnette's experiment through fog,³¹ the aerosol scattering pattern may be narrower than instrumentation limitations such as field-of-view or dynamic range, so that the classical aerosol MTF rather than practical aerosol MTF may be relevant. In addition, it is also possible that the climates and weather conditions involved in the experiments cited by Belen'kii were such that aerosol loading was rather low. Consequently, if there are imaging experiments in Belen'kii's references 5 - 9, they do not necessarily contradict our practical aerosol MTF model. His non-imaging experiment references are definitely irrelevant. Since we believe that for *sufficiently large optical depths* (≥ 1) both turbulence and aerosol blur are significant, time dynamic properties of point spread functions do not show there is no aerosol blur accompanying the turbulence blur.

Interestingly enough, Belen'kii does not comment on whether his references 5 - 9 do corroborate his inner scale turbulence MTF model.

2. Belen'kii's model is such that "with increasing wavelength... the knee frequency decreases ($\Omega_k \sim \lambda^{-1}$).". This result of his is in *complete contradiction to our measurements*, as can be clearly seen in Figs. 5 and 9 of Ref. 21, where spatial frequency dependence of the measured knee frequencies clearly increase with increasing wavelength. These are explained there by the specific intensities or point spread functions shown in Figs. 8 and 10 respectively of that reference which *are calculated based upon measured aerosol size distributions*. Hence, since the knee spatial frequencies are seen clearly to *increase* with increasing wavelength, Belen'kii's inner scale turbulence theory *cannot explain our experimental results*, which are explained by *aerosol size distribution* and its effect on scattering diagram or phase function and its effect on the specific intensity or point spread function.
3. At the end of Section 2 Belen'kii claims "It should be noted that, to my knowledge, the predictions of the instrumentation-based theory have never before been quantitatively compared with the measured data." *This statement is factually incorrect*. In our paper discussed by Belen'kii [ref. 2 here], Fig. 13 (model) is compared to experiment (Figs. 1 - 3). This is in addition to references 9, 21, 23, 25, and 26 here which strongly deal with other comparisons of practical aerosol MTF model calculations to experiment, in which aerosol specific intensities (spread functions) and MTFs are calculated from aerosol size distribution using the step-by-step procedure of reference 4.
4. Belen'kii objects to our C_n^2 measurement on the grounds that spherical wave models for C_n^2 should have been used instead of those for plane waves. *This statement is also factually incorrect*. It should be noted that most of our papers do feature *spherical wave calculations* for experimental measurements. For example, see Eqns. (1) and (2) in ref. 3 and Eqns. (2) and (3) in ref. 21. Only ref. 25 involves plane waves. Nevertheless this is valid in MTF calculation as long as plane waves are used in the C_n^2 determination from angle-of-arrival fluctuations. From Eq. (2) in ref. 21, the path-integrated value of C_n^2 yields

$$a C_n^2 L = < \alpha_x^2 > D^{5/3} / 2.92, \quad L_0 > D \gg \sqrt{\lambda L} \quad (1)$$

where L is path length, D is aperture diameter, α_x is horizontal component of angle-of-arrival, L_0 is outer scale, and "a" = 1 for a plane wave and 3/8 for a spherical wave. From Eq. (3) in this last reference the long exposure turbulence MTF can be expressed as

$$M_T = \exp \left[-57.53 \Omega_r^{5/3} \lambda^{-1/3} a C_n^2 L \right] \quad (2)$$

where Ω_r is angular spatial frequency and λ is wavelength. The term " $a C_n^2 L$ " in (2) is evaluated from (1), yielding

$$M_T = \exp \left[-57.53 \Omega_r^{5/3} \lambda^{-1/3} < \alpha_x^2 > D^{5/3} / 2.92 \right] \quad (3)$$

which is independent of "a". Therefore, one can use the *plane wave approximation* and obtain the *exact same MTF calculation as for spherical waves* provided the same plane wave approximation is used in (1) to obtain C_n^2 from the angle of arrival fluctuations. This is what is done in ref. 25. Consequently, there is no basis whatsoever for any criticism on this point. There is therefore no underestimation of the turbulence MTF in ref. 25 where plane wave formulation is used for both C_n^2 determination (on the basis of angle-of-arrival fluctuations) and MTF calculation. In any event, there is *certainly no basis for criticism* on this point regarding refs. 3 and 21 where aerosol MTF is compared to turbulence MTF since those papers *do indeed involve spherical wave formulation from beginning to end*.

In addition, our weather-prediction model for C_n^2 , based upon our measurements of C_n^2 , has been supported independently by measurements carried out in France by meteorologist R. M. Smith of the U.S. Army (Ft. Belvoir, VA) in which we were not involved. Our model yielded excellent correlation of C_n^2 prediction with measurement. A limited distribution report was issued. The details of the report are unknown to us. The model is based upon a limited range of weather conditions, and its accuracy under *those conditions* is supported

too by independent measurements of Indian and American scientists as well. Hence, not only our results but also our *methods* of C_n^2 measurements have been confirmed independently by many scientists.

5. Belen'kii objects to the fact that "a measure horizontal angle-of-arrival variance... was doubled, so as to include variance in the vertical direction." His point is that turbulence can be anisotropic. He claims that the vertical component of angle-of-arrival variance can be *smaller* than the horizontal one, so that doubling the horizontal angle-of-arrival variance can lead to an underestimation of C_n^2 . We wish to make it clear that we did in fact measure both the horizontal and vertical angles-of-arrivals and did indeed calculate the variance of each. The variances were found to be identical, except in the middle of very hot summer days when the vertical angle-of-arrival variance was found to be slightly *larger* than the horizontal angle-of-arrival variance, their ratio being on the order of 1.1 - 1.2. Therefore, there was no anisotropy in most of our measurements. However, on the few occasion when there was, our technique led to an *overestimation* of C_n^2 , rather than an underestimation.
6. Belen'kii's model is also contradicted by weather dependences of the inner scale and our measurements of overall atmospheric MTF as described below.

In conclusion, Belen'kii's theory is contradicted strongly by a broad range of different types of experimental and theoretical results and measurements described in our papers cited by him, as well as those uncited by him. (In fairness, one⁹ of the latter, a key one, was not published until after Belen'kii's paper was accepted.) These many techniques are independent. The practical instrumentation-based aerosol MTF has been validated by theoretical calculations and experimental measurements over a very broad range of concepts. Some of these measurements actually contradict Belen'kii's theoretical predictions for inner scale turbulence MTF, especially as regards wavelength dependence of MTF knee frequency. This is in addition to overall atmospheric MTF wavelength dependence which was measured to be quite inconsistent with turbulence MTF wavelength dependence way back in our initial papers regarding aerosol MTF for both horizontal³² and vertical³³ imaging. That horizontal path³² was 4.15 km long at an average elevation of about 4 to 5 m. The vertical path was through the whole atmosphere and involved imaging the edge of the sun.³³ The wavelength dependences could not be explained by turbulence, but could be by aerosol MTF. They were our first indication that turbulence MTF does not describe all atmospheric blur. Those wavelength-dependent results too have nothing to do with inner scale turbulence effects. Wavelength dependences changed with increased aerosol loading in those experiments. When windspeed increased the aerosol loading increased because soil-derived particles were uplifted by the wind. This caused the overall atmospheric MTF slope decrease at longer wavelengths to be sharper even at larger wavelengths.^{32,33} These events are very consistent with our aerosol MTF modeling. However, Belen'kii's inner scale turbulence modeling predicts the opposite. It is well known that increased winds decrease turbulence strength because of increased air mixing. This increases inner scale size l_0 .³⁴ This means that under higher wind conditions Belen'kii's atmospheric MTF would decrease less slowly with spatial frequency, which is contrary to the observed results.^{32,33} Such weather effects constitute an additional contradiction between Belen'kii's comments and our measurements.

Many experienced reconnaissance *experimenters* in industry and the armed forces have known for many years that clear weather atmospheric blur (not scintillations and not image dancing) for elevations more than a few meters above the surface and optical depths ≥ 1 derives almost totally from aerosol blur. Under dust storm or high aerosol loading conditions such as haze, aerosol blur closer to the surface can also be more significant than that of turbulence. Our experiments confirm their experiences and led to our model which is supported both qualitatively and quantitatively by the large scope of experiments described above. It is unfortunate that Belen'kii made his comments on our experiments without ever having seen our lines-of-sight. Such practical details are critical in turbulence measurements.

A major point we wish to emphasize here is that the time has come for broad system engineering approaches³⁵ to atmospheric optics rather than the narrow pure turbulence, pure aerosol, pure absorbing atmosphere approaches that have commonly been used in the past.

REFERENCES

1. M. Belen'kii, "Effect of the inner scale of turbulence on the atmospheric modulation transfer," *J. Opt. Soc. Am. A* **13**, pp. 1078-1082, May 1996.
2. D. Sadot and N. S. Kopeika, "Imaging through the atmosphere: practical instrumentation-based theory and verification of aerosol modulation transfer function," *J. Opt. Soc. Am. A* **10**, pp. 172-179 (1993).

3. I. Dror and N. S. Kopeika, "Aerosol and turbulence modulation transfer functions: comparison measurements in the open atmosphere," *Opt. Lett.* **17**, pp. 1532-1534 (1992).
4. N. S. Kopeika and D. Sadot, "Imaging through the atmosphere: practical instrumentation-based theory and verification of aerosol transfer function: reply to comment," *J. Opt. Soc. Am. A* **12**, pp. 1017-1023 (1995).
5. D. Sadot and N. S. Kopeika, "Forecasting optical turbulence strength on the basis of macroscale meteorology and aerosols: models and validation," *Opt. Eng.* **31**, pp. 200-212 (1992).
6. G. de Leeuw, "Profiling of aerosols concentration, particle size distributions and relative humidity in the atmospheric surface layer area over the North Sea," *Tellus* **43B**, pp. 342-354 (1990).
7. A. D. Sarma and R. J. Hill, "Effect of blowing snow and ground blizzards on millimeter wave scintillation spectra," *Int. J. Infrared & Millimeter Waves* **12**, pp. 997-1022 (1991).
8. J. R. Hummel and E. P. Shettle, "Effects of solar heating by aerosols and trace gases on the temperature structure constant," *Geophysics Lab. Hanscom AFB, MA 01731-5000*, Report No. GL-TR-90-0349, Scientific Report No. 6, 9 August, 1990.
9. D. Sadot, S. Shamriz, I. Sasson, I. Dror, and N. S. Kopeika, "Prediction of overall atmospheric MTF with standard weather parameters: comparison with measurements with two imaging systems," *Opt. Eng.* **34**, 3239-3248 (1995).
10. D. Sadot and N. S. Kopeika, "Effects of absorption on image quality through a particulate medium," *Appl. Opt.* **33**, pp. 7107-7111 (1994).
11. Y. Kuga and A. Ishimaru, "Modulation transfer function and image transmission through randomly distributed spherical particles," *J. Opt. Soc. Am. A* **2**, pp. 2330-2335 (1985).
12. P. Donelli, P. Brusaglioni, A. Ismaelli, and G. Zacanti, "Experimental validation of a Monte Carlo procedure for the evaluation of the effect of a turbid medium on the point spread function of an optical system," *J. Mod. Opt.* **38**, pp. 2189-2201 (1991).
13. M. T. Valley, "Numerical method for modeling nonspherical aerosol modulation transfer functions," in *Atmospheric Propagation and Remote Sensing*, A. Kohnle and W. B. Miller, eds., *Proc. SPIE* **1688**, pp. 73-85 (1992).
14. P. Brusaglioni, P. Donelli, A. Ismaelli, and G. Zacanti, "A numerical procedure for calculating the effect of a turbid medium on the MTF of an optical system," *J. Mod. Opt.* **38**, pp. 129-142 (1991).
15. E. P. Zege, A. P. Ivanov, and I. L. Katseve, *Image Transfer through a Scattering Medium* (Springer-Verlag, Berlin, 1991).
16. H. T. Yura, "Small angle scattering of light by ocean water," *Appl. Opt.* **10**, pp. 114-118 (1971).
17. R. L. Lutomirski, "Atmospheric degradation of electrooptical system performance," *Appl. Opt.* **17**, pp. 3915-3921 (1978).
18. A. Ishimaru, "Limitation on image resolution imposed by a random medium," *Appl. Opt.* **17**, pp. 348-352 (1978).
19. A. Zardecki, S. A. W. Gerstl, and J. F. Embury, "Multiple scattering effects in spatial frequency filtering," *Appl. Opt.* **23**, pp. 4124-4131 (1984).
20. A. Zardecki, S. A. W. Gerstl, W. G. Tam, and J. F. Embury, "Image-quality degradation in a turbid medium under partially coherent illumination," *J. Opt. Soc. Am. A* **3**, pp. 393-400 (1986).
21. I. Dror and N. S. Kopeika, "Experimental comparison of turbulence MTF and aerosol MTF through the open atmosphere," *J. Opt. Soc. Am. A* **12**, pp. 970-980 (1995).
22. D. Sadot, G. Kitron, N. Kitron, and N. S. Kopeika, "Thermal image through the atmosphere: atmospheric MTF theory and verification," *Opt. Eng.* **33**, pp. 880-887 (1994).
23. D. Sadot, A. Dvir, I. Bergel, and N. S. Kopeika, "Restoration of thermal images distorted by the atmosphere, based upon measured and theoretical atmospheric modulation transfer function," *Opt. Eng.* **33**, pp. 44-53 (1994).
24. D. Sadot and N. S. Kopeika, "Effects of aerosol forward scatter of infrared and visible light on atmospheric coherence diameter: theory and validation," *Opt. Eng.* **34**, pp. 261-268 (1995).
25. D. Sadot, A. Melamed, N. Dinur, and N. S. Kopeika, "Effects of aerosol forward scatter on long and short exposure coherence atmospheric coherence diameter," *Waves in Random Media* **4**, pp. 487-498 (1994).
26. D. Sadot, G. Lorman, R. Lapardon, and N. S. Kopeika, "Restoration of thermal images distorted by the atmosphere using predicted atmospheric modulation transfer function," *IR Phys. Tech.* **36**, pp. 565-576 (1995).
27. D. Sadot, R. Rosenfeld, G. Shuker, and N. S. Kopeika, "High resolution restoration of images distorted by the atmosphere, based upon average atmospheric MTF," *Opt. Eng.* **34**, pp. 1799-1807 (1995).
28. D. Sadot, D. Shemtov, and N. S. Kopeika, "Theoretical and experimental investigation of image quality through an inhomogeneous turbulent medium," *Wave in Random Media* **4**, pp. 177-189 (1994).
29. D. Sadot, N. S. Kopeika, and S. R. Rotman, "Target acquisition modeling for contrast-limited imaging: effects of atmospheric blur and image restoration," *J. Opt. Soc. Am. A* **12**, pp. 2401-2414 (1995).

30. N. S. Kopeika, T. Sheayik, Z. Givati, N. Corse, I. Dror, D. Sadot, and A. Karnieli, "Imaging vertically through the atmosphere: restoration of satellite images based on atmospheric MTF evaluation from surface weather," submitted for publication.
31. L. R. Bissonnette, "Imaging through fog and rain," *Opt. Eng.* **31**, pp. 1045-1052 (1992).
32. N. S. Kopeika, S. Solomon, and Y. Gencay, "The wavelength variation of visible and near IR resolution through the atmosphere: dependence on aerosol and meteorological conditions," *J. Opt. Soc. Am.* **71**, pp. 892-901 (1981).
33. N. S. Kopeika, "Spatial frequency and wavelength-dependent effects of aerosols on atmospheric modulation transfer function," *J. Opt. Soc. Am.* **72**, pp. 1092-1094 (1982).
34. R. R. Beland, "Propagation through atmospheric optical turbulence" in *Atmospheric Propagation of Radiation*, F. G. Smith, ed., *The Infrared and Electro-Optical Systems Handbook*, vol. 2, J. S. Accetta and D. L. Shumaker, executive editors, Environmental Research Institute of Michigan and SPIE Optical Engineering Press, Bellingham, WA., pp. 159-232, 1993.
35. N. S. Kopeika, *A System Engineering Approach to Imaging* SPIE Optical Engineering Press, Bellingham, WA., 1997, in press).

Characteristics of Shipborne Targets in Warm Coastal Environment in Mid and Long Wave IR

Karin Stein

FGAN Forschungsinstitut für Optik (FfO)
72072 Tübingen, Germany

ABSTRACT

In July 1996 FGAN-FfO participated in the LAPTEX (Low Altitude Point Target Experiment) trial in Crete. Aim of this experiment was to improve the knowledge of environmental factors that impact EO system performance in the marine boundary layer. The atmospheric conditions were subtropic with absolute humidities higher than 15 g/m^3 . FGAN-FfO used two IR-cameras working in different bands for tracking an IR point source mounted on a ship sailing away from the observation site to the horizon. This paper deals with the analysis of the signal decrease with range under different atmospheric conditions. The measurements are compared with LOWTRAN 7 model predictions. Moreover, we studied the detection range performance under certain refraction conditions and the signal increase due to atmospheric focusing effects near the sea surface.

1. INTRODUCTION

The range performance of IR Search and Track (IRST) systems is very much dependent on environmental conditions. Especially the detection and tracking of low-level flying targets depend on boundary effects produced at the air-sea interface. Research Study Group 5 of NATO AC/243 Panel 4 organized a measurement campaign to quantify the impact of atmospheric effects on IR sensors in warm humid conditions. An overview of this campaign, called LAPTEX (Low Altitude Point Target Experiment) is given. During the experiment FGAN-FfO used two digital staring array cameras whose main characteristics are listed. Using a LOWTRAN 7 model, the transmission in the observed wavebands is calculated and from these calculations the observational range is estimated. For the marine boundary layer LOWTRAN or MODTRAN computations are not valid. Phenomena near the sea surface are taken into account in IRBLEM (IR Boundary Layer Effects Model) which has been developed by DREV, Ca and TNO-FEL, NL. Results of IRBLEM computations will be presented. The thermal range model for point target detection, a model which has been developed at FfO will be explained. This model computes the signal to noise ratio, its results are compared with the experiment.

2. THE LOW ALTITUDE POINT TARGET EXPERIMENT (LAPTEX)

LAPTEX was carried out to improve the knowledge of maritime environmental effects in warm humid areas. The experiment was conducted during July 1996 at NATO FORACS near Souda on the island of Crete, Greece (Fig. 1). Measurements were performed by Canada, Denmark, Germany, Italy, The Netherlands, United Kingdom and the US whereas Greece provided the logistic and technical support.

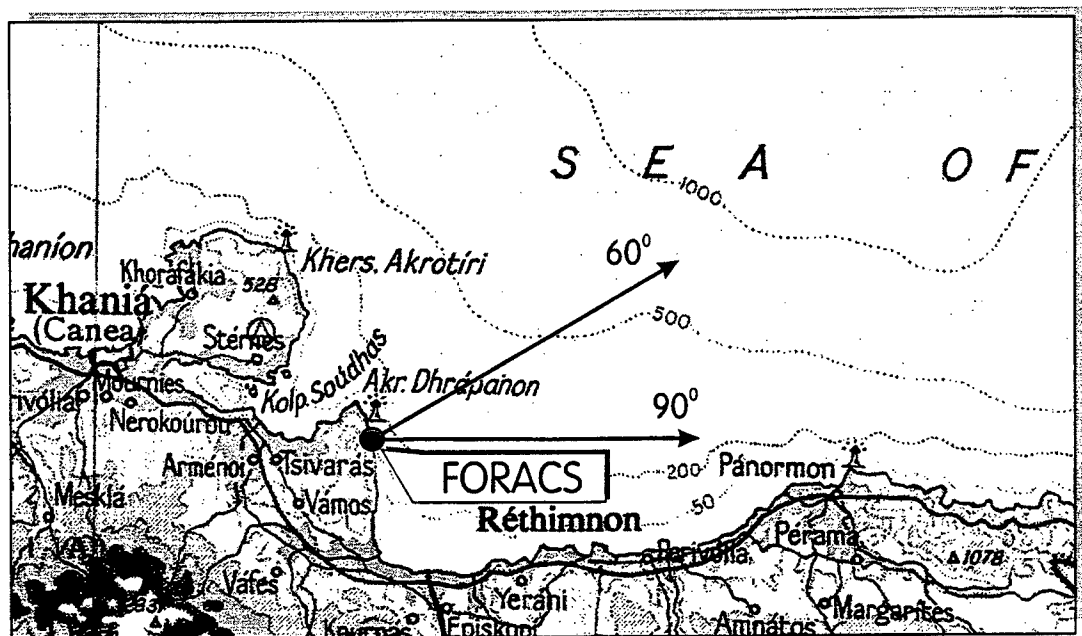


Fig. 1: The location of the FORACS test-site in Crete.

A collective review of the LAPTEX trial is given in the testplan (Ref. 1). The general objectives were:

- Validation of models that predict the performance ofIRST sensors against low altitude incoming point targets in a warm coastal environment.
- Validation of atmospheric and background models, that determine the performance of IR-Sensors against low altitude point targets and small surface targets.
- Validation of ship signature models by means of test panels and background radiance measurements.
- Determination of detection and identification probability of low flying and small surface targets in coastal areas.

To meet the objectives listed above, different types of experiment were performed, like the tracking of in- and outbound air and shipborne point targets. A complete list of the experiments executed can be found in Ref. 2. This paper focuses on the ship experiment.

3. THE SHIPBORNE POINT TARGET EXPERIMENT

The shipborne point target experiment was carried out with the Greek research vessel Strabon. Four IR sources were mounted on the ship at 7.6 and 13.6 m height above sea level. One upper and lower source were emitting forward, one upper and lower source were emitting backward. The emitting area of the source is 423 cm², its radiant intensity in various spectral bands is (Ref. 3):

- 3.6 - 4.0 μm 38 W/ster
- 4.54 - 4.95 μm 50 W/ster
- 7.8 - 14 μm 130 W/ster

During the experiment the Strabon was sent away beyond the horizon. A typical trajectory was 60 degrees from North (see Fig. 1).

3.1 Measurement Equipment of FGAN-FfO

A complete description of the experiments FGAN-FfO performed during LAPTEX and of the equipment used is found in Ref. 4. The shipborne point target experiment was recorded with two digital staring array cameras whose characteristics are listed in Table 1.

	IRRIS 256-LN Cincinnati Electronics	IRC 128-LWIR CEDIP
Detector	InSb	HgCdTe
Spectral Filter	3 μm .. 5 μm	8 μm .. 12 μm
Number of Elements	256 x 256	128 x 128
A/D Dynamic Range	12 bit	14 bit
Pixel Size	23 μm x 23 μm	37 μm x 37 μm
Array Size	7.68 x 7.68 mm	6.4 x 6.4 mm
Focal Length	250 mm	200 mm
IFOV	0.092 mrad	0.21 mrad
FOV	1.8° x 1.8°	1.8° x 1.8°
D* Peak	3*10 ¹¹ jones	9*10 ¹⁰ jones

Table 1: List of Sensor Parameters

Both cameras were located at FORACS site at a height of 19.4 m above sea level.

3.2 Atmospheric Parameters

Several runs were carried out with the ship and the point source. From these runs two were selected for detailed analysis: one run at night and one in the evening. In both runs the ship was going beyond the horizon until all IR-cameras at FORACS lost sight of the upper IR source. During the night run on July 17 the ship was going out to 35 km. The CEDIP lost the ship at about 11 km whereas the IRRIS tracked the Strabon to more than 31 km. On July 22 the Strabon was going out to 33 km. The CEDIP, now, saw it further to 12 km, the IRRIS only to 28 km.

The detection ranges vary due to different meteorological conditions. The meteorological data were recorded throughout the experiment at different locations: at the test-site, at two buoys and on the Strabon. The following Table 2 shows the meteorological data for the selected runs. (Most of the propagation path was over sea, therefore, the Strabon data have been chosen.)

Date Local Time	17. July 1996 2.00 .. 3.30 h	22. July 1996 19:30 .. 20:30 h
Air Temperature in °C	25.3	24.3
Sea Temperature in °C	24.8	24.8
ASTD in °C	+ 0.5	- 0.5
Pressure in hPa	1008	1014
Relative Humidity in %	77.7	68.9
Absolute Humidity in g m⁻³	17.5	15.1
Wind Speed in m s⁻¹	3.8	5
Wind Speed (24 hrs average in m s⁻¹)	3.23	7.8
Wind Direction in °	260	320
Air Mass Parameter	8	8
Visibility in km	20	20

Table 2: Meteorological Data

On both days sea and water temperature were around 25 °C. The difference between air and sea temperature, the ASTD, is ± 0.5 °C on July 17 and - 0.5 °C on July 22.

These meteorological data find input in a LOWTRAN 7 model calculation. We used the Navy Maritime Model without taking into account aerosols. The next Figure 2 shows the band transmittance versus range R.

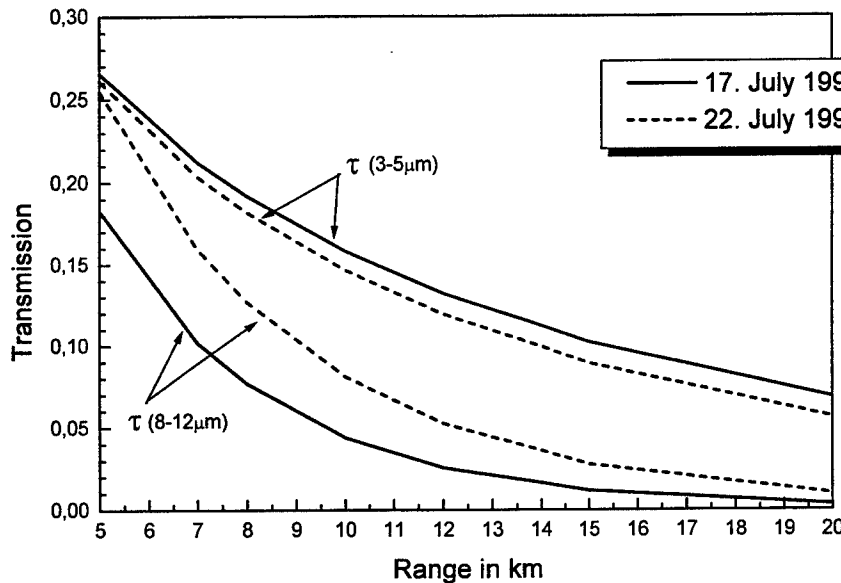


Fig. 2: Transmission in the 3-5 μm and 8-12 μm waveband region as calculated by the LOWTRAN 7 Navy Maritime model.

On both days the transmittance in the 3 - 5 μm band is better than in the 8 - 12 μm region. Absolute humidity has a great influence on transmission, especially in the long wave IR. On the night of July 17, 1996, the absolute humidity was very high (more than 17.5 g m^{-3}) which explains the short observation range of the CEDIP-camera.

3.3 Observation Range

The range at which a target can be detected is estimated by using the sensor parameters, listed in Table 1 and the transmission computation by LOWTRAN 7. The irradiance is given by formula 1:

$$E_{eff} = \frac{A_T}{R^2} \tau_{eff}(R) \int L(\lambda) R_n(\lambda) d\lambda \quad (1)$$

with:

A_T : Target Size

R : Target Range

τ_{eff} : effective Transmittance

L : Target Radiance

R_n : Detector Responsivity

Moreover the irradiance at the sensor is given by formula 2:

$$E_{eff} = SNR \frac{\sqrt{\frac{A_D}{2\tau_{int}}}}{A_{opt} \cdot \tau_{opt} D^*} \quad (2)$$

with:

SNR : *Signal to Noise Ratio*

A_D : *Detector Size*

τ_{int} : *Detector Integration Time*

A_{opt} : *Size of Entrance Pupil*

τ_{opt} : *Transmission of Optic*

D^* : *Detectivity*

So, for a given minimum Signal to Noise Ratio (SNR) of 4, the maximum detection range can be calculated for both sensors by equate formula 1 with formula 2.

On July 17, the resolvable limit of the long wave CEDIP sensor is reached at a range of 10.66 km, the mid wave IRRIS sensor allows an observation up to 35.4 km. On July 22 the CEDIP might „see“ up to 12.4 km, the IRRIS to 34 km. For an observer at 19.4 m height asl, the geometrical horizon of the upper IR source (13.6 m) of the Strabon would be at 28.6 km. Thus, the predicted observation range for the CEDIP camera is always much less than the horizon. Whereas, the observation range of the IRRIS camera is far beyond the horizon.

For the CEDIP camera, the predicted range (for $SNR = 4$) and the observed range are in very good agreement (see also chapter 3.2 and Table 3). For the IRRIS camera we find the observed range to be less than the predicted. On July 22, this camera observed the IR source to a range slightly shorter than the horizon, on July 17, beyond the horizon.

The observation of a subject beyond the horizon is a refraction phenomena. It is called superrefraction and occurs near the water surface when the water is cooler than the air.

3.4 Refraction Effects

When air and water have different temperature in low wind conditions, temperature gradients tend to occur. The ray bending is always into the direction of the higher refraction index, so cooler air. Therefore, if the ground (water) is cold and air is warm the rays are bended beyond the horizon. On the other hand if the ground (water) is warm the rays are bended skyward. The observation range is less than the horizon. This effect is called subrefraction. Another refraction phenomena is illustrated in Figure 3. Under certain conditions the rays may be bend in a way that the object is seen under two different angles. This double image effect is called mirage.

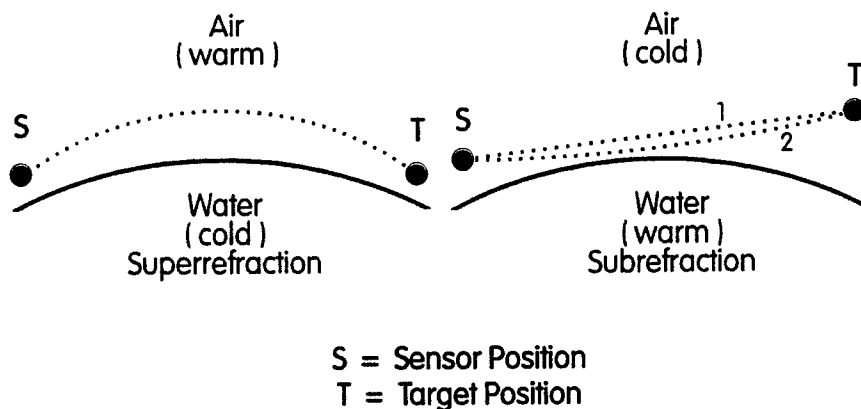


Fig. 3: Atmospheric refraction phenomena near the water surface (Ref. 5)

The meteorological data (Table 2) show a positive ASTD (Air Sea Temperature Difference) on July 17, a negative ASTD on July 22. So, we expect superrefraction on the 17th and subrefraction on the 22nd of July.

The MODTRAN model does not take into account refraction effects. Therefore, TNO-FEL, NL and DREV, Ca., have cooperatively developed a model which integrates all critical atmospheric effects in the marine surface layer. This model is called IRBLEM (IR Boundary Layer Effects Model) and it is valid for an elevation less than 1 degree centred at the horizon (Ref. 6).

The next functional diagram of IRBLEM (Fig. 4) is taken from the computer code description by D. Dion of DREV. Input data are the meteorology and sensor data. Spectral transmittance is calculated by MODTRAN. Refraction, turbulence and aerosol extinction are calculated by different TNO-FEL and DREV modules. Refractivity N , turbulence structure constant C_n^2 and atmospheric extinction α , as a function of height and the spectral transmittance τ serve as input for the ray-tracing model. This model computes the spectral path radiance, band parameters and the ray tracing diagram.

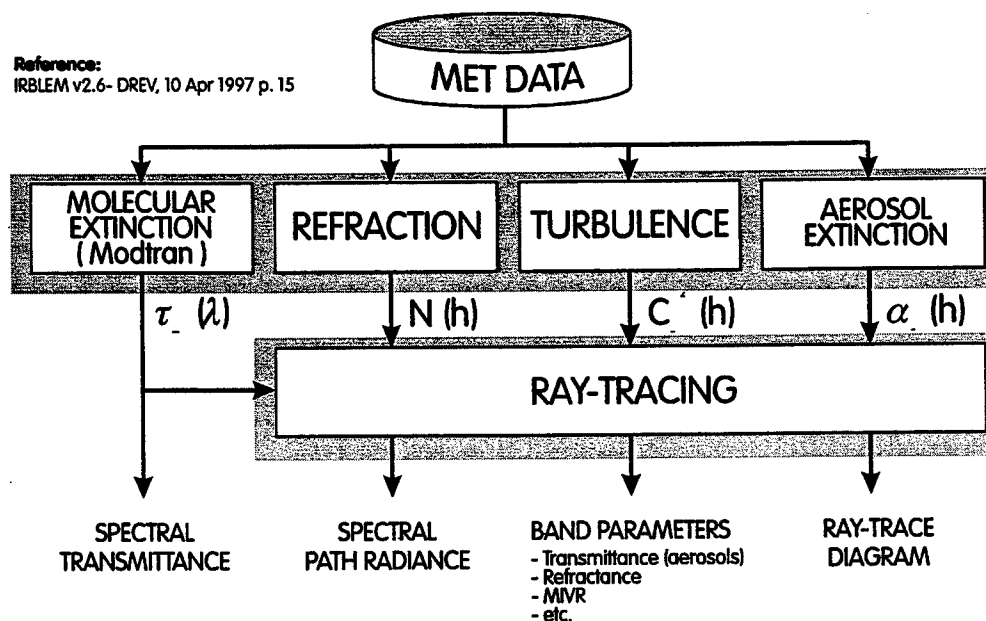


Fig. 4: Functional diagram of IRBLEM

For the meteorology data shown before and for the sensors we used, IRBLEM was run. The raytracing diagrams are shown below in Figures 5 and 6.

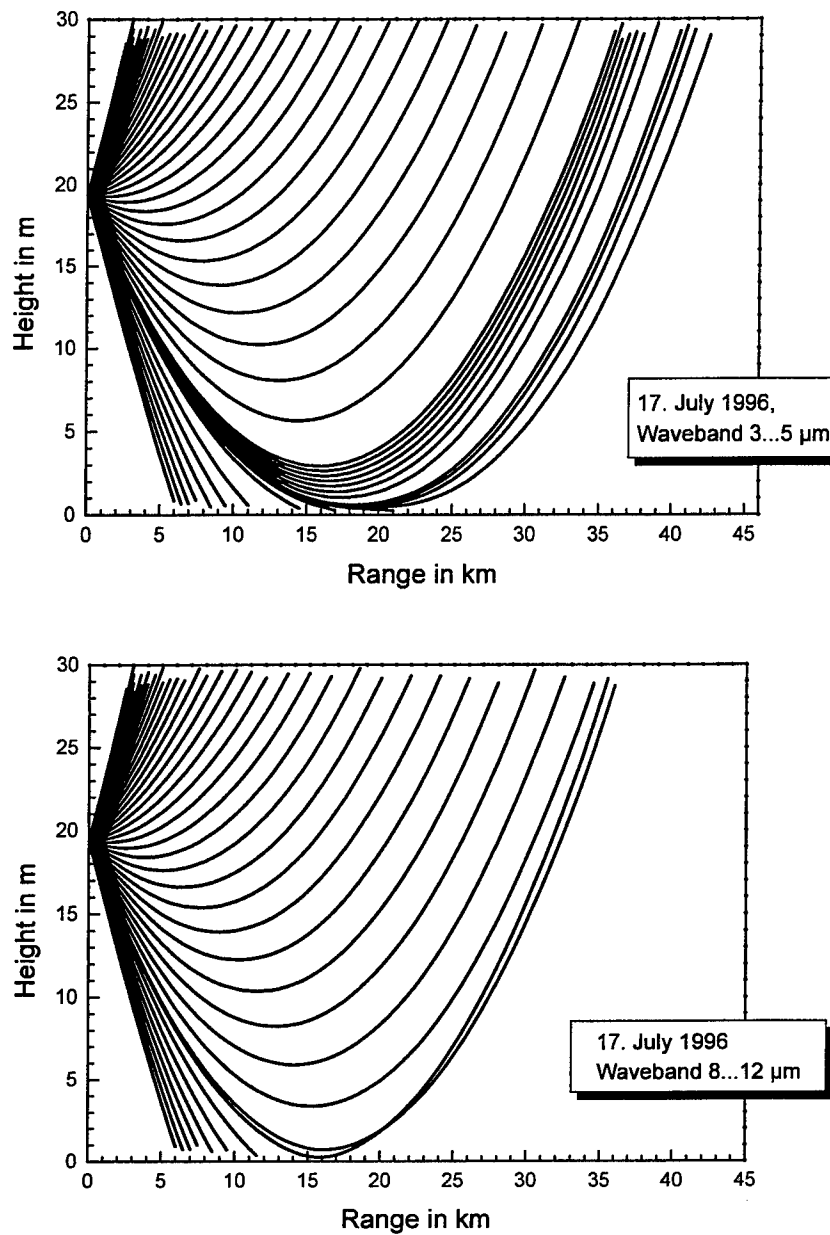


Fig. 5: Raytracing diagrams for both wavebands on July 17, local time 2:30 h

Figure 5 shows the diagrams for July 17. The upper picture for the 3 - 5 μm waveband the lower for the 8 - 12 μm region. The x-axis shows the range in km, the y-axis the height in m. The location of our cameras (19.4 m) is indicated. IRBLEM gives information of the Maximum Intervention Range (MIVR) and of the mirage characteristics. In the mid wave IR, the MIVR of an object of 13 m

height is more than 35 km, in the long wave IR it is less. The diagram for the 8 - 12 μm indicates a small mirage zone, marked by the crossing of rays.

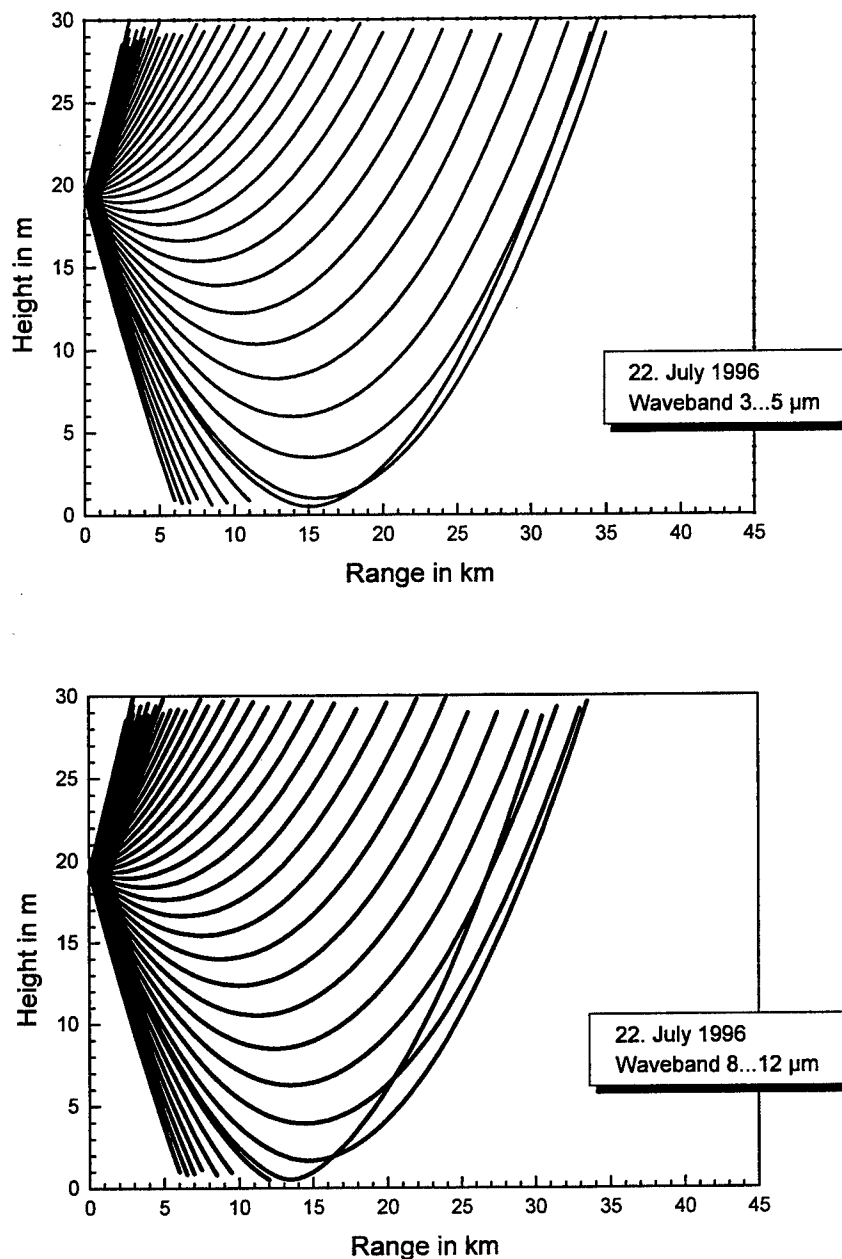


Fig. 6: Raytracing diagrams for both wavebands on July 22, local time 20:00 h

On July 22 the MIVR is far less than on July 17; for both wavebands. Both diagrams show a mirage zone, wider in the long wave than the the mid wave region.

Table 3 summarises the results of range calculations for both wavebands on the different days. The first column gives the observed ranges, the second gives the ranges predicted by equalising formula 1 and 2. The results of the IRBLEM computation are given in column 3 and 4: the beginning of the mirage zone and the maximum intervision range.

	Observed Range in km	Max. Range (S/N=4) in km	Mirage Zone in km	MIVR in km
IRRIS (3 - 5 μm) 17 July 1996	31.3	35.4	0	35.4
Cedip (8 - 12 μm) 17 July 1996	10.9	10.66	28.8	29.2
IRRIS (3 - 5 μm) 22 July 1996	28.0	34.0	27.3	28.0
Cedip (8 - 12 μm) 22 July 1996	12.3	12.4	24.3	26.4

Table 3: Comparison of observed and predicted ranges for an IR source of 13.6 m height (see text)

July 17 shows superrefractive conditions, in both wavebands the MIVR is extended beyond the horizon. On July 22, we find subrefractive conditions, the MIVR is less than the geometrical horizon and both wavebands are characterised by a mirage zone.

The mid wave IRRIS camera observes to the MIVR. Double images were not detected. For the long wave CEDIP camera an observation to the MIVR is not possible due to the limited range calculated by equation 1 and 2. Therefore, it was not possible to see any mirages.

3.5 The Thermal Range Model for Point Target Detection (TRP)

The The FGAN institutes FfO and FIM (Research Institute for Image Processing and Pattern Recognition) performed a feasibility study for long rangeIRST systems, called POSEIDON (passive location of point targets in a North and Baltic Sea atmosphere) (Ref.8). In the context of the POSEIDON project an analytic model had been developed to estimate the range of a point target detection system working in the infrared (Ref. 8). Sub-models consider the electro-optical transfer from the source (point target) to the sensor output (Fig. 7):

- the target-background model computes the radiance difference between target and background;
- the transmitting medium model considers atmospheric extinction and angel fluctuation due to turbulence;
- the sensor model takes into account the jitter of the platform, optical parameters, the scan procedure and the detector sensitivity and size.

One of the results of TRP is the signal to noise ratio (SNR) and the spatial distribution of the target signal at the sensor output.

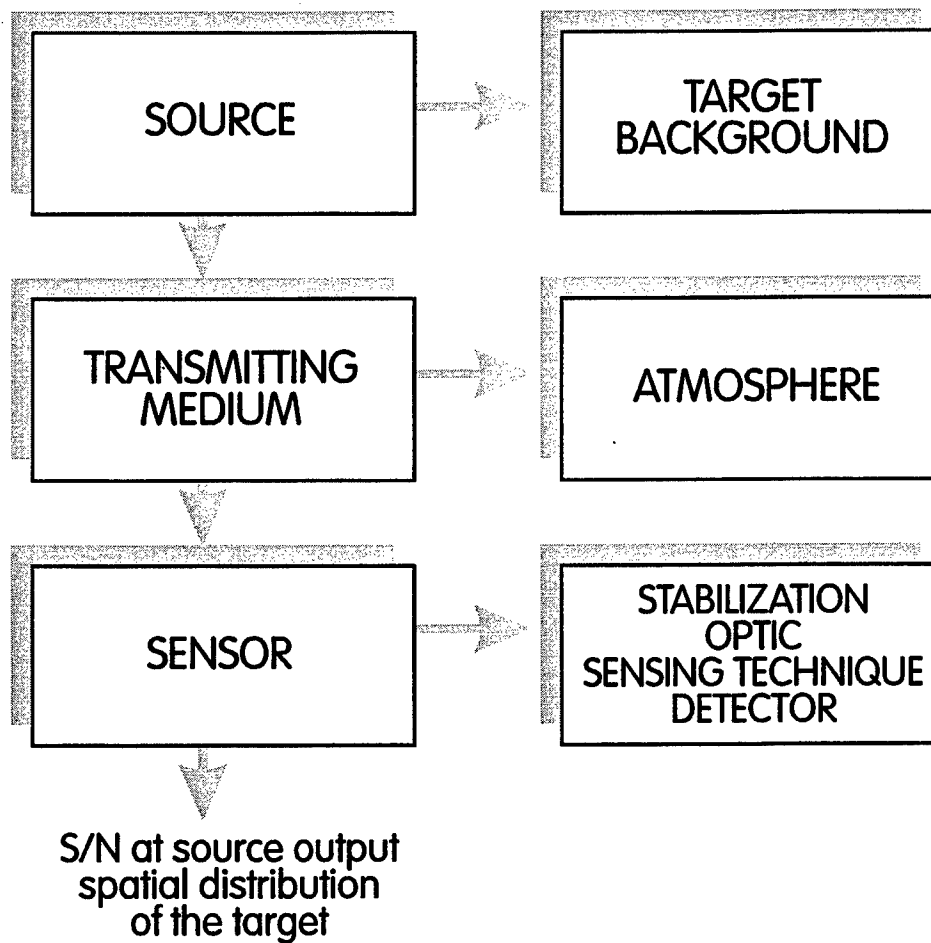


Fig. 7: Functional diagram of TRP

The grey scale values of the sequences recorded were analysed. Maximum value, mean background value and SNR were calculated and compared with computations of the Thermal Range Model for Point Target Detection. The input data for the TRP were shown in the former tables. The results are shown in Figures 8 and 9.

The SNR is plotted versus the distance of the target. The black line shows the TRP calculations for both sensors, the triangles and squares are the averaged SNRs for the IRRIS and CEDIP camera, respectively, as calculated from the digital sequences.

Figure 8 gives the result for July 17:

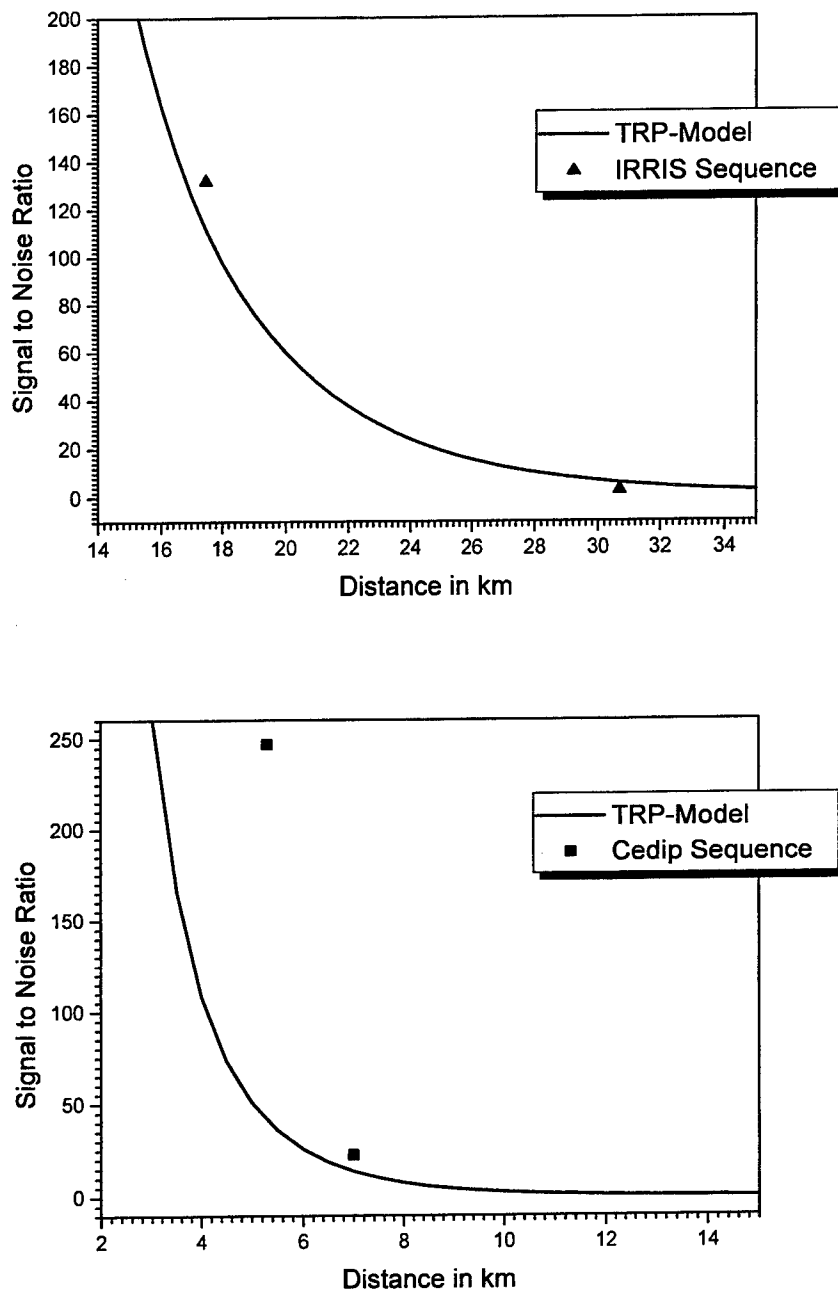


Fig. 8: Comparison of experimentally and theoretically achieved SNR for the sequences of 17. July 1996

In the case of the IRRIS sequence the agreement is quite good. For the CEDIP sequence there is a deviation for short ranges. This discrepancy can be explained: at short ranges the target does not appear point like, the TRP, however, is only valid for point targets.

The next Figure 9 gives the results for July 22:

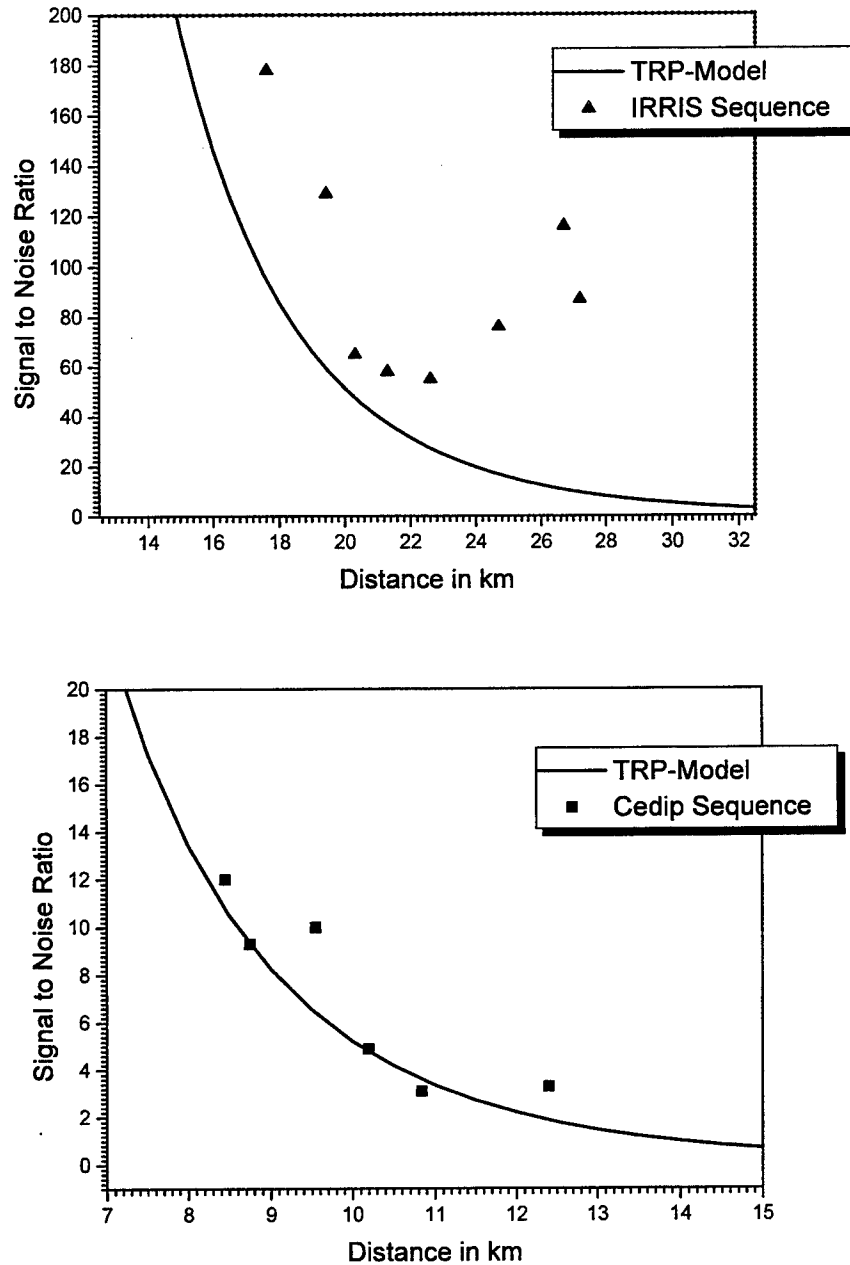


Fig. 9: Comparison of experimentally and theoretically achieved SNR for the sequences of 22. July 1996

For the CEDIP camera the agreement between model prediction and measured values is very good. But, in case of the IRRIS camera a big difference occurs: at long ranges the SNR increases to a maximum at 27 km afterwards it decreases again. This increase of

signal shows an atmospheric focusing effect. Due to the IFOV of the IRRIS a double image was not observed, the pixel size is too big to separate two images, but we see a focusing of the signal in the mirage zone.

4. CONCLUSIONS

In this paper the detection range of a point source has been analysed. The source was mounted on a ship going outbound beyond the horizon. The target was recorded in two different wavebands: the 3 - 5 μm and 8 - 12 μm region.

Calculations based on LOWTRAN 7 show a good agreement with measurements for short ranges but differ substantially around the horizon.

Phenomena near the water surface lead to sub- and superrefraction effects. For a description of these effects we used the IRBLEM model which was developed by DREV, Ca and TNO-FEL, NL. This model computes the ray tracing and an effective transmittance. With these results the observed ranges can be explained. The TRP model from FGAN-FfO is used to calculate the Signal to Noise Ratio (SNR). The experimentally obtained SNR is compared with model calculations and a very good agreement is found. The increase of SNR in one sequence can be explained by atmospheric focusing effects.

5. REFERENCES

1. LAPTEX testplan, TNO-Report FEL-96-I195
2. LAPTEX - A summerised trials description, TNO-Report FEL-96-I196
3. LAPTEX point target data analysis, TNO-Report FEL-97-A067
4. German Contribution to the NATO Trial LAPTEX, Report FfO 1996/101
5. Atmospheric and Background Effects on EO/IR Sensors NATO AC/243 RSG.5 and.8, to be published
6. IRBLEM computer code v2.6 CRDV/DREV, Val-Belair, Quebec, Canada
7. A. Kohnle et al., Evaluation of Essential Design Criteria for IRST Systems, SPIE Vol 2020,1993
8. W. Schuberth, TRP, Report FfO 1992/20

Satellite feature reconstruction using reflective tomography – field results

Charles L. Matson,^a Donald Holland,^b Diego Pierrottet,^a Donald Ruffatto,^c Stanley R. Czyzak,^a and Debora Mosley^a

^aOptical Sensing Division, Air Force Phillips Laboratory, Kirtland AFB, NM, USA 87117-5776

^bLockheed Martin Engineering and Science, Stennis Space Center, MS, USA

^cTextron Systems Division, Maui, HI, USA

ABSTRACT

The Air Force Phillips Laboratory is in the process of demonstrating an advanced space surveillance capability with a heterodyne laser radar system to be used, among other applications, for range-resolved imaging of orbiting satellites. In this paper, we present our first satellite feature reconstruction from field results using reflective tomographic techniques.

Keywords: laser radar, ladar, reflective tomography

1. INTRODUCTION

Range-resolved reflective tomography using short-pulselength lasers has been shown^{1,2,3} to be an image reconstruction method which can be used to recover image information about an object with a non-imaging laser radar (ladar) system. In range-resolved short-pulselength reflective tomography, laser light is reflected off of an object using a pulse length which is short relative to the range extent of the object. The resulting time-dependent return signal is collected by a non-imaging optical system, which provides a one-dimensional signal as a function of range. This one-dimensional signal is related to a one-dimensional slice of the spatial 3-D Fourier transform of the object. If the object rotates, different slices of the 3-D Fourier transform can be obtained. If a sufficient number of Fourier-domain slices which lie in a plane are collected, a two-dimensional image can be reconstructed by inverse Fourier transforming the Fourier-domain plane which contains the slices.

The Phillips Laboratory, through its High Performance CO₂ Ladar Surveillance Sensor (HI-CLASS) program, is developing a high power heterodyne CO₂ ladar system for installation on the Maui Space Surveillance Site (MSSS) 60cm beam director. The ladar is operated at 11.13 microns, which has advantages for atmospheric transmission, but prevents angular resolution of objects in orbit. High range resolution can be achieved, however, using the mode-locked pulse train output from the laser. Each pulse in the train is less than 1.5 nanoseconds in duration, permitting reconstruction of range-resolved images. In previous work, we have developed⁴ a mathematical model for the HI-CLASS system and analyzed system issues, developed⁵ and validated⁶ range-resolved signal-to-noise (SNR) expressions for projections generated from the HI-CLASS returns as well as for images reconstructed using reflective tomographic techniques, and demonstrated^{7,8} that reconstructions using the intensity information of the satellite reflectivities contained in the HI-CLASS returns provides superior image quality when compared to reconstructions obtained using E-field information as is typically done with synthetic aperture radar.

In this paper, reconstructed image information about the LACE satellite⁹ is presented. The data used in the image reconstruction was obtained during a field experiment using a low-power version of the HI-CLASS CO₂ laser, called the Phase One system. The outline of the paper is as follows: section 2 contains a description of the Phase One field experimental setup, section 3 contains the reconstructed image information as well as discussions, and section 4 contains conclusions. Our data processing methods will be published in a future report.

2. EXPERIMENTAL SETUP

A detailed description of the Phase One system can be found in Ref. 10; only an overview description of the system will be given here. The Phase One system, shown schematically in Figure 1, can be operated in both a single longitudinal mode configuration or in a mode-locked (pulse-burst) configuration. The first configuration produces a pulse-tone (that is; gain-switched¹¹) waveform consisting of a gain-switched spike (pulse) approximately 100ns in duration, followed by a slowly-decaying lower-amplitude waveform (tone) which lasts a few microseconds. A plot of the Phase One system's output for this mode of operation is shown in Figure 2(a). The second configuration produces a sequence of micropulses, each of which are a few nanoseconds in duration. The micropulse amplitudes are modulated by the pulse-tone envelope of the laser. We call this second configuration the pulse-burst mode and the sequence of micropulses, modulated by the pulse-tone waveform, is called a macropulse. A plot of the Phase One system's output for this mode of operation is shown in Figure 2(b). It is this latter mode which is used for the data presented in section 3. The micropulses in the pulse-burst waveform were evenly separated with a spacing of approximately 22.7ns and, for the Phase One system, with a duration (full-width half-max) of approximately 2.5ns. The total energy of a macropulse was approximately 2.5 Joules. Because the micropulses are separated by 22.7ns, we can unambiguously resolve objects with range dimensions less than 3.4m. As we will see in section 3, this complicates the determination of image dimensions from the LACE reconstructions.

For the results in this paper, the Phase One system was operated in a heterodyne detection mode with a local oscillator beam shifted from the outgoing beam frequency by 10MHz to 60MHz independent of Doppler shifts caused by target motion. Because orbiting satellites impose Doppler shifts on the return waveform on the order of hundreds of megahertz, and because the Phase One system had no provision for removing the imposed Doppler shift from the data, our recorded data suffered from either aliasing or frequency foldover depending upon the magnitude of the imposed Doppler shift. We use the phrase "frequency foldover" to describe the overlap of the Fourier spectra centered at the positive heterodyne frequency with the Fourier spectra centered at the negative heterodyne frequency. In the final HI-CLASS system configuration, bulk Doppler effects are removed before digitizing and an appropriately-sized heterodyne frequency is used to overcome aliasing and frequency foldover problems.

For either configuration, the laser beam was sent out through a 60cm transmit/receive aperture. Depending upon the experimental plans, the beam was directed either to targets on the ground or at satellite targets in space. Reflections from the targets were collected by the same aperture and mixed with the local oscillator prior to detection using a single element detector. The return was digitized using a sample rate of 1GHz and a window duration of 32 μ sec. For satellites, a predictive program was used to locate this window in time to when returns were expected to be received from the satellite. Each pulse sent out by the HI-CLASS system was time-tagged with an accuracy of 1/100 of a second.

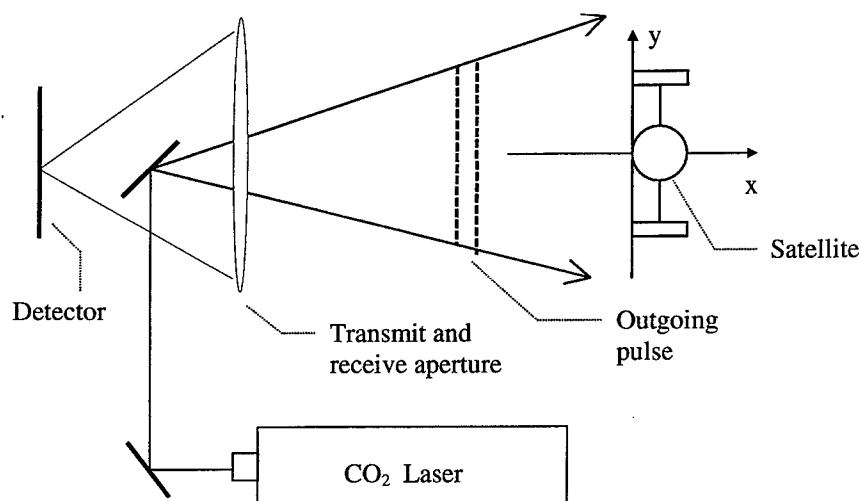


Figure 1. Conceptual schematic of the HI-CLASS ladar system. The heterodyne detection system is not shown.

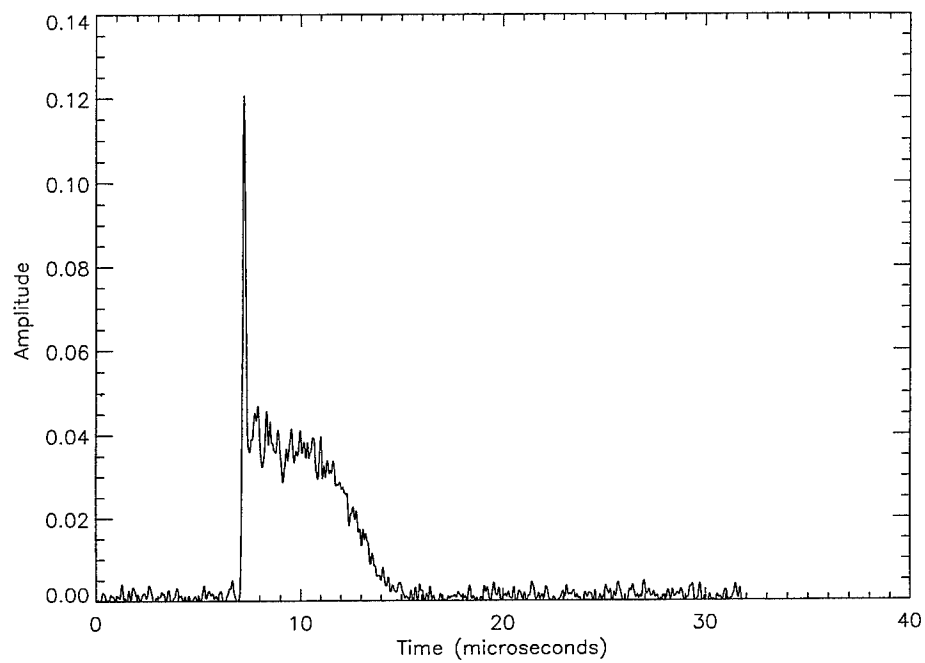


Figure 2(a). Single longitudinal mode pulse output by the Phase One HI-CLASS system. The vertical axis is voltage and the horizontal axis is time.

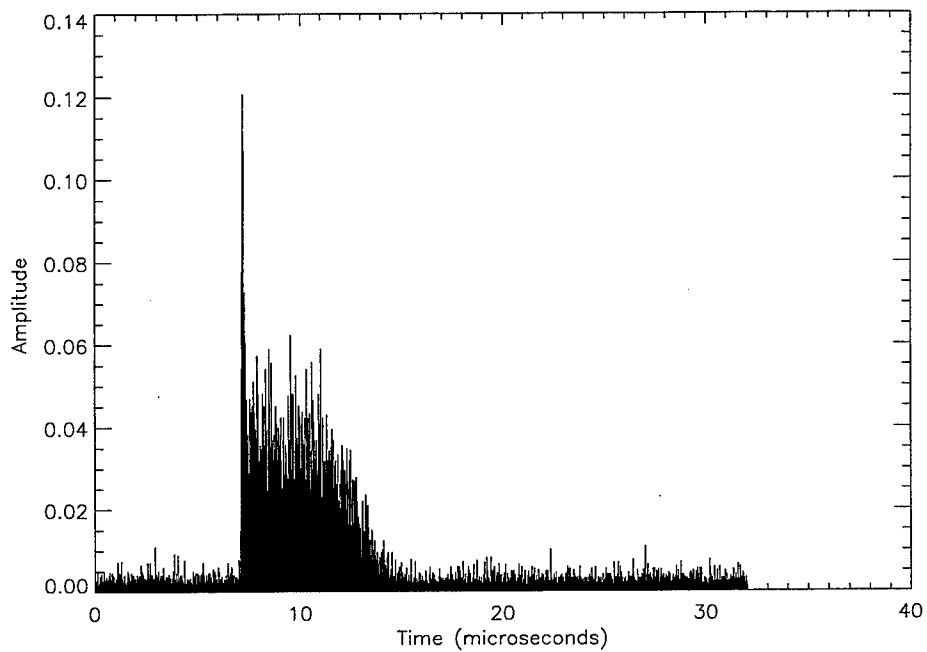


Figure 2(b). Mode-locked pulse output by the Phase One HI-CLASS system. The vertical axis is voltage and the horizontal axis is time.

3. RECONSTRUCTION RESULTS

In this section we present the details of our observations, experimental data, and the image feature reconstruction obtained of the LACE satellite. We observed the LACE satellite using the HI-CLASS Phase One system in the spring of 1995. We chose to illuminate the LACE satellite for these reconstructions because it carries a number of retroreflectors which enabled us to obtain strong returns with our relatively low-power Phase One system. For a detailed description and pictorial representation of the LACE satellite, see Refs. 9 and 12. For our purposes, it is sufficient to provide a simplified description of the satellite. The LACE satellite consists of a main body and three booms – a gravity-gradient boom pointing away from the earth, and two booms which extend in opposite directions in the along-track direction. Although the along-track booms were originally designed to be movable, according to the LACE final report¹² they are currently fixed with the leading boom extending approximately 4.5m from the satellite body and the trailing boom extending approximately 30m from the satellite body. Germanium retroreflectors, pointing in the nadir direction, are mounted on the ends of the two along-track booms and on the body. In addition, over 200 open (mirrored) and solid retroreflectors are mounted on a 76cm plate located at the end of the leading boom to support atmospheric compensation experiments. Because the footprint of the HI-CLASS laser beam illuminating the LACE satellite was between 9m and 18m in diameter during our observations, only the satellite body retroreflector and (usually) the leading boom retroreflectors were illuminated. Because of the strength of the retroreflector returns, we did not see any diffuse component in the measured returns.

One concern in the reconstruction process was ensuring that the same region of the object was illuminated and reflecting light for all the returns used for the reconstruction. This was a problem with most of the retroreflectors on the leading boom because they were tilted at various angles to ensure returns for a variety of illumination angles. However, any given retroreflector would not necessarily produce a return for all the illumination angles because the illumination angles of the laser beam relative to the retroreflector angle sometimes exceeded the retroreflector's cutoff angle. Since a fundamental tomographic assumption is that an elemental region of the object contributes light to each return, regardless of illumination angle, retroreflectors which only return light for some of the illumination angles cause reconstruction problems. Therefore, we chose to reconstruct an image of the satellite using returns only from the germanium retroreflectors mounted on the body and the leading boom. Because of their large cutoff angle (~60 degrees) they reflected light back to the receiver over virtually all the entire observation time. We were able to isolate returns from the germanium retroreflectors because the solid retroreflectors did not reflect light beyond 2 μ m and the open retroreflectors had cutoff angles such that essentially no light was reflected from them for elevation angles less than ~42 degrees. Therefore, we chose to use returns from the part of the satellite pass where the elevation angles ranged from 30 to 40 degrees. Because the germanium retroreflectors point in the nadir direction, we received returns from them for elevation angles greater than 30 degrees.

A second concern was the required processing of data to overcome aliasing and foldover effects. Recall from the discussion in section 2 that the orbital motion of the satellite determines the heterodyne frequency of the data collection system. In addition, the maximum unaliased frequency of our detection system is 500MHz while the bandwidth of our return is approximately 400MHz. Thus, for small values of satellite-imposed Doppler shifts, we suffer from frequency foldover because we require a 400MHz heterodyne frequency to prevent overlap of the Fourier spectra. However, for that large of heterodyne frequency, we suffer from aliasing because our system bandwidth is only 1GHz. Therefore, we have to correct for one effect or the other, or both. To analyze this further, we show in Figure 3 the bulk Doppler shift imparted by the satellite motion during the satellite pass along with the times of data collection. Data was not collected along the entire satellite pass due to predictive avoidance procedures used to ensure that only the LACE satellite was illuminated. We see that the set of data collected prior to culmination has Doppler shifts from 200MHz to 900MHz. For these values, both aliasing and frequency foldover are problems. For the second set of data, the Doppler shifts are within 100MHz of 1GHz. For this set of data, the aliasing is so severe that the spectra are aliased back down near zero frequency, so that frequency foldover is the only problem. However, only the second set of data contains significant numbers of returns corresponding to elevation angles between 30 and 40 degrees. Therefore, we used primarily the second set of data for the image reconstruction. As a result, only frequency foldover effects were required to be compensated. This compensation was accomplished using only a priori system information which enabled us to determine the regions in Fourier space which contain meaningful signal. Because these regions were so small relative to the total Fourier extent, frequency foldover never resulted in signal regions from the spectra centered at the negative heterodyne frequency overlapping signal regions from the Fourier spectra centered at the positive heterodyne frequency. We comment in passing that, to correct aliasing effects in a return, it is also necessary to determine the heterodyne frequency of that return, and so aliasing effects require both system and signal information, while frequency foldover effects require only system information.

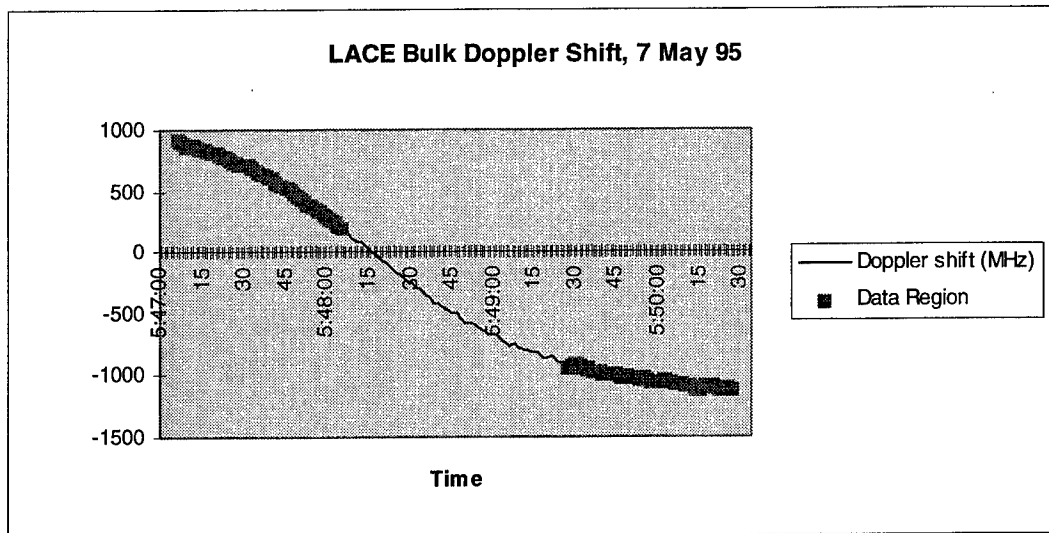


Figure 3. Bulk Doppler shift imposed by satellite motion on the return pulse. The vertical axis is the Doppler shift, in MHz, while the horizontal axis is the observation time.

Using our algorithms, we reconstructed projections from the second set of data collected on the LACE satellite for elevation angles between 30 and 40 degrees. These projections were then normalized in amplitude so that the returns from the retroreflector mounted on the body for all the projections had the same height. There were a total of 14 returns which had detectable return from both retroreflectors. The projections calculated from these returns, normalized and aligned in time so that the returns from the body's retroreflector all overlapped, are shown in Figure 4. These projections, although only gathered over a 10 degree angle spread, are sufficient to determine the separation of the two retroreflectors. However, the limited view resulted in very poor image quality. Therefore, based upon the known retroreflector separation, the returns from the first data set collected prior to culmination were analyzed to determine which returns had reflections from the two germanium retroreflectors. These returns were processed into projections and included in the image reconstruction process. The image that results from the raw tomographic reconstruction process is shown in Figure 5. Notice the typical tomographic "banding" effect. In the limit of an infinite number of views spaced around a full 360 degrees, the intensity of the image features would dominate in the reconstruction and thus the banding effects would disappear. However, because of our limited view and finite number of views, we must threshold the image to mimic the effects of a full set of views. This is done for the image in Figure 6, where we can see the images of the two germanium retroreflectors.

After reconstructing an image of the germanium retroreflectors, we analyzed the image to determine the information that can be obtained from it. First, we notice that the image of the leading retroreflector is further in range than the body retroreflector. This is consistent with the known satellite configuration.⁹ Next, we used the image to determine the retroreflector separation, assuming that the satellite booms are still pointed in the along-track direction. Based upon the known image scale and the measured separation, we determined that the retroreflector spacing was 1.8m. However, it is known that the boom could be retracted no further than 4.5m. Therefore, our image interpretation suffers from the range ambiguity problem which is caused by the micropulse separation of 22.7ns, which permits only a 3.4m unambiguous range determination. Because the object consists of two point reflectors, we are able to unravel the range ambiguity to a certain degree. Based purely upon the micropulse separation and knowledge of the observation angles, we determined that the possible separations of the retroreflectors are 1.8m, 6.2m, 10.7m, 15.1m, 19.6m, and so forth. We have already determined that the separation cannot be 1.8m because of prior knowledge of the satellite structure. To determine an upper limit, we analyzed the beam diameter at the target, which was no greater than 15m (peak to approximately first minimum). This fact, along with our observed strong returns from both retroreflectors, makes separations of 6.2m or 10.7m most likely. A final piece of prior knowledge is that it was reported¹² that the boom was left extended approximately 4.5m at the end of the LACE program. Therefore, based upon the satellite structure, we believe the correct answer is the 6.2m separation. Our estimate is

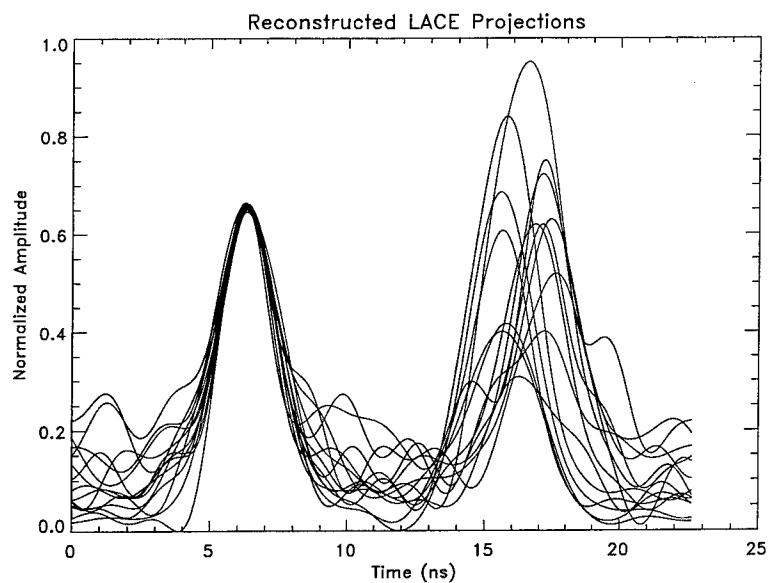


Figure 4: Lace reconstructed projections, aligned and normalized relative to the returns from the retroreflector mounted on the body of the satellite.

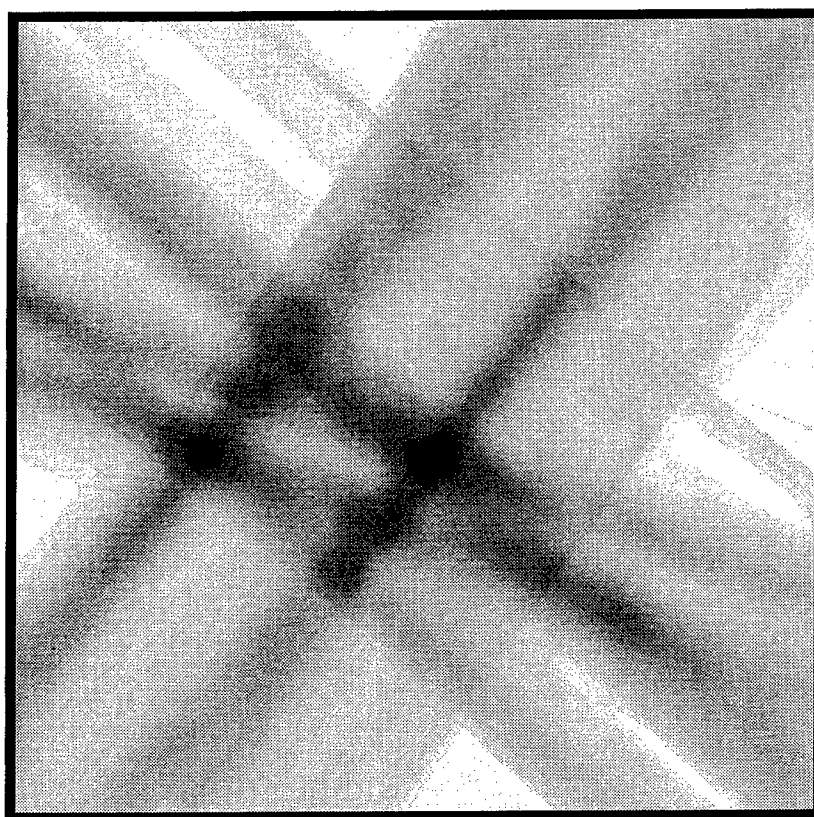


Figure 5: Lace germanium retroreflector reconstruction without applying thresholding to minimize limited-view artifacts. The range dimension is to the top of the image, while the along-track direction is to the left.

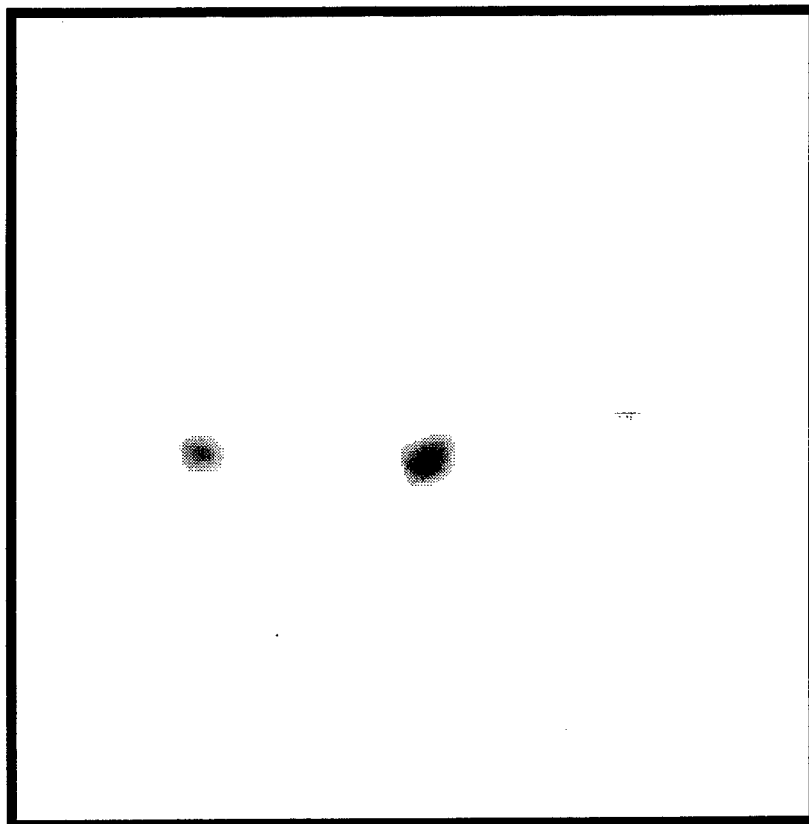


Figure 6: LACE germanium retroreflector reconstruction with thresholding applied to remove artifacts. The range dimension is to the top of the image, while the along-track direction is to the left.

a little larger than would be expected from the satellite geometry; therefore, we suspect that the boom was not retracted quite as far as was reported, if the satellite was still stabilized so that the booms point in the along-track direction. An alternate analysis of the satellite configuration is required if the reported final length of the boom is correct. In this case, the information from our measurements indicates that the satellite booms are not pointing in the along-track direction. This would be an indication of the failure of the satellite's momentum wheel.

4. CONCLUSIONS

We have presented the first image feature reconstruction from field data of an orbiting satellite obtained using reflective tomographic reconstruction methods. Prior knowledge of the satellite structure was used to isolate returns from the germanium retroreflectors and to resolve range ambiguities caused by the micropulse separation in the HI-CLASS waveform. Our image feature reconstruction is consistent with known LACE satellite morphology.

REFERENCES

- ¹ J.K. Parker, E.B. Craig, D.I. Klick, F.K. Knight, S.R. Kulkarni, R.M. Marino, J.R. Senning, and B.K. Tussey, "Reflective tomography: images from range-resolved laser radar measurements," *Applied Optics*, vol.27, pp.2642-2643 (1988)
- ² F.K. Knight, D.I. Klick, D.P. Ryan-Howard, J.R. Theriault, Jr., B.K. Tussey, and A.M. Beckman, "Two-dimensional tomographs using range measurements," *Proceedings of the SPIE*, vol.999, pp.269-280 (1988)
- ³ R.M. Marino, R.N. Capes, W.E. Keicher, S.R. Kulkarni, J.K. Parker, L.W. Swezey, J.R. Senning, M.F. Reiley, and E.B. Craig, "Tomographic image reconstruction from laser radar reflective projections," *Proceedings of the SPIE*, vol.999, pp.248-268 (1988)

- ⁴ C.L. Matson, E.P. Magee, and D.E. Holland, "Reflective tomography using a short-pulselength laser: system analysis for artificial satellite imaging," *Optical Engineering*, vol.34, pp.2811-2820 (1995)
- ⁵ C.L. Matson, "Reconstructed image signal-to-noise issues in range-resolved reflective tomography," *Optics Communications*, vol.137, pp.343-358 (1997)
- ⁶ C.L. Matson and J. Boger, "Laboratory validation of heterodyne laser radar intensity projection signal-to-noise expressions," *Applied Optics*, vol.36, pp.3165-3173 (1997)
- ⁷ C.L. Matson, D. Holland, S.Czyzak, D. Pierrottet, D. Ruffatto, "Heterodyne laser radar for space object imaging - results from recent field experiments," *Proceedings of the SPIE*, vol.2580, pp.288-295 (1995)
- ⁸ C.L. Matson, "Tomographic satellite image reconstruction using lidar E-field or intensity projections - computer simulation results," *Proceedings of the SPIE*, vol.2566, pp.166-176 (1995)
- ⁹ K.I. Schultz and S. Fisher, "Ground-based laser radar measurements of satellite vibrations," *Applied Optics*, vol. 31, pp.7690-7695 (1992)
- ¹⁰ D. Senft, M.J. Fox, J.D Gonglewski, J.A. Dowling, R. Highland, and S.R. Czyzak, "Long path CO₂ lidar measurements," *Proceedings of the SPIE*, vol.2580, pp.38-46 (1995)
- ¹¹ W.J. Witteman, *The CO₂ Laser*, Springer Series in Optical Sciences, vol.53, Koichi Shimoda, ed., Springer-Verlag (1987)
- ¹² D.M. Horan, R.E. Perram, and R.E. Palma, "The NRL LACE program final report," NRL report number NRL/FR/8121-93-9565, August 1993

A low cost seeing monitor to measure the isokinetic patch on the edge of the Moon

A. Ghedina¹, R. Ragazzoni², A. Baruffolo², J. Farinato¹

¹Department of Astronomy, University of Padova;

²Astronomical Observatory of Padova;
vicolo dell'Osservatorio 5, I-35122 Padova (Italy)

ABSTRACT

In most of the techniques currently proposed to overcome the well known limitation of the laser Guide Star to do not provide an useful tip-tilt signal, the size of the isokinetic patch plays a major role. Isokinetic patch size, defined as the distance at which the tilt correlation falls below a given threshold, can be measured, in principle, using a star cluster, as the few available measurements in the literature report. The edge of the Moon or of the Sun have been used to sense the tilt and/or to establish a reference system for Speckle Transfer Function. We have used the edge of the Moon as a reference for the measurement of the tilt correlation over angles spanning from a few arcsec to several arcminutes. The edge of the Moon is bright, its curvature is negligible for the purposes of this measurement, and, in most places of astronomical interest, it reaches significant elevations over the horizon. We constructed a seeing monitor using a 20cm portable telescope coupled, through a pair of commercial objectives, with an anamorphic optical relay and a small, commercially available, 12bit CCD. The image of the edge of the moon (relayed using the anamorphic relay and so allowing to have good tilt resolution even with a large covered field of view along the isokinetic patch measurement direction) is frame-shifted in groups of 6 or 8 in a fast manner and later it is read-out. In this way there is no need of fast Analog to Digital converter and only a minor modification to the original, commercially available, devices is needed. A 3-days run at the Asiago Observatory during January 1997 has been performed. The collected data have been extensively analyzed in order to assure their reliability. A comparison with seeing measurements done simultaneously at the focus of the main observatory is shown giving good agreement. Dispersion of the edge tilts consistent with Poisson statistics (due to the low number of covered realization) is pointed out. Scaling to the planned run at the Canary Island in order to pursue the Adaptive Optics module for the TNG telescope is briefly discussed together with the implication of the results with the various LGS tilt-recovery techniques.

Keywords: Laser Guide Star, Tip-Tilt, Isokinetic patch

1. INTRODUCTION

The effect of anisoplanatism is known to play a major role in the propagation of light through the atmosphere. Light from objects subtending an angle which is greater than the isoplanatic one are characterized by different transfer functions owing to the fact that it goes through distinct portions of the atmosphere.

A ground based adaptive optics system is not able to correct for multiple transfer functions and it is then a fundamental constraint to have a reference source within the isoplanatic patch of the scientific target: otherwise images can no longer be diffraction limited. In particular, atmospheric turbulence introduces random fluctuation in the angle-of-arrival of the light and this effect, known as tip-tilt perturbation, represents nearly 87% of the wavefront phase variance¹. It is clear that a compensation of the higher order terms is nonsense when the tip-tilt is not corrected.

The size of the isokinetic patch θ_0 depends upon the diameter D of the telescope and on the typical distance \tilde{h} of the perturbing layer and, from a theoretical point of view, these quantity are related with the following equation:

$$\tilde{h} \approx 0.3 \frac{D}{\theta_0}. \quad (1)$$

Other author information: e-mail: ghedina@astras.pd.astro.it; ragazzoni@astrpd.pd.astro.it; baruffolo@astrpd.pd.astro.it; farinato@astras.pd.astro.it. Send off-print requests to R. Ragazzoni

Given a certain telescope, one can argue that observing (or not) a certain correlation between two stars which are an angle θ apart corresponds to the scanning of a turbulent layer whose height is respectively less (or more) than \tilde{h} . Quantitative measurements of the isokinetic patch can be found in the literature and are usually based upon the observation of small star clusters^{2,3,4} or of speckle interferometry of double stars⁵. The isokinetic patch is measured tracking the RMS centroid motion of a star with respect to a reference star. Also observations of stellar trails⁶ and of stellar scintillation⁷ is a useful method to estimate the tilt induced anisoplanatism. By the way, with these techniques the atmosphere is sampled over angles spanning discrete distances and information about the atmospheric turbulence between two stars is not available.

Some of the above measurements are shown in Fig.1 in a peculiar way. In fact the estimated value for the isokinetic patch size is normalized to the telescope diameter. It is the same as to compare the \tilde{h} of the perturbing layers. There

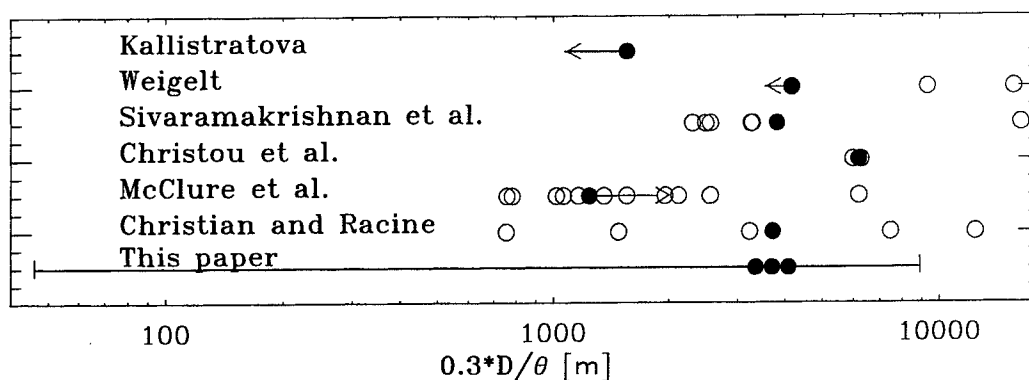


Figure 1. For those authors who have measured the isokinetic patch size from differential centroid motions of multiple stars, the angular separation from the reference star, normalized to the telescope diameter, is shown with an empty circle. The filled circle corresponds to the estimated isokinetic patch size; arrows departing from these circles mean that they must be intended as upper or lower limits. Note that some measures are affected by the presence of dominant ground layers (Kallistratova⁸ and McClure *et al.*³)

also exists a former estimation of the isokinetic patch based upon observations of the edge of the Sun⁸ which did not show any loss of correlation up to 20 arcsec. By the way, the edge of the Moon has also been used during a solar eclipse to provide a reference source for speckle transfer functions⁹.

The limitation introduced by the anisoplanatism is evident when considering Natural Guide Stars as reference sources for the adaptive correction. The sky coverage achievable with NGSs is a few percentage of the whole sky (depending on the magnitude and on the galactic latitude of the stars) and the most promising technique, up to now, seems to be the use of a Laser Guide Star¹⁰ (or LGS). The basic idea is to fire a laser beam through the atmosphere in order to make a reference source within the isoplanatic patch of the target. Though the LGS can be projected anywhere in the sky there are two fundamental drawbacks due to the propagation of the laser beam through the atmosphere, i.e. the tilt indetermination problem¹¹ and the focal anisoplanatism¹².

The problem of tilt indetermination arises because the tilt effect in the upward path of the laser beam is nearly completely compensated, at least when the projector uses the same mirror of the observing telescope, by a reciprocal perturbation introduced during the downward propagation.

To overcome this drawback several techniques have been proposed¹³⁻²². In some of these techniques it is useful, or even necessary, to know the size of the isokinetic patch. In fact using auxiliary telescopes¹⁷ or auxiliary projectors²⁰, or in any situation in which the laser is projected from a position on the ground different from where it is observed, the projection in the sky of the LGS is seen as an elongated strip. This strip is affected mainly by two perturbations (see Fig.2) and, one, is observed as a rigid movement σ_t of the whole beam around a mean position while the other one is seen as a corrugation ψ of the beam, instead of having a straight propagation. While the tilt of the whole beam is due to the atmospheric turbulence met by the laser in its upward propagation and near to the projector, the corrugation ψ of the strip is caused by the fact that the elongated LGS is in general much bigger than the typical isokinetic patch. The light coming from different portions of the strip is thus affected in different ways by

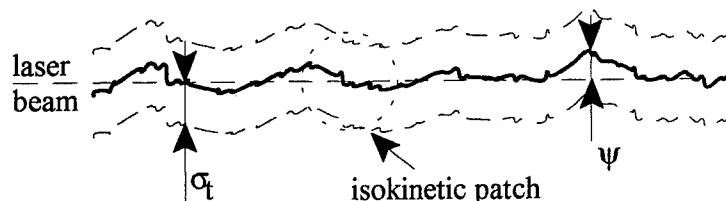


Figure 2. The effect of the atmosphere on the elongated laser beam is seen as a double perturbation

the turbulence it goes through.

It is in principle possible to measure ψ perpendicularly to the direction of propagation of the beam. Considering that if a portion θ of the strip is imaged and the size of the isokinetic patch is found from Eq.1, there are

$$N = \frac{\theta}{\theta_0} \quad (2)$$

independent estimations of ψ with a gaussian distribution around a mean position. Another example of the importance of quantitative measurements of the isokinetic angle can be found considering a bistatic²⁰ configuration. The laser fired from an auxiliary telescope, separated from the observing one, must be projected within the isokinetic patch of the target and, considering another technique²², also of a NGS. Without an estimation of the size of the isokinetic patch it is not possible to know how far from the target one is allowed to aim with the projector.

In this framework of having a valuable estimation of statistical parameters which characterize the atmospheric turbulence, both for tilt recovery techniques and for independent seeing measurements, we have developed this seeing monitor. Our measures of the isokinetic patch are based upon observations of the edge of the Moon and this gives a continuous spatial sampling of the atmosphere (see Fig.1) over a wide range of distances.

In testing our seeing monitor the lunar limb is considered as an elongated LGS and thanks to the brightness of the Moon it has been possible to use low cost instrumentation (a 20 cm telescope and a commercially available CCD). Nevertheless, with a minimal modification to the software and with the introduction of an anamorphic system we obtained a versatile and valuable seeing monitor.

2. THE SEEING MONITOR

Even with a modest telescope it is not difficult to obtain good images of the Moon. We built the seeing monitor starting from a Meade 2080, a Schmidt-Cassegrain telescope with a diameter of 203 mm (8 inches) and a $F/10$ focal ratio. The instrument was equipped with an equatorial mount, an off-axis guide and only the right ascension synchronous motor.

Data concernig the CCD we used, a Texas Instrument TC211 with 12 bit A/D converter, can be found in Tab.1. The control software of the CCD was originally conceived to save the images directly onto the hard disk of the

rows \times columns	165 \times 192
pixel size [μ m]	16 \times 13.75
height by width [mm]	2.64 \times 2.64
arcsecs per pixel	1.6 \times 1.4

Table 1. Technical data about the TC211 CCD

computer. This procedure would have taken a huge amount of time with respect to the typical coherence time of the atmosphere to save a single image of the Moon. We modified the software in order to avoid the waste of precious time in the A/D conversion between two consecutive images. Knowing that the matrix of pixels is read by shifting the rows, one at a time, towards the serial register, we adopted the solution of keeping most of the Moon outside of the CCD (see Fig.3) and leave the lunar edge in the rows opposite to the serial register. A frame transfer procedure

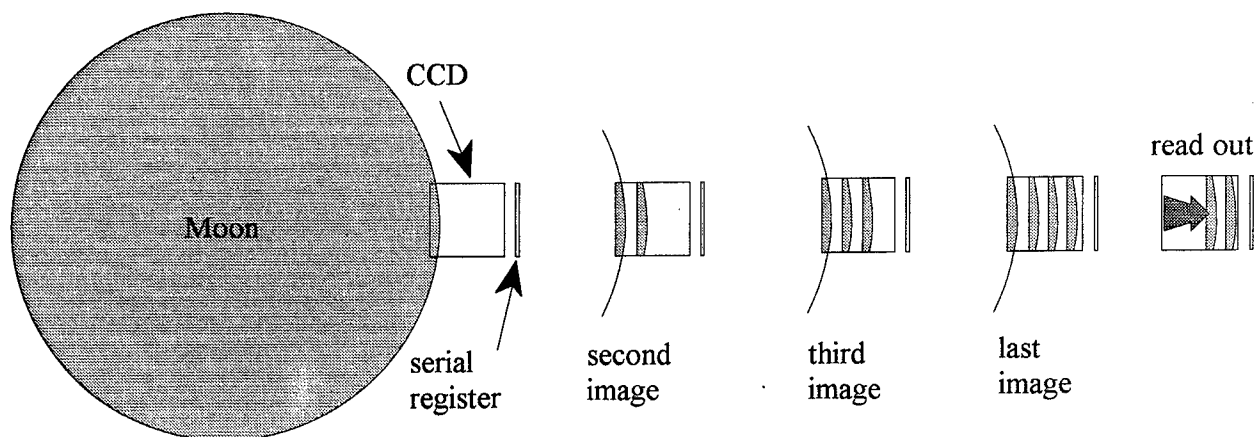


Figure 3. The frame transfer technique with only four images of the Moon

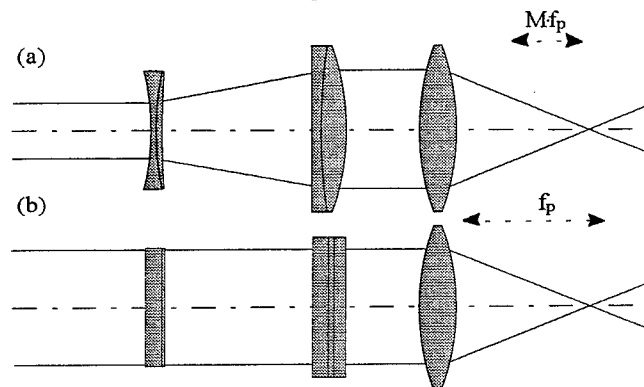


Figure 4. The anamorphic objective seen in two perpendicular plane in combination with a main objective. The focal length f_p of the latter objective is shortened of a factor $M \approx 2$ in only one meridian plane (a)

has been implemented to obtain more than one edge of the Moon on the same image. In this way it is possible to maintain an equivalent frame rate of nearly 20 Hz.

Some images have been obtained introducing an anamorphic optical relay between the telescope and the CCD. The use of the anamorphic relay is meant to increase (or relax) the scaling factor of the seeing monitor. In fact, an anamorphic objective, similar to those used in the Cinemascope projection systems, is a combination of cylindrical lenses (see Fig.4) and is able to give different scaling factor (in orthogonal directions) on the same frame. Two camera objectives (Fig.5) create the collimated beam that goes through the anamorphic objective and so the astigmatic aberration introduced by the cylindrical lenses is minimized. It is to be pointed out that properly orienting the anamorphic relay it is possible to choose, among the other combinations, either to have a larger field of view on the CCD (imaging a bigger portion of the lunar edge) or to increase the scale of the observed atmospheric perturbations.

3. FIRST EXPERIMENTAL OBSERVATIONS

In the nights of January 15th, 16th and 17th, 1997, we made intensive tests of the seeing monitor at the Astrophysical Observatory of Asiago. Considering the typical e -folding time of the atmospheric turbulence²³ we chose to get sequences of images separated of approximately 20 minutes one from the other. Tab.2 reports the times of the test runs and the respective zenithal distances of the Moon. The data collected have been reduced under IDL²⁴ with an automatic procedure that performs the following steps (assuming to have an image with 6 frames and that the edges of the Moon are perpendicular to the columns):

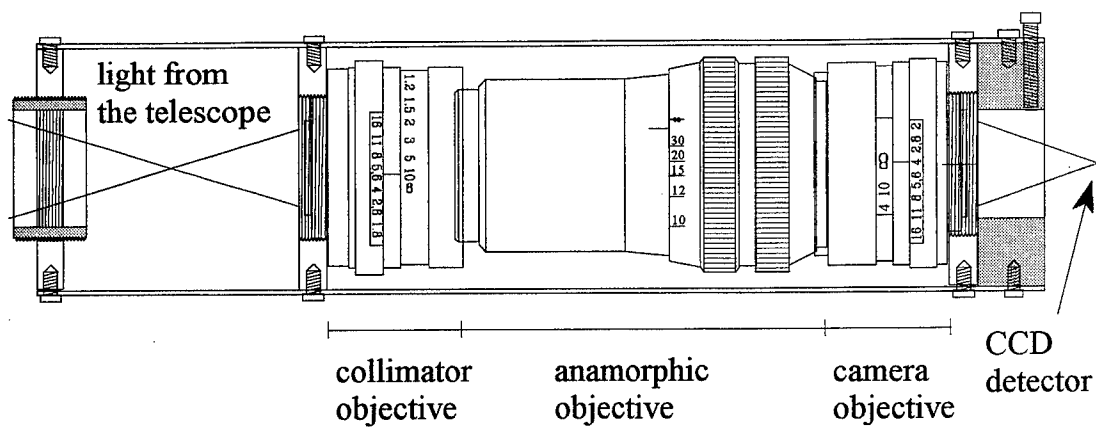


Figure 5. Drawing of the anamorphic relay used for the seeing monitor

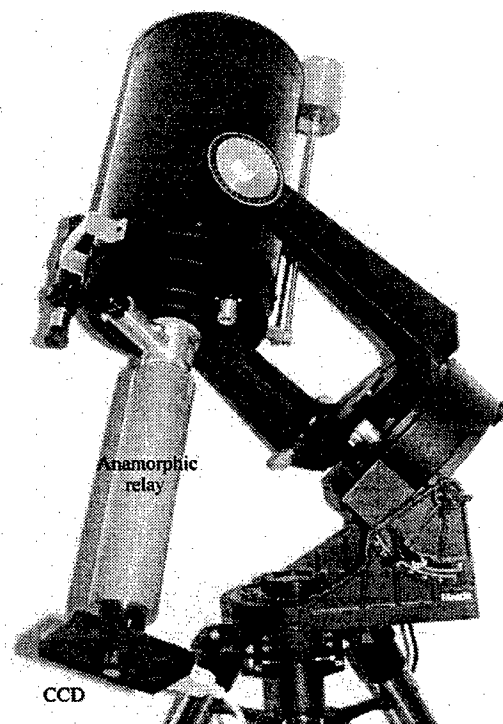


Figure 6. The set-up of the seeing monitor. The black rectangular box is the CCD fixed to the anamorphic relay (the clear tube) which on its own is behind the off-axis guide and the telescope. A counterweight, visible in the front part of the telescope, has been necessary to balance the system

night	UT	ζ [deg]
15	20.40 – 21.45	50.6 – 60
16	18.15 – 20.20	36.2 – 39.3
17	17.50 – 21.10	40 – 32.5

Table 2. Time of the observations and relative zenithal distances of the Moon. The starting time of the observations strongly depended upon weather condition and on the set up of the seeing monitor

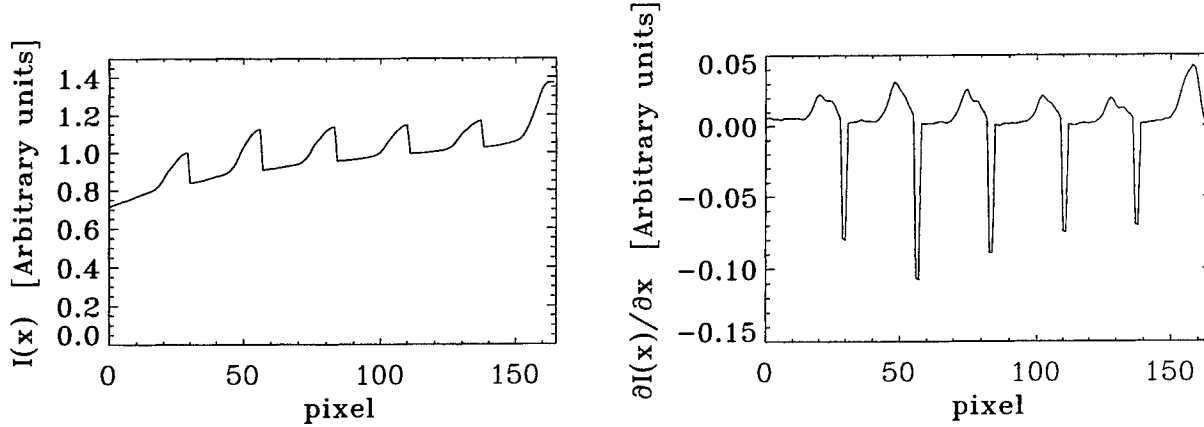


Figure 7. Intensity plot along one column and its derivative. The three pixels next to each local maximum of the derivative are interpolated with a parabola: its vertex gives the position of the edge with higher accuracy, even within the pixel

1. it scans the image along each column (see Fig.7 left) and finds the pixels with the highest brightness gradient $\partial I(x)/\partial x$ (Fig.7 right): this gives the position of the edge within each frame;
2. it chooses a reference point on the edges and, for increasing distances, it measures the RMS standard deviation of correspondent pixels around the mean position;
3. it plots and interpolates the data (Fig.8) with the following empirical function:

$$f(\theta) = \sqrt{2}\sigma_\theta \left[1 - \cos(p\theta) \exp\left(-\frac{\theta}{\theta_0}\right) \right] \quad (3)$$

giving an estimation both for θ_0 and for r_0 (Tab.3).

A few things have to be pointed out as far as Eq.3 is concerned, and first of all the fact that it is just a rough approximation of the expected theoretical behaviour²⁵. The exponential term is needed to find the value of θ_0 (Tab.3, second column), that is when the correlation decreases of a factor $1/e$. We also introduced a cosinus term with a parameter p trying to measure the anticorrelation that can be seen in some of the data plots. However scattering values of the p parameter prevented us from obtaining a valuable estimation of this perturbation. From a theoretical point of view the anticorrelation experienced at moderate angular distances can be explained remembering that the Coma term introduces a certain amount of tilt and this sums to the true tip-tilt term. Knowing a reliable method to distinguish between the true tilt and the coma contribution can be useful to have more accurate comparisons between the observed turbulence power spectrum and the Kolmogorov's one.

In Eq.3, σ_t is the asymptotic value to which the data approach and corresponds to the RMS dispersion of tilt. It can be used to estimate the value of r_0 (Tab.3, third column) with the following equation:

$$\sigma_t \approx k \frac{\lambda}{D} \left(\frac{D}{r_0} \right)^{5/6} \quad (4)$$

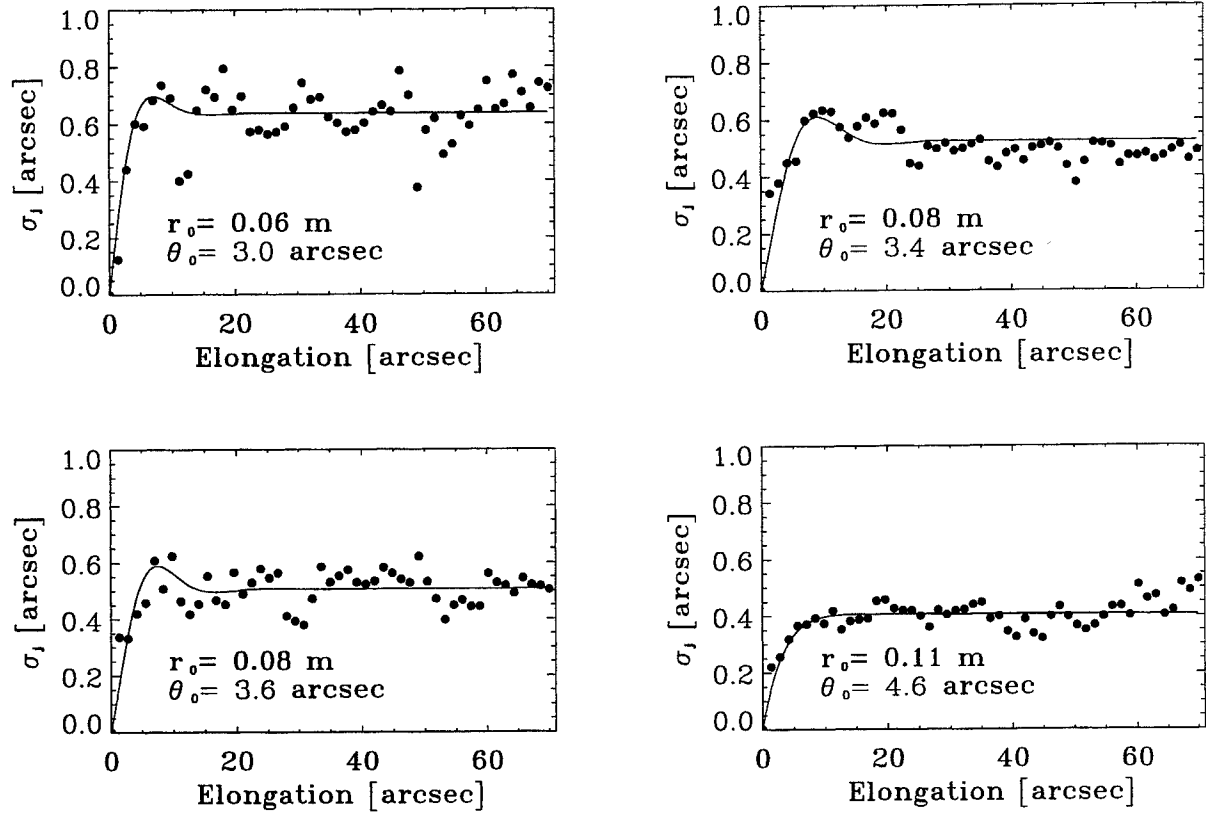


Figure 8. Four examples of the data collected during the test. Only the interesting portion of the field of view is plotted. The loss of correlation moving away from the reference point is clearly visible; note also the anticorrelation that has been experienced in several occasions

night	θ_0 "	$r_0 \pm \delta_{r_0}$ [cm]	\tilde{h} [m]	δ_{sm} "
15	4.0	9.4 ± 2.1		
15	3.4	7.7 ± 0.8	≈ 3350	1.2 ± 0.1
16	2.4	8.2 ± 1.7		
16	2.9	7.2 ± 1.2		
16	3.5	14.2 ± 2.5		
16	4.6	10.5 ± 2.1	≈ 3750	1.1 ± 0.3
17	3.2	6.6 ± 1.0		
17	3.5	8.1 ± 0.9		
17	2.4	5.9 ± 0.9	≈ 4100	1.5 ± 0.2

Table 3. Measured values for the isokinetic patch and for the Fried parameter. The estimated mean values of the height of the perturbing layer and of the seeing δ_{sm} for each night are reported in the last two columns

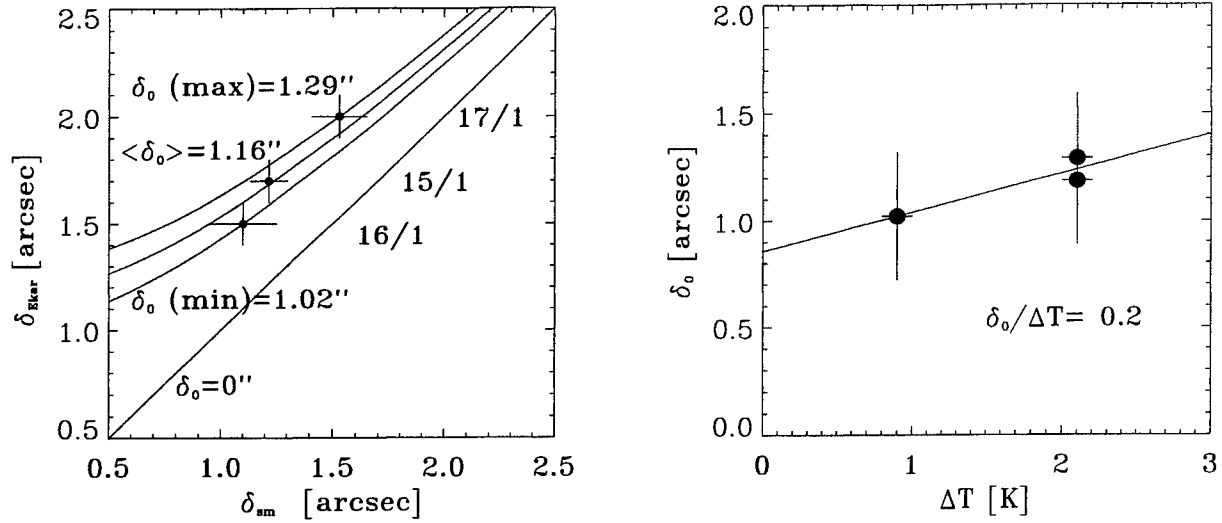


Figure 9. The seeing measured at Ekar is δ_{Ekar} is compared to the seeing monitor δ_{sm} estimates (left plot). The right plot shows the difference observed in the seeing estimates (δ_0) versus the temperature gap between the inside and outside of the dome

in which the parameter $k \approx 0.4$ has different values depending on the authors, from²⁶ $k = 0.413$ to²⁷ $k = 0.427$, and D is the diameter of the observing telescope (but it works also for the laser projector). Finally, the multiplicative factor $\sqrt{2}$ has a statistical meaning and it is introduced because when you force all the edges to have the same value in the reference point, the variance of this pixel sums quadratically with the variance of each other pixel. Also the dispersion of the data points around the value of σ_t is a statistical result²⁸ and it is due to the low number of samples available for each measure of θ_0 .

4. FURTHER MEASUREMENTS

Even if we did not have a different seeing monitor to show the reliability of our measurements, we have been able to verify the consistency of the data obtained. In Fig.9 it can be seen a comparison with independent seeing estimates, obtained from the FWHM of the lines along the spatial scale at the Echelle Spectrograph (Cima Ekar, 1.82 m telescope) One can note that the seeing measured at Ekar is affected by the presence of an additional quadratic term δ_0 that can be ascribed to dome seeing and to optical aberrations. The mean thermal gradient between the inside and the outside of the dome at Cima Ekar, measured during the three nights of the test, when compared to δ_0 approximatively follows a law of this kind (Fig.9, right):

$$\delta_0 \approx 0.2\Delta T. \quad (5)$$

With three available points, one for each night, it is only possible to show the direct proportionality between ΔT and δ_0 : a comparison with other "seeing/temperature" relations^{29,30} shows that the data collected with this experiment may fall in the range of values given by those authors. It can eventually be argued that the seeing difference measured at null temperature gradients is due to optical aberrations introduced with the Echelle spectrograph (for example the spherical aberration introduced to move the focus or the anamorphism of the grating).

5. CONCLUSIONS

We have built and tested a low cost seeing monitor, with the option of an anamorphic relay, able to measure both the size of the isokinetic patch and of r_0 from a sequence of images of the lunar edge.

The results suggest that further observations are necessary. More data need to be collected to test the effective reliability of the seeing monitor and to perform deeper statistical analyses of the parameters that characterize the atmospheric turbulence. The latter has a considerable importance in places where an LGS adaptive optics system is

foreseen, i.e. the Canary Islands³¹ for the Telescopio Nazionale Galileo.

One can see from Fig.1 that, apart from our measurements, only few of the reported references have a distribution of stars useful to scan the the atmosphere at distances close to the estimated value of θ_0 .

Eventually a double set of measures could be performed with the same seeing monitor by alternatively placing and removing a diaphragm in front of the telescope: the linearity between D and θ_0 should allow for an immediate comparison of the collected data.

Further reasonings can be undertaken about the range of angular distances that can be sampled simultaneously using the seeing monitor. Considering a CCD of N pixels and a pixelsize of μ meters, when the sampling distance is not determined by the angular separation of the stars but has a continuous range, it is clear from Eq.1 that the maximum value of \tilde{h} is:

$$\tilde{h}_{max} = 0.3 \frac{Df}{\mu} \quad (6)$$

where f is the focal length and D is the full diameter of the telescope; obviously \tilde{h}_{min} is N times smaller. This does not yet represent the limit achievable with the seeing monitor: the diaphragm in front of the telescope can lower \tilde{h}_{min} . The true limit is found when λ/D is larger than the pixel size or alternatively, larger than the wandering of the lunar edge. The latter situation must be expected in good astronomical sites, where r_0 is usually comparable to the diameter of this seeing monitor.

6. ACKNOWLEDGEMENTS

We would like to thanks Enzo Bellettato and the Astronomical Observatory of Rovigo for the use of the anamorphic objective and of the CCD, and also Gianni Baù for the mechanical building of the anamorphic relay.

REFERENCES

1. Noll R.J., "Zernike polynomials and atmospheric turbulence", *J. Opt. Soc. A.*, **66**, 3 (1976)
2. Christou J. C., Ellerbroek B., Fugate R. Q., Bonaccini D., Stanga R., "Rayleigh Beacon Adaptive Optics Imaging of ADS 9731: Measurements of the Isoplanatic Field of View", *Astrophys. Jou.*, **450**, 369 (1995)
3. McClure R. D., Arnoud J., Fletcher J. M., Nieto J.-L., Racine R., "A measurement of isoplanatism with the high-resolution camera at the Canada-France-Hawaii telescope", *Publ. Astron. Soc. Pac.*, **103**, 370 (1991)
4. Sivaramakrishnan A., Weymann R. J., Beletic J. W., "Measurements of the angular correlation of stellar centroid motion", *Astron. Jou.*, **110**, 430 (1995)
5. Weigelt G. P., "High-resolution astrophotography. New isoplanicity measurements and speckle holography applications", *Optica Acta*, **11**, 1351 (1979)
6. Christian C. and Racine R., "Dependence of seeing correlation on image separation at the CFH Telescope on Mauna Kea", *Publ. Astron. Soc. Pac.*, **97**, 1215 (1995)
7. Winick K.A. and Marquis D.vL., "Stellar scintillation technique for the measurement of tilt anisoplanatism", *J. Opt. Soc. A.*, **5**, 1929 (1988)
8. Kallistratova M. A., "Fluctuations in the direction of propagation of light waves in an inhomogeneous turbulent medium", *Radiophys. Quantum. Electron.*, **9**, 50 (1966)
9. de Boer, C. R., "Empirical speckle transfer function measurements from partial eclipse observations of the Sun", *Astron. Astrophys. Supp. Ser.*, **114**, 387 (1995)
10. Foy R., Labeyrie A., "Feasibility of adaptive telescopes with laser probe", *Astron. Astrophys.*, **152**, L29 (1985)
11. Pilkington J. D. H., "Artificial guide star for adaptive imaging", *Nature*, **330**, 116 (1987)
12. Tallon M., Foy R., "Adaptive telescope with laser probe. Isoplanatism and cone effect", *Astron. Astrophys.*, **235**, 549 (1990)
13. Foy R., Boucher Y., Fleury B., Grynberg G., McCulloch P. R., Migus A., Tallon M., "ATLAS status report and tilt sensing using multicolour laser reference star " *ESO Conf. proc.*, **42**, 437 (1992)
14. Belen'kii M. S., "Fundamental limitations in Adaptive Optics: how to eliminate it? A full aperture tilt measurements technique with a laser guide star", *SPIE proc.*, **2201**, 321 (1994)
15. Belen'kii M. S., "Full aperture tilt measurement with a laser guide star", *SPIE proc.*, **2471**, 289 (1995)

16. Foy R., Migus A., Biraben F., Grynberg G., McCulloch P. R., Tallon M., "The polychromatic artificial sodium star: a new concept for correcting the atmospheric tilt", *Astron. Astrophys. Supp. Ser.*, **111**, 569 (1995)
17. Ragazzoni R., Esposito S., Marchetti E., "Auxiliary telescopes for the absolute tip-tilt determination of a laser guide star", *Mon. Not. R. Astron. Soc.*, **276**, L76 (1995)
18. Belen'kii M. S., "Tilt angular correlation and tilt sensing techniques with a laser guide star", *SPIE proc.*, **2828**, 280 (1996)
19. Ragazzoni R., Marchetti E., "Further techniques for LGS tilt recovery: the perspective and the predictive approach", *SPIE proc.*, **2871**, 948 (1996)
20. Ragazzoni R., "Absolute tip-tilt determination with laser beacons", *Astron. Astrophys.*, **305**, L13 (1996)
21. Ragazzoni R., "Propagation delay of a laser beacon as a tool to retrieve absolute tilt measurements", *Astrophys. Jou.*, **465**, L73 (1996)
22. Ragazzoni R., "Robust tilt determination from laser guide star using a combination of different techniques", *Astron. Astrophys.*, **319**, L9 (1997)
23. Racine R., "Temporal fluctuations of the atmospheric seeing", *Publ. Astron. Soc. Pac.*, **108**, 372 (1996)
24. Research Systems, Inc., "IDL User's Guide. Version 2.0", Boulder (CO), (1990)
25. Valley G. C. and Wandzura S. M., "Spatial correlation of phase-expansion coefficients for propagation through atmospheric turbulence", *J. Opt. Soc. Am.*, **69**, 712 (1979)
26. Acton D. S., "Simultaneous daytime measurements of the atmospheric coherence diameter r_0 with three different methods" *Appl. Opt.*, **34**, 4526 (1995)
27. Olivier S. S., Max C. E., Gavel D. T., Brase J. M., "Tip-tilt compensation: resolution limits for ground based telescopes using laser guide star adaptive optics", *Astrophys. Jou.*, **407**, 428 (1993)
28. Sarazin M., Roddier F., "The ESO differential image motion monitor" *Astron. Astrophys.*, **227**, 294 (1990)
29. Lowne C. M., "An investigation of the effects of mirror temperature upon telescope seeing", *Mon. Not. R. Astr. Soc.*, **188**, 249 (1979)
30. Bridgeland M. T., Jenkins C. R., "Measurements of mirror seeing in the laboratory and at the telescope", *Mon. Not. R. Astr. Soc.*, **287**, 87 (1997)
31. Vernin J. and Muñoz-Tuñón, "Optical seeing at La Palma Observatory. II. Intensive site testing campaign at the Nordic Optical Telescope" *Astron. Astrophys.*, **284**, 311 (1994)

SESSION 3

Propagation and Imaging through Optical Turbulence

Carrier-to-noise ratio for an equal gain coherent laser radar receiver array system: theory and experiment

L. C. Andrews* and D. E. Kelly

Department of Mathematics and
Center for Research and Education in Optics and Lasers (CREOL)
University of Central Florida, Orlando, FL 32816

R. L. Phillips,[†] A. R. Weeks, J. Harvey, J. Xu, C. Gagge, A. Notash, G. Luvera, and
G. Sellar

Department of Electrical and Computer Engineering and
Center for Research and Education in Optics and Lasers (CREOL)
University of Central Florida, Orlando, FL 32816

ABSTRACT

In this paper, a theoretical comparison is made of the mean carrier-to-noise ratio (CNR) for a coherent (heterodyne detection) equal gain (EG) optical array receiver system with that predicted by a conventional single-aperture monolithic coherent detector system. Our analysis shows that the mean CNR for an EG array receiver system improves significantly over that of a single aperture system. Experimental data taken from a recent outdoor experiment over a range up to 1 km between target and transceiver are also presented and compared with the theory for a particular eight-element EG system developed at the University of Central Florida. Optical signals received by the EG receiver array are launched into eight single mode optical fibers. Phase compensation between the individual receivers is accomplished by wrapping the fibers around PZT cylinders that are controlled by phase compensating electronics.

Keywords: atmospheric optics, coherent receiver, carrier-to-noise ratio, laser radar

1. INTRODUCTION

Since the 1960s, there have been numerous papers published on coherent laser radar (CLR) theory (an extensive list of references can be found in the paper by Frehlich and Kavaya¹). The majority of these papers have been directed at the more common CO₂ laser systems operating at 10 μ m wavelength, but recent interest has focused on extending the technology to shorter wavelengths in the 1 μ m range. However, the extension of CLR theory to shorter wavelength systems requires a more detailed knowledge of the effects of atmospheric turbulence.

The performance of a CLR system is usually measured on the basis of carrier-to-noise ratio (CNR) and heterodyne efficiency. Past studies of CLR systems have revealed that the performance of a single element detector can be seriously degraded by atmospheric turbulence, and the effective receiver aperture size is directly related to the atmospheric coherence radius of the received optical wave.¹⁻⁴ The use of a coherent receiver array can overcome such effects by appropriately combining the intermediate frequency (IF) signals from a number of independent receivers

* E-Mail: landrews@pegasus.cc.ucf.edu; Fax: (407) 823-6253

[†] E-Mail: PHILLIPS@mail.creol.ucf.edu; Fax: (407) 823-6880

appropriately spaced. In a recent paper by Gatt *et al.*,⁵ three common types of space diversity receiver architectures were compared on the basis of average CNR and fading characteristics associated with an optical wave reflected from a rough target. Here it was shown that the mean CNR for an equal gain (EG) receiver array with independent receivers increases linearly with the number of array elements M and the variance of CNR decreases at a rate close to $1/M$. The EG system analyzed by Gatt *et al.*⁵ utilizes sparsely distributed array elements, each of which directs the received signal into a single-mode fiber optic heterodyne receiver. Real time phase alignment of the RF carriers is performed with an optical/electronic phase-locked loop. As the name implies, an EG receiver array applies the same gain to all RF signals. Also, only the phase of the local oscillator (LO) is matched to the received signal—no amplitude adjustment is necessary. Although not quite as good as a maximal ratio receiver array, the EG receiver array has the advantage of simpler hardware requirements.⁵

A diagram of the EG system under study in this paper is provided in Fig. 1. The use of a single mode fiber for spatially aligning the return echo wave and the LO field requires coupling the incident echo field into the fiber. For an individual lens, this coupling requires the field of the echo signal in the focal plane of the lens to match the single mode profile of the guided wave and alignment to the fiber core. Poor fiber coupling can result from either spot size mismatch or spot position mismatch, the latter being directly related to angle-of-arrival fluctuations across the collecting lens. From our analysis, angle-of-arrival fluctuations caused by atmospheric turbulence are negligible in comparison with the spot size mismatch caused by atmospheric effects.

In this paper we present an analysis of the gain in average CNR in the presence of atmospheric turbulence for a CLR system using an EG receiver array and compare results with those predicted for a conventional single aperture monolithic receiver. We also report here the findings of a field experiment that was conducted at the BMDO Innovative Science and Technology Experimentation Facility (ISTEF) on a real-time, eight-aperture, continuous wave, EG coherent laser radar receiver array system. The ISTEF site is located at Kennedy Space Center and the experiment was conducted during the month of December, 1996. The eight receiver apertures of the system, 1 cm in diameter and arranged in a circular array of diameter 10 cm, acted in a bistatic mode. At the center of the array was another 1 cm aperture that could operate as a monostatic source/receiver but was used in our experiment only for the transmitted beam.

2. THEORY

For a conventional system using a single lens of diameter D , the average CNR is given by²

$$CNR = \frac{\eta}{h\nu B} \frac{\pi A_s^2 r_0^2}{8} \Psi(r_0) \quad (1)$$

where η is the detector quantum efficiency (taken to be constant over the detector area), h is Planck's constant, ν is optical frequency, B is the bandwidth of a lowpass filter, A_s is the amplitude of the signal in the absence of turbulence, r_0 is the atmospheric coherence length, and $\Psi(r_0)$ is the normalized CNR factor defined by

$$\begin{aligned} \Psi(r_0) &= \frac{16}{\pi} \left(\frac{D}{r_0} \right)^2 \int_0^1 x \left[\cos^{-1} x - x(1-x^2)^{1/2} \right] \exp \left[-3.44(D/r_0)^{5/3} x^{5/3} \right] dx \\ &\approx \frac{(D/r)^2}{\left[1 + (D/r_0)^{5/3} \right]^{6/5}} \end{aligned} \quad (2)$$

In the case of an EG system with M apertures, the corresponding normalized CNR expression is

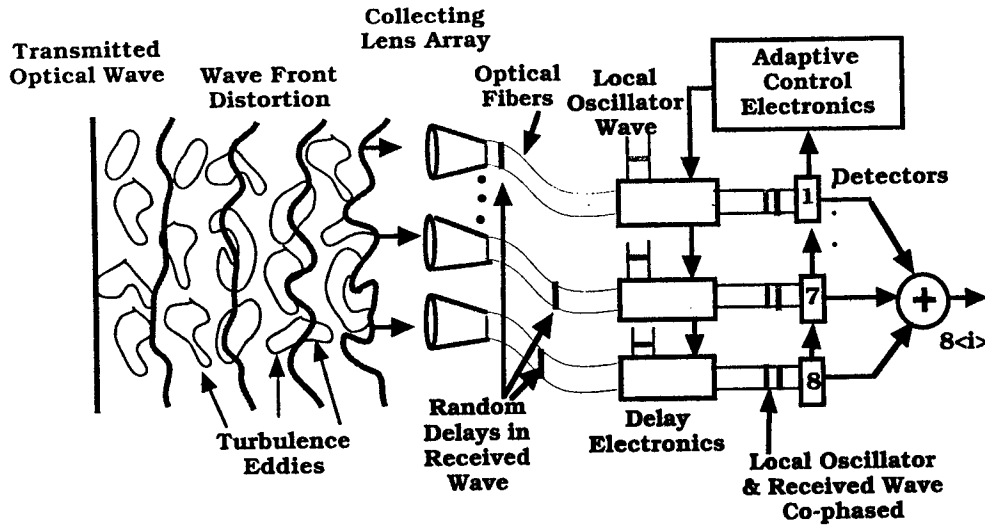


Figure 1 Diagram of the EG system.

$$\Psi(r_0) = \left(\frac{4}{\beta^2} \right) \frac{M(d/r_0)^2}{\left[1 + (d/r_0)^{5/3} \right]^{6/5}} \left[1 + (M-1) \exp\left(-\frac{1}{4} \sigma_I^2 \right) \right], \quad (3)$$

where d represents the diameter of each lens and σ_I^2 is the scintillation index at the focal plane of the lens. The factor $4/\beta^2$ represents the mismatch between the actual spot size of the beam in the focal plane and the ideal spot size for the fiber. The quantity β is defined by

$$\beta = (W_e/W)^2 + (W/W_e)^2 \quad (4)$$

where W is the ideal spot size and W_e is the effective spot size due to turbulence given by

$$W_e = W \left[1 + \left(\frac{d}{r_0} \right)^{5/3} \right]^{3/5} \quad (5)$$

The last factor in Eq. (3) involving the scintillation index is based on a lognormal model for intensity fluctuations. Although not appropriate for strong turbulence conditions, we believe it probably represents a worse case result as atmospheric effects become stronger. For the purpose of this analysis, we consider a point source in the far field

and use a Kolmogorov power law spectrum for the refractive index fluctuations. Under these assumptions, the scintillation index takes the form

$$\sigma_I^2 = 0.5C_n^2 k^{7/6} L^{11/6} = 7.7\Omega^{5/6} (d/r_0)^{5/3} \quad (6)$$

where L is path length from the source, k is optical wave number, and $\Omega = L/kd^2$.

2.1 Results

For the purpose of comparing the EG system array with a conventional monolithic system, we will assume the lens area of each system is the same, *i.e.*, $d = D/\sqrt{M}$. In Figs. 2-4 we show the normalized CNR defined by Eq. (2) for a conventional system and Eq. (3) for the EG system. In Fig. 2 we compare a single aperture EG system ($M = 1$) with the conventional system. Here we see that a single aperture EG system begins to perform more poorly for $D/r_0 > 0.5$ owing to the mismatch of effective spot size and ideal spot size. The case $M = 4$ is illustrated in Fig. 3 and the case $M = 8$ in Fig. 4. In these last two figures we can clearly see an improvement in the normalized CNR of the EG system over that of a conventional single aperture system. However, this analysis also shows that the EG system begins to perform more poorly when the atmospheric coherence length is smaller than the diameter of the large lens conventional system.

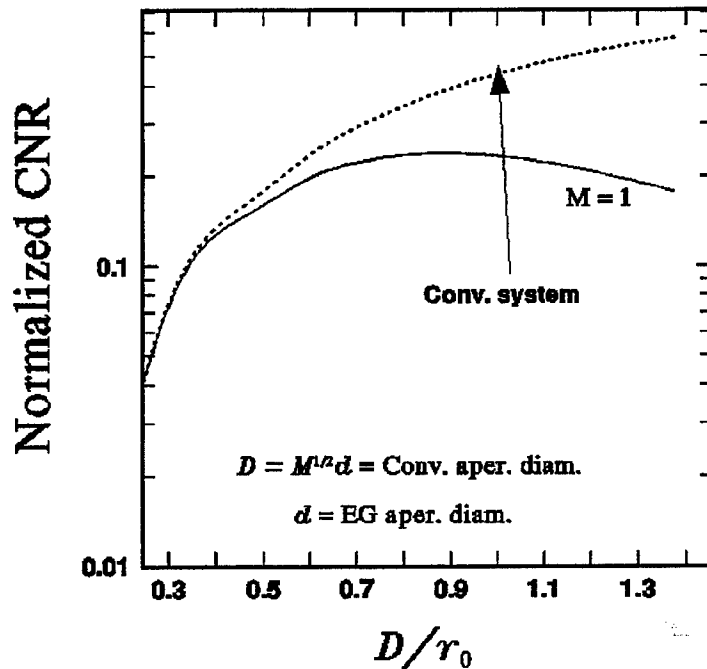


Figure 2 Normalized CNR as predicted by Eq. (2) (dotted curve) and Eq. (3) (solid curve) with $M = 1$.

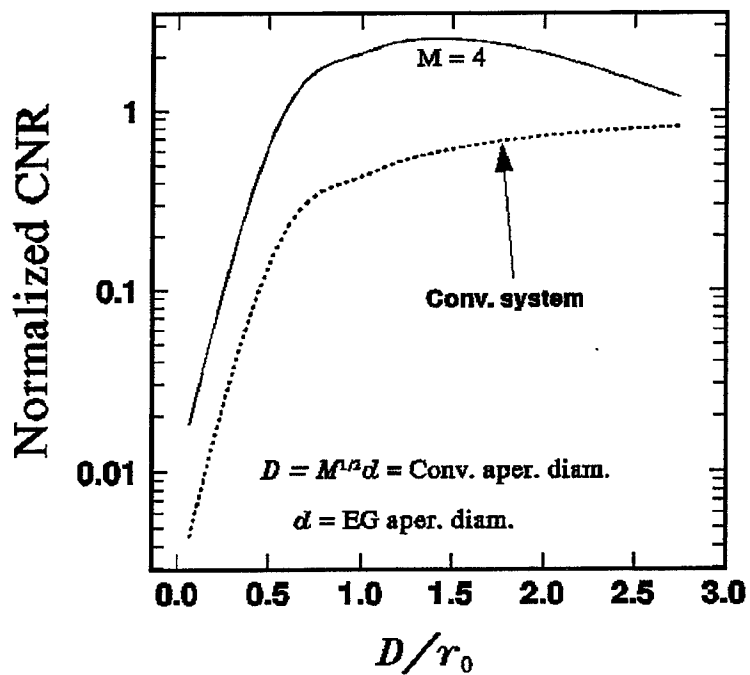


Figure 3 Normalized CNR as predicted by Eq. (2) (dotted curve) and Eq. (3) (solid curve) with $M = 4$.

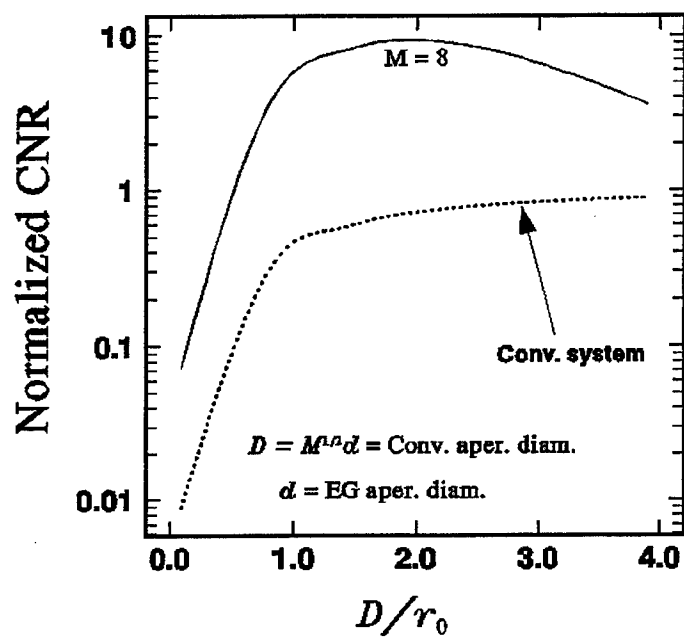


Figure 4 Normalized CNR as predicted by Eq. (2) (dotted curve) and Eq. (3) (solid curve) with $M = 8$.

3. EXPERIMENT

The transmitter for the EG system used to acquire data presented in this paper is a 60 mW diode-pumped Nd:YAG laser operating at wavelength 1.06 μm . An acousto-optical modulator shifts the transmission beam up by 27.12 Mhz (IF frequency) while a portion of the unshifted beam is split off by a polarizing beam splitter to serve as the LO which is fiber-coupled to a 1×8 optic fiber divider for the receiver. The receiver array consists of eight 1-cm-diameter apertures arranged in a ring configuration. Each aperture is fiber-coupled to a 2×2 optic fiber combiner which mixes the receiving signal with the LO signal to form the IF signal. The eight signals from the receivers are co-phased to a reference signal to obtain phase coherence between each of the received signals. Finally, the co-phased IF signals are summed together with equal gain.

The experiment was conducted during daytime hours on December 16, 17, and 20, 1996. A 1.06 mm Nd:YAG laser source was transmitted through the center aperture of the array system to a large rough (diffuse) retroreflectance target located at 480 m or 970 m downrange. The reflected wave from the target was received back at the source plane by the eight element receiver array system. Data samples over 1 minute intervals were used to calculate the mean CNR for individual and summed outputs of the received IF signals. A scintillometer instrument was used to measure values of the atmospheric index of refraction structure constant C_n^2 and inner scale l_0 of the optical turbulence at the ISTEf range at all times during the experiment. Simultaneous measurements of wind speed and temperature were also recorded. Wind speeds were typically on the order of 1-3 m/s and the mid-day clear-sky temperature on December 16 and 17 was approximately 75° F, whereas on December 20 the data were taken only in the morning on a much colder and cloudy day with temperatures ranging over 34-45° F.

Data from the December measurements are shown in Figs. 5 and 6 as a function of the number of receiver apertures M . We define the CNR Gain Factor as the ratio of the average CNR for the sum of signals from two or more apertures and that of a single aperture. The data in Fig. 5 was taken with the target 480 meters from the transceiver whereas that in Fig. 6 was taken with the target at 970 meters from the transceiver. Although the CNR Gain Factor of the actual data do not equal the number of apertures, it does show a significant improvement over that of a single aperture system. Shown in Fig. 7 are theoretical curves as deduced from Eq. (3) for various values of d/r_0 . Values of the ratio d/r_0 obtained during the experiment vary from $d/r_0 = 0.3$ to 1.2. These theoretical curves clearly reveal that the EG system performs better when the aperture diameter is smaller than the atmospheric coherence length r_0 . Also shown in Fig. 7 are the data from Figs. 5 and 6. Although the target characteristics, as well as inner scale effects, are not taken into account in our theoretical model, the data are still reasonably consistent with the theory.

Figs. 8 and 9 show values of the structure constant C_n^2 as a function of time of day for all 3 days of the experiment and the simultaneous values of the inner scale of turbulence as a function of time of day.

4. DISCUSSION

The theoretical analysis presented here has shown that the mean CNR of a multi-aperture EG array receiver system can significantly exceed that of a conventional CLR system with a single aperture. Experimental data obtained from a particular eight-aperture system shows good agreement with the theoretical model.

ACKNOWLEDGMENT

Funding for this work was partially provided by the Ballistic Missile Defense Organization's Innovative Science and Technology Directorate and administered by Guy Beagler of the Naval Command, Control, and Ocean Surveillance Center, Research Development Test and Evaluation Division, San Diego, CA through Delivery Order Number 0073 under Contract N66001-92-D-0082 with the San Diego State University Foundation.

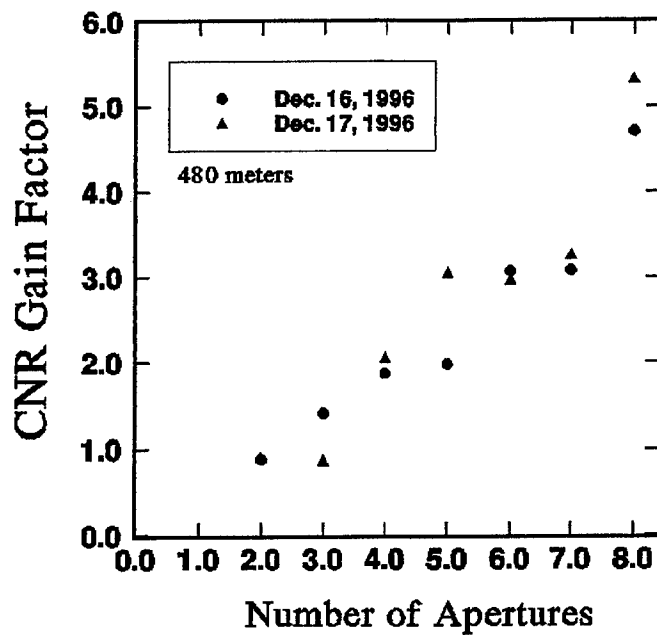


Figure 5 CNR Gain Factor for the EG system as a function of number of receiver apertures. The target was located 480 m from the transceiver.

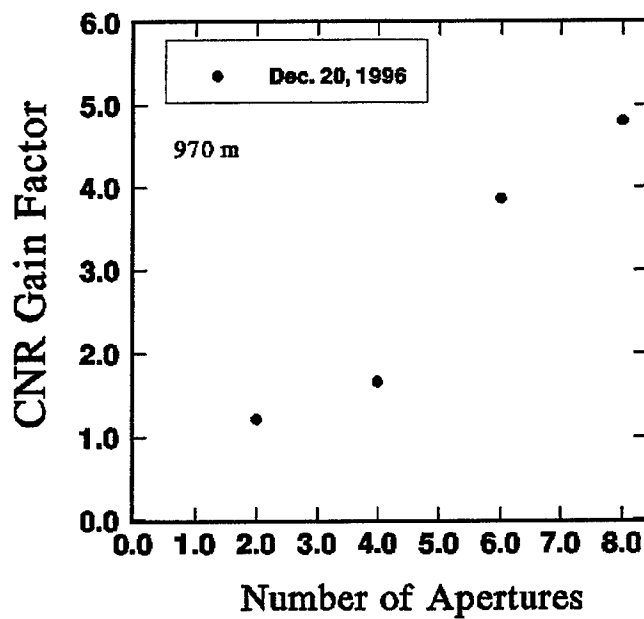


Figure 6 CNR Gain Factor for the EG system as a function of number of receiver apertures. The target was located 970 m from the transceiver.

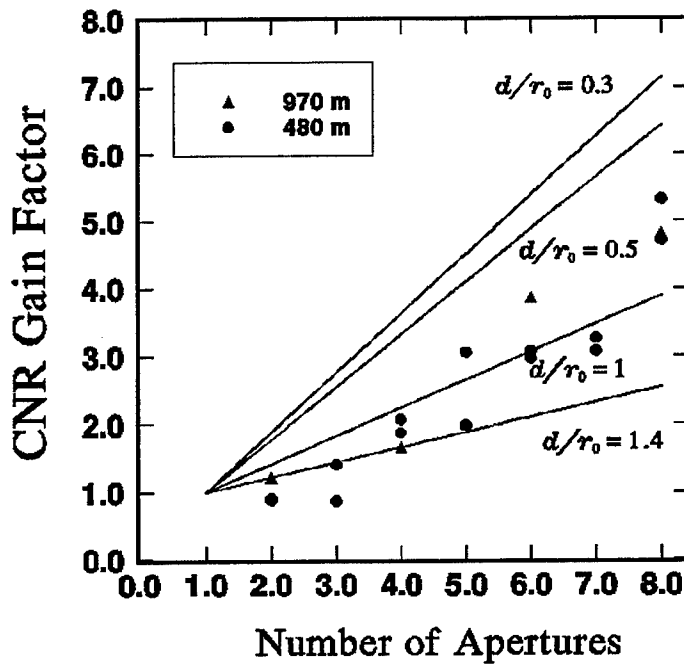


Figure 7 Theoretical prediction of CNR Gain Factor (solid curves) as deduced from Eq. (3). The data shown are taken from Figs. 5 and 6.

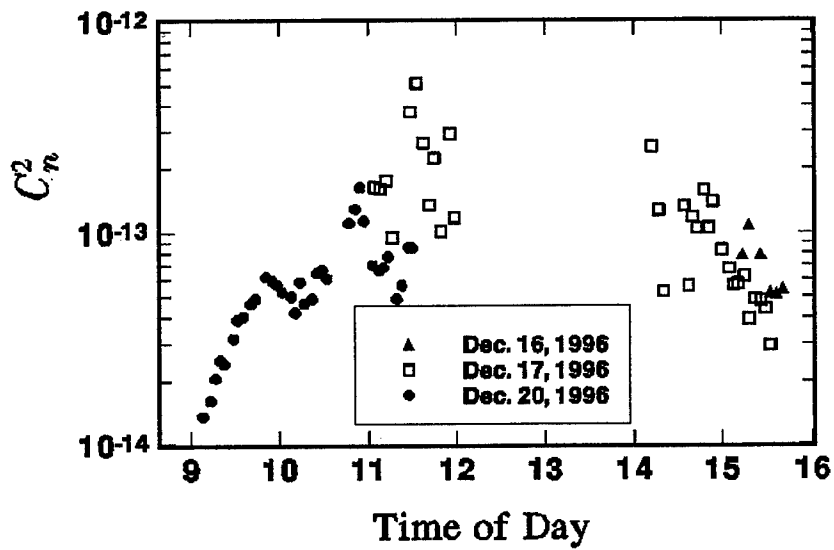


Figure 8 Measured values of the refractive index structure constant as a function of time of day.

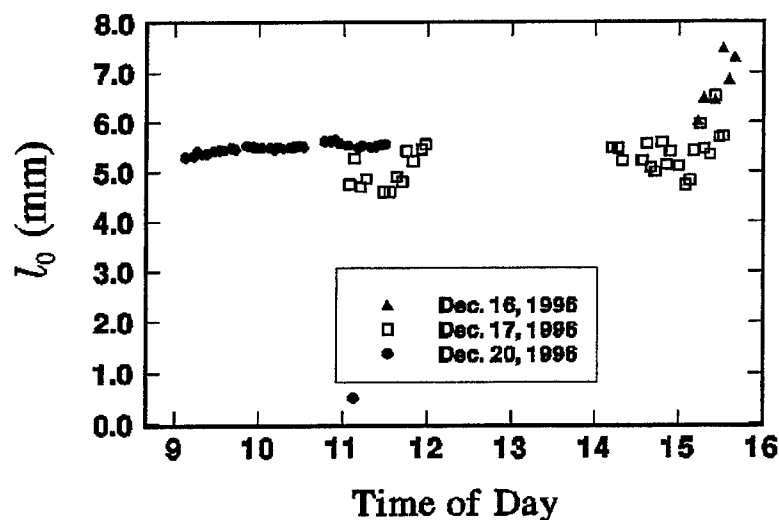


Figure 9 Measured values of the inner scale as a function of time of day.

REFERENCES

1. R. G. Frehlich and M. J. Kavaya, "Coherent laser radar performance for general atmospheric refractive turbulence," *Appl. Opt.* **30**, 5325-5352 (1991).
2. D. L. Fried, "Optical heterodyne detection of an atmospherically distorted signal wave front," *Proc. IEEE* **55**, 57-67 (1967).
3. S. F. Clifford and S. Wandzura, "Monostatic heterodyne lidar performance: the effect of the turbulent atmosphere," *Appl. Opt.* **20**, 514-516 (1981).
4. J. H. Shapiro, B. A. Capron, and R. C. Harvey, "Imaging and target detection with a heterodyne-reception optical radar," *Appl. Opt.* **20**, 3292-3313 (1981).
5. P. Gatt *et al.*, "Coherent optical array receivers for the mitigation of atmospheric turbulence and speckle effects," *Appl. Opt.* **30**, 5999-6009 (1996).

Some Aspects of Beam-Pointing Instability Problem at Laser Beacon Generation

Vadim A. Parfenov

Research Centre "S.I. Vavilov State Optical Institute"
12 Birzhevaya liniya, 199034, St. Petersburg, Russia
Fax: (812) 218-3720

ABSTRACT

Results of the experimental study of beam pointing stability of Nd:YAG lamp-pumped lasers are described. Possible ways of beam angular position stabilization are considered.

Key words: artificial guide star, laser beam pointing stability

2. INTRODUCTION

At the artificial guide star generation, high angular stability ($\sim 1...2$ arcsec) of laser beacons is required for atmospheric compensation with adaptive optics. One of the main reasons which can influence on beacon stability is pointing instability of projected laser beam.

This work is devoted to some applied aspects of the problem. We have investigated a beam pointing stability of Nd:YAG lasers both at fundamental and at second harmonic wavelengths of radiation. As known, Nd:YAG lasers generating at second harmonic wavelength of 532 nm may be used for guide star generation by Rayleigh optical scattering by air molecules in the stratosphere [1], and lasers generating at fundamental wavelength (in the case of sum frequency mixing of the 1064 and 1319 nm lines that result in sodium resonance radiation) can be applied for generation of beacon by optical scattering by atoms of Na in the mesosphere [2,3].

The main goal of our work was to reveal the basic reasons causing the instability of beam angular position of Nd:YAG lasers and to measure values of beam axis displacements. Also we have considered some ways of laser beam stabilization.

It is necessary to note, that in this work we have studied only own stability of angular position of laser beams, but instability caused by atmosphere turbulence was not considered here. However, this problem will be a subject of our future investigations.

3. EXPERIMENTAL RESULTS

Part I. Measurement of laser beam pointing stability

We have investigated several available cw, frequency-doubled Nd:YAG arc-lamp-pumped lasers with output power of 0.2...1 W. In experiments we have used the original device on the base of the four-quadrant photodiode. This device is the real-time photoelectric dual-coordinate displacement converter described in paper [4] in detail.

It should be noted that accurate choice of measurement device is very important to obtain correct results. In modern scientific literature a stability of laser beam angular position is described, as a rule, with help of the parameter "beam pointing stability" characterizing an extreme angle within which a beam axis can oscillate. As it was shown in paper [4], laser beam axis can undergo both fast spasmodical oscillations about its middle position and slow drift from original position to some new spatial one. In fact, the parameter "beam pointing stability" is a characteristic of fast angular displacements. However, at artificial guide star generation information about character of beam slow displacements for a long time interval is very important too. The feature of the given work is that both fast oscillations and slow displacements of laser beam axis were investigated. That is why, describing experimental results we use here more correct (from our point of view) term "stability of the beam angular position" instead of term "beam pointing stability". This parameter characterizes stability of angular position of energy center of laser beam. But for measurement of position of light energy center a metrology system based on four-quadrant photodiodes are most preferable. So, we have used mentioned device.

The experiments were carried out according the following routine. The laser and the measurement device were rigidly attached to an optical table with purpose to reduce the influence of vibrations. The laser beam was isolated to diminish the influence of air flows. Mounted in the far field of the laser beam, the positive lens ($F = 1$ m) focused radiation onto the photosensitive surface of the four-quadrant photodiode (see Fig.1). In this case the light field distribution corresponding to the laser radiation angular spectrum was formed in the lens focal plane. The angular measurements sensitivity limit is determined by a signal/noise ratio and zero drift of the photodetector. For our geometry of the optical scheme the sensitivity was about 0.1 arcsec.



Fig.1. Measurement scheme

As it was mentioned above, we have investigated different lasers, but in all cases we have obtained similar results. That is why, in this paper we describe experimental results only for one of lasers.

The optical scheme of the laser is shown in Fig.2. The laser crystal was 4x90 mm in single-lamp-pumped elliptical reflector. The nonlinear crystals $\text{Ba}_2\text{NaNb}_5\text{O}_{15}$ (BNN) and KTiPO_4 (KTP) were applied for the second harmonic generation (SHG). The maximum output power at the wavelength of 532 nm was 200 mW for the former and was 60 mW for the latter.

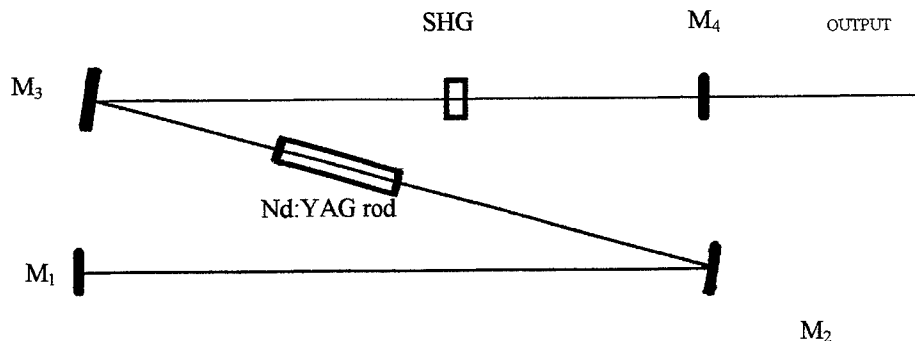


Fig. 2. Optical scheme of laser

To obtain more correct data the measurements were carried out during the long period of laser action (a few of hours), were repeated several times and then the results were averaged.

The experiments revealed both the slow drift of the laser beam axis and its fast oscillations with the frequency in the range of 0.01...1 Hz. The maximum fast oscillations of the beam axis occurred during the first five minutes of laser action, when the generation steady-state was established. In this case the amplitude of the fast oscillations was as high as 30 arcsec. Later the amplitude of these fast oscillations was gradually diminishing. As for the slow drift of the beam axis, during some period from the start of laser action its beam axis continuously was moving from an original position to another one. When this movement was finished, the axis revealed small oscillations with respect to this position. The total slow displacement of the radiation beam from an original position during 1 hour of laser action was about 15 arcsec. After that beam axis revealed slow oscillations with respect to this new position within the angle interval of ± 2 arcsec. The overlapped fast oscillations with spread up to 3 arcsec occurred.

To our opinion, the following destabilizing factors may result in instability of the frequency-doubled, lamp-pumped Nd:YAG laser beam angular position: presence of thermal induced lenses in the active element and in nonlinear crystal, transient process caused by the establishment of SHG regime, thermal deformations of the resonator construction and mirrors, vibrations (caused, in particular, by the influence of a cooling agent on the active element), as well as disturbances of convection air flows and acoustic oscillations on the cavity.

To reveal the rate of action of these factors the experiment was complicated. First of all, the nonlinear crystal was replaced. The crystal KTP was placed into the cavity instead of the crystal BNN. The crystal replacement was carried out for the following purpose. It is known that crystal BNN has very narrow bandwidth of temperature synchronism and needs precise tuning of the temperature with accuracy of about 0.05-0.1 °C. So it is natural to suppose, that use of such crystal can result in SHG establishment process characterized by significant over-oscillations. In comparison with BNN a crystal KTP has more wide bandwidths of temperature and angular synchronism. Therefore, the SHG establishment process must be more calm, when a crystal KTP is used.

The experiments confirmed this supposition. After the crystal replacement the fast oscillations amplitude during the first minutes of laser action decreased by a factor of 1.5 (maximum displacements were not more 20 arc sec). This result makes it possible to draw the conclusion that fast oscillations of laser beam axis during the first minutes of laser action are caused, mainly, by the process of SHG establishment.

The next stage of the experiments was extraction the nonlinear crystal off the cavity, after that the measurements were carried out on the fundamental radiation wavelength of 1064 nm. In this case the character of a slow angular displacement of the beam has been found to be kept. However, the frequency and amplitude of fast oscillations during the first minutes of laser action are drastically decreased. This difference in a character of fast oscillations of the beam energy center, perhaps, is caused by the process of SHG establishment process in the former case.

An external shock mechanical disturbances onto the laser head resulted in fast oscillations of the beam; their frequency correlated with frequency of shock disturbances. However, these disturbances did not result in variation of the character of

beam slow displacements. At the same time, the use of laser heads characterized by different heat sinking of parameters revealed the difference in the value of the total slow beam angular displacement from the original position. So, slow beam drift is caused, mainly, by the thermal processes.

Part II. Stabilization of laser beam

In this work we also have considered some ways of laser beam stabilization. For solution of this problem, in principle, can be used two possible approaches: use of intra-resonator or external means. There are two ways of control of laser beam angular position: use of passive or active stabilization. The latter uses the systems of an automatical regulation via feedback and may be realized, for instance, on the base of piezoceramics base [5] or on the base of a 2-coordinate acousto-optical deflector [6].

However, it should be note, that the active stabilization method has some significant disadvantages. Among them are the narrow range of the compensated angles of displacements (in the case of piezoceramics) as well as high cost and complicated equipment (in the case of acousto-optical deflector). That is why, it is very attractive to develop a passive stabilization system not having such disadvantages.

We propose here the simple, but efficient approach to the passive stabilization of the laser beam angular position which is based on the use of fiber-optical waveguides. The laser radiation near the output mirror is carried by the positive lens and focused on the input end of the fiber. In this case the stability of the laser beam, transmitted through the fiber, is determined by the stability of the fiber output end position. In the case when the collimating lens is used for the creation of the parallel beam at the output end of the fiber, the output beam stability is determined by this lens position stability. Such an approach needs not the use of an expensive equipment.

We have carried out the experiments, which have shown the possibility of this method realization in principle. We have studied the possibility to stabilize the axis angular position of beams of investigated lasers using this approach. In experiments we have used single-mode optical fiber (cutoff wavelength 470 nm, core diameter 5 μm , numerical aperture 0.1). At the fiber output end the sapphire microlens is mounted rigidly, excluding any possibility of its displacement with respect to the fiber. In this case, we have not observed the displacements of the laser beam transmitted through the fiber within the limits of our measurement apparatus accuracy.

One of disadvantages of this stabilization method is the intensity variation of the laser radiation, transmitted through the fiber, during first minutes after laser switching on, as well as the radiation power losses, that is inevitable in the case of the radiation input into the fiber. In our experiments we did not carry out the optimization of radiation coupling into the fiber. That is why, the power losses were about 70%. Though this parameter may be improved (for example, by 40 % as in work [7]), nevertheless, use of this stabilization method is limited. That is why, use of active stabilization of laser beams is still actual.

In the frames of this work we also have developed the stabilization system based on 2-coordinate acousto-optical deflector. This system has been builded, but yet not investigated. So, investiagation of this system will be subject of our future experiments.

4. CONCLUSIONS

Our work allowed to obtain experimental data about reasons, character and values of angular displacements of beams of cw, lamp-pumped, Nd:YAG lasers.

In particular, it was shown in experiments carried out, the basic destabilizing factors causing a beam pointing instability of lamp-pumped, frequency-doubled Nd:YAG lasers are the thermal deformations of the active element, transient processes induced by the establishment of second harmonic generation regime, thermal deformations of the resonator construction

and mirrors as well as the vibrations of the laser cavity elements (caused, in particular, by influence of a cooling agent on the active element).

In this paper we have described only preliminary results of our investigations in this field. To follow up this work we plan to carry out the experimental study of beam pointing instability caused by atmosphere turbulence. Moreover, laser beam stabilization by means of use of active system based on 2-coordinate acousto-optical deflector will be checked under natural (not laboratory) conditions. So, these experiments will be carried out and the results will be published later.

5. ACKNOWLEDGMENTS

Author of this work would like to thank Mr. S.N.Rodin for his assistance in the experiments.

REFERENCES

1. R.Foy, M.Tallon, M.Sechaud and N.Hubin, *Proceedings of SPIE*, Vol. 1114, P. 174-183 (1989).
2. Th.H.Jeys, A.A.Brailove, and A.Mooradian, *Applied Optics*, Vol. 28, No. 13, P. 2588-2591 (1989)
3. M.B.Danailov, and P.Apai, *J.Appl.Phys.*, Vol. 75, No. 12, P.8240-8242 (1994).
4. N.I.Kulikova, V.A.Perebyakin, I.Sh.Etsin, *Soviet Journal of Optical Technology*, No. 9 (1986).
5. S.V.Yakushkin et.al. *Pribory i tehnika experimenta*, No. 4, P. 147 (1987). (in Russian)
6. US Patent 4,637,725 1/1987.
7. T.Honda, H.Matsumoto, *Optics Letters*, Vol. 15, No.6, P.308-311 (1990).

"Effective outer scale of turbulence" for imaging through the atmosphere

Vladimir P. Lukin, Boris V. Fortes, Eugenii V. Nosov
Institute of Atmospheric Optics RAS, Tomsk, 634055, Russia

ABSTRACT

We discuss here some possibilities of introducing the distortions of an optical wave phase, propagating along vertical atmospheric path, as an integral characteristic, describing the turbulence along the path. Several models of the turbulence outer scale profile have been analyzed as well as the structural characteristic of the atmospheric refractive index fluctuations in order to find the value of the efficient outer scale. The error in the Strehl ratio determination was estimated. This ratio was computed using the efficient outer scale and compared to its value computed by the model profile of the outer scale.

Keywords: turbulence, outer scale, models, ground-based telescope, astronomy

The work on design of a large telescope requires the knowledge of its predictable characteristics including the information about parameters of a model¹ of height profiles of atmospheric turbulence such as turbulence intensity and the outer turbulence scale in the planned location of the telescope. These characteristics are the point spread function (PSF) and the efficient angular resolution.

One of the traditional ways to estimate the angular resolution of a designed telescope is to measure the parameters of the image (long-exposition PSF) obtained on a telescope of small diameter. However, the turbulent PSF of a small telescope will correspond to the PSF of a larger telescope if only the outer turbulence scale considerably exceeds the dimension of the telescope diameter in both cases. According to some experimental works² performed in different observatories throughout the world in recent years, this condition is broken for modern projects of telescopes with aperture dimensions of the order of 8–10 m (VLT 4×8 m, Keck 2×10). Saying about the outer scale one should keep in mind that this parameter changes with the height, i.e., it is necessary to use the information about measured parameters of the model of height profiles of atmospheric turbulence.

The influence of the outer scale on spatial and dynamic characteristics of the phase distortions for different models of the atmospheric turbulence spectrum in the region of low frequencies (i.e., large spatial scales) was considered in several papers.^{3–7} The possibility to introduce an efficient outer scale as an integral characteristic of turbulence is of great interest as it can permit one to change the height profile for the outer scale. One of the reasons to introduce this parameter is that the applicability of the models of height profiles of atmospheric turbulence is restricted due to their dependence on geographical location. It will also permit one to simplify mathematical calculations connected with the account for influence of the atmospheric turbulence on the phase of optical waves.

2. PARAMETERS OF THE MODEL OF HEIGHT PROFILES OF ATMOSPHERIC TURBULENCE

In this paper we consider some related problems: the principal possibility to introduce such a parameter, the class of problems in which it is worth to be applied, and the accuracy of description. We also study how the change of the height profile for the efficient outer scale influences the image parameters; in particular, we estimate the error in calculation of the Strehl parameter of a turbulent PSF by use of the efficient outer scale in comparison with the value obtained by calculation with respect to the model height profile of the outer scale.

Semiempirical profiles of turbulence intensity $C_n^2(h)$ corresponding to the best

$$C_n^2 = (h[\text{km}]) = 5.19 \cdot 10^{-16} \cdot 10^{-0.86h} + 10^{-18.34+0.29h-0.0284h^2+0.000743h^3}$$

and the worst

$$C_n^2 = (h[\text{km}]) = 9.50 \cdot 10^{-14} \cdot 10^{-2.09h} + 10^{-14.39+0.17h-0.0348h^2+0.000959h^3}$$

vision conditions were taken from Ref. 8.

At present, there exist a lot of models of height profiles $L_0(h)$. Some models chosen for the study are presented below:

$$(A) \quad L_0(h) = \begin{cases} 0.4, & h \leq 1m, \\ 0.4h & h > 1m, \end{cases}$$

$$(B) \quad L_0(h) = \begin{cases} 0.4, & h \leq 1m, \\ 0.4h & 1 < h \leq 25m, \\ 2\sqrt{h}, & h > 25m, \end{cases}$$

$$(C) \quad L_0(h) = \begin{cases} 0.4, & h \leq 1m, \\ 0.4h & 1 < h \leq 25m, \\ 2\sqrt{h}, & 25 < h < 1000m, \\ 2\sqrt{1000}, & h > 1000m, \end{cases}$$

$$(D) \quad L_0(h) = \frac{5}{1 + \left[\frac{h - 7500}{2000} \right]^2}$$

$$(E) \quad L_0(h) = \frac{5}{1 + \left[\frac{h - 500}{2500} \right]^2}$$

The model (A) is recommended in Ref. 9 for small heights, (B) is proposed by D.L. Fried,^{1,10} and (C) is a generalization of (A) and (B). The model (A) was not studied in this paper because of the limitedness of its applications. The models (D) and (E) are obtained by generalizing results of measurements performed in the USA, France, and Chile.^{1,11,12}

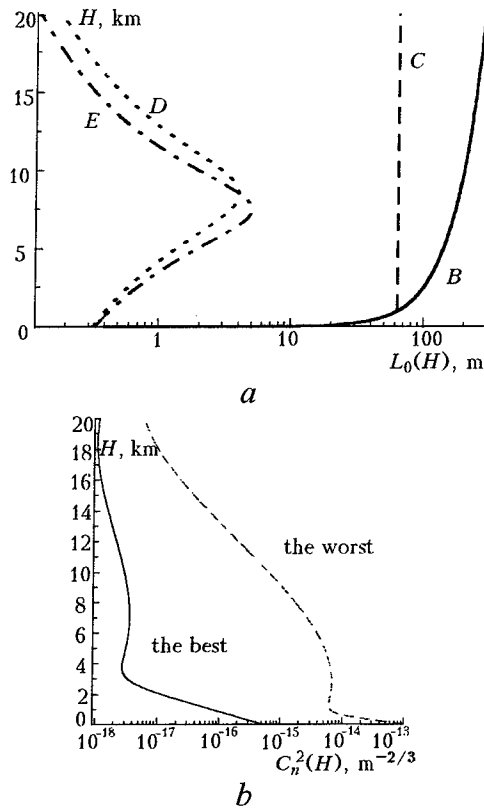


FIG. 1. The height profiles of the outer scale $L_0(h)$ (a) and turbulence intensities $C_n^2(h)$ (b).

The vertical profiles corresponding to these models are presented in Fig. 1. As one can see, the graphs (D) and (E) are similar in the character of growth and the presence

of the maximal value at a certain finite height; so one can study one of the models and generalize the obtained results for the second. Here we chose the model (D). By the same criteria, it is possible to choose one model from (B) and (C), let it be the model (C).

3. THE EFFICIENT OUTER SCALE OF ATMOSPHERIC TURBULENCE. DETERMINATION METHODS.

We propose two methods for determining the effective outer scale, namely, by the discrepancy between structure functions of phase fluctuations and by the saturation level.

3.1. Determination by the discrepancy

To determine the effective outer scale by this model, minimization of the integral square discrepancy of structure functions of phase fluctuations

$$\Delta(L_0) = \int_0^{\rho_{\max}} d\rho [D_\varphi(\rho L_0) - D_\varphi(\rho, L_0(h))]^2$$

is used. Here $D_\varphi(\rho, L_0(h))$ is the structure function of phase fluctuations corresponding to the height profile of the outer scale $L_0(h)$, $D_\varphi(\rho, L_0)$ is the function corresponding to the constant value of the outer scale L_0 . The variable ρ_{\max} depends on the studied range (Fig. 2) and has a value of either 10 m (what corresponds to the largest diameter of existing telescopes) or $\text{Arg}(90\%)$, i.e., the argument at which the structure function reaches 90% of the saturation level.

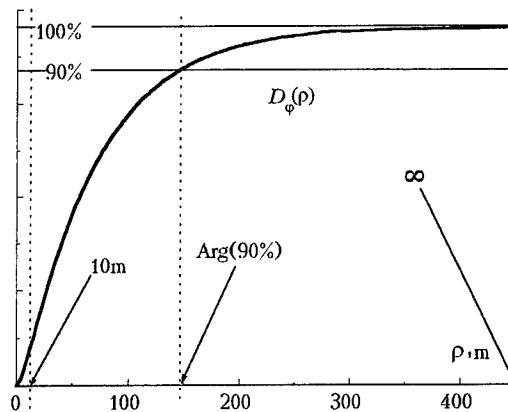


FIG. 2. Variants of introducing ρ_{\max} .

The structure function was calculated by modified von Karman spectrum of atmospheric turbulence

$$_n(\kappa, \xi) = 0.033 C_n^2(\xi) (\kappa^2 + L_0^{-2}(\xi))^{-11/6},$$

where ξ is the current coordinate along the propagation path; for the case of a vertical path $\xi = h$, where h is the height over the underlying surface.

The discrepancy introduced in such a way defines the divergence degree for two structure functions. The value of the outer scale L_0^* , at which the discrepancy $\Delta(L_0)$ is minimal will be called the effective outer scale of atmospheric turbulence.

3.2. Determination by the Saturation Level

The name of the method is directly derived from the fact that the value of argument at which the structure function saturates is taken as the upper boundary of the range studied

$$L_0^* = \left[\int_0^\infty L_0^{5/3}(h) C_n^2(h) dh / \int_0^\infty C_n^2(h) dh \right]^{3/5}$$

The results presented below indicate that the method is close to the determination by discrepancy $[0 \dots \text{Arg}(90\%)]$ in its characteristics.

4. Comparison of the Results

We shall only comment the results of applying the method $[0 \dots 10 \text{ m}]$ to the profile (C) since other methods and profiles have qualitatively similar results.

Figure 3a presents the graph of the structure function corresponding to the profile $L_0(h)$ – (C) together with the family of structure functions calculated using some constant values of the outer scale. One can assume that there exists certain value L_0^* at which the functions $D_\varphi(\rho, L_0^*)$ and $D_\varphi(\rho, L_0(h))$ (model of outer scale of turbulence is (C)) are most close. Figure 3b demonstrates that this assumption is true, namely, the minimum corresponding to the value $L_0^* \approx 32.5 \text{ m}$ is shown by the dashed line. Comparing the curves $D_\varphi(\rho, L_0(h))$ (model – (C)) and $D_\varphi(\rho, L_0^* = 32.5 \text{ m})$ in Fig. 3c, we see their similarity indicating the efficiency of the method for the profile $L_0(h)$ – (C).

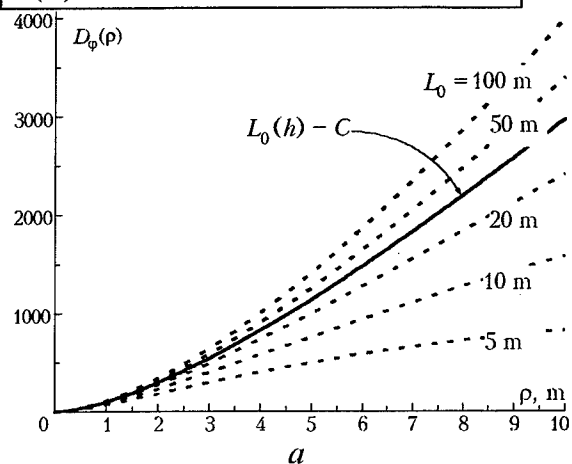
The results of calculation of L_0^* (in meters) by the above-mentioned methods for different models of $L_0(h)$ and $C_n^2(h)$ are presented in Tables I and II.

TABLE I.

Model $L_0(h)$	$C_n^2(h)$ – the best		
	Method		
	0...10 m	0...Arg(90 %)	0...∞
(B)	34.7	50.6	58.4
(C)	32.5	39.9	42.9
(D)	0.60	0.66	0.71
(E)	0.68	0.75	0.84

TABLE II.

Model $L_0(h)$	$C_n^2(h)$ – the worst		
	Method		
	0...10 m	0...Arg(90 %)	0...∞
(B)	55.4	88.5	98.0
(C)	40.6	49.3	52.3
(D)	1.04	1.13	1.78
(E)	1.31	1.46	1.56



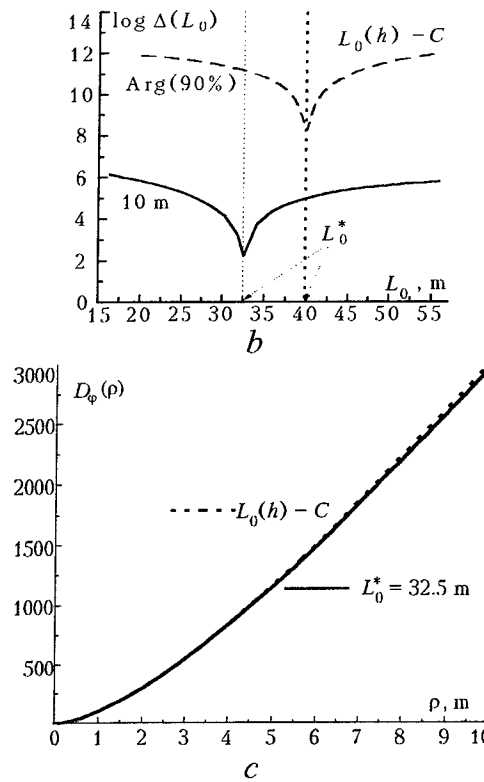


FIG. 3. The structure function for the profile (C) and the family of structure functions calculated for fixed values of $L_0(h)$. Discrepancy in the method [0...10 m] and the method [0...Arg(90%)] (b). The structure function for the profile $L_0(h) - C$ and for the corresponding effective external scale $L_0^* - (C)$.

4.1. Comparison of the methods

Analysis of the value L_0^* obtained by different methods for the same height profile $L_0(h)$ demonstrates that its growth

$$\text{i.e., } L_0^*[0...10 \text{ m}] < L_0^*[0...Arg(90\%)] < L_0^*[0...\infty]$$

is caused by the necessity to compensate for increasing influence of the $D_\varphi(\rho, L_0(h))$ portions at large argument values with the increase of $\rho_{\max} r_{\max}$

$$(\text{i.e., } \rho_{\max}[0...10 \text{ m}] < \rho_{\max}[0...Arg(90\%)] < \rho_{\max}[0...\infty]).$$

To reduce the increased discrepancy, i.e., to reduce the area between two structure functions, it is necessary "to lift" the structure function $D_\varphi(\rho, L_0^*)$ to the structure

function $D_\varphi(\rho, L_0(h))$. And Fig. 3a demonstrates that the "lift" of $D_\varphi(\rho, L_0^*)$ occurs with the increase of the value L_0^* .

4.2. Comparison by the models of $\chi_n^2(h)$ used

Studying the dependence of the value L_0^* on the model of $\chi_n^2(h)$ one can say that lower value of L_0^* for the "best" vision conditions is caused by essential distinctions in the behavior of $\chi_n^2(h)$. As one can see in Fig. 1b, that the "best" profile $\chi_n^2(h)$ rapidly falls off with the growth of height, and the probability of appearance of large-scale fluctuations diminishes. This leads to the decrease of the structure function and L_0^* .

4.3. Comparison by the models of $L_0(h)$ used

The considerable difference between the value L_0^* for the models $L_0(h)$ – (model C) and $L_0(h)$ – (model D) can be explained by the following reasoning. The characteristic property of the model $L_0(h)$ – (model D) is the presence of a finite maximal value of L_0 followed by its decrease at heights above 7–8 km (see Fig. 1a), so the appearance of larger scales is impossible. At the same time, the growth of L_0 with the height is inherent in the model $L_0(h)$ – (model C) what increases the influence of large-scale fluctuations and, consequently, one can expect the growth of $D_\varphi(\rho, L_0(h))$ what finally leads to the increase of L_0^* .

5. CONCLUSION

In the final analysis one can arrive at the following conclusions.

1. One can introduce the effective outer scale of turbulence as an integral parameter describing the character of atmospheric turbulence along the whole propagation path.
2. Introduction of the effective outer scale can considerably simplify mathematical calculations connected with the account for the influence of atmospheric turbulence on the phase of optical wave propagated along vertical atmospheric paths.
3. The description accuracy studied demonstrate that the error caused by the change of the height profile of the outer scale for a constant value, i.e., the effective outer scale, considerably varies depending both on the model of a parameter profile and the method of determination.
4. The error in determination of the Strehl parameter does not exceed 16% in the situation when the effective outer scale is larger than the diameter of a telescope.

REFERENCES

1. R.E. Good, R.R. Beland, E.A. Murphy, J.H. Brown, and E.M. Dewan, "Atmospheric models of optical turbulence", SPIE Proc. **928**, pp.165–186, 1988.
2. T. Stewart McKeckney, "Atmospheric turbulence and the resolution limits of large ground-based telescopes", J. Opt. Soc. Am. A **9**, pp. 1937–1954, 1992.
3. V.P. Lukin, "Optical measurements of the outer scale of atmospheric turbulence", Atmos. Oceanic Opt. **5**, pp. 229–242, 1992.
4. V.P. Lukin, "Investigation of some peculiarities in the structure of large-scale atmospheric turbulence", Atmos. Oceanic Opt. **5**, pp. 834–840, 1992.
5. V.P. Lukin, "Intercomparison of models of the atmospheric turbulence spectrum", Atmos. Oceanic Opt. **6**, pp. 628–631, 1993.
6. V.V. Voitsekhovich, J. Opt. Soc. Am. A **12**, pp.1346–1353, 1995.
7. V.V. Voitsekhovich and S. Cuevas, J. Opt. Soc. Am. **12**, pp.2523–2531, 1995.
8. A.S. Gurvich and M.E. Gracheva, "Simple models of turbulence", Izv. Akad. Nauk SSSR, Fiz. Atmos. Okeana, No. 10, pp.1107–1111, 1980.
9. V.I. Tatarskii, *Wave Propagation in the Turbulent Atmosphere*, Nauka, Moscow, 1967.
10. D.L. Fried, Proc. IEEE **55**, No. 1, 1967.
11. C.E. Coulman, J. Vernin, Y. Coquegniot, and J.L. Caccia, Appl. Opt. **27**, pp.155–160, 1988.
12. "Site Testing for the VLT. Data Analysis Part I", European Southern Observatory, VLT Report, No. 55, 1987.
13. A. Ishimaru, *Wave Propagation and Scattering in Random Media*, Academic Press, New York, 1978.
14. V.P. Lukin, E.V. Nosov, and B.V. Fortes, "Effective Outer Scale of Atmospheric Turbulence", in: *Abstracts of Reports at the Third Interrepublic Symposium on Atmospheric and Oceanic Optics*, Tomsk, pp. 31–33, 1996.
15. V.P. Lukin, E.V. Nosov, and B.V. Fortes, in: *Abstracts of Reports at the Third Interruption Symposium on Atmospheric and Oceanic Optics*, Tomsk, pp. 33–34, 1996.
16. V.P. Lukin, E.V. Nosov, and B.V. Fortes, "Effective Outer Scale of Atmospheric Turbulence", Atmos. Oceanic Opt. **10**, pp. 162–171, 1997.

Method for Fast Computation of Infrared Radiation from Heated Turbulent Jets Viewing through Thick Atmosphere Layers

Andrey Bril, Vitaliy Kabashnikov, Yuriy Khodyko, Natalya Kuzmina
Institute of Physics Belarus Academy of Sciences, Minsk, Belarus, 220072

ABSTRACT

The simple effective method for computing the spectral thermal radiation intensity from jets of hydrocarbon fuel combustion products viewing through thick atmosphere layers is proposed. The method is based on 1) similarity of radiation characteristics of optically thin turbulent jets and 2) three-group approximation. The first approach can be used because jet radiation filtered by sufficiently thick atmospheric layer is concentrated mainly at frequencies where radiating volume is optically thin. Within three-group approximation developed for radiation transfer calculation in molecular rotational-vibrational bands the lines in each spectral interval are approximated by several (up to 3) groups of lines with the same lower energy levels. This allows one to account for the contribution of so called "hot" lines that arise due to transitions between excited states and are weakly absorbed in low temperature atmosphere.

Keywords: heat radiation, hydrocarbon fuel combustion products, turbulent jets, atmospheric propagation.

1. INTRODUCTION

The infrared radiation of combustion products is formed mainly by molecules of H_2O , CO_2 , SO_2 , CO , NO , and other minor impurities including particles of soot. Typically, the concentrations of soot, sulphur oxide, carbon and nitrogen oxides, etc. are so small that their radiation is actually volumetric, i.e. the radiation intensity is proportional to local radiation emissivity integrated over the volume of the jet. But as a rule it is not correct for H_2O and CO_2 that are the main combustion products of hydrocarbon fuels. The radiation of H_2O and CO_2 is mainly concentrated in rotational-vibrational bands, formed by partially overlapped spectral lines. The spectral optical thickness of the radiating volume changes sharply within the band limits. In the gaps between the spectral lines, it is much less unity, while at the line centers it may significantly exceed the unity. It is natural that the radiation of the jet is not volumetric in this case.

However, often it is not the original radiation of the jet is of interest, but the radiation passing through the atmosphere. Atmospheric transparency is also determined to a large extent by water vapour and carbon dioxides. Further, the atmospheric absorption spectra of H_2O and CO_2 strongly correlate with the radiation spectra of these gases. Owing to atmospheric H_2O and CO_2 , the jet radiation is primarily absorbed in the spectral regions with the greatest optical thickness, namely in the band and spectral line centers. As a result only the radiation in the wings of the bands and lines reaches a receiver positioned at a sufficiently large distance from the source. The radiation filtered by the atmosphere is concentrated mainly at frequencies where the radiating volume is optically thin. Because of this only the optically thin case is considered in this paper.

A primary condition for an optical similarity is the gasdynamic similarity of flows. The similarity of gasdynamic characteristics in the far field of jet flows is the well-known fact. However, the main portion of thermal radiation is generated by the most heated near-nozzle section of a jet (near field). In the near field the flow depends strongly on a number of uncertain or poorly measured initial parameters, in particular, on the initial level of turbulence kinetic energy. Nevertheless it was shown that for the near field of non-buoyant jets some universal relationships for the gasdynamic parameters are approximately valid if we use special longitudinal scale X_T .

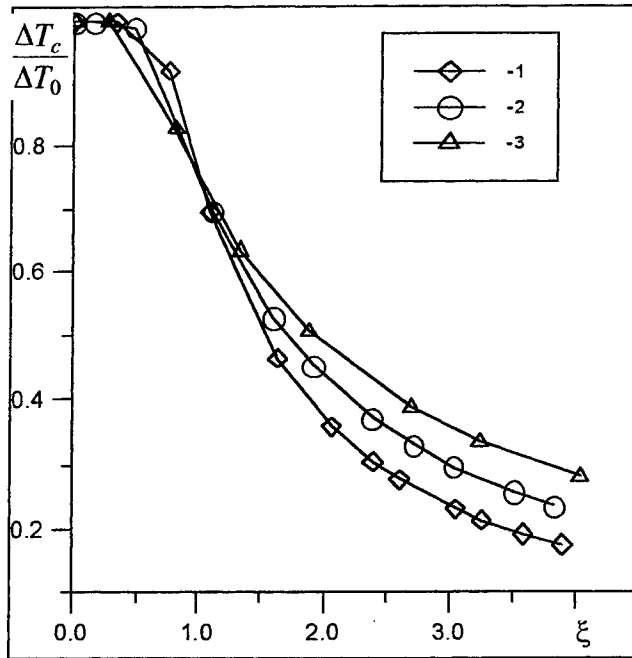


Fig. 1. Dependence of the excess temperature on the dimensionless axial coordinate of a non-buoyant jet for various initial levels of turbulence. 1, $k_0 = 0.0022 U_0^2$; $\varepsilon_0 = 0.0003 U_0^3/D$; 2, 0.01; 0.0014; 3, 0.04; 0.0074

It was shown previously^{1,2} on the basis of experimental and numerical investigations, that distributions of temperature and concentration for non-buoyant round jets in a wide range of initial flow parameters can approximately be reduced to unified relationships:

$$\frac{T(x, r) - T_\infty}{T_0 - T_\infty} = \frac{C(x, r) - C_\infty}{C_0 - C_\infty} = f(\xi, \eta), \quad R_T = R_T(\xi) \quad (1)$$

where x and r are the cylindrical coordinates, $\xi = x/X_T$, $\eta = r/R_T$, X_T is equal to the value of X at which $\Delta T_c = 0.75 \Delta T_0$, and R_T is equal to the value of r at which the excess temperature is half of its axial value. The longitudinal scale X_T depends on the initial parameters of the flow (ρ_0/ρ_∞ , initial level of turbulent kinetic energy k_0 , etc.).

Recently³ the relationships of an optical similarity was generalised for vertical buoyant jets. It was shown that we can introduce previously defined characteristic scales (longitudinal and radial)

$$X_T = X_T(k_0, F), \quad R_T = R_T(\xi, F), \quad (2)$$

which now depend on single additional parameter, Froude number F , and it allow us to use the approximate relations (1), describing excess temperature and concentration profiles for buoyant vertical jets.

As an example the longitudinal profiles of $\Delta T_c(\xi)/\Delta T_0$ for non-buoyant jets, corresponding to three initial values of the turbulent kinetic energy varied by using replaceable conic nozzles are presented in Fig. 1⁴. Calculations for non-buoyant jets were carried out using the k - ε model proposed by Launder⁵. The values of k_0 and ε_0 used for calculations were selected on the basis of the best agreement between experimental and calculated profiles of temperature and concentration. The normalisation of the longitudinal coordinate using X_T also allows one to reduce the axial profiles of the excess temperature approximately to a universal function of ξ for a wide range of change in the Froude number F (Fig. 2).

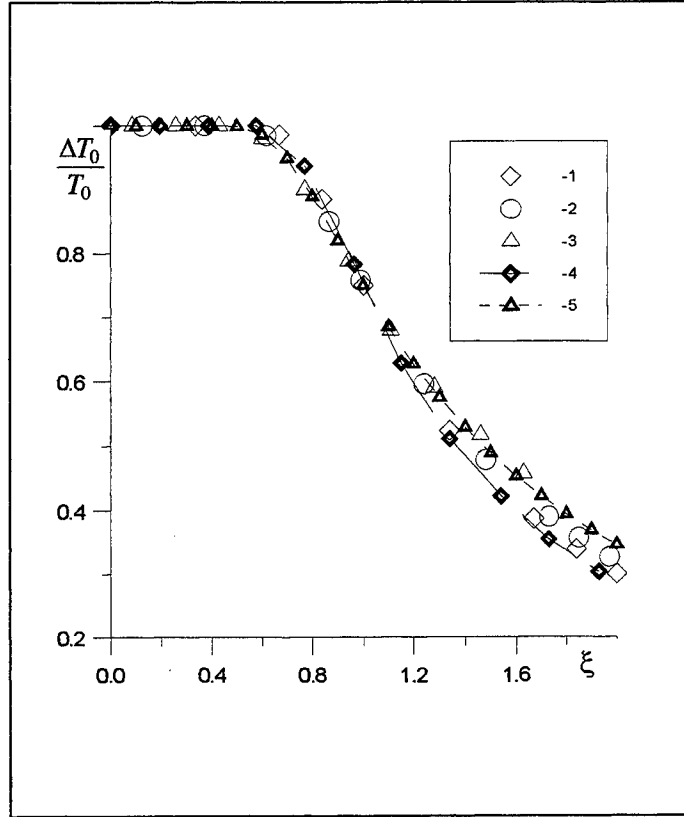


Fig. 2. Dependence of the excess temperature on the axial coordinate for various values of the Froude number. 1, 4, $F = 1$; 2, $F = 5$; 3, 5, $F = 50$. 1-3 correspond to calculation with the use of the Boussinesq approximation, and 4 and 5 — to calculation without using of this approximation.

2. THERMAL RADIATION SIMILARITY

We consider thermal monochromatic radiation of a jet with one optically active component and assume that the background radiation is the Planck radiation with the temperature T_∞ . Within a optically thin approximation the contrast radiance of the jet in the direction perpendicular to the jet symmetry axis is determined by the expression

$$I(x, y) = 2\tau \int_y^\infty \frac{rdr}{\sqrt{r^2 - y^2}} [B(T) - B(T_\infty)] k_{STP}(T) \frac{300}{T} C(r, x), \quad (3)$$

where y is the distance between the line of sight and the jet axis; B is the Planck function; k_{STP} is the gas absorption coefficient, reduced to the standard temperature and pressure; τ is atmosphere transmittance. Here, the indices that indicate the radiation frequency are omitted for simplicity. Note that volumetric concentration should be used in expression (3), whereas similarity relations (1) are satisfied for mass concentrations. However, Eq. (1) are also valid for volumetric concentrations if an average molecular weight of a flowing-out gas mixture is approximately equal to the ambient one. This usually holds for exhaust jets with a large amount of excess air.

Along with gasdynamic similarity the unified temperature dependence of the absorption coefficient at all the frequencies and for all the radiative components is needed for optical similarity. This dependence can be presented by the following approximate expression that is valid over a wide range of temperatures

$$\frac{300}{T} k_{STP} = \theta \exp\left(-\frac{a}{T}\right), \quad (4)$$

where a and θ are the parameters that depend on frequency and on the type of radiative component. The radiation intensity of the near outlet jet section with the length x is given by the expression

$$S(x) = 2 \int_0^x dx \int_0^\infty dy I(x, y). \quad (5)$$

If the values R_T and X_T are normalized with respect to the nozzle radius R_0 the following relations take place in the Wien spectra region

$$S(x) = I_0 X_T(k_0, \varepsilon_0, F) R_0 G\left(\xi, F, \frac{a}{T_0}, \frac{h\nu}{T_0}, \frac{\Delta T_0}{T_0}, \frac{\Delta C_0}{C_0}\right), \quad (6)$$

where

$$\begin{aligned} I_0 &= 2R_0 C_0 k_{STP}(T_0) \frac{300}{T_0} [(B(T_0) - B(T_\infty))] = \\ &= 2R_0 C_0 q \left(e^{-\frac{b}{\kappa T_0}} - e^{-\frac{b}{\kappa T_\infty}} \right) e^{-\frac{a}{\kappa T_0}}, \end{aligned} \quad (7)$$

$$G = \left(1 - \frac{\Delta C_0}{C_0}\right) G_0 + \frac{\Delta C_0}{C_0} G_1, \quad (8)$$

$$\begin{aligned} G_k &= \left[g_k\left(\xi, F, \frac{A}{T_0}, \frac{\Delta T_0}{T_0}\right) - \exp\left(-\frac{b\alpha(1)}{T_0}\right) \cdot g_k\left(\xi, F, \frac{a}{T_0}, \frac{\Delta T_0}{T_0}\right) \right] \cdot \\ &\quad \left[1 - \exp\left(-\frac{b\alpha(1)}{T_0}\right) \right]^{-1}, (k = 0, 1), \end{aligned} \quad (9)$$

$$g_k\left(\xi, F, p, \frac{\Delta T_0}{T_0}\right) = \pi \int_0^\xi R_T^2(\xi, F) d\xi \int_0^\infty \eta d\eta f^k \exp[-p\alpha(\varphi)], (k = 0, 1), \quad (10)$$

$$\alpha(\varphi) = t\varphi / (1 - t\varphi), \quad t = \frac{\Delta T_0}{T_0}, \quad \varphi = 1 - f(\xi, \eta), \quad (11)$$

where $A=a+b$, $b = hc\nu/k$, $q = 2hc^2 \nu^3 \theta$, ν is the radiation frequency expressed in reciprocal centimeters, h is Planck's constant; here, k is Boltzmann's constant, c is the speed of light, $f(\xi, \eta)$ is defined by Eq.(1).

Thus, the jet radiation intensity can be written using two universal functions g_0 and g_1 , each being dependent on four arguments. Considerable simplifications take place, however, in some limiting practically important cases.

i) If the outlet concentration of the radiating gas greatly exceeds that of the ambient gas ($C_\infty/C_0 \ll 1$), the jet radiation intensity is determined only by the function g_1 .

ii) If the Planck function at jet temperature significantly exceeds the background radiance ($b\alpha(1)/T_0 \gg 1$), we have

$$G_k = g_k\left(\xi, F, \frac{A}{T_0}, \frac{\Delta T_0}{T_0}\right). \quad (9')$$

iii) It follows from (10) that the magnitude of $t\phi$ can be neglected in the denominator of the expression for $\alpha(\phi)$ (11) if the jet temperature is low enough ($t \ll 1$) or if the parameter $p \gg 1$. As a result, the number of arguments of functions g_k is reduced to three:

$$g_k = g_k(\xi, F, pt). \quad (12)$$

All the three cases mentioned occur simultaneously in the short-wave region of the spectrum in the absence of the radiative component in the ambient air. Then the radiation intensity of the jet can be expressed by

$$G = g_1\left(\xi, F, \frac{A\Delta T_0}{T_0^2}\right). \quad (13)$$

Optical similarity relations established previously for non-buoyant jets^{1,2} follow from (6) - (11) as a particular case under the condition $F \rightarrow \infty$.

Expressions (6) - (13) can be proposed for the development of the optical diagnostic techniques. The radiation intensity of the near nozzle jet section depends on the magnitudes of k_0 and ε_0 . As a rule, they are unknown and, therefore, the optical signal carries uncertain information. But if only X_T depends strongly on k_0 and ε_0 and the dependence of $R_T(\xi)$ and $f(\xi, \eta)$ on these parameters can be neglected, the ratio of spectral intensities for different frequencies does not depend on the initial turbulence level and can be used for estimating of the temperature or the ratio of the concentrations for different components.

3. THERMAL RADIATION OF MOLECULAR GAS JETS

The jet radiation averaged over the finite spectral interval $\Delta\nu \sim 10 - 50 \text{ cm}^{-1}$ is often of main interest. In the case of molecular gas emission that interval contains a great quantity of spectral lines. The frequency averaged radiation is often calculated by using the statistical band model which implies that the frequency averaging can be replaced by the averaging over the positions of spectral lines^{6,7}. We used the three-group method⁸, based on the statistical band model, to estimate the frequency-averaged radiation. The AFGL⁹ spectral line compilation was used as input data to obtain the group parameters. The application of this method is especially effective for gases presented in both the jet and the atmosphere (H_2O and CO_2) because it takes into account "hot lines" that arise between high energy levels and that experience only slight absorption in the atmosphere.

In the three-group method the lines in each spectral interval $\Delta\nu$ are approximated by three groups of lines with the same lower energy levels and the same intensity within each group. A position of each line is random and statistically independent of the lines of both the same and other gases. The temperature dependence of the absorption coefficient stipulated by the lines of one group is approximately the same for all the frequencies within the spectral interval, since it is defined mostly by the energy of the lower level. So, the effective radiation volume G for the lines of one group does not depend on frequency and only the production of the atmosphere transmittance and jet absorption coefficient has to be averaged. The Curtis-Godson approximation^{6,8} is used to take into account the radiation path non-uniformity. We have

$$\begin{aligned}
\overline{k_v \tau} &= \overline{\left(\sum_{m,n} k_{mn} \right) \left(\prod_{k,l} \tau_{kl} \right)} = \sum_{m,n} \overline{k_{mn} \tau_{mn}} \prod_{\substack{k \neq m \\ l \neq n}} \overline{\tau_{kl}} = \\
&= \sum_{m,n} \overline{k_{mn} H_{mn} \tau_{mn}} \prod_{\substack{k \neq m \\ l \neq n}} \overline{\tau_{kl}} = \left(\prod_{k,l} \overline{\tau_{kl}} \right) \sum_{m,n} \overline{k_{mn} H_{mn}} = \\
&= \overline{\tau} \sum_{m,n} \frac{S_{mn}(T)}{d_{mn}} H_{mn}(T),
\end{aligned} \tag{14}$$

where the bar designates the frequency averaging, m is the line group number, n is the radiating substance number; τ_{mn} and k_{mn} are atmosphere the transmittance and absorption coefficient stipulated by mn group of the spectral lines. The quantity $\overline{\tau}$ is the spectral atmospheric transmittance with respect to a grey source; S_{mn} is the spectral line intensity, and d_{mn} is the mean spacing between the lines of the mn group.

$$\overline{\tau_{mn}} = \exp \left[-A_{mn} (1 + A_{mn}^2 / B_{mn})^{-1/2} \right], \tag{15}$$

$$A_{mn} = \int_0^L S_{mn}(x) d_{mn}^{-1} dx, \tag{16}$$

$$B_{mn} = 4 \int_0^L S_{mn}(x) \gamma(x) d_{mn}^{-2} dx, \tag{17}$$

γ is the Lorentz line half-width. The integrals in Eqs. (16) and (17) are taken along the atmosphere path with the length L between the jet and a receiver; H_{mn} is the frequency correlation between jet radiation and atmospheric absorption stipulated by the mn group of the spectral lines:

$$H_{mn}(T) = \left(1 + \frac{2\gamma(T)}{d_{mn}} \frac{A_{mn}^3}{B_{mn}^2} \right) \left(1 + \frac{A_{mn}^2}{B_{mn}} \right)^{-3/2}. \tag{18}$$

In Eq.(24) the line intensity $S_{mn}(T)$ varies directly as the n -gas concentration and depends on the jet temperature. The function $H_{mn}(T)$ depends on the jet temperature only by means of the line half-width. Taking into account Eq.(24), we can write the spectral radiation intensity of the circular jet as

$$\begin{aligned}
\overline{S}(\xi) &= 2R_0^2 X_T \overline{\tau} [B(T_0) - B(T_\infty)] \cdot \\
&\sum_{m,n} C_{0n} \frac{S_{mn}^{STP}(T_0)}{d_{mn}} \frac{300}{T_0} H_{mn}(T_0) G \left(\xi, F, \frac{a_{mn}}{T_0}, \frac{b}{T_0}, \frac{\Delta T_0}{T_0}, \frac{\Delta C_{0n}}{C_{0n}} \right),
\end{aligned} \tag{19}$$

where a_{mn} is an analogue of the constant a from Eq. (4):

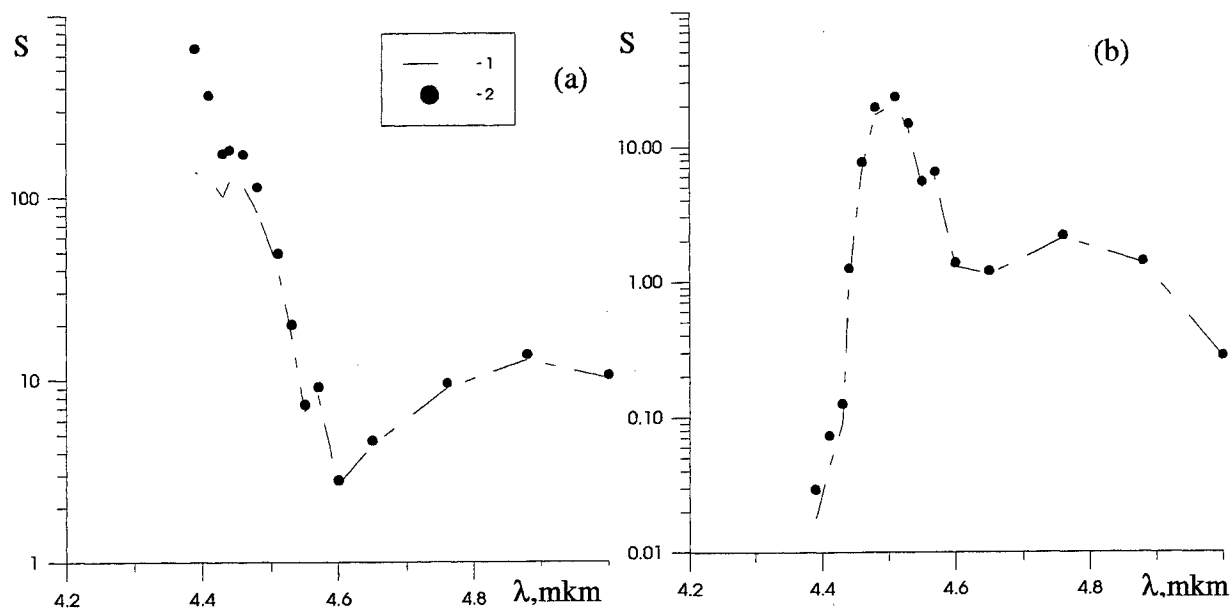


Fig. 3. Spectral distribution of radiation intensity ($W/\mu m sr$) of the jet near-nozzle section for viewing distances of 200 m (a) and 10 km (b). 1, calculations on the basis of numerical integration over the jet area¹⁰; 2, calculations with the use of the optical similarity relationships.

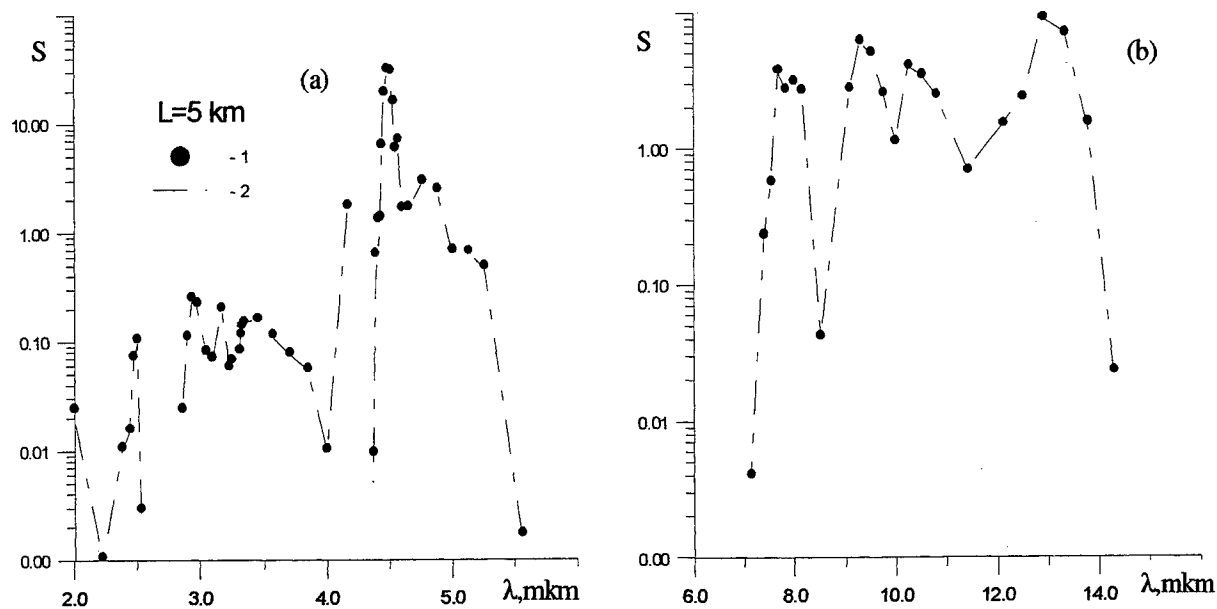


Fig. 4. Spectral distribution radiation intensity ($W/\mu m sr$) of a jet near-nozzle section for the viewing distance of 5 km. 1, calculations on the basis of numerical integration over the jet area¹⁰; 2, calculations with the use of the optical similarity relationships.

$$a_{mn} = T_0^2 \frac{d}{dT_0} \ln \left\{ \frac{S_{mn}^{STP}(T_0)}{d_{mn}} \frac{300}{T_0} \right\}. \quad (20)$$

As H_{mn} depends only slightly on the temperature, we used in Eq. (19) the constant value $H_{mn}(T_0)$ which is close to the magnitudes of H_{mn} in the jet region giving main contribution into the value of the integral (5).

Direct computation of the values of G using Eqs. (18)-(21) requires the knowledge of the functions $f(\xi, \eta)$ and $R(F, \xi)$. It is more convenient to estimate values g_k ($k=0,1$) by numerical integration of the expression $C^k(x, r) \exp[-A/T(x, r)]$ over the jet volume followed by normalisation of the result with respect to the expression $2R_0^2 X_T C_0^k \exp(-A/T_0)$. The values of g_1 computed by this method at $\xi = 2$ are presented in Table 1 for three Froude numbers.

The spectral intensity of radiation emitted by a buoyant jet containing only water vapour and carbon dioxide was calculated by two methods. The first (traditional) method¹⁰ includes calculation of the jet concentration and temperature fields followed by numerical integration over the jet surface area of the spectral radiance that passed through the atmosphere. The second method is based on the use of Eq. (19) and the effective radiation volume data from Table 1.

Table 1. The Values of the Effective Radiating Volume Determined Numerically.

F	$\Delta T_0/T_0$	A/T_0								
		1	2	4	6	8	10	15	20	25
1	0.2	2.77	2.48	2.02	1.68	1.43	1.25	0.95	0.78	0.67
	0.3	2.58	2.17	1.62	1.27	1.06	0.91	0.70	0.59	0.53
	0.4	2.37	1.88	1.31	1.01	0.84	0.73	0.58	0.51	0.47
	0.45	2.27	1.74	1.19	0.92	0.77	0.67	0.55	0.49	0.45
5	0.2	3.19	2.84	2.30	1.90	1.61	1.40	1.05	0.86	0.74
	0.3	2.96	2.48	1.82	1.43	1.18	1.01	0.77	0.64	0.57
	0.4	2.71	2.13	1.46	1.12	0.93	0.80	0.63	0.55	0.50
	0.45	2.59	1.97	1.32	1.02	0.84	0.74	0.59	0.52	0.47
50	0.2	3.91	3.47	2.78	2.28	1.91	1.63	1.18	0.93	0.78
	0.3	3.62	3.01	2.18	1.67	1.35	1.13	0.82	0.66	0.57
	0.4	3.31	2.58	1.72	1.28	1.02	0.86	0.64	0.54	0.48
	0.45	3.15	2.38	1.54	1.14	0.91	0.78	0.59	0.50	0.45

The comparison was carried for a vertical jet with the following outlet parameters: $T_0 = 475$ K, $D=2$ m, $C_0(\text{CO}_2)=C_0(\text{H}_2\text{O})=0.04$. The atmosphere parameters were chosen in the following manner: $T_\infty = 273$ K, $C_\infty(\text{CO}_2) = 0.00033$, atmospheric pressure was 1 atm, humidity was 80%. In the case under consideration we can neglect the content of CO_2 and H_2O in the atmosphere and put $G = g_1$.

The validity limits of the optically thin approximation were given previously¹¹. The approach based on Eq.(19) may bring a large error in the spectral regions where the optically thin approximation is violated. It can take place in the absorption bands of the main combustion products of the hydrocarbon fuels CO_2 and H_2O if the distance of viewing is not large enough. As it is seen from Fig.7, where the jet spectral intensity in the $4.3 \mu\text{m}$ band of CO_2 is presented, the result based on Eq.(19) differs considerably from the exact one¹⁰ at relatively small distance of 200 m (see Fig.3a). But the "non-volumetric" portion of radiation is absorbed by the atmosphere and the discrepancy between the exact method¹⁰ and the approximation based on Eq.(19) becomes smaller as the viewing distance increases. It can be seen from Fig.3b where the results for the distance of 10 km are presented. Similar comparison is shown in Fig. 4 for the spectral range $2-14 \mu\text{m}$ at the atmosphere layer of 5 km thick. The discrepancy between the two calculation techniques does not exceed 20

or 30%. F noticeable difference (up to 100%) is observed only in the narrow spectral interval in the region of the CO₂ 4.3 μ m band.

Thus the method based on Eq.(19) reduces the computational expenditures considerably and provides a reasonable accuracy in the prediction of the thermal radiation of non-buoyant and buoyant turbulent jets. The method does not require a detailed information about the jet gas dynamics structure and gives simple relation between the jet radiation intensity and the outlet jet parameters.

ACKNOWLEDGEMENT

This work was partially supported by International Science Foundation and the Government of the Republic of Belarus under the grant #F95100.

REFERENCES

1. I.Yu.V. Belyayev, A.N. Kuzmin, O.B. Zhdanovich, and Yu.V. Khodyko, "Experimental verification of optical similarity of heated molecular jets", *High Temperature* **29**, pp.961-966, 1991.
2. A.I. Bril , V.P. Kabashnikov, and Yu.V. Khodyko, "The similarity of the radiation properties of heated jets", *High Temperature* **29**, pp. 995-1001, 1991.
3. A. I. Bril, V. P. Kabashnikov, N. V. Kuzmina, and V. M. Popov, "Similarity of heat radiation from turbulent buoyant jets", *Int. J. Heat&Mass Transfer* (to be printed).
4. Yu.V.Khodyko, A. I. Bril and O.B. Zhdanovich, Utilization of model passive impurity concentration distribution functions to compute turbulent flow radiation, *J. of Eng. Phys.* **57**, pp. 1005-1012, 1989.
5. *Handbook of Turbulence. Volume 1. Fundamentals and Application*. Ed. by W. Frost and T. H. Moulden. N. Y. (1977).
6. R.M. Goody, *Atmospheric Radiation*. Oxford University Press, Oxford (1964).
7. S. S. Penner, *Quantitative Molecular Spectroscopy and Gas Emissivities*. Addison- Wesley, Reading, MA (1959).
8. Yu. V. Khodyko, A. A. Kurskov and N. V. Antiporovich, "The multi-group method for calculating for calculating the selective IR radiation transfer in inhomogenous media", *J of Applied Spectrosc.* **44**, pp. 284 - 288, 1986.
9. L.S. Rothman, R. Gamache, A. Goldman et al., The 1986 edition of the HITRAN data base compiled by the Air Force Geophysics Laboratory, *Applied Optics* **26**, pp. 4058 - 4097, 1987.
10. C. B. Ludwig, W. Malcmus, J. E. Reardon and J. A. L. Thompson, *Handbook of Infrared Radiation from Combustion Gases*. Scientifical and Technical Information Office, Washington, D. C. (1973).
11. A.I. Bril , V.P. Kabashnikov, N.V. Kuzmina and Yu.V. Khodyko, "A method for computing the ir radiation of molecular gas jets in the volumetrical approximation", *J. of Applied Spectrosc.* **55**, pp. 934 - 939, 1991.

Probability distribution of laser beam wandering on near-land atmosphere range

Vitaly L.Okoulov, George Yu.Snezhkov, Alexander P.Shestakov, Valery I.Venglyuk

Research Institute for Complex Testing of Optoelectronic Devices
Sosnovy Bor, Leningrad region, 188537 Russia

ABSTRACT

The wandering of laser beam energy center was experimentally investigated on near-land atmosphere range of 980 m length under the weak turbulence. The hypothesis about the independence and normal distribution of horizontal and vertical deviations was checked up by Kolmogorov-Smirnov criterion. In the most cases the experimental histograms don't statistically conform to normal (Gaussian) distribution. It is shown, that the subtraction of linear trend from the temporal dependence of angular deviations improves the agreement of experimental data with normal law of distribution.

Key words: near-land atmosphere, atmospheric turbulence, laser beam wandering, probability distribution.

1. INTRODUCTION

One of the basic point of turbulent atmosphere optics is the assumption that pursuant to central limit theorem the random changes of log-amplitude and phase of optical wave passed through a lot of turbulent eddies obey Gaussian (normal) distribution. Hence, the random horizontal and vertical angular deviations of energy center of laser beam propagated in turbulent atmosphere must obey normal distribution, too. Also this proposition holds true for the random deviations of remote object image in focal plane of receiving optical system.¹

However the phenomenological models with more complicated distribution of amplitude and phase were advanced for the explanation of wave propagation in real atmosphere²⁻⁴. But the experimental verifications^{5, 6} of various models were performed by comparison of histograms of experimental measured intensity with expected probability distribution of wave intensity in the receiving plane. We know only one early work⁷ where the probability distribution of horizontal wandering of focused laser beam was experimentally determined by direct method. However the volume of sample in the experiments⁷ added up to 60-80 measurements, it's obviously deficient for the quantitative valuation of distribution law. Besides the accuracy of experiments⁷ was not very high as far as the method of measurements concerned with the direct photographing of laser beam and further optical processing of photo-pictures by illumination through the rotating mask with varying transmission.

Using the most direct method of measurements, in this work we tried to estimate the probability distribution of horizontal and vertical random deviations of laser beam energy center in real atmosphere conditions and to evaluate the statistical independence (correlation) of components of laser beam angular wandering. The focused laser beam as well as divergence one from a point source were used in our experiments.

Further author information -
V.L.O. (correspondence): E-mail: BOR.POST @ REX.IASNET.RU; Telephone/Fax: (812-69)-624-11

2. EXPERIMENTAL CONDITIONS

We carried out the experiments on September and October on the optical atmospheric range of 980 m length which is located in a forest on a seashore. The optical axis of range was at a height of 2 m. In this paper we describe in detail the results of experiments with divergence beam from the point source of laser radiation.

The optical schematic of experiments is shown on Fig.1. As a remote point source we used a diaphragm illuminated by He-Ne laser ($\lambda = 0.63 \mu\text{m}$). The laser radiation passed through the turbulent layer of near-land atmosphere was focused by lens telescope with aperture of 0.48 m. The object (diaphragm) image in focal plane of telescope was optically projected on the receiving plane of 4-cell (quadrant) photo-diode matrix by additional optical elements. The precision adjustment were carried out visually with the help of auxiliary visual tube (not shown) until the sharp image of test object located in diaphragm plane. The calibration of photo-diode matrix was executed immediately before the experiment in the same optical scheme with the use of rotating optical wedge. The procedure of calibration was mainly the testing of linearity of transformation coefficient "the angle of beam arrival - the output signal", though this coefficient was directly evaluated in some experiments.

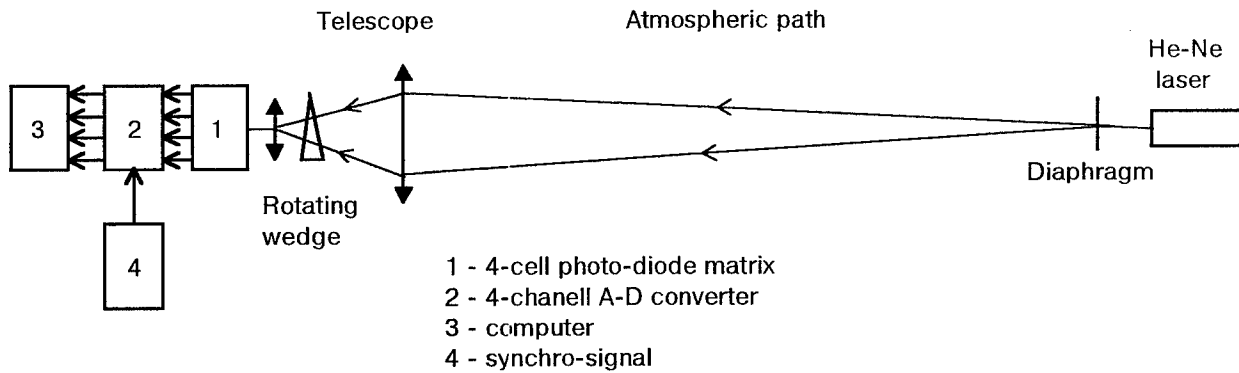


Fig.1. Optical schematic of experiments.

The analog signals from all sensitive cells of photo-diode matrix were converted to digital code by 10-bit ADC and then processed by computer. On the values and ratio of signals from the receiving cells of photo-diode matrix we calculated the horizontal X_i and vertical Y_i angular coordinates of instant situation of energy center in light exposure distribution of distorted image of point object. Due to earth refraction we could not execute the absolute adjustment of optical scheme, therefore the angular position of optical axis (M_X , M_Y) was defined statistically as the averaged value of sum of all instant situation of laser beam energy center during the experiment:

$$M_X = (\sum X_i) / N \quad M_Y = (\sum Y_i) / N$$

So the horizontal X , vertical Y and absolute R_w angular deviations of laser beam energy center are:

$$X = X_i - M_X \quad Y = Y_i - M_Y \quad R_w = (X^2 + Y^2)^{1/2}$$

The frequency of signal registration was 25 - 200 Hz in various experiments. The duration of experiments was about 10 - 40 sec (the volume of each sample more than 1000 values).

All the standard meteorological parameters were monitored in our experiments. The most important parameter is the structural characteristic of refractive index fluctuations (C_n^2), which is varied from $3 \cdot 10^{-16} \text{ m}^{-2/3}$ to $8 \cdot 10^{-15} \text{ m}^{-2/3}$ in the days of experiments. These values of C_n^2 basically correspond the weak atmospheric turbulence⁸:

$$\beta_0^2 = 1.23 \cdot C_n^2 \cdot k^{7/6} \cdot L^{11/6} < 1 \quad (1)$$

where L - the length of optical range, $k = 2\pi / \lambda$ - the wave-number.

3. EXPERIMENTAL RESULTS AND DISCUSSION

All the experiments are tentatively possible to separate on 2 cycles: at weak turbulence and at moderate turbulence. In the first case the turbulence parameter β_0^2 from eq. (1) was less than 0.08, in the second case $\beta_0^2 = 0.3-0.4$. In both cases it is not found out the significant distinction in statistical behavior of random angular deviations of laser beam energy center. The typical time dependence of horizontal and vertical displacements of energy center in light-exposure distribution of object image are shown on Fig.2 (graph for vertical component is shifted by 5 μrad).

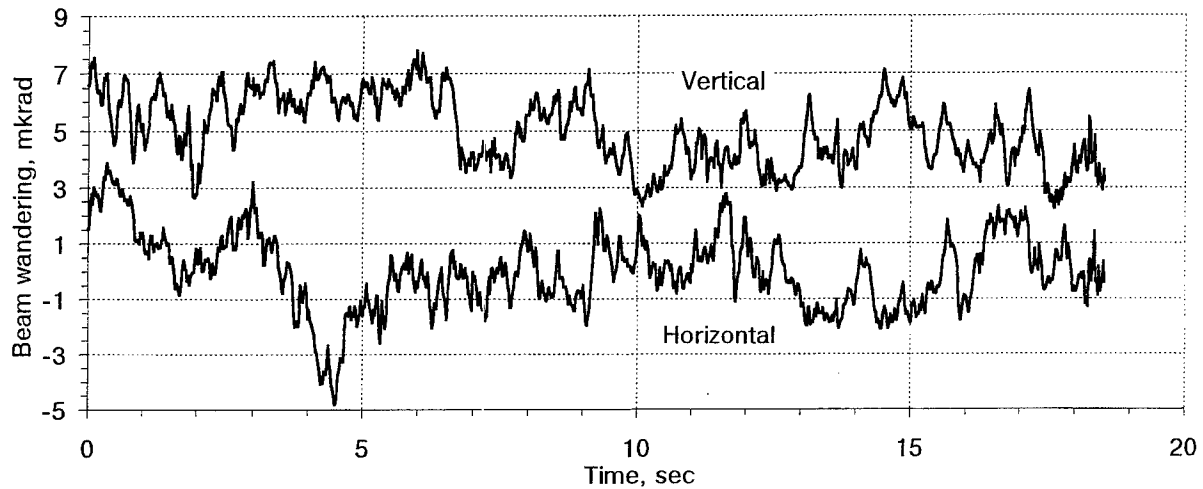


Fig.2. Time dependence of wandering of object image energy center. October 13 (15:44). $C_n^2 \approx 9 \cdot 10^{-16} \text{ m}^{-2/3}$.

The experimental measured variances of X , Y angular deviations of object image energy center are well agree with the theoretical predictions⁸:

$$\sigma_t^2 = (3/4) \cdot 0.033 \cdot \pi^2 \cdot \Gamma(1/6) \cdot C_n^2 \cdot L \cdot F^2 \cdot (R^2 / 2)^{-1/6} \quad (2)$$

where R - the effective radius of receiving aperture, F - the equivalent focus of optical system, $\Gamma(\)$ - Gamma-function. Note, that the values σ_t^2 from (2) are the top valuation, as far as they don't take into account the outer scale of turbulence which should play the essential role in our experimental conditions because the diameter of light beam is comparable with the height of optical range.

The duration of experiment was chosen from the condition $T_{\text{exp}} \gg R / v_{\perp}$, where v_{\perp} - the cross-component of wind speed on the range. On the other hand the duration of experiment should not exceed 1-2 minutes because the disalignments of optical scheme and changes of meteorological conditions on the range have been possible. The most essential errors of measurements took place due to 2 reasons: the non-linearity of transformation of the sensor of beam position; the instability of transformation coefficient of this sensor. The non-linearity of transformation of the sensor was checked by rotating wedge. The instability of transformation coefficient was connected with the fluctuations of effective width of point-object image on the receiving plane. The experimental

data⁹ show that these fluctuations obey log-normal distribution with the small variance at the weak turbulence, therefore we hope that they don't give rise to fatal errors during the determination of energy center position.

We estimated the statistical independence of X, Y components of laser beam wandering by 2 ways: using t-test for independence samples and calculating the correlation coefficient. For the evaluating of normality of probability distribution of horizontal (vertical) random deviations we used the Kolmogorov-Smirnov test¹⁰. The skewness and kurtosis of experimental distribution and their confidence level were calculated too. We didn't use the χ^2 -criterion as it has the high sensitivity to distinctions at the tail of distribution; really the used sensor of energy center position generates the maximal error just at maximal deviation of laser beam energy center from the center of photoreceiver.

Statistical data for all reliable experiments are presented in Table 1: time and duration of measurements; the value of C_n^2 ; the conformity to normal distribution (1-st value - X-component of laser beam wandering, 2-nd - Y-component); the correlation coefficient between X and Y components (K_{XY}); the ratio of variances of X and Y angular deviations (σ_X/σ_Y). The conformity to normal distribution takes the form of significance level (p-level). The value of p-level is in fact the probability of mistake if the hypothesis about normality is rejected.

Table 1. Experimental results.

Time, duration	C_n^2 , m ^{-2/3}	p-level, X & Y components	Correl. coeff.K _{XY}	σ_X/σ_Y	p-level, X & Y components
					Trend subtracted
October 5 :- low turbulence $\beta_0^2 < 0.02$					
12:35, 10s	4·10 ⁻¹⁶	norm.; <0.05	0.02	1.19	norm.; norm.
12:41, 20s	4·10 ⁻¹⁶	<0.05; <0.01	0.01	1.13	<0.1; <0.01
13:00, 10s	3·10 ⁻¹⁶	norm.; <0.1	0.25	1.20	norm.; norm.
October 13 :- low turbulence $\beta_0^2 = 0.04-0.08$					
14:32, 10s	1·10 ⁻¹⁵	<0.01; <0.05	0.22	1.17	<0.01; <0.1
14:43, 30s	8·10 ⁻¹⁶	norm.; <0.01	-0.22	1.22	norm.; <0.01
15:07, 20s	1.5·10 ⁻¹⁵	<0.05; norm.	0.11	1.19	norm.; norm.
15:44, 20s	9·10 ⁻¹⁶	norm.; <0.01	-0.11	1.28	norm.; norm.
October 11 :- moderate turbulence $\beta_0^2 = 0.3-0.4$					
12:25, 10s	8·10 ⁻¹⁵	norm.; <0.01	0.03	1.24	norm.; <0.05
14:10, 20s	7·10 ⁻¹⁵	norm.; <0.01	-0.06	1.42	<0.2; norm.
14:21, 20s	6·10 ⁻¹⁵	<0.01; <0.01	-0.25	1.35	norm.; <0.01
September 29 :- moderate turbulence $\beta_0^2 = 0.25-0.4$					
12:58, 20s	5·10 ⁻¹⁵	<0.01; norm.	0.13	1.50	<0.01; norm.
13:05, 10s	6·10 ⁻¹⁵	norm.; norm.	-0.13	1.90	norm.; norm.
13:15, 40s	5·10 ⁻¹⁵	norm.; <0.01	0.01	1.90	norm.; <0.01
14:57, 20s	5·10 ⁻¹⁵	<0.05; <0.01	-0.08	1.26	<0.2; <0.05
15:10, 10s	8·10 ⁻¹⁵	<0.05; norm.	0.00	0.94	norm.; norm.

From the data of Table 1 one can see that the hypothesis about normality of distribution of horizontal and vertical deviations of object image should be rejected in the most experiments. (The conformity to normal law of

distribution is marked bold). We think that the slow temporal trend in angular deviations is the reason of discrepancy between experimental histograms and expected normal distribution. More often this trend was observed for vertical component of wandering (see Fig.2). The appearance of trend indicates that some processes follow in the atmosphere and more than likely these processes don't concern the pure turbulence. The rather high correlation coefficient in some experiments can also be connected with these processes. The histograms of horizontal and vertical angular deviations of object image agree with the normal distribution much better when the linear trend is subtracted from the experimental data (see last column in Table 1).

The graphs of observed frequency distribution of horizontal and vertical angular deviations of point-object image and expected frequencies from the normal law are shown on Fig.3. The dots are the experimental values, the line is the theoretical prediction (X-component, for example):

$$Fr(X) = N \cdot p(X) = N \cdot (2\pi \cdot \sigma_X^2)^{-1/2} \cdot \exp[-(X - M_X)^2 / 2 \cdot \sigma_X^2] \quad (3)$$

On Fig.3 the x-axis is standardized for the convenience. It is seen that the agreement between dots and line is close enough.

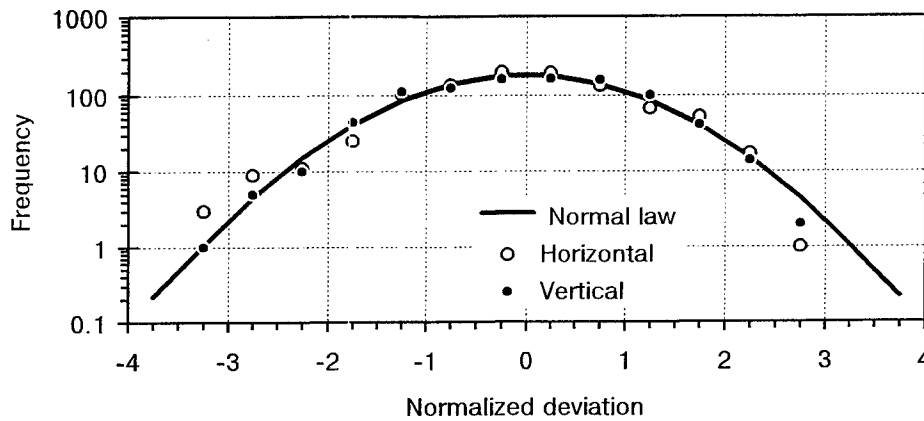


Fig.3. Experimental and expected frequency distributions of horizontal and vertical deviations of object image energy center in turbulent atmosphere. October 13 (15:44). $C_n^2 \approx 9 \cdot 10^{-16} \text{ m}^{-2/3}$. Line - eq.(3).

The data from Table 1 demonstrate that the variances of horizontal and vertical angular deviations are different. At our sight it can be an evidence of anisotropy of outer scale¹¹ of atmosphere turbulence as far as the random refraction of optical radiation is basically determined by the large-scale turbulent eddies. Therefore follows to expect that at $(K_{XY})^2 \ll 1$, where K_{XY} is the correlation coefficient¹⁰, the absolute angular deviations of object image energy center R_w obey general Rayleigh distribution:

$$p(R_w) = R_w \cdot (\sigma_X \cdot \sigma_Y)^{-1} \cdot \exp[-R_w^2 \cdot (\sigma_X^{-2} + \sigma_Y^{-2}) / 4] \cdot J_0 [R_w^2 \cdot (\sigma_X^{-2} - \sigma_Y^{-2}) / 4] \quad (4)$$

where J_0 - Bessel-function.

In the specific case of closeness of variances $\sigma_X^2 \approx \sigma_Y^2$ and at absence of correlation between X and Y components of wandering it is simple Rayleigh distribution. The observed frequency distribution of absolute angular wandering of object image energy center and expected frequencies $Fr(R_w) = N \cdot p(R_w)$ from Rayleigh law (4) are shown on Fig.4. The agreement between experimental dots and theoretical line is close enough.

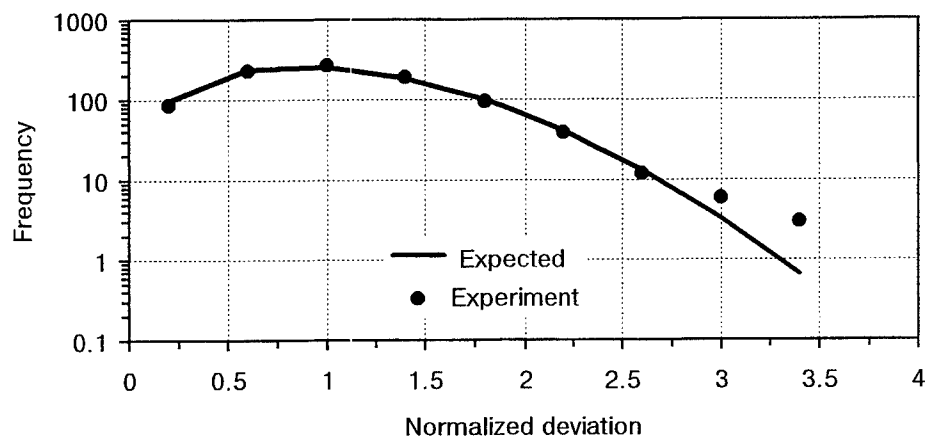


Fig.4. Experimental and expected frequency distributions of absolute deviations of object image energy center in turbulent atmosphere. October 13 (15:44). $C_n^2 \approx 9 \cdot 10^{-16} \text{ m}^{-2/3}$. Line - eq.(4)

Similar experiments were carried out with the use of focused laser beam. The radiation of He-Ne laser was focused at the end of atmospheric range by lens telescope with the aperture of 0.48 m. The wandering of energy center of laser beam was registered by quadrant receiver. The measurements with focused beam and with divergence beam were made at the same time. However the results of experiments with focused laser beam are not so unambiguous. In the most experiments the horizontal and vertical components of beam wandering don't obey to normal distribution. If the linear trend is subtracted from time series of angular deviations, the experimental histograms better comply with normal law (χ^2 -statistic and Kolmogorov-Smirnov d-statistic are reduced). But the hypothesis about normality of X, Y components of focused beam wandering should be nevertheless rejected even if the linear trend is subtracted. We don't understand the reason of this distinction in probability distributions of wandering of focused beam and divergence beam.

4. CONCLUSIONS

Thus on the base of our experiments it is possible to assert that the horizontal and vertical angular deviations of object image on the near-land atmospheric range under the weak and moderate turbulence are independent and non-correlate. Both components of random wandering obey Gaussian (normal) distribution if the slow atmospheric processes which result to temporary trend in angular wandering is not take into account. The absolute angular deviations of beam wandering obey a general Rayleigh distribution.

ACKNOWLEDGMENTS

We want to thank V.E.Sherstobitov (Research Institute for Laser Physics, S.-Petersburg) for useful discussion.

REFERENCES

1. J.W.Goodman. *Statistical Optics*, J.Wiley & Sons, 1985.
2. P.Beckman. *Probability in communication engineering*, New-York, Harcourt, 1976.
3. D.A.DeWolf. "Waves in turbulent air: A phenomenological model", *Proc.IEEE*, v.62, 11, pp.1523-1529, 1974.

4. A.G.Borovoy, G.Ya.Patrushev, A.I.Petrov. "Laser beam propagation through the turbulent atmosphere with precipitation", *Appl. Opt.*, v.27, 17, pp.3704-3710, 1988.
5. G.Ya.Patrushev, O.A.Rubtsova. "Phenomenological investigation of probability density of fluctuations in turbulent atmosphere", *Optika atmosfery i okeana*, v.8, 9, pp.1284-1288, 1995. (in Russian)
6. E.R.Milutin, A.A.Taklay. "The law of probability density distribution of fluctuations of a received power due to optical beam wandering in turbulent atmosphere", *Radiotekhnika i elektronika*, v.32, 8, pp.1611-1617, 1987. (in Russian)
7. E.I.Gel'fer, N.I.Murav'ev, S.E.Finkelshtein, A.M.Chermuhin. "Method of measurements of displacement of light beam energy center passed through the turbulent atmosphere", *Izv.VUZ-ov, Radiophysica*, v.14, 12, pp.1838-1841, 1971. (in Russian)
8. V.E.Zuev, V.A.Banakh, V.V.Pokasov. *Optics of turbulent atmosphere*, Gidrometeoizdat, Leningrad, 1988. (in Russian)
9. E.R.Milutin, A.A.Taklay. "Distribution of fluctuations of a received power due to laser beam width variations in turbulent atmosphere", *Optika atmosfery i okeana*, v.8, 4, pp.583-588, 1995. (in Russian)
10. *Handbook of applied mathematics* (chief editor: W.Lederman). *Volume VI: Statistics*. Part A (ed. by E.Lloyd), J.Wiley & Sons, 1984.
11. A.S.Drofa. "Evaluation of some parameters of atmospheric turbulence from optical measurements", *Izvestiya of Academy of Science of USSR. Atmospheric and ocean physics*, v.16, 6, pp.524-532, 1979. (in Russian)

SESSION 4

Mitigation of Atmospheric Effects and Systems Performance

Linear Phase Conjugation for Atmospheric Aberration Compensation

Robert J. Grasso and Eddy A. Stappaerts
Northrop Grumman Corporation
Electro-Optics and Infrared Technology, M/S L5200
Electronic Systems
Rolling Meadows, IL 60008

ABSTRACT

Atmospheric induced aberrations can seriously degrade laser performance, greatly affecting the beam that finally reaches the target. Lasers propagated over any distance in the atmosphere suffer from a significant decrease in fluence at the target due to these aberrations. This is especially so for propagation over long distances. It is due primarily to fluctuations in the atmosphere over the propagation path, and from platform motion relative to the intended aimpoint. Also, delivery of high fluence to the target typically requires low beam divergence, thus, atmospheric turbulence, platform motion, or both results in a lack of fine aimpoint control to keep the beam directed at the target. To improve both the beam quality and amount of laser energy delivered to the target, Northrop Grumman has developed the Active Tracking System (ATS); a novel linear phase conjugation aberration compensation technique. Utilizing a silicon Spatial Light Modulator (SLM) as a dynamic wavefront reversing element, ATS undoes aberrations induced by the atmosphere, platform motion, or both. ATS continually tracks the target as well as compensates for atmospheric and platform motion induced aberrations. This results in a high fidelity, near-diffraction limited beam delivered to the target.

Keywords: 1) Linear Phase Conjugation, 2) Atmospheric Aberrations, 3) Spatial Light Modulator, 4) Laser Radar, 5) Lidar, 6) Atmospheric Turbulence, 7) IRCM, 8) EOCM, 9) Dynamic Wavefront Reversal, 10) Electronic Holography

1. INTRODUCTION

Atmospheric induced aberrations can seriously degrade laser performance, greatly affecting the beam that finally reaches the target. This is especially true for propagation over long distances in the atmosphere. Lasers propagated over any distance in the atmosphere suffer from a significant decrease in fluence at the target due to atmospheric aberrations. This is primarily due to fluctuations in the atmosphere over the propagation path, and from the motion of the platform relative to the intended aimpoint. Also, delivery of high fluence to the target typically requires a low divergence beam, thus, atmospheric turbulence or platform motion results in a lack of fine aimpoint control to effectively keep the beam directed at the target. Northrop Grumman's Active Tracking System (ATS) continually tracks the target as well as compensates for atmospheric and platform motion induced aberrations [1,2]. This results in a high fidelity, near-diffraction limited beam delivered to the target.

Energy deposited on target depends upon several factors including atmospheric turbulence strength, signal-to-noise ratio, and system latency time. With ATS, gains of one to several orders of magnitude increase in laser fluence at the target have been demonstrated. Additionally, a multitude of operational wavelengths may be addressed due to the linear system architecture, and powers well in excess of 1 kW can be routinely handled with the use of silicon-based SLMs. With ATS, and as a result of the aberration compensation and target tracking capability, lasers with very low divergence may be utilized. In this manner, a greater amount of laser energy is able to be delivered to the target. Some areas that can benefit from ATS include IRCM, EOCM, LIDAR, and laser radar.

2. ABERRATION COMPENSATION CONCEPT

The ATS concept is illustrated in Figure 1; its operation consists of two discrete steps. In the acquisition step, a low power illumination laser transmits a highly diverging beam to the target. Ideally, the divergence of this acquisition beam is matched to the uncertainty of the target direction. An OA return is received. This return is collected and interfered with a

reference beam from the local oscillator (LO) on an integrating focal plane array (FPA) detector to form an electronic hologram. The hologram is read from the FPA, processed, and the conjugate written to the spatial light modulator (SLM). In the engagement step, a beam from a second laser is reflected off the SLM. The SLM acts as a phase modulator and the reflected energy is contained in a beam that is the phase-conjugate of the target return. Now, this beam, which is the conjugate of the original beam, retraces the path to the target. During this time, any wavefront distortions are undone, thus resulting in near-diffraction limited energy delivered to the target. By continually repeating the acquisition and engagement steps, moving targets can be tracked (whether the target is moving relative to the platform or the platform is moving relative to the target) and compensation performed for time varying aberrations in the atmosphere.

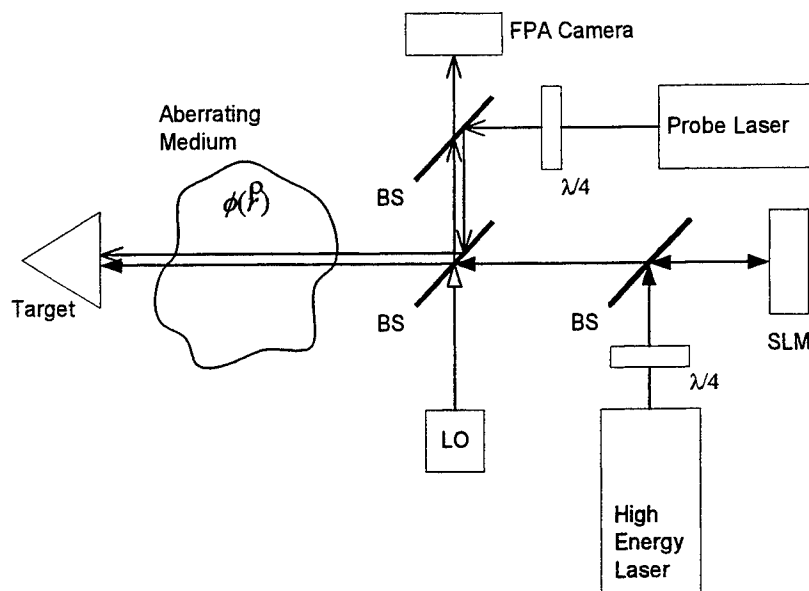


Figure 1. ATS Operation

The maximum energy-on-target enhancement factor for the high energy laser is equal to the number of SLM pixels multiplied by the hologram efficiency. Thus, for 64×64 pixel devices, and with a 0.4 hologram efficiency (the maximum efficiency for a plane, binary phase hologram) the enhancement factor is about 1640. Hence, the greater the number of SLM pixels, the greater the performance improvement that will be realized. Energy deposited at the target depends upon several factors including, atmospheric turbulence strength, signal-to-noise ratio, and system latency time, but gains of one to several orders of magnitude can be expected.

ATS provides automatic target acquisition within its field-of-view, as well as atmospheric aberration compensation. When compared to conventional adaptive optical schemes, no wavefront reconstruction algorithms are required. Additionally, when compared to all-optical phase conjugation schemes that require very high optical amplification factors, up to 10^{15} , amplification of the target return is not required. The energy of the propagated beam is limited only by the laser's maximum energy and the SLM damage limit.

The homodyne process utilized in ATS exhibits the high gain of a coherent detection process without the field-of-view limitation characteristic of the heterodyne process. If desired, even greater sensitivity may be attained using a multiple-step "bootstrapping" process, whereby targets with a signal-to-noise ratio of much less than unity can be detected. It allows target acquisition with low initial photon counts. Bootstrapping is an iterative process that utilizes a sequence of pulses, each pulse corrected by the return from the preceding pulse. Here, the illumination laser is reflected off the SLM; even very noisy holograms will slightly increase the illumination energy on the target, resulting in a higher signal-to-noise ratio in the subsequent hologram. This iterative process typically converges to a maximum energy-on-target in three to four pulses. This bootstrapping process is depicted in Figure 2.

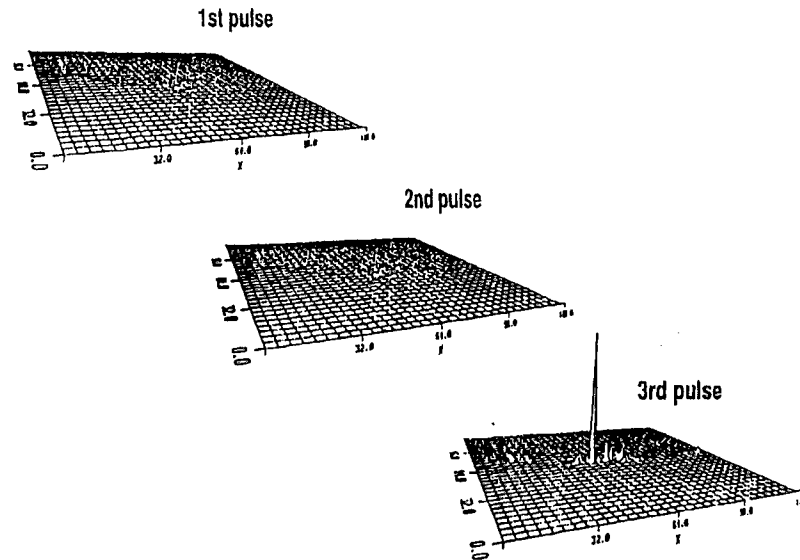


Figure 2. Bootstrapping Process

An advantage of ATS, when compared to all-optical phase conjugation techniques, is that the hologram that contains information about the target and the intervening medium is available in electronic form. This information can be stored in computer memory and processed to extract information about the target. With the very high processor speeds available, this may be performed very quickly. As an example, by computing the Fourier transform of the hologram, target direction relative to the optical axis is obtained. In cases where multiple targets are present, targets can be removed in the Fourier domain, thus allowing sequential target engagement.

3. SPATIAL LIGHT MODULATOR AND ELECTRONICS SUBSYSTEM

Northrop Grumman has developed a novel silicon SLM capable of displaying the phase information required for atmospheric correction. This SLM behaves as a dynamic wavefront reversing element to undo aberrations induced by the atmosphere, platform motion, or both. A hologram formed on an FPA camera is transferred, pixel-by-pixel, to the SLM. This hologram, the conjugate of that formed on the FPA, contains both intensity and phase information about the intervening medium between the SLM and the target. Due to their close interaction, the FPA, hologram processor, and SLM form a single subsystem. Their interrelationship is shown in Figure 3.

The SLM is fabricated using silicon micromachining techniques [2]. Figure 4 shows a diagram of the SLM constructed of a movable (deformable) diaphragm and a backplate to which an interconnect board and driver electronics are connected. The diaphragm is subdivided into N by N pixels [3]; each supported from the backplate by an oxide grid. Individual pixels are etched with a flexure region, thus deflecting in a piston-like motion. In practice, the SLM behaves in much the same manner as a phased array antenna. The backplate, constructed from a flat, thick piece of silicon, serves as a support for the pixelated diaphragm and a structural surface to maintain device rigidity. Electrostatic attraction between the conductive silicon diaphragm (ground potential) and a deflection electrode requires a modest voltage (≈ 20 volts) to achieve deflection. The electrical connection from a deflection electrode to the X-Y addressable electronics through the interconnect passes through a via under each element. Additionally, this via serves as a vent for critical (fluid) damping of the diaphragm.

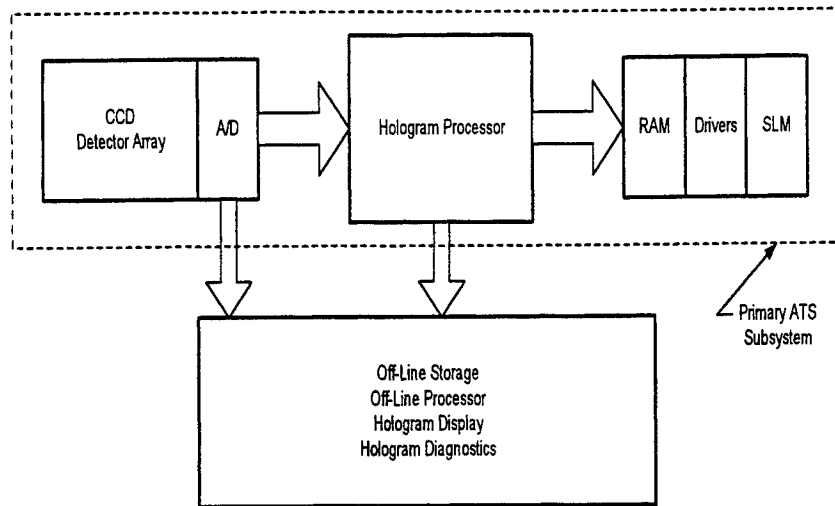


Figure 3. Camera, Hologram Processor, SLM Subsystem

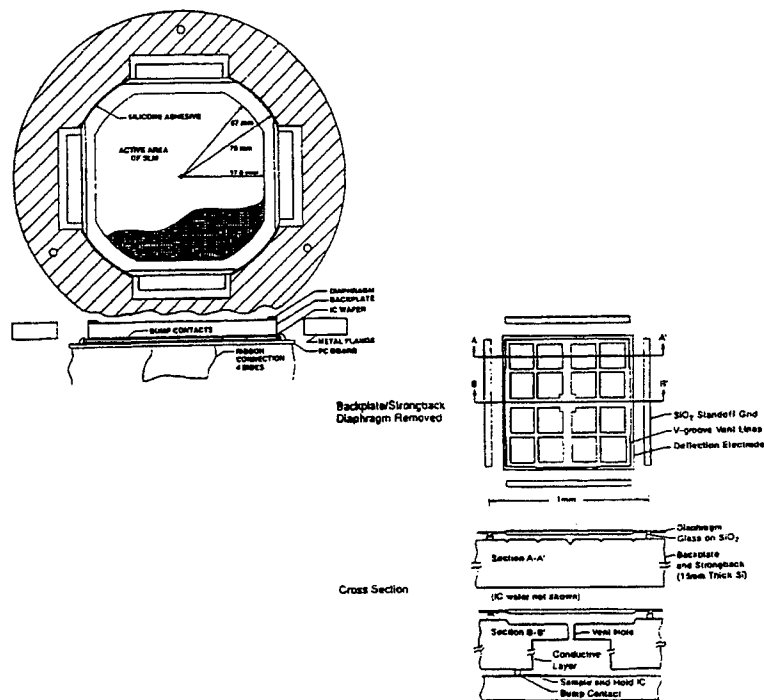


Figure 4. Design for N by N Pixel Silicon SLM

The N rows of the FPA are read-out in parallel, converted from analog to digital signals, and written to the SLM. The detected hologram (digital FPA output) and the processed hologram (written to the SLM) are stored electronically for post-processing, if desired. Mathematically, an expression for the intensity forming the hologram pattern is given by:

$$H(i, j) \sim |R(i, j)|^2 + o(i, j)R(i, j)^* + o(i, j)^* R(i, j) + |o(i, j)|^2 \quad (1)$$

where $R(i, j)$ and $o(i, j)$ are the complex electric fields of the reference beam and the object beam at pixel (i, j) . The reference beam profile, the first term on the right, must be nearly uniform across the FPA array while the object intensity, the fourth term on the right, must be small compared to the reference intensity. The second and third terms contain information about the target and the intervening medium.

The homodyne detection SNR is given by the expression:

$$SNR = \frac{2n_R n_{o,rms} (T_o / T_R)}{n_R + n_{o,rms} + n_B + n_D + n_j^2} \quad (2)$$

where n_R , $n_{o,rms}$, n_B , n_D , and n_j are the number of photoelectrons due to the reference beam, the object beam, the background, the detector dark-current, and the Johnson/readout noise, respectively. T_R and T_o are the pulse width of the reference beam pulse and the object beam pulse, respectively. Ideally, these two pulse widths would be equal, but, in practice, $T_R > T_o$ in order to reduce the required accuracy of the target-return arrival time.

The primary function of the hologram processor is to subtract the reference intensity term as shown in Equation 1. This term represents the bias and can be subtracted since it does not contain any useful information. However, since its value is considerably larger than that of the information containing terms, this subtraction must be performed with a high degree of accuracy.

The dynamic range of the FPA array and, hence, the number of bits in the analog-to-digital (A/D) converter is dictated primarily by the requirement to keep the object beam, which acts as a noise term, small when compared to the other terms in the hologram expression. The magnitude of this term varies both spatially and temporally because of atmospheric scintillation. Analysis indicates that the minimum number of bits is about eight, with higher numbers desirable to improve performance and reduce the accuracy to which the target range must be known. The minimum FPA bucket size is primarily determined by the requirement that the Shot noise count due to the reference beam be greater than the noise count due to the other noise sources.

4. PERFORMANCE

ATS presents several distinct advantages as compared to a conventional approach: 1) since most targets are found using OA, bootstrapping can permit a system utilizing this concept to lock onto targets incorporating significant cross section reducing counter countermeasures (CCM); 2) ATS acquisition beam may be several times wider than with a system not utilizing this technique, thus reducing pointing accuracy requirements with regard to the search beam; 3) there is a significant increase in the energy-on-target, thus minimizing engagement laser energy requirements (delivering a high fidelity, near-diffraction limited beam over the laser propagation path is essential to laser damage applications); 4) the automatic, vibration-insensitive, pointing capability eliminates the necessity for complex and expensive gimbals used in conventional pointing systems, and; 5) provision for sequential engagement of multiple targets within its field-of-view. Therefore, the output energy of the engagement laser may be significantly reduced, or, for a given engagement laser energy, the energy-on-target can be increased and the engagement range extended.

Figure 5 and Figure 6 show the fraction of energy-on-target without ATS and with ATS, respectively, for various degrees of atmospheric turbulence, C_n^2 . Here, the transmit aperture is 10 cm and the target has a 5 cm receive aperture; the wavelength selected is 0.85 μm . Notice in Figure 5, the non-compensated case, that the energy-on-target decreases rapidly as the C_n^2

increases. Thus, for a C_n^2 of 10^{-14} at a 3 km range, the energy-on-target would be about 0.015 of that from the engagement laser. Now, for the compensated case, Figure 6, and identical conditions for a C_n^2 of 10^{-14} at a 3 KM range, the energy-on-target would be nearly 0.4 of that from the engagement laser. Therefore, if 10 mJ of energy is required on target, the non-ATS case would require a 670 mJ laser, while the compensated case would require only a 25 mJ laser; twenty-seven times more laser energy would be required for non-compensated laser case. Indeed, this would have a significant impact on system performance, size, weight, and cost, especially if greater energy or range performance is required.

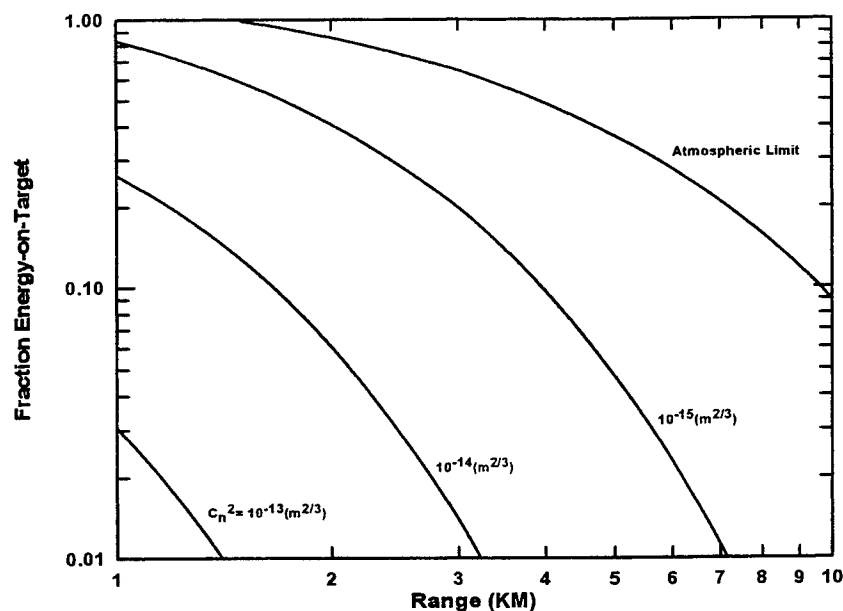


Figure 5. Typical Performance Without Compensation

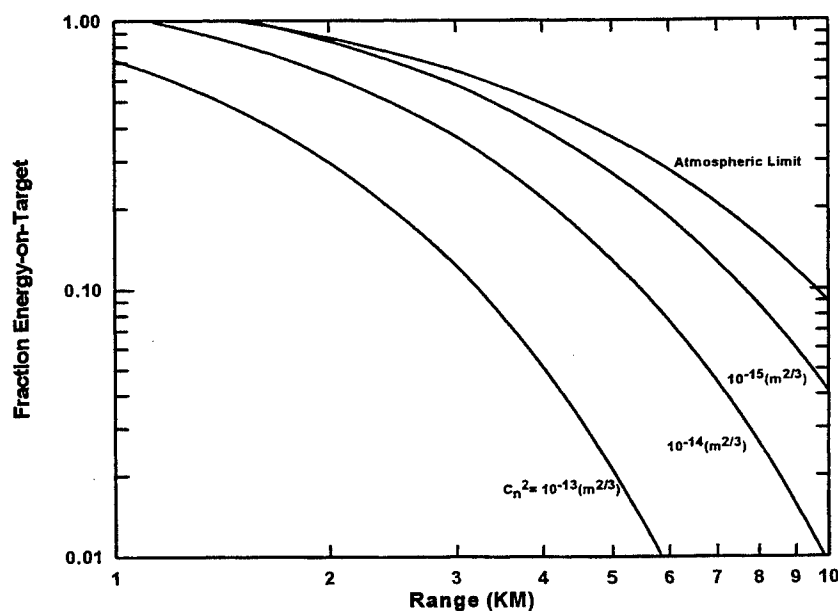


Figure 6. Typical Performance With Compensation

5. TEST RESULTS

Analytical, simulated, and experimental results of Strehl ratio (peak intensity to diffraction limited peak intensity) as a function of SNR is shown in Figure 7. Here, excellent agreement was obtained between theory and experiment, even at SNRs as low as 0.1. The difference between the analytical results and the computer simulations is due to the statistical nature of the noise. Figures 8 and 9 show computer simulations and experimental data, respectively, for bootstrapped operation. The top row in each figure shows the hologram written to the SLM and the bottom row shows the resulting intensity distribution at the target plane. Experimental results are shown as an intensity profile through the peak intensity.

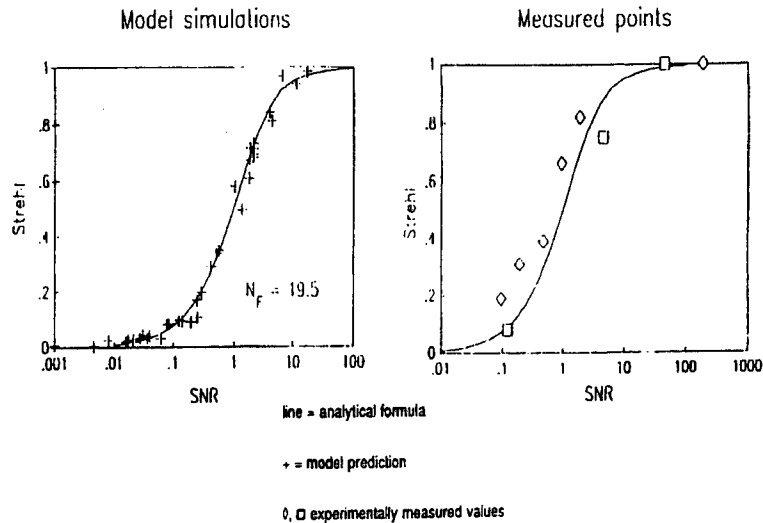


Figure 7. Simulated and Measured Target Intensity versus SNR

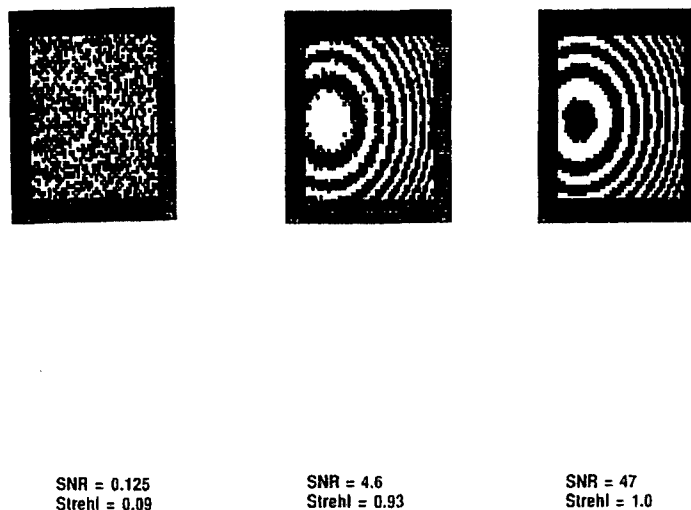


Figure 8. Bootstrapped Operation Model Predictions

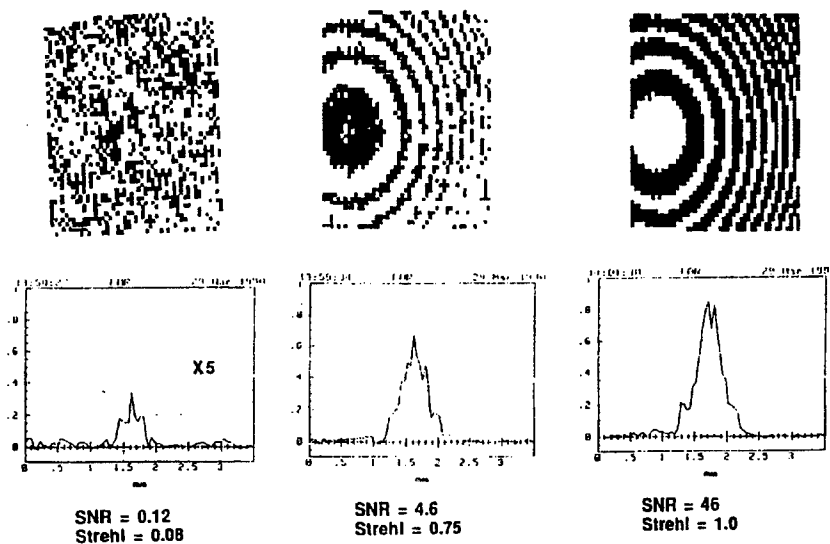
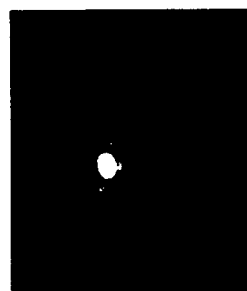


Figure 9. Bootstrapped Operation Experimental Results

Performance tests were carried out both during the daytime and at night to a range of 3 km; target acquisition tests were performed to a range of 5 km. Test objectives were to compare the performance of ATS with the performance of a non-ATS system, without aberration compensation. The goal was to demonstrate a five-fold increase in energy-on-target as compared to the non-ATS system. In actuality, more than a seventy-five-fold increase in energy-on-target was demonstrated. Figure 10a shows the variance in energy-on-target without ATS. It is important to notice how distorted the beam appears over the 3 km path. Figure 10b shows the improvement realized with ATS. Here, the near diffraction limited beam is clearly observed [4].



10a. Aberrated Farfield Image



10b. Improvement with ATS

Figure 10. Performance Improvement Realized with ATS

6. SUMMARY

It is quite apparent that ATS can provide tremendous gains in increasing the laser energy delivered to a target. When coupled with a laser radar, IRCM, or EOCM system, a high fidelity, near diffraction limited beam is delivered to the target. In most cases, this translates into either an increase in energy on target for a given laser energy, or a reduction in laser energy required to deliver a specific amount of energy to the target. With ATS, laser size, weight, and cost may be reduced therefore making certain IRCM, EOCM, and LIDAR, and laser radar applications feasible.

REFERENCES

1. Grasso, R.J. and Stappaerts E.A., "Linear Phase Conjugation for Atmospheric Aberration Compensation," Proceedings of the 1997 IRIS Symposium on Active Systems, (Environmental Research Institute of Michigan, Ann Arbor, MI) (1997).
2. Grasso, R.J. and Burns, B.E., "Silicon Spatial Light Modulators for Atmospheric Aberration Compensation," Spatial Light Modulators, Spring Topical Meeting, Paper STuBl-1,Invited (Optical Society of America, Washington, DC) (1997).
3. Burns, B.E., Ionescu, A.C., Geneczko, J.M., Grasso, R.J., Davidson, S.F., "Silicon Spatial Light Modulator Fabrication," Spatial Light Modulators, Spring Topical Meeting, Paper STuBl-1,Invited (Optical Society of America, Washington, DC) (1997).
4. U.S. Patent Number 5,170,283, December 1992.
5. Final Report, Active Tracking System, DARPA Contract Number DAAB-07-90-C-F417.

Negative optical feedback correction for the extended range of distortions

V.Yu.Venediktov

Institute for Laser Physics, SC "Vavilov State Optical Institute",
199034, St.-Petersburg, Russia

ABSTRACTS

Proposed is the novel method of dynamic nonlinear-optical correction for distortions in wide spectral band. The method is based on combining of the negative optical feedback correction and dynamic holography correction in the system, using optically addressed phase modulators.

Keywords: negative optical feedback, dynamic holography, optically addressed liquid crystal modulator.

1. BACKGROUND AND STATE-OF-THE-ART

In mid-80es there was proposed¹ and realized in several experiments^{2,3} the scheme of the nonlinear-optical correction for distortions of optical radiation wavefront, using the optically addressed spatial phase modulator, introduced into the negative optical feedback (NOF) loop (see Fig.1).

In such a scheme the probe beam of radiation of the auxiliary laser source passes via the aberrated optical beamlet and through the layer with the controlled optical thickness (the layer of liquid crystal, LC, in the optically addressed spatial light modulator, SLM⁴). The optical thickness of this layer, i.e. phase retardation of the probe beam, depends on the intensity of controlling optical signal coming to the corresponding zone of photoconductor of the SLM. In our case such a signal is the interference pattern of the probe beam with the coherent and coaxial nondistorted reference beam. So in the system there is realized the optical feedback. In the case of appropriate phase shift between the probe and reference beams this feedback reveals itself as the negative feedback, and the system as a whole drifts to the state, in which the wavefront distortions, imposed by the induced relief of optical thickness of LC layer, add approximately to those imposed by the aberrated beamlet and thus correct for them. Note, that such a corrector works not only at the wavelength of the auxiliary probelaser source, but can be (with the accuracy of spatial dispersion of the LC refraction index) used across the overall spectral range of LC transparency.

The basic limitation, preventing this technique use for practical purposes is the so called 2π -problem (see Fig.2). In any scheme of output signal stabilization, using the negative feedback, the maximal magnitude of the error corrected is limited by the width of monotonous range of variation of the signal, used for the control of actuator with this error variation. In our case the control signal is produced by the dual beam interference in the Michelson, Mach-Zander etc. interferometer. Correspondingly, the range of monotonous variation of the intensity at the output of such an interferometer vs. relative phase shift between the reference and probe wave (i.e., the magnitude of the corrected distortion of wavefront) can not exceed the wavelength of the auxiliary laser source radiation.

In the case of larger distortions, exceeding these limits, the aperture of the corrector splits into several independent domains with the abrupt phase shift at the edge. Such a system is not stable, the acute edges of the domains result in significant diffraction losses of radiation. But the most important disadvantage is that the regions of the corrected wavefront, corresponding to different domains, obtain the relative phase shift in several wavelengths. Such a "broken" corrector can be efficiently used not in the whole range of LC transparency, but only in the rather narrow spectral zone $\Delta\lambda \ll \lambda$.

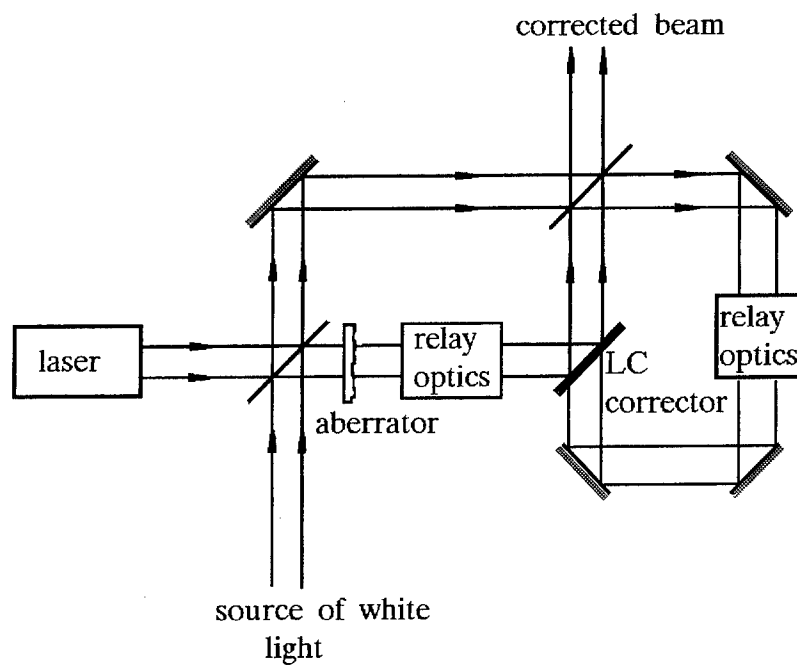


Fig.1. Usual scheme of NOF-correction for distortions

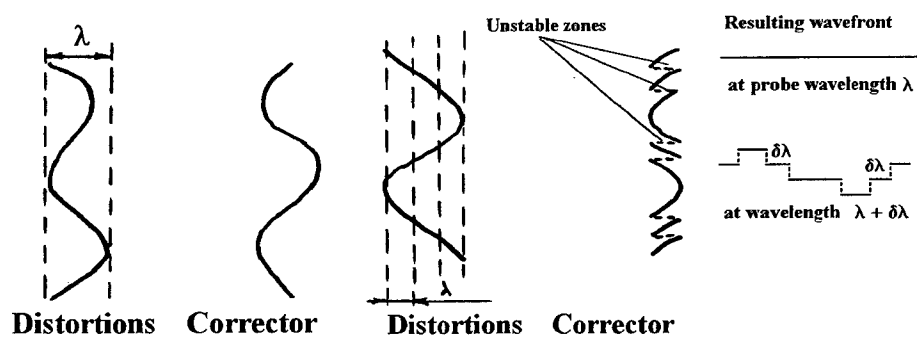


Fig.2. 2π -problem in NOF correction: phase retardation in the corrector for small (left) and large (right) magnitudes of distortions.

There are several possibilities of the system performance improvement so as to enlarge the range of magnitudes of the corrected distortions with the preservation of wide spectral range of the corrected radiation wavelengths. For example, some improvement can be obtained just by enlargement of the auxiliary laser source radiation wavelength. However, the significant shift to the mid-IR range of spectrum (several microns) is limited by the reduce of LC media transparency and by the lack of sensitive photoelectric media.

D.M.Pepper⁵ has suggested to use the spectrum-zonal approach. One can split the spectral range of correction into several narrow ranges and to use separate corrector for each of these ranges. This approach, however, is very complicated and results in significant energy losses due to the necessity of complicated spectral separation.

2. INTERFEROMETER WITH THE ENCOARSED SENCITIVITY

We propose another approach to this problem solution, which seems now to be the most prospective. The simple dual beam interferometer, forming the NOF signal in the discussed schematics, can be replaced by the sophisticated interferometry scheme, in which the variation of the output intensity from minimum to maximum will be smooth and monotonous along the phase shift range, whose magnitude equals several wavelengths of probe radiation.

Such an interferometer can, in particular, implement the following property of the thin (plain, non-Bragg) dynamic hologram (Fig.3). Let us record such a hologram as the interference pattern of the nondistorted plain wave and probe wave with some phase modulation of its wavefront (both waves have the wavelength λ_1). Let us then reconstruct this hologram at the shifted wavelength λ_2 . In this case we shall obtain the reconstructed probe wave with the phase modulation of its wavefront, equal to that of the primary probe wave, measured in terms of wavelength of radiation. I.e., the reconstructed probe wave would have the phase modulation of its wavefront, scaled in the ratio (λ_2/λ_1) with the respect to that of primary probe wave. The use of this feature, in particular, makes it possible to obtain the mutually coherent light beams with the similar, but scaled wavefront distortions, which can be, in turn, used in the above mentioned sophisticated interferometer.

3. NOF CORRECTION SCHEMATICS FOR THE EXTENDED RANGE OF DISTORTIONS

One of variants of the NOF-corrector, using the interferometer with the reduced sensitivity and expanded range of monotonous output signal, is shown in the Fig.4.

In this case the auxiliary laser system has to emit the radiation at two wavelengths λ and λ' ; the difference of these wavelengths has to be small: $\Delta\lambda = \lambda - \lambda' = \lambda / m \ll \lambda, \lambda'$; $m \gg 1$. The probe beams at both wavelengths read out the wavefront distortions, imposed by the aberrant beamlet and momentary profile of the corrector. Than the probe beam at the wavelength λ' interferes with the coherent nondistorted reference beam in the medium, providing recording of the thin dynamic hologram. This hologram is read out by another reference beam at the wavelength λ and reconstructs the distorted probe beam with the scaled distortions. This beam is combined coaxial with the distorted probe beam at the same wavelength. The intensity in the interference pattern of these two beams varies monotonously from minimum to maximum at the range of phase shifts, imposed by the aberrant beamlet and corrector, m times exceeding that in usual scheme and thus providing the possibility of their correction.

There are possible other optical schematics, based on the same principles. As to the medium for recording of the thin dynamic hologram, the optically addressed LC SLM, similar to that used as NOF-corrector, seems to be the most promising medium⁶.

4. CONCLUSION

The proposed schematics requires experimental feasibility study. As we have said already, there are possible several variants of the interferometer with the reduced sensitivity; one has to choose the optimal.

Even more important seems to be the problem of residual non-corrected error. Similarly to any schematics of stabilization, using the negative feedback, the point of dynamic equilibrium of the system is somewhat shifted with respect to the minimal error signal. In our case it means, that the profile of the dynamic corrector does not completely correspond to the profile of the distortions, imposed by the aberrant beamlet.

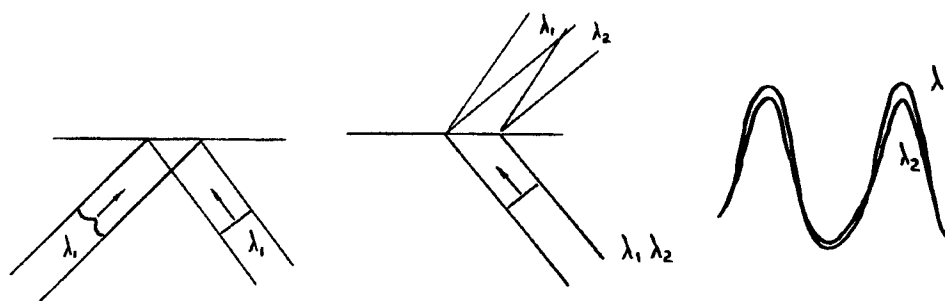


Fig.3. Writing-in of the thin dynamic hologram, its reconstruction on two wavelengths and scaling of wavefront distortions

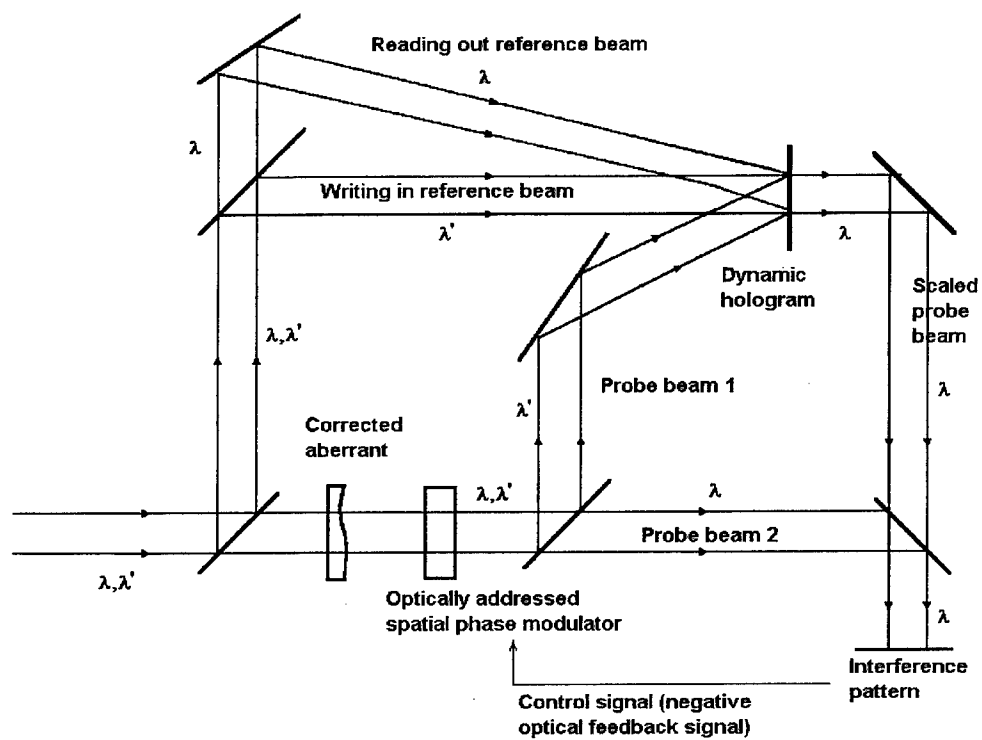


Fig.4. The use of interferometer with the encoarsed sensitivity in the scheme of NOF-correction

The magnitude of the residual distortions of the output wavefront, imposed by the summary action of this beamlet and corrector, has to be sufficient for provision of the required distorted profile of the corrector. This problem was not yet analyzed, for the magnitude of the distortions, coped with by the traditional scheme of NOF-correction, was not large and one could neglect these residual error.

Anyhow, there is simple, at least in principle, solution of this problem. One can mount afterwards the first contour of NOF-correction, using the encoarsed interferometer, the second one of the similar schematics or the one, based on the traditional NOF-correction schematics. However, the evaluation of the necessity of such a complication of the system has to be based on more detailed analysis and numerical simulation.

As to the technological problems in realization of NOF-corrector with the expanded range of corrected magnitudes, the most important seems to be that of fabrication of the "thick" optically addressed LC SLM. The depth of modulation of LC refraction index equals 0.1 - 0.2, so the correction for distortions with the magnitude of dozen wavelength requires the use of LC layer with the thickness of $\sim 10^{-1}$ mm or LC SLM of the sophisticated design. The problem of fabrication of the elements of such a class was already discussed with respect, in particular, of their use as the actuator in the linear adaptive systems⁷. This problem, however, requires much more thorough study, because, in particular, this very element will determine the response time of the overall system.

In addition to shortening the response time, one of the basic problems in design of the "thick" modulators is the problem of fabrication of the elements of the high and reproducible optical quality. Note that in the case of NOF-correction this factor has much lower importance, than in, say, case of linear adaptive actuator, for in our case the correcting LC layer is itself introduced into the correction loop.

ACKNOWLEDGMENTS

The author is grateful to Dr.V.A.Berenberg, Dr.A.A.Leshchev, Dr.L.N.Soms and Dr.M.V.Vasil'ev for helpful discussions.

REFERENCES

1. Vorontzov M.A., Shmalgauzen V.I. Izvestiya VUZov. Seria Radiofizika, Vol.25, #10, p.1179-1187, in Russian
2. Vorontzov M.A., Kirakosyan M.E., Larichev A.V. Kvantovaya Elektronika, Vol.18, #1, p.117-126, 1991, in Russian
3. Pepper D.M. et al. Innovative adaptive optics and compensated imaging using a liquid crystal light valve. CLEO'93, Technical Digest, paper CThO2, p.464-466.
4. Warde C., Fisher A.D., Spatial light modulators: applications and functional capabilities. In "Optical Signal Processing", J.L.Homer, ed., Academic Press, NY, 1987, p.477-523.
5. Pepper D.M., private communication.
6. Berenberg V.A., Kamanina N.V., Soms L.N. Holographic correction of distortions using the liquid crystal light modulator for differing frequencies of recording and reading radiation. Izvestiya AN SSSR, Ser.Fizicheskaya, 1991, v.55, #2, p.236-238, in Russian.
7. Onokhov A.P. et al. Optical wavefront corrector based on liquid crystal concept. Proceedings of SPIE, Vol.2201, pp.1020-1026, 1994.

Adaptive optics using a liquid crystal phase modulator in conjunction with a Shack-Hartmann wave-front sensor and zonal control algorithm

David Dayton^a, Steve Sandven^a, John Gonglewski^b, Steve Browne^c,
Samuel Rogers^d, Scot McDermott^e

^aApplied Technology Associates, 1900 Randolph SE, Albuquerque, NM 87106

^bLIMI, USAF Phillips Laboratory, Kirtland AFB, NM 87117

^cthe Optical Sciences Company, 1341 S. Sunkist St., Anaheim, CA 92825

^dWillow Systems, Ltd., 15100 Central SE, Albuquerque, NM 87123

^eLogicon-RDA, 2600 Yale SE, Albuquerque, NM 87106

Abstract

Multi-segment liquid crystal spatial light modulators have received much attention recently for use as high-precision wavefront control devices for use in astronomical and non-astronomical applications. They act much like piston only segmented deformable mirrors. In this paper we investigate the use of these devices in conjunction with a Shack-Hartmann wave-front sensor. Previous investigators have considered Zernike modal control algorithms. In this paper we consider a zonal algorithm in order to take advantage of high speed matrix multiply hardware which we have in hand.

Keywords: Adaptive Optics, Spatial Light Modulators

1. Introduction

Multi-segment spatial light modulators (SLM) have recently received much attention for use in adaptive optics applications¹. These devices have the advantage that they are compact, light weight, and less expensive than deformable mirrors. They can also be used in transmission, which is desirable for some applications. These attributes make them useful in many applications including those not associated with astronomy. At present the devices are somewhat slow and have a limited dynamic range; however, it is envisioned that their speed will be increased considerably in the near future. The throw of the device can be increased by double passing the optical beam, or by stacking several of the devices.

When used with polarized light, the device can be made to act like a multi-segment piston-only deformable mirror. In order to form a closed loop adaptive optics system, the device must be used in conjunction with a wavefront sensor. Although a number of different types of wave-front sensors exist, the Shack-Hartmann sensor has the advantage that it is simple, easy to build and can be operated at a high temporal bandwidth when only the centroids of the sub-aperture spots are used to determine the average wave-front tilt across the sub-aperture.

Because the SLM can only perform piston wave-front correction, it can introduce waffle modes into the wavefront that are not observable by the Shack-Hartmann sensor. In addition, the multiple segments may introduce high order diffraction patterns into the spots produced by the individual Shack-Hartmann sub-apertures. These effects limit the operable configurations of the SLM/wave-front sensor combination.

The purpose of this paper is to discuss experiments and analysis using the Meadowlark hexagonal 127 element liquid crystal array in conjunction with a hexagonal Shack-Hartmann wave-front sensor. These experiments were performed in an attempt to understand and quantify the effects associated with this combination.

2. Higher Order Diffraction Modes and Waffle

Because the SLM acts like a piston only adaptive optic we must be concerned with the diffraction effects associated with the interference of light passing through adjacent displaced SLM segments. Figure 1 shows a computer simulated one-dimensional cross-section of a Shack-Hartmann spot produced when two adjacent segments are displaced with respect to each other. We can see from the plots that for small displacements each Shack-Hartmann lenslet will produce a well defined spot. However as the relative displacement increases, the intensity of one of the side lobes increases. As the displacement reaches one half wave, the spot breaks in two. This effect cannot be detected by a simple centroid operation.

Although high order aberrations can be calculated in the Shack-Hartmann spots, most wave-front sensors only work with the spot centroids. As the side-lobes in the diffraction pattern become significant, the error in the estimation of the centroid location increases. Figure 2 shows the percent error in the centroid calculations as a function of SLM segment displacement. It is seen that as the displacement approaches one half wave, the error approaches one hundred percent due to the bi-modal spot. This error introduces an ambiguity into the wave-front measurements that can lead to waffle modes developing in the SLM segments when we operate it as a closed-loop adaptive optic. In order to mitigate this problem, the commands applied to the SLM segments must be constrained such that the relative inter-segment displacements are less than one-half wave.

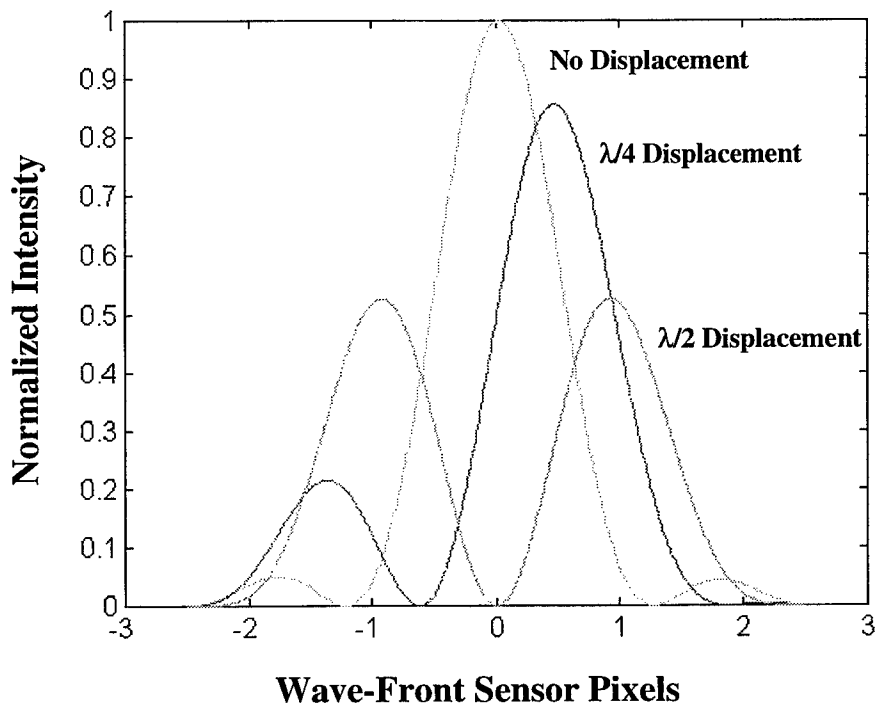


Figure 1 Simulated one dimensional cross sections of Shack-Hartmann spot

3. Zonal Control of The Spatial Light Modulator

The use of the SLM in a closed loop adaptive optics configuration, has been demonstrated in several places using a zernike modal control algorithm in conjunction with a Shack-Hartmann wave-front sensor^{1,2}. In the references cited between ten and twenty zernike modes were corrected using the SLM, in a modal control algorithm.

Large aperture adaptive optics designed to work in the visible typically encounter turbulence with D/r_0 greater than ten. In order to obtain near full order correction for such systems, several hundred zernike modes need to be corrected by the adaptive optics. In such instances zonal control algorithms, using a multi-input multi-output control algorithm are often used³ in order to take advantage of high speed matrix multiply hardware. In this paper we investigate the use of a zonal control algorithm with the SLM similar to one used with a continuous face hexagonal deformable mirror.

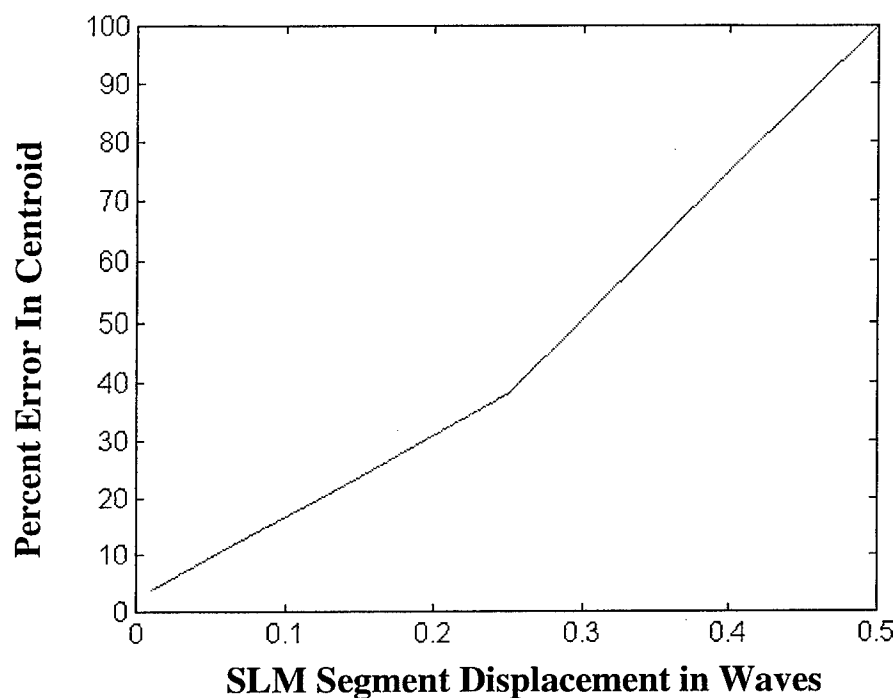


Figure 2 Shack-Hartmann centroid error as a function of segment displacement

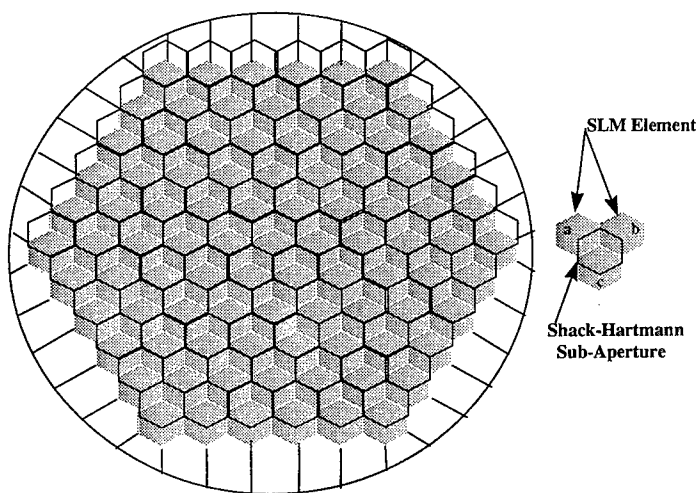


Figure 3 Arrangement of SLM Elements and Shack-Hartmann Lenslets

Figure 3 shows the arrangement of Shack-Hartmann sub-apertures with respect to SLM segments that we used in our study. Each Shack-Hartmann sub-aperture is centered at the vertex of three SLM segments. One particular set of segments is shown at the right side of the full array. As discussed in the previous section, the piston only segments do not provide a smooth tilt across the Shack-Hartmann sub-aperture as a continuous face sheet deformable mirror would. The effect of the phase discontinuity is illustrated in Figure 4 which shows an image of a few of the Shack-Hartmann spots with varying amounts of displacement of a single SLM segment. Figures 4a and 4b show that for small displacements of the segment, the three surrounding spots move outward as desired. Figure 4c shows that as the segment displacement approaches one-half wave, the three spots become bi-modal. The side-lobes from these three spots coalesce to form a spot at the center of the SLM segment location. This effect causes errors in the centroid calculation for each of the three Shack-Hartmann spots and limits the relative displacement that can be allowed between two adjacent SLM segments.

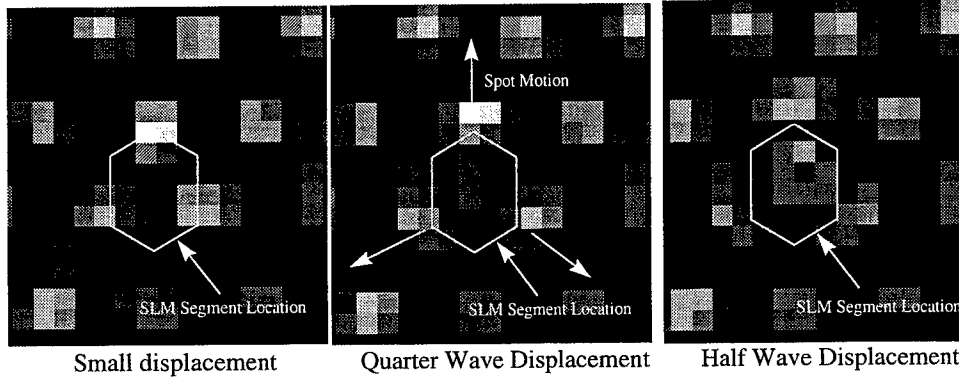


Figure 4 Effect of SLM segment displacement on Shack-Hartmann Spots

In the following we assume that for small displacements of adjacent segments, we can treat the control problem in the same way as for a continuous face sheet mirror. Referring to the three segment basic cell shown in the right hand side of Figure 3, an approximate relationship between the piston in the SLM segments and the spot displacement seen by the Shack-Hartmann sensor can be given as follows.

$$\phi_x = \frac{\sqrt{3}}{2}(x_{11} - x_{12}) \quad (1)$$

$$\phi_y = x_{21} - \frac{x_{11} + x_{12}}{2} \quad (2)$$

Where the sub-scripted x variables represent the piston of the various SLM actuators, and ϕ is the phase gradient measured by the wave front sensor. We then follow the standard least squares MIMO control approach³ and put equations (1) and (2) in matrix form.

$$\Phi = \Gamma X \quad (3)$$

where Φ is the Shack-Hartmann phase gradient measurement vector, and X is the SLM segment displacement vector.

$$\Phi = \begin{bmatrix} \phi_{x11} \\ \phi_{x12} \\ \vdots \\ \dots \\ \phi_{y11} \\ \phi_{y12} \\ \vdots \end{bmatrix} \quad (4)$$

$$X = \begin{bmatrix} x_{11} \\ x_{12} \\ \vdots \\ x_{21} \\ x_{22} \\ \vdots \end{bmatrix} \quad (5)$$

The matrix Γ is given by

$$\Gamma = \begin{bmatrix} \sqrt{3}/2 & -\sqrt{3}/2 & 0 & 0 & 0 & \dots \\ 0 & \sqrt{3}/2 & -\sqrt{3}/2 & 0 & 0 & \dots \\ \dots & \dots & \dots & \dots & \dots & \dots \\ -1/2 & -1/2 & \dots & 1 & 0 & \dots \\ 0 & -1/2 & -1/2 & \dots & 1 & \dots \end{bmatrix} \quad (6)$$

The MIMO control matrix, H , is then formed using the pseudo inverse operation.

$$H = \Gamma^T (\Gamma^T \Gamma)^{-1} \quad (7)$$

The H matrix is incorporated in a summation control algorithm, which attempts to drive the wave-front centroid errors to zero. The commands to the SLM segments can be described by:

$$C_k = C_{k-1} - gH(\Phi - \Phi_0) \quad (8)$$

Where Φ_0 is a set of nominal centroid offsets obtained from a wave-front sensor calibration. The term C_k represents SLM segment commands at time step k , and g represents the loop gain.

The closed loop feedback control system is shown in the following block diagram.

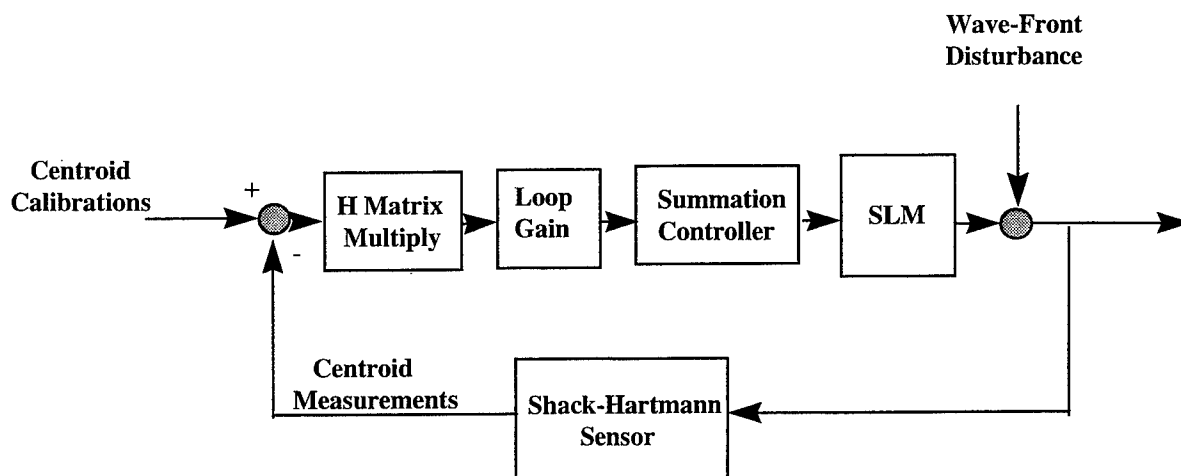


Figure 5 Block Diagram Zonal Control of Spatial Light Modulator

4. Experimental Results

In this section we describe results of experimentation with the SLM configured in the zonal feedback control loop discussed previously. Figure 6 shows the optical layout of the experiment.

We first show results with a static aberration. Approximately one wave peak-to-valley of defocus and astigmatism was applied to the wave-front using a plate aberrator. The open and closed loop focal plane spots are shown in Figure 7. The open loop Strehl ratio was approximately .16 while the closed loop was .25.

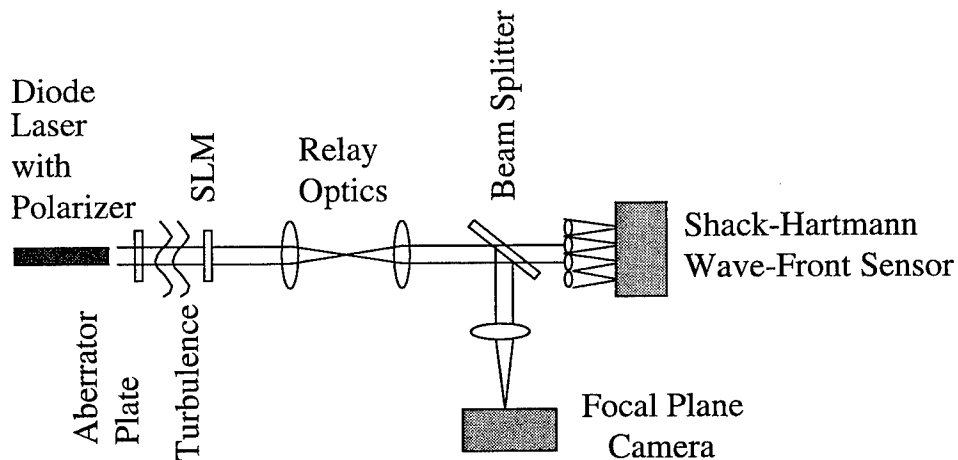
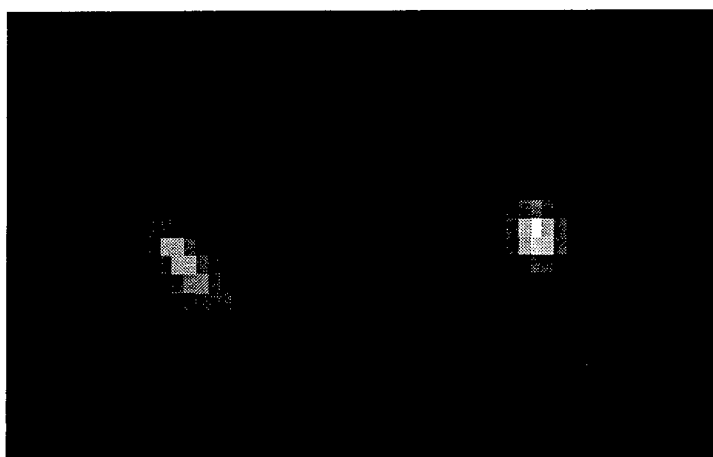
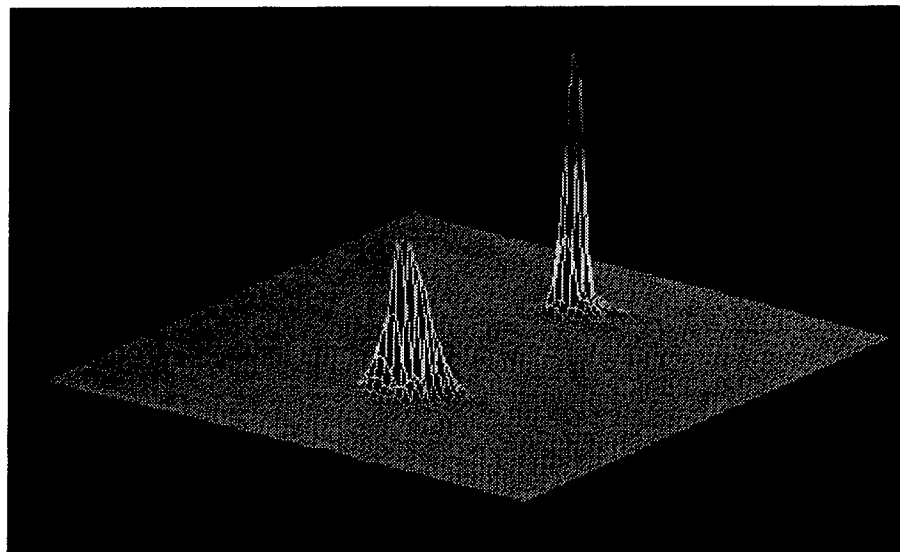


Figure 6 Experimental Layout for Closed Loop Tests With LCPM as Wave-Front Corrector



Open Loop
Strehl = .16

Closed Loop
Strehl = .25

Figure 7 Open and Closed Loop results with a Static Aberration

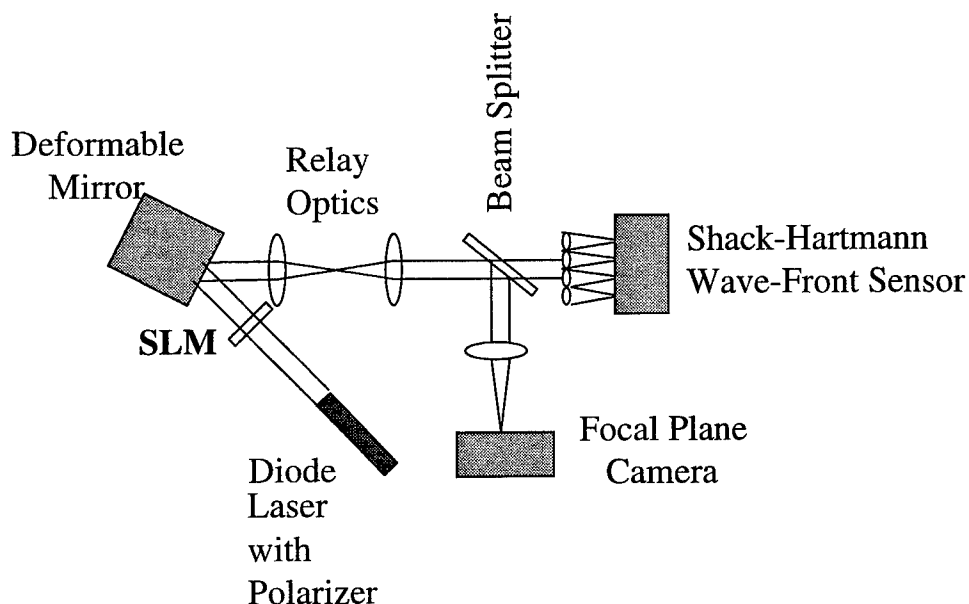


Figure 8 Laboratory Layout for Dynamic Disturbances with Deformable Mirror

We next wish to consider dynamic time varying aberrations. In order to generate the time varying sequence we use a continuous face sheet deformable mirror. A series of phase screens were calculated to simulate $D/r_0=6$ turbulence. The turbulence was generated using the first 36 Zernike polynomials to simulate Kolmogorov statistics. The sequence of phase screens was cycled at a rate of about five hertz. The system layout for dynamic aberration correction is shown in figure 8. In figure 9 the long exposure open and closed loop images are shown. The open loop Strehl ratio for the long exposure image was about .098, while the closed loop was .1816. This represents about an 80 percent increase in the Strehl ratio.

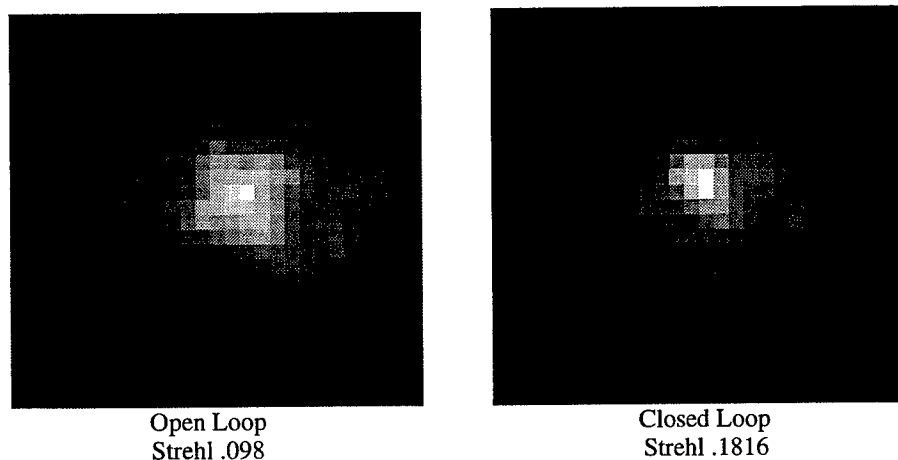


Figure 9 Long Exposure Dynamic Correction $D/r_0=6$

5. Conclusions

The liquid crystal spatial light modulator is a compact low cost alternative to deformable mirrors for adaptive optics systems. When used with polarized light, it acts like a piston only segmented deformable mirror. High order aberrations, produced by the discontinuities at the segment boundaries, can have an adverse effect when used with a Hartmann sensor. Special care must be exercised to mitigate this effect.

Zernike modal controllers have been proposed for use with this mirror in a closed loop feedback adaptive optics configuration. Such controllers have been shown to work well when only a few zernike modes are required to provide sufficient correction. However when working with a visible adaptive optics system, with D/r_0 values greater than 10, several hundred zernike modes would be required to achieve near full order correction. The computational complexity associated with fitting such a large number of zernike modes makes a zonal control algorithm attractive. We have in hand high-speed matrix multiply hardware for implementing real-time zonal control algorithms. For this reason we have been investigating the application of zonal control to the SLM.

The experimental results show that under the constraints discussed, a zonal control algorithm, similar to one used with a continuous face sheet hexagonal deformable mirror, can be used to control the SLM with a closed loop band-width of several hertz. The experimentation used one Shack-Hartmann sub-aperture per SLM segment. The Shack-Hartmann sub-apertures were off-set from the SLM segments by half a row and half a column. This allowed control of all 127 degrees of freedom possible with the corrector.

Static and dynamic disturbances were applied to the control system. The static disturbance wave-front had about one wave peak-to-valley distortion. Thus the displacements between SLM segments required to correct the wave-front were small and we did not have problems with the Shack-Hartmann spots breaking up. In addition the SLM segments have a maximum throw of only a little more than one wave, so the system can't correct for larger distortions. The dynamic disturbance was applied with a deformable mirror and was designed to have Kolmogorov statistics with $D/r_0=6$. System performance was limited by the small amount of throw, only one wave, possible with each SLM segment. In future experiments we plan to investigate a double pass configuration to increase the throw of each segment.

References

1. G.D. Love, "Wavefront Correction and production Zernike modes with a liquid crystal SLM", *Appl. Optics* **36**, (1997).
2. J. Gourley, G.D. Love, P.M. Birch, R.M. Sharples, A. Purvis, "A real-time closed loop liquid crystal adaptive optics system: first results", *Optics Comm.* **137** (1997).
3. W. Wild, E. Kibblewhite, R. Vuilleumier, "Sparse matrix wave front estimators for adaptive-optics system for large ground based telescopes," *Optics Lett.* **20** (9), 995-957 (1995).

Polychrome correction for telescope lens distortions using the liquid crystal optically addressed spatial light modulator

V.A.Berenberg, A.A.Leshchev, M.V.Vasil'ev, V.Yu.Venediktov

Institute for Laser Physics, SC "Vavilov State Optical Institute",
199034, St.-Petersburg, Russia

ABSTRACTS

Given are the results of experimental study on the quasi real time holographic correction for the lens distortions in the passive observational telescope in the visible range of spectrum, using the liquid crystal optically addressed spatial light modulator.

Keywords: dynamic hologram, holographic corrector, liquid crystal spatial light modulator, passive imaging telescope.

1. INTRODUCTION

The method of holographic correction for distortions, imposed by the primary mirror (lens) of the telescope, was first proposed and realized in the experiment in ^{1,2}. The holographic corrector was recorded by the coherent radiation, and its chromatism (grating disperse) was corrected for by use of the auxiliary diffraction grating, providing thus the possibility of imaging in the comparatively wide spectral range. These works, as well as much later investigations in USA ³⁻⁵ were realized with the use of static holographic media, providing thus correction only for the static distortions.

The principle of the holographic correction for the telescope lens distortions is illustrated by the Fig.1. Let the telescope is comprised by the distorted lens 1 and the eye-piece 2. This system is imaging the remote self-luminous object 4 in the registration plane 3. In the case of the high optical quality of the elements 2 and 3 the system resolution is determined by the properties of the lens 1. One can compensate for the lens distortions by the holographic corrector 5, mounted in the plane to which the eye-piece 2 images the pupil of the lens 1 ^{1,2}. The hologram is recorded by the coherent radiation as the interference pattern of the plain reference wave and the object wave, emitted by the point source, mounted in the plane of the object 4.

The light wave from this point source which has passed through the distorted lens bears the information on its distortions. This information is encoded in the hologram. On the stage of the hologram reconstruction the radiation, emitted by the point source and distorted on its path through the telescope will diffract on the hologram into the plain wave, coinciding with the reference wave, used for the hologram recording. Any luminous object can be treated as a set of the point sources. Hence the radiation from the object, distorted by the telescope, will diffract to the set of plain waves. These waves will reconstruct in the plane 3 the non-distorted image of the object notwithstanding the arbitrary distortions of the telescope lens 1.

The non-monochrome radiation from the object would be expanded by the hologram to the spectrum. This chromatism is to be corrected by the auxiliary static diffraction grating whose spatial frequency is equal to the spatial carrier of the holographic corrector.

2. THE CHOICE FOR THE CORRECTING ELEMENT

One can use the nonlinear optical phase conjugation for the dynamic correction for the primary lens (mirror) distortions⁶. In particular, in^{7,8} it was realized with the use of the stimulated Brillouin scattering. In this case, however, the imaged object is either to emit the coherent radiation or to be illuminated by such a radiation.

The highest efficiency among the nonlinear-optical media for holograms recording, providing dynamic correction for distortions in the wide spectral range, is revealed by the liquid crystal spatial light modulators (LC SLM)⁹ and by the photorefractive crystals¹⁰. For example, in¹¹, the use of LC SLM made it possible to correct for distortions in the spectral band with the width 10 nm, separated from the hologram recording wavelength in 90 nm. However, in this experiment the own chromatism of the hologram was not corrected, thus reducing the correction rate. In¹² the correction for the distortions of the optical elements was realized with the use of the photorefractive crystals BSO and NBS with the hologram record at the wavelength 514 nm. The holograms were reconstructed by the Ar-ion laser radiation at several discrete wavelength in the range of 476..514 nm.

Not that for the correction for distortions, imposed by the lens into the image of the distant and spatially-incoherent radiation it is sensible to use the thin holograms. The use of the volume (thick) holograms will result in extra limitations due to their angular and spectral selectivity¹², resulting in most cases in the impossibility to realize the most important advantage of this class of holograms - the high diffraction efficiency. So, to our opinion, the LC SLM medium is more prospective from the point of view of dynamic correction than the photorefractive media. The comparison of the combination of such a basic parameters, as the sensitivity, response time, reversibility, resolution and depth of phase modulation, realized in these two media, also puts the LC SLM ahead.

This paper is devoted to the experimental results on thermal object imaging in the wide spectral range by the model telescope with the dynamic holographic correction for its primary lens and auxiliary correction for the hologram chromatism. The dynamic hologram was recorded in LC SLM, using the polymer photoconductor^{13,14}; the holograms were recorded in pulsed mode^{15,16}.

The SLM was realized as the sandwich structure, mounted in the gap between two glass substrata with the clear diameter 35 mm. The light was modulated by S-effect. The layer of LC thickness was $\sim 4 \mu\text{m}$, the optical anisotropy at $0.63 \mu\text{m}$ equaled 0.16. The thickness of the polyimide photo layer was $\sim 1.4 \mu\text{m}$.

Such a SLM can be used for recording of the CW or pulsed radiation while controlled by the CW or pulsed voltage. According to the previous studies the best diffraction efficiency and the smallest influence of the electro-chemical processes onto the SLM action are realized when the record is done by the short (some dozen μsec or shorter) radiation pulses, and SLM is controlled by the rectangular voltage pulse.

The SLM action in this case is based on the transient processes in photosensitive and LC layers and can be clarified in the following way. The SLM is fed by the rectangular voltage pulse, whose duration and width are chosen from the requirement of the highest diffraction efficiency obtaining. Due to the proper relationship between the resistance of these two layers the voltage, applied to the LC layer is sufficient for the LC reorientation from the primary planar orientation to the homeotropic one. Hence during the controlling voltage pulse the reorientation of LC molecules is impossible. Recording pulse of radiation reaches the element in several hundred of milliseconds after the start of the voltage pulse; the value of diffraction efficiency of the hologram is insensitive to this delay duration. The photoinduced free carriers of the charge are drawn by the electric field to the semiconductor layer boundaries and stored there, screening thus its volume. The image relief thus induced in the structure is stored till the transient processes complete.

After switching off the voltage pulse the charges, stored at the photoconductor layer boundaries begin move inside this layer under the action of the polarization field and recombine. The voltage, applied to LC layer is thus reduced and the LC molecules begin relax to the primary planar orientation. The parameters of the relaxation process depend on the structure of the recorded image relief.

Variation of the voltage pulse, feeding the SLM, duration and of its synchronization with respect to the light pulse provides the control of the temporal delay from the hologram recording to the moment of its highest diffraction efficiency. In our experiments we could vary this delay from 100 msec to several dozen seconds, while the overall lifetime of the hologram was 0.2 sec FWHM.

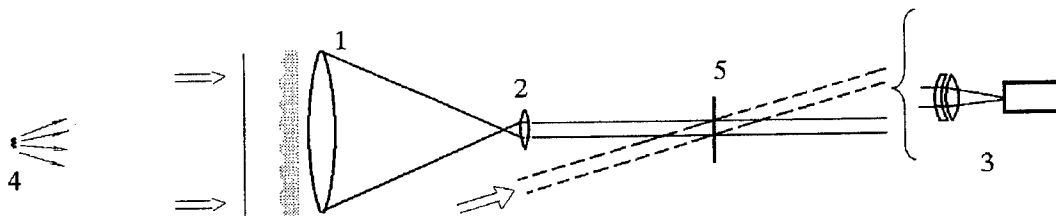


Fig. 1. Principle scheme of holographic correction for telescope lens distortion

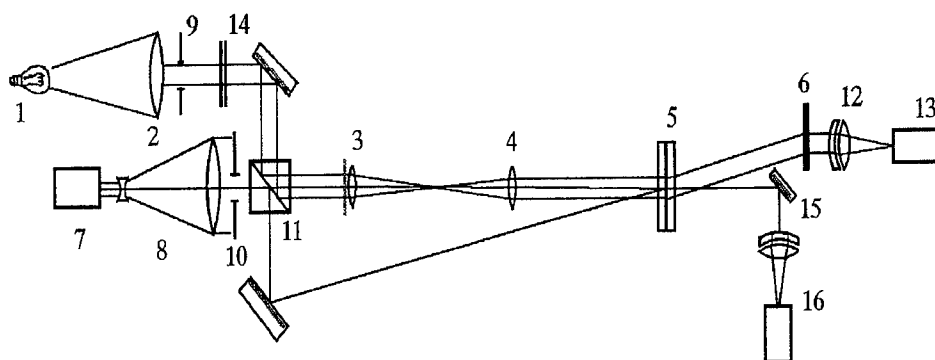


Fig. 2. Experimental setup



Fig. 3. Images of self luminous wire:

- (a) non-corrected, primary lens distorted by scattering plate with the divergence 6×10^{-3} rad;
- (b) corrected, primary lens distorted by scattering plate with the divergence 2×10^{-3} rad, spectral bandwidth 10 nm;
- (c) corrected, primary lens distorted by scattering plate with the divergence 6×10^{-3} rad, overall visible spectrum.

3. EXPERIMENTAL SETUP

The experimental setup is shown in the Fig.2. The thermal source at the infinity was simulated by the tungsten wire of the lamp 1, mounted in the focal plane of the auxiliary lens 2. This object was imaged by the lens telescope, comprised by the primary lens 3 to be corrected and the eye-piece 4. The angular size of the imaged object was some 10^{-2} rad. Two identical achromatic lenses with the focal length of 230 mm were used as the elements 3 and 4. The corrector unit comprised the LC SLM 5, the transparent phase (holographic) diffraction grating 6 for the dynamic hologram chromatism compensation and the scheme for the corrector recording.

The hologram-corrector was recorded by the pulsed radiation of second harmonics ($0.54 \mu\text{m}$) of Nd:YAP laser 7 as the interference pattern of the plain reference wave and the object wave, transmitted via the telescope. The telescope 8 ($10\times$) improved the spatial homogeneity of the recording beams. The useful clear aperture of the SLM was determined by the apertures 9 and 10 and equaled 15 mm. Beam split cube 11 (transparency 50 %) separated the recording beams and, in a time, combined the radiation from the imaged object 1 and the probe beam of laser radiation.

The eye-piece 4 imaged the pupil of the lens 3 in the plane of the corrector 5. The spatial carrier frequency of the dynamic hologram was equal to the spatial frequency of the grating 6 and was equal 95 mm^{-1} . Such a value was chosen as the trade-off value, providing both spatial separation of the object images in different diffraction orders and sufficiently high diffraction efficiency, reduced with the further spatial carrier increase: the temporal behavior of the diffraction efficiency of the dynamic hologram, recorded by two plain waves of the pulsed radiation ($0.54 \mu\text{m}$), was studied in special experiment. This hologram was reconstructed by the CW radiation of He-Ne laser. The maximal momentary value of the diffraction efficiency for the spatial carrier of 100 mm^{-1} equaled 20..25%, for 150 mm^{-1} - 6..9%, 200 mm^{-1} - 2% and 300 mm^{-1} - 1%.

The radiation from the thermal source, diffracted from the grating 6, was caught by the lens 12 and focused to the CCD-matrix 13. The filters 14 provided variation of the spectral band, used for the object imaging. The zero order diffraction on element 5 radiation from the thermal object was caught by the plain mirror 15 and used for control non-corrected image of the object, registered by the system 16.

4. EXPERIMENTAL RESULTS

The primary lens distortions were simulated by various distorters, mounted before this lens. For example, the Fresnel biprism simulated the local wedge distortions, equivalent to the effect of mutual tilt of the synthesized mirror segments. The small scale distortions of the lens were simulated by the glass plates, etched in the hydrofluoric acid. In the Fig.3a is shown the non-corrected image of the wire, corresponding to the latter case of distortions.

With the use of the band filter (width 10 nm, maximal transparency at 530 nm) the corrected image quality (Fig.3b) was nearly diffraction limited both with the use of wedge distorter or of the scattering plates with the divergence of the scattered beam up to 2×10^{-3} rad (FWHM). The use of strong ($\sim 6 \times 10^{-3}$ rad) scattering plate resulted in some background in the image, leading to the image contrast deterioration, but not to washing out of the image. Similar results were observed with the use of filter, selecting the band of 80 nm width with the maximum at 545 nm.

The quality of the image, registered in the overall visible spectrum without the color filters to a large extent depended on the character of distortions applied. Wedge distortions resulted in significant spectral washing out of the image. Note, that the complete compensation of the chromatism of the dynamic hologram is possible only for the equal spatial frequencies of this hologram and auxiliary grating. The wedge-like distortions modify the former frequency and thus lead to the residual non-compensated chromatism, growing with the spectral band width.

The growth of the small-scale distortions rate resulted in the image contrast deterioration. However, even with the strongest distorter used ($\sim 6 \times 10^{-3}$ rad) the image, registered in the overall visible spectrum, was of satisfactory quality (Fig.3c).

5. CONCLUSION

In the reported experiment the source of coherent radiation, used for the corrector record, was mounted in the plane of the object (or, generally speaking, optically conjugate plane). In practice of imaging of the remote object it is impossible. In the so called bypass optical schemes⁷ the source of the radiation, used for reading out of the primary lens (mirror) distortions can be mounted nearby this lens or mirror, say, in the latter center of curvature. In this case the distortions are compensated (corrected) not completely, but down to some residual error. However, depending on the telescope design the surplus can be some dozen or hundred times^{7,8}.

Hence the results of the reported experiment promise the successful use of the optically addressed LC SLM as the dynamic holographic media for the record of the holographic correctors to be used in the passive bypass imaging telescopes.

REFERENCES

1. Denisuk Yu.N., Soskin S.I. Holographic correction of deformational aberrations of the primary mirror of the telescope. *Opt. Spektrosk.*, 1971, Vol. 31. No. 6, p. 991-997, (in Russian).
2. Denisuk Yu.N., Soskin S.I. Holographic correction of deformational aberrations of the primary mirror of the telescope. *Opt. Spektrosk.*, 1972, Vol. 33, No. 5, p. 994-996, (in Russian).
3. Munch J., Wuerker R. Holographic technique for correcting aberrations in a telescope//*Appl. Opt.* - 1989. - Vol. 28, No. 7. - P. 1312-1317.
4. Munch J., Wuerker R., Heflinger L. Wideband holographic correction of an aberrated telescope objective//*Appl. Opt.* - 1990. - Vol. 29, No. 16. - P. 2440-2445.
5. Andersen G., Munch J., Veitch P. "Holographic correction of large telescope primaries by proximal, off-axis beacons// *Appl. Opt.* -1996-V.35, No.4 P. 603-608.
6. Zel'dovich B.Ya., Pilipetsky N.F., Shkunov V.V. Phase conjugation. - Moscow, 1985, 240 p. (in Russian).
7. A.A.Leshchev, G.A.Pasmanik, V.G.Sidorovich, M.V.Vasil'ev, V.Yu.Venediktov. Compensation for distortions in the imaging systems, using phase conjugation technique. *Izvestiya Akademii Nauk SSSR*, v.55, 2, p.260-266, 1991. (In Russian).
8. Leshchev A. A., Sidorovich V. G., Vasil'ev M. V., Venedictov V.Yu., Pasmanik G.A. Nonreciprocal optical systems with phase-conjugating mirrors - a new class of optical imaging systems. *International Journal of Nonlinear Optical Physics.* - 1994. - Vol. 3, No. 1. - p. 89-100.
9. Vasil'ev A.A., Casasent D., Kompanets I.N., Parfenov A.V. Spatial light modulators. Moscow, Radio i Svyaz. 1987. 320 p. (in Russian)
10. M. P. Petrov. S. I. Stepanov. A. V. Khomenko. Photorefractive crystals in coherent optics. St.-Petersburg. Nauka. 1992. 320 p. (in Russian)
11. Kramer M. A., Wetterer C. J., Martinez Ty. One-way imaging through an aberrator with spatially incoherent light by using an optically addressed spatial light modulator// *Appl. Opt.* - 1991. - Vol. 30, No. 23. - P. 3319-3323.
12. Dimakov S.A., Klimentiev S.I., Svetsitskaya N.A., Sherstobitov V.E. Compensation for optical elements distortions by means of dynamic holography in "white light". *Opt. Spekt.*, 1996, Vol.80. No 4, p. 699-704 (in Russian).
13. Groznov M.A., Myl'nikov V.S., Soms L.N., Tarasov A.A. Liquid crystal spatial light modulator with the resolution of more than 1000 lines per mm. *Zh. Tekh. Fiz.*, 1987, Vol. 57. No. 10. p. 2041-2042, (in Russian).
14. Myl'nikov V.S. Liquid crystal spatial light modulators with the organic polymer photoconductor. *Optical Journal*, 1993, #7, p.41-45 (in Russian).
15. Kamanina N.V., Soms L.N., Tarasov A.A. Holographic correction for distortions using the liquid crystal phase light modulators. *Opt. Spektrosk.*, 1990. Vol. 68. No. 3, p. 691-693 (in Russian).
16. Berenberg V.A., Kamanina N.V., Soms L.N. Holographic correction for distortions using the liquid crystal phase light modulators under different frequencies of recording and reconstructing radiation. *Izv. Akad. Nauk SSSR, Ser. Fiz.*, 1991, Vol. 55. No. 2. p. 236-238, (in Russian).

System electronic design for a telescope mounted deformable mirror system

Samuel C. Rogers, Scot W. McDermott
Logicon RDA
Albuquerque, New Mexico U.S.A.

Steve Sandven
Applied Technology Associates
Albuquerque, New Mexico U.S.A.

ABSTRACT

Logicon RDA and Applied Technology Associates have supported PL/LIMI on various imaging experiments during the past years. We are currently supporting an adaptive optics experiment using a 349 actuator deformable mirror. We discuss the system requirements, the design schedule, the final hardware configuration, simulated and actual system performance and planned enhancements.

Keywords: Deformable Mirror, Actuator, Electronic system

1. INTRODUCTION

At the Phillips Laboratory in Albuquerque New Mexico we are conducting experiments with adaptive optics. Our instrumentation for atmospheric compensation of passive illuminated objects is a deformable mirror mounted on a telescope. In September of 1995 we employed a 197 actuator deformable mirror using a single Sun Workstation. Today we have designed a four computer system using 349 actuators with the power to image in the daytime. We will start with the old system and its performance and then show the needed enhancements for controlling 152 more actuators real time.

2. BACKGROUND AND BASICS

The diagram of our system is shown in figure 1. A sun illuminated object is seen through atmospheric distortion by a telescope. Relay optics transfer the light to a pupil and image plane cameras. The light to the pupil plane is altered by a two dimensional lenslet array focused at the camera. The effect is an two dimensional array of spots called subapertures representing the wavefront on the imager. A matrix multiplication is performed with the subaperture centroids and a matrix defining the geometry of the deformable mirror. The calculation results in a set of actuator commands for the deformable mirror. The actuator commands are then manipulated by a control law algorithm before the actuators are commanded to position.

The difficulties with this experiment is controlling the deformable mirror and bandwidth. In theory, the approach is to freeze the image, make the matrix calculation and update the mirror before the atmosphere changes. We presently have a fast camera from Lincoln Laboratorys with a frame rate of 1 millisecond to, in theory, freeze the image. Our hardware, although, is limited. The sequence of calculations mentioned above must occur in nearly one camera frame time, to correctly control the deformable mirror. In our first experiment with 197 actuators, it didn't take long to realize that we weren't creative enough to write high level software, like C, for an I860 board to sustain that kind of timing. The only way our setup could keep up with the camera frames rates was to build hardware modeled exactly after the matrix calculation. Although there are several methods using hardware like a DSP chip for each actuator available, our requirements for the telescope limited us to the direct calculation.

The direct calculation was then broken up into two parts, a subaperture centroider and a matrix multiplication board. The control algorithm was implemented on a CSPI SuperCard. The results of the bandwidth are presented in figures 2 and 3.

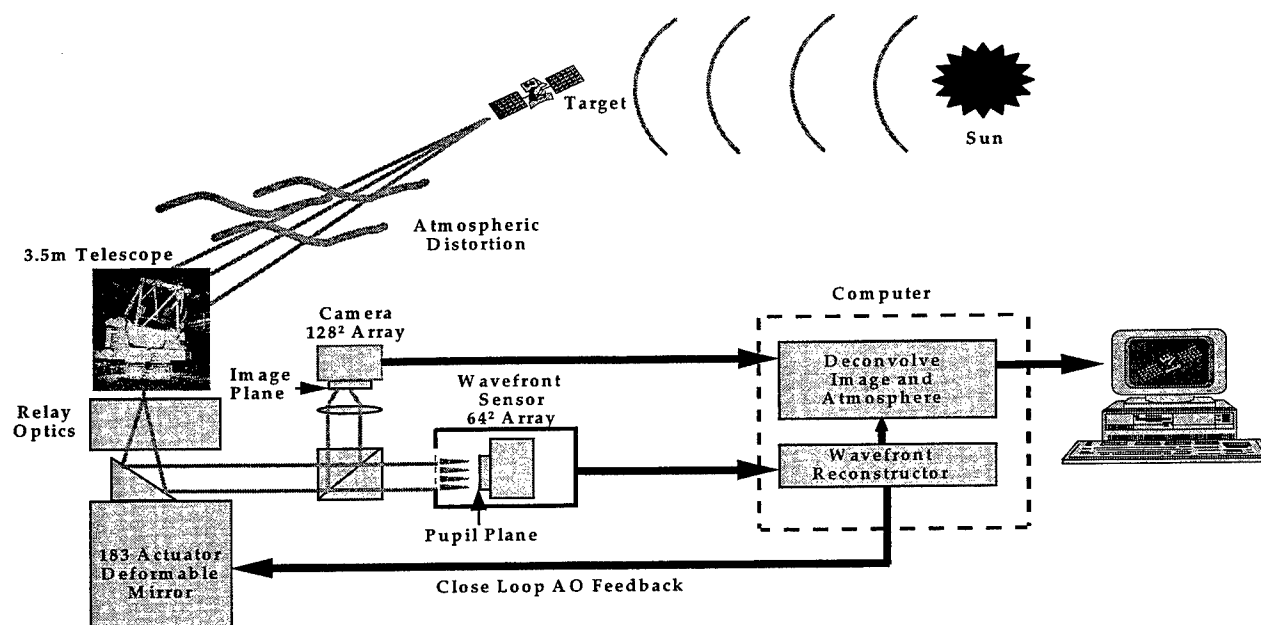


Figure 1. Deformable Mirror System

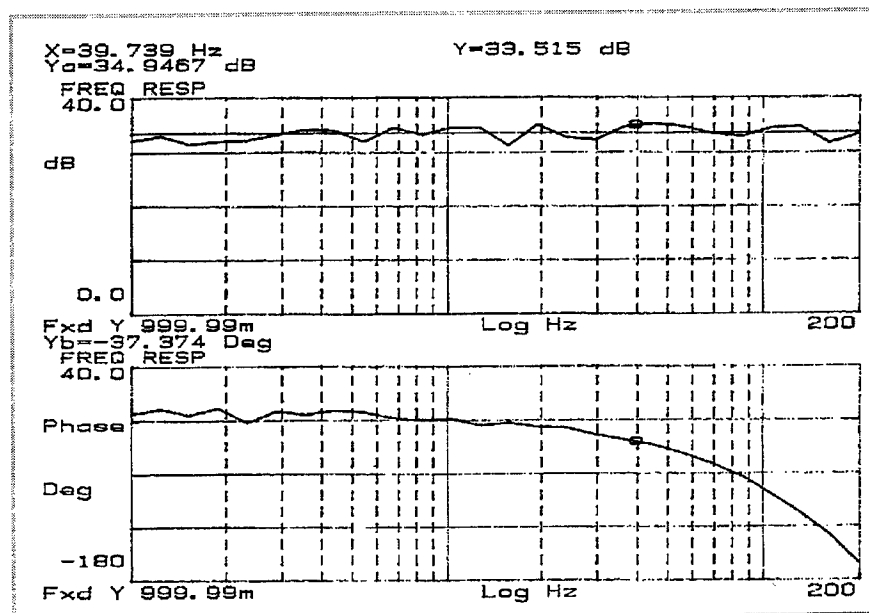


Figure 2. Open loop measurement.

It should be mentioned that the bandwidths on the figures are optical and not electrical. The feedback to the control loop is digital video data.

3. DESIGN

In the first deformable mirror experiment we gained experience in deformable mirrors and adaptive optic systems. Our next step was to upgrade the existing system to adaptive optic correction with daytime imaging. We also wanted to incorporate a new camera with a faster frame rate and a new deformable mirror with more actuators. The new system basically had to run faster with more calculations than the old experiment. Past experience showed an increase in bandwidth would only come about with designing specific hardware rather than writing software to conform to commercial hardware. Adhering to this hardware specific design, the system was divided into tasks where printed circuit boards performed exact calculations. The software was then used to set values on the boards like image size, region of interest, etc. This method left the host computer accessing board specific diagnostics real time while the hardware performed autonomously. Figure 5 shows an overview of the system designed to achieve our goals. One should notice the separation of focal plane processing, pupil plane processing, GUI implementation, and data analysis. The process of focal and pupil plane sensors will be discussed in detail.

The focal plane process was divided into three subprocesses as shown in figure 6. The subprocesses are the background mitigation and display, the full frame centroid and the fast steering mirror control law. At the input of the mitigation board digital video is clocked in at 10 megapixels per second. Digital video data seen at the input includes horizontal and vertical synchs with 12 bit pixel values and a pixel clock. The mitigation board has the ability to use data from sections of the input called the region of interest. The VME host sets this input region of interest with values from 64×64 to a 256×256 pixel array. This feature is designed into the board for general use of camera arrays like the pupil plane at 64^2 and the focal plane at 128^2 in our experiment. Lincoln Laboratory cameras come equipped with four extra lines furnishing the process with 2 bias lines and 2 background lines at the start of the frame. The mitigation board can average one of these four lines selected by the VME host for subtraction from the same frame. This result actually helps bring down the noise in the image caused by the sensor and associated electronics. Farther into the mitigation board is an on board full frame storage ram. The memory is used to collect up to 16 full frames of data for a single averaged frame. In real time this data is read out, scaled and subtracted from the incoming video stream. The result is a background subtracted image essential for daytime imaging. The mitigation board can also take snapshot images at selected process points for diagnostic monitoring and data acquisition. The mitigation board also supplies a progressive scan 8 bit pseudo color display with 800×600 pixels, 70 hertz refresh with 4 bit overlays. This board is a fully functional VME A24:D16 Slave with interrupt capabilities.

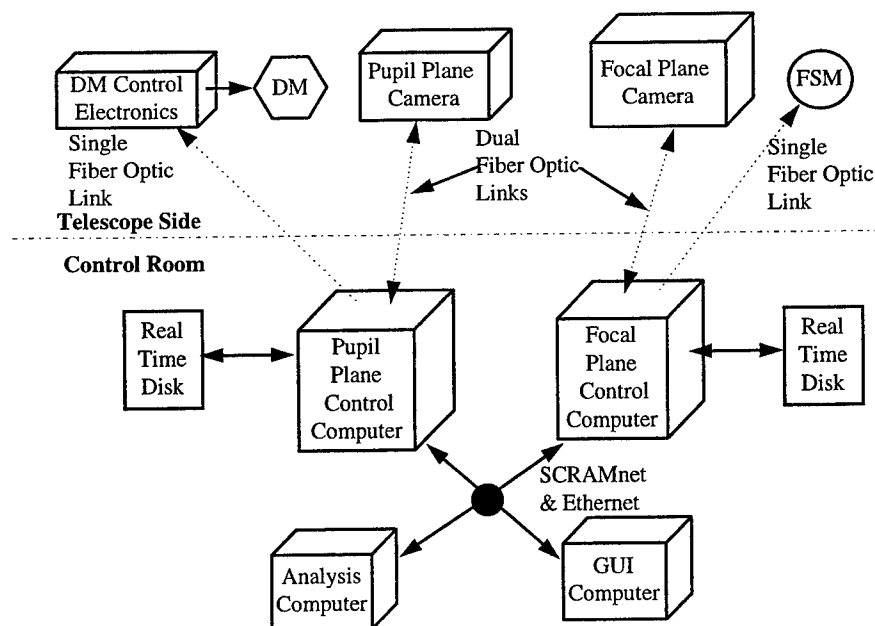


Figure 5. Deformable Mirror System

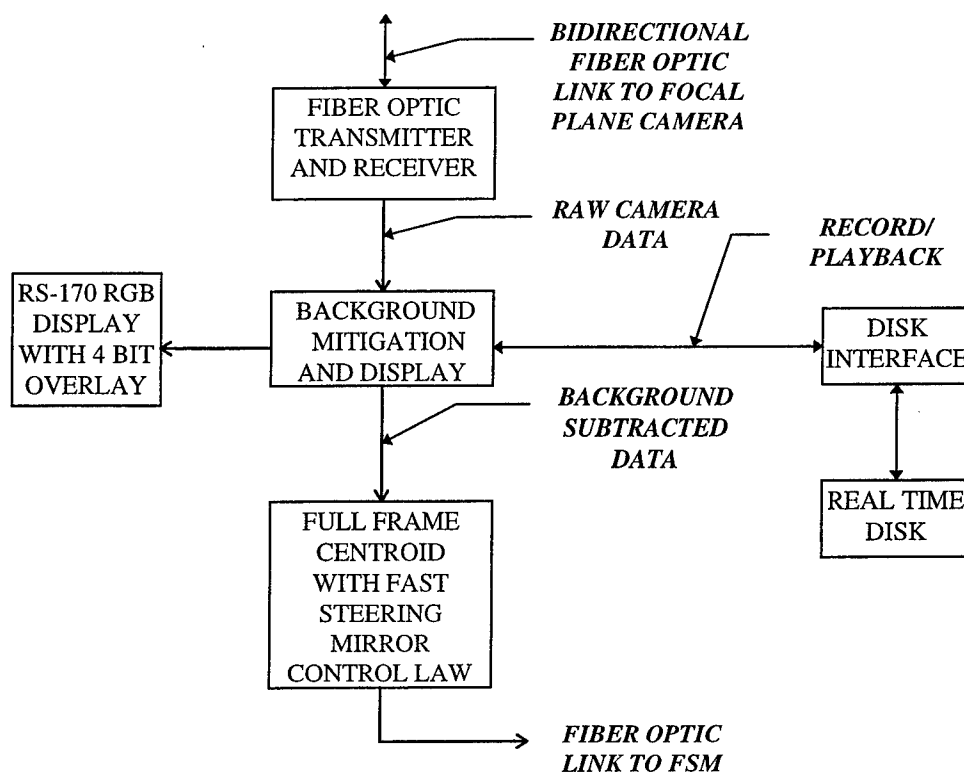


Figure 6. Focal Plane Process

The full frame centroid board is the next process in the chain of events. Data enters this centroid board with a few pixel latency following the mitigation board. The centroid board accepts data up to 10 megapixels per second and contains a similar VME controlled region of interest as the mitigation board to remove unneeded pixel data. The board then computes x and y moments and a total sum of the image. The results of a division between the moments and the total sum, a centroid or x and y spot location, is then modified by the autonomous control law calculation based on a leaky integrator. The final result or position command is sent to the Fast Steering Mirror electronics via fiber optic link communications. The VME host can also download a threshold value to exclude pixel values from these calculations if needed. The VME host again can alter the gain, leakage, and the control point. The full frame centroid board is also a fully functional VME A24:D16 Slave with interrupt capabilities.

The pupil plane process is shown figure 7. Similar to the focal plane process, data is received from the telescope by fiber optic communication and clocked forward to the mitigation board. Data then enters the wavefront slope calculation printed circuit board. The input data rate here again is 10 megapixels per second and the pixel array region of interest is controlled by registers accessible by the VME host. As in the full frame centroid board, x and y moments, total sums, and slopes are computed on the slope calculator board except in a scaled version. Each subaperture is small like three by four pixels, instead of an entire image. The size of the subapertures are variable and are located anywhere within an image. The VME host loads an on board memory which represents a single frame of camera data. Each location in this memory dictates whether a pixel value is included in a subaperture centroid. Data not included in the calculation is ignored. Thresholding is also another option designed into this slope calculator board. The host computer can load a value for pixel thresholding prior to the x and y moment and total sum calculations as well as a total count in a subaperture. These options give the user the flexibility to actual exclude pixel values and subapertures in the real time reconstruction of an image. Diagnostics included in the hardware design are all values of x and y moments, total sums and x and y slopes computed in a single camera frame. This board also complies the VME Slave A24:D16 protocol and interrupts if request to at the end of a the calculation.

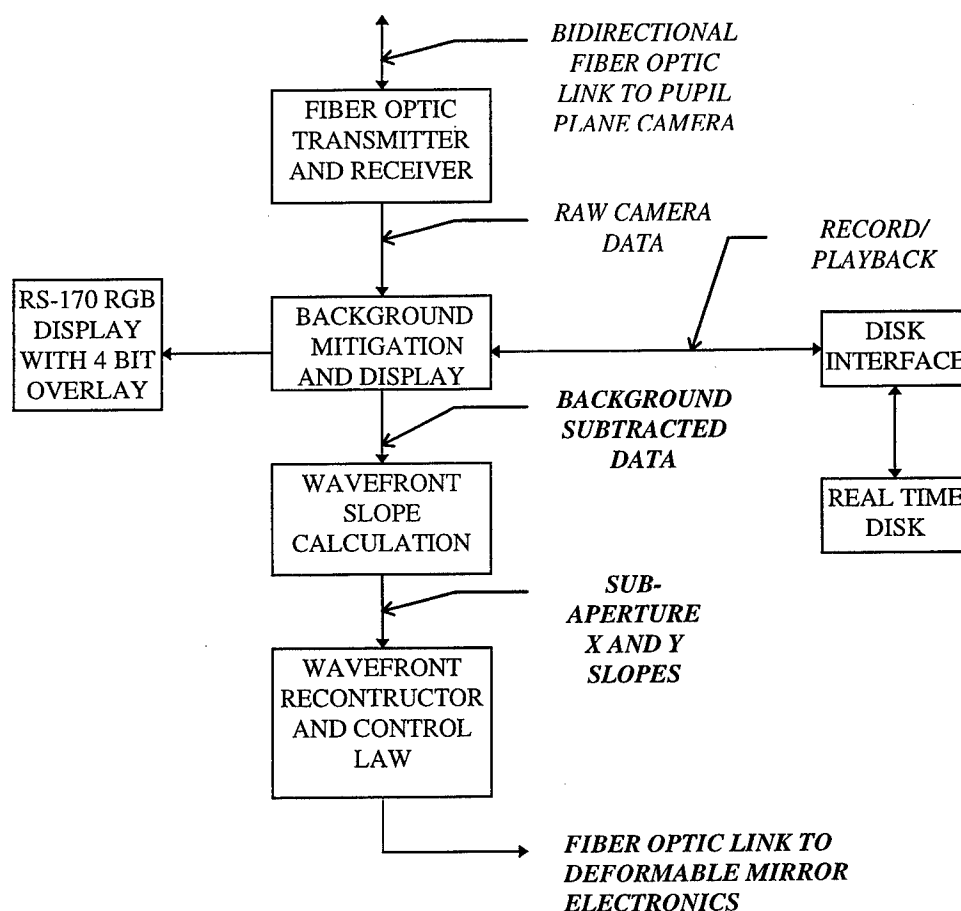


Figure 7. Pupil Plane Process

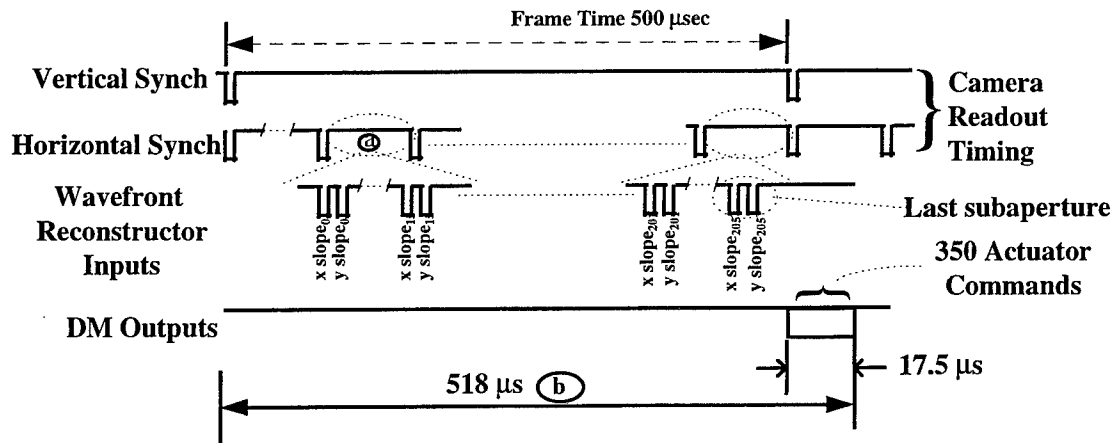
The next board in the pupil plane process is the Wavefront Reconstructor. The Wavefront Reconstructor performs a matrix multiplication,

$$\mathbf{p} = \mathbf{H} \mathbf{s}, \quad (1)$$

used to control the deformable mirror¹. Where \mathbf{H} , is a matrix characterizing the geometry of the deformable mirror, \mathbf{s} is a column vector of supaperture slopes from the Slope Calculation Board and \mathbf{p} is a column vector of wavefront phases better known as actuator positions. The \mathbf{H} matrix is limited to 393,216 elements or 512 acutators with 384 subapertures and is downloadable by the host computer. The process of matrix multiplication is divided into six parallel processing paths yielding 480 mega-multiply accumulates and an aggregate of 2.4 giga-operations per second. This number of paths and speed demanded a creative printed circuit board layout for a VME 6U form factor. The final design, three different circuit boards, was implemented to ease in debugging and testing. The main board, which is a VME Slave A24:D16 interrupter, latches in the slope data from the Slope Calculation Board and directs the data the second board. Board two distributes the slopes to the parallel processing section or six copies of board three, where the matrix multiplication occurs. The results of the multiplication is feed back to board one at the control law calculation. The control law is again based on the leaky integrator with each actuator having independent gain, leak and control point, all which are downloadable by the host computer. The output of the control law, the actuator position commands, are directed to the deformable mirror electronics via high speed fiber optic link. The fiber link has the capability to update 350 actuators in 17 microseconds running at 50 Mbytes per

second. Also included on the Reconstructor is snapshot memory accessible by the host containing actuator commands before and after the control law.

Figure 8 below details the wavefront timing of the deformable mirror's system. The diagram includes the relationship between the pupil plane camera's readout timing, the wavefront reconstructor inputs and the deformable mirror outputs.



(a) Horizontal Synch every 7.4 μs. Number of subapertures per line varies.

(b) Calculation Latency $250 \mu s(1/2 \text{ frame}) + 518 \mu s = 768 \mu s$

FIRST ORDER PREDICTED CLOSED LOOP PERFORMANCE

$$1 / (\text{Latency} * 10) \Rightarrow \sim 130 \text{ Hz}$$

Figure 8. Deformable Mirror Timing Diagram

4. Status

The 349 actuator mirror design status is as follows. The background mitigation and display and full frame centroid boards have been completely tested. The wavefront slope calculation board is designed and awaits manufacturing. The wavefront reconstruction board is in the design quality assurance phase. The date for system integration is not scheduled.

5. Conclusions

As shown in the previous pages, the older wavefront processing hardware performed as expected, yielding the predicted closed loop bandwidth for a 163 actuator deformable mirror. We are using the same approach and anticipate no problems with the newer hardware. We believe that the wavefront reconstruction approach outlined in this paper is scaleable, cost effective solution to control a medium sized deformable mirror (up to 500 actuators) with a wavefront sensor running at rates in excess of 2000 frames per second to the Wavefront Reconstructor Board and the fiber optic timing.

References

- [1] Browne, S. L., Vaughn, J. L., Tyler, G. A., Gonglewski, J. D., "A Computationally Efficient Method For Wavefront Reconstruction", *Topical Meeting On Adaptive Optics*, Cullum, M., pg125-130, Garching Bei Munchen, Germany, October 2-6, 1995.

Author Index

- Anderson, Gail P., 2
 Andrews, Larry C., 84
 Baruffolo, Andrea, 73
 Berenberg, Vladimir A., 147
 Bousek, Ronald R., 11
 Bril, Andrey I., 107
 Browne, Stephen L., 138
 Chetwynd, James H., 2
 Conley, T. D., 2
 Czyzak, Stanley R., 65
 Dayton, David C., 138
 Devir, Adam D., 2
 Dowling, James A., 11
 Dror, Itai, 44
 Farinato, Jacopo, 73
 Fortes, Boris V., 98
 Fox, Marsha J., 11
 Gagge, Chie L., 84
 Ghedina, Adriano, 73
 Gonglewski, John D., 138
 Grasso, Robert J., 124
 Grigorov, Ivan, 34
 Harvey, James E., 84
 Holland, Donald, 65
 Kabashnikov, Vitaly P., 29, 107
 Kelly, Brian T., 11
 Kelly, Deborah E., 84
 Khodyko, Yuriy V., 107
 Kolev, Ivan N., 34
 Kopeika, Norman S., 44
 Kopytin, Yuri D., 20
 Kuzmina, Natalya V., 29, 107
 Leshchev, Alexey A., 147
 Lukin, Vladimir P., 98
 Luvera, Giovanni, 84
 Matson, Charles L., 65
 McDermott, Scot W., 138, 152
 Metelskaya, Natalya S., 29
 Mosley, Debora E., 65
 Nadile, Richard M., 2
 Nosov, Evgenii V., 20, 98
 Nosov, Victor V., 20
 Notash, Ali, 84
 Okoulov, Vitaly L., 116
 Parfenov, Vadim A., 93
 Parvanov, Orlin, 34
 Phillips, Richard L., 84
 Pierrottet, Diego F., 65
 Ragazzoni, Roberto, 73
 Ratkowski, Anthony J., 2
 Richter, Dale A., 11
 Rogers, Samuel C., 138, 152
 Ruffatto, Donald, 65
 Sadot, Dan, 44
 Sandven, Steven C., 138, 152
 Sellar, R. Glenn, 84
 Senft, Daniel C., 11
 Shestakov, Alexander P., 116
 Skakalova, Toni, 34
 Snezhkov, George Yu., 116
 Stappaerts, Eddy A., 124
 Stein, Karin, 52
 Vasil'ev, Michael V., 147
 Venediktov, Vladimir Yu., 133, 147
 Venglyuk, Valery I., 116
 Weeks, Arthur R., 84
 Xu, Jing, 84